Analysis and Performance of Symmetric Nonaqueous Redox Flow Batteries

James Saraidaridis

DPhil in Engineering Science

St. Peter's College

University of Oxford

"*And the only mode in which you can derive even a tolerable idea of the whale's living contour, is by going a whaleing yourself; but by so doing, you run no small risk of being eternally stove and sunk by him. Wherefore, it seems to me you had best not be too fastidious in your curiosity touching this leviathan.*"

– Herman Melville

Acknowledgements

This dissertation and my improvement as a researcher over the course of its production were facilitated by the technical and moral support of others. Professor Charles Monroe, my advisor, has been the largest influence on this project and my graduate education. Professor Monroe knows where he stands, a confidence that I respect and strive for myself. I admire his commitment to enriching students and returning them to the world improved. I am grateful for the freedom he afforded me during my graduate studies, which has allowed me to mature as a researcher and an individual.

Other technical advisors have helped me over the past 5 years. Professor Bart Bartlett and Dr. Emily Nelson offered their chemistry expertise and the use of their lab equipment over the course of early graduate projects on magnesium electrolyte synthesis and spectroelectrochemical analysis. Professor Melanie Sanford and her then post-doctoral researchers, Dr. James Suttil and Professor Christo Sevov, provided synthetic expertise and lab equipment vital to the synthetic efforts pursued in this dissertation. More recently, Professor Michael Willis and his post-doctoral researcher, Dr. Robert Straker, shared their synthetic expertise and executed scale-up efforts that allowed laboratory-scale organic flow cell experiments. I am indebted to all these researchers for their guidance and willingness to share resources, not least of which was their time.

The members of the Monroe group are an enduring source of technical knowledge and camaraderie. From my predecessors who were exemplars that influenced my development and early efforts: Dr. Aaron Shinkle, Dr. Sun-Ung Kim, Dr. Jing Liu, Dr. Gulin Vardar, and Dr. Lucas Griffith. To my capable peers whose shared

effort made all our lives easier: Saber Hou, Priyamvada, Howie Chu, Simran Dhillon, Dr. Guanchen Li.

In particular, Luke demonstrated versatility across experimental and mathematical research topics that I still strive to emulate. His proficiency at understanding, maintaining, and repairing laboratory equipment still impresses me, especially after those responsibilities fell on my shoulders. Saber and Howie have been vital experimental teammates that shared the task of rebuilding and maintaining the new laboratory in Oxford. Priyam, who replaced Jing as the group's resident modeling reference, is similarly willing to share her time to ponder my often confusedly posed questions.

There are several funding sources that supported my work both in Ann Arbor and Oxford. Denso funded my first year at the University of Michigan while I was on a magnesium-oxygen battery project. NSF supported the remainder of my time at the University of Michigan *via* Prof. Monroe's CAREER award (1252544). Since moving to the University of Oxford, the Department of Engineering Science and Siemens UK sponsored my work.

The last 5 years were not spent only in the lab and that remainder, spent with friends and family, replenished my motivation and defined my experiences in the small cities of Ann Arbor and Oxford. The strength of the friendships I formed with Trevor, Josh and Libby truly surprised me. Dana was a source of stability during a tumultuous time. Tino and Matt generously adopted an American curmudgeon into their midst. Ethan, Jessie, Karl, and Nick continued their efforts to maintain our long-distance friendships. My family made completing this degree possible not only with their love and support throughout its duration, but with the character they sought to foster in me beforehand.

Research Publications and Conference Presentations

1. J. D. Saraidaridis, C. W. Monroe. Economic case for symmetric nonaqueous redox flow batteries. *In preparation.*

2. J. D. Saraidaridis, C. W. Monroe. Flowrate dependent performance of a symmetric, nonaqueous vanadium flow battery with a porous separator. *In preparation.*

3. J. D. Saraidaridis, J. A. Suttil, C. W. Monroe. High-voltage organic-powered symmetric redox flow batteries. *In submission.*

4. Current and Flowrate Performance of a Nonaqueous Symmetric Redox Flow Cell. J. D. Saraidaridis, C. W. Monroe. *UK RFB Network Launch Meeting*, Manchester, United Kingdom. June, 2017.

5. Exploring Rate Capabilities of Symmetric Nonaqueous Redox Flow Batteries. J. D. Saraidaridis, C. W. Monroe. *ECS Spring Meeting*, New Orleans, Louisiana. May, 2017.

6. Large-scale preparation of redox active organics for symmetric nonaqueous redox flow batteries. J. D. Saraidaridis, R. Straker, C. S. Sevov, J. A. Suttil, M. S. Sanford, M. C. Willis, C. W. Monroe. *ACS Spring Meeting*, San Francisco, California. April, 2017.

7. Towards Symmetric All-Organic Flow Batteries. J. D. Saraidaridis, C. S. Sevov, J. A. Suttil, M. S. Sanford, C. W. Monroe. *International Flow Battery Forum 2016*, Karlsruhe, Germany. June, 2016.

8. J. D. Saraidaridis, B. M. Bartlett, C. W. Monroe. Spectroelectrochemistry of Vanadium Acetylacetonate and Chromium Acetylacetonate for Symmetric Redox Flow Batteries. Journal of the Electrochemical Society. **163**: 7(2016): A1239-A1246.

9. Organic Active Species for Nonaqueous Redox Flow Batteries. J. D. Saraidaridis, J. A. Suttil, C. S. Sevov, M. S. Sanford, C. W. Monroe. *ECS Conference on Electrochemical Energy Conversion & Storage with SOFC-XV*, Glasgow, Scotland, United Kingdom. July, 2015.

10. Electrochemical Analysis of Chromium Acetylacetonate for Nonaqueous Redox Flow Batteries. J. D. Saraidaridis, C. W. Monroe. *ECS Annual Meeting*, Cancun, Quintana Roo, Mexico. October, 2014.

11. Plating/Stripping Performance of Different Substrates in Magnesium Borohydride Solution. J. D. Saraidaridis, G. Vardar, A. Sleightholme, D. Siegel, C. W. Monroe. AIChE Annual Meeting, San Francisco, CA. November, 2013.

12. S. Sen, J. D. Saraidaridis, S. Y. Kim, G. T. R. Palmore. Viologens as Charge Carriers in a Polymer-Based Battery Anode. *ACS Applied Material & Interfaces*. **5**: 16(2013): 7825-7830.

Table of Contents

Acknowledgements ..... **v**
Research Publications and Conference Presentations ..... **vii**
Table of Contents ..... **viii**
List of Figures ..... **ix**
List of Tables ..... **xv**
List of Abbreviations ..... **xvi**
Abstract ..... **xviii**
1 Introduction **1**
1.1 Large-Scale Energy Storage *1*
1.2 Redox Flow Batteries *5*
1.3 Aqueous RFBs *8*
1.4 Nonaqueous RFBs *11*
1.5 Symmetric RFBs *17*
1.6 Cost-Effective Symmetric Nonaqueous RFBs *19*
2 Cost Considerations **21**
2.1 Large-Scale EES Analysis *22*
2.2 RFB Cost Models *27*
2.3 Nonaqueous RFBs *33*
2.4 Symmetric RFBs *38*
2.5 Summary and Discussion *39*
3 Coordination-Complex Active Species **42**
3.1 Experimental *44*
3.2 Voltammetry *53*
3.3 Spectroelectrochemistry *57*
3.4 Batch Reactor Charge-Discharge *67*
3.5 Alternative Solvent Chemistry *69*
3.6 Summary and Discussion *71*
4 Organic Active Species **73**
4.1 Experimental *75*
4.2 Solvent Selection *83*
4.3 Functionalized DPA Analogues *89*
4.4 Alternative Aromatic Centers *100*
4.5 Synthesis Scale-Up *103*
4.6 Summary and Discussion *105*
5 Symmetric Nonaqueous Redox Flow Cells **107**
5.1 Experimental *109*
5.2 $V(acac)_3$ Cyclability *117*
5.3 Organic Active Species *127*
5.4 $V(acac)_3$ Flow-Rate and Current Study *147*
5.5 Summary and Discussion *157*
6 Conclusions **160**
6.1 Future Work *168*
References **170**
A. Appendix **181**
A.1 Oxford Laboratory *181*
A.2 Synthesis and Characterization *184*
A.3 Scale-Up Synthesis and Characterization *204*
Appendix References **214**

List of Figures

Figure 1.1. RFB Schematic. 5

Figure 1.2. Cyclic voltammogram of 0.05 M $TEABF_4$ in ACN with (red) and without (blue) 0.01 M $V(acac)_3$ active species, platinum, 500 mVs^{-1}, 25 °C. 13

Figure 1.3. Cyclic voltammogram of 0.05 M $TEABF_4$ in ACN support solution with (red) and without (blue) 0.01 M $Cr(acac)_3$ active species, platinum, 500 mVs^{-1}, 25 °C. 16

Figure 2.1. Analysis flow chart – cost comparison between commercial Li-ion and AVRFBs for large-scale energy storage. 23

Figure 2.2. Analysis flow chart – identifying the cost components of RFBs. 28

Figure 2.3. Analysis flow chart – cost implications of RFB technology step-changes. . 34

Figure 3.1. Schematic diagram and photograph of the spectroelectrochemical cell. 49

Figure 3.2. Batch-reactor charge-discharge cell. 53

Figure 3.3. Linear-sweep voltammograms at 1 mVs^{-1} probing a) the first reduction and b) the first oxidation of 0.01 M $Cr(acac)_3$, 0.05 M $TEABF_4$ in ACN on Pt at 25 °C under an Ar atmosphere. Each panel presents three data sets; each data set includes both a forward and reverse voltage sweep. Horizontal dashed lines indicate zero current, and magnitudes of limiting currents, labeled i_L^+ and i_L^-. 56

Figure 3.4. UV spectrogram of 0.003 M H(acac), 0.025 M $TEABF_4$ in ACN before (black) and after (green) chronoamperometric reduction at –2.40 V vs. Ag/Ag^+ for 450 seconds. 59

Figure 3.5. Change in visible absorbance of 0.005 M a) $V(acac)_3$ and b) $Cr(acac)_3$ supported by 0.025 M $TEABF_4$ in ACN upon reduction (green) and oxidation (purple). The inset shows a baseline absorbance spectrum collected before the application of potential. 60

Figure 3.6. Change in UV absorbance of 0.001 M $V(acac)_3$, 0.025 M $TEABF_4$ in ACN after reduction at –2.05 V vs. Ag/Ag^+ for 930 seconds (green) and oxidation at 0.65 V vs. Ag/Ag^+ for 930 seconds (purple). The inset shows a baseline absorbance spectrum collected before the application of potential. 61

Figure 3.7. Change in UV absorbance of 0.001 M $Cr(acac)_3$, 0.025 M $TEABF_4$ in ACN after reduction at –2.4 V vs. Ag/Ag^+ for 930 seconds (green) and oxidation at 1.5 V vs. Ag/Ag^+ for 930 seconds (purple). The inset shows a baseline absorbance spectrum collected before the application of potential. 63

Figure 3.8. Change in UV absorbance of 0.001 M $Cr(acac)_3$, 0.025 M $TEABF_4$ in ACN after being held at OCP (–0.12 V vs. Ag/Ag^+) for 930 seconds (dark red) and when

left disconnected, with reference electrode replaced by glass plug, for 930 seconds (orange). The inset shows a baseline absorbance spectrum collected before the application of potential. 64

Figure 3.9. Charge-discharge of a cell with Celgard 4560 separator and graphite electrodes containing 0.05 M $Cr(acac)_3$, 0.5 M $TEABF_4$ in ACN, cycled in a glovebox under an Ar atmosphere at 25 °C. a) Cycles 1-4; b) Cycles 23-25. 68

Figure 3.10. Cyclic voltammogram of 0.01 M $V(acac)_3$, 0.5 M $TBABF_4$ in DME, glassy carbon, 400 mVs^{-1}, 25 °C. 70

Figure 3.11. Cyclic voltammogram of 0.01 M $Cr(acac)_3$, 0.5 M $TBABF_4$ in DME, glassy carbon, 400 mVs^{-1}, 25 °C. 71

Figure 4.1. Chemical structure of DPA. 74

Figure 4.2. Suzuki-Miyaura cross-coupling reaction scheme to produce *para*-functionalized DPA. 76

Figure 4.3. Chemical structure of DMPA. 77

Figure 4.4 Chemical structure of DMOPA. 77

Figure 4.5. Chemical structure of DMBA. 77

Figure 4.6. Trans-esterification reaction scheme to produce long-chain ester functionalized DPA. 78

Figure 4.7. Chemical structure of DePA. 78

Figure 4.8. Chemical Structure of DdPA. 79

Figure 4.9. Chemical structure of m-DMBA. 80

Figure 4.10. Chemical structure of eDdPA. 80

Figure 4.11. Chemical Structure of DMBN. 81

Figure 4.12. Chemical structure of DdPN. 81

Figure 4.13. Cyclic voltammogram of 1 mM DPA loading, 0.5 M $TBABF_4$ in a)ACN, b) DME, c)DMF, d) THF, e)DMSO glassy carbon, 400 mVs^{-1}, 23 °C. 84

Figure 4.14. Cyclic voltammogram of 1 mM DPA loading, 0.5 M $TBABF_4$ in ACN, glassy carbon run at a) 50 (red), 100 (orange), 200 (green), 400 (blue), 800 (purple) mVs^{-1} and b) influence of scan rate on peak height for the reduction (downward triangle) and oxidation (upward triangle) peaks in the reduction couple (red) and oxidation couple (black). 86

Figure 4.15. Cyclic voltammograms of 1 mM DPA loading, 0.5 M $TBABF_4$ in DME, glassy carbon, run at a) 50 (red), 100 (orange), 200 (green), 400 (blue), 800 (purple) mVs^{-1} and b) influence of scan rate on peak height for the reduction

(downward triangle) and oxidation (upward triangle) peaks in the reduction couple (red) and oxidation couple (black). 87

Figure 4.16. Densitometric solubility limit determination of DPA in (a) ACN and (b) DME..... 89

Figure 4.17. Cyclic voltammogram of 1 mM DMPA, 0.5 M $TBABF_4$ in ACN, glassy carbon, 400 mVs^{-1}, 23 °C. 91

Figure 4.18. Cyclic voltammogram of 1 mM DMOPA, 0.5 M $TBABF_4$ in ACN, glassy carbon, 400 mVs^{-1}, 23 °C. 91

Figure 4.19. Cyclic voltammogram of 1 mM DMBA, 0.5 M $TBABF_4$ in ACN, glassy carbon, 400 mVs^{-1}, 23 °C. 91

Figure 4.20. Cyclic voltammogram of 1 mM DePA, 0.05 M $TEABF_4$ in ACN, glassy carbon, 500 mVs^{-1}, 23 °C. 93

Figure 4.21. Densitometric solubility limit determination of DPA in (a) ACN and (b) DME..... 94

Figure 4.22. Cyclic voltammogram of 1 mM DdPA, 0.5 M $TBABF_4$ in (a) ACN (b) DME, glassy carbon, 400 mVs^{-1}, 23 °C. Voltammograms in ACN run at c) 50 (red), 100 (orange), 200 (green), 400 (blue), 800 (purple) mVs^{-1} and d) influence of scan rate on peak height for the reduction (downward triangle) and oxidation (upward triangle) peaks in the reduction couple (red) and oxidation couple (black). 95

Figure 4.23. Cyclic voltammogram of 1 mM eDdPA, 0.1 M $TBABF_4$ in ACN, glassy carbon, 400 mVs^{-1}, 23 °C. 97

Figure 4.24. Charge/discharge performance of 10 mM DPA, 0.5 M $TBABF_4$ in DME: (a) cycling behavior, (b) coulombic (blue) and energy (red) efficiency performance over 25 cycles. 98

Figure 4.25. Charge/discharge performance of 10 mM DdPA, 0.1 M $TBABF_4$ in ACN: (a) cycling behavior, (b) coulombic (blue) and energy (red) efficiency performance over 25 cycles (c) coulombic efficiency (blue) and charge capacity (red) over 25 cycles..... 99

Figure 4.26. Cyclic voltammogram of 1 mM DdPN, 0.5 M $TBABF_4$ in a)ACN and b) DME, glassy carbon, 400mVs^{-1} 23 °C. Voltammograms run at c) 50 (red), 100 (orange), 200 (green), 400 (blue), 800 (purple) mVs^{-1} and d) influence of scan rate on peak height for the reduction (downward triangle) and oxidation (upward triangle) peaks in the reduction couple (red) and oxidation couple (black). 102

Figure 5.1. Schematic showing individual reactor components of one half of the cell (the other half is a mirror image) and a photograph of the constructed cell. 111

Figure 5.2. Cyclic voltammograms of 0.1 M $V(acac)_3$ from Sigma (red) and Strem (blue), 0.5 M $TEABF_4$ in ACN, glassy carbon, 400 mVs^{-1}, 23 °C. 119

Figure 5.3. Galvanostatic charge-discharge cycling a) curves at 10 $mAcm^{-2}$ and 25 $mLmin^{-1}$ of 0.1 M $V(acac)_3$, 0.5 M $TEABF_4$ in ACN and b) performance: voltage efficiency (blue upward pointing triangles), coulombic efficiency (red circles), energy efficiency (black squares), energy capacity on charge (purple stars), energy capacity on discharge (green downward pointing triangles). 120

Figure 5.4. Nyquist plots from EIS experiments on flow cell with stagnant 0.1 M $V(acac)_3$, 0.5 M $TEABF_4$ in ACN battery solution a) before b) after charge-discharge testing c) and control experiment without any $V(acac)_3$. Insets show the system response at high frequencies. 122

Figure 5.5. Cyclic voltammograms of pristine 0.1 M $V(acac)_3$, $TEABF_4$ in ACN (blue) and a) negolyte and b) posolyte after charge-discharge cycling (black), glassy carbon, 400 mVs^{-1}, 23 °C. 123

Figure 5.6. Galvanostatic charge-discharge cycling a) curves at 2 $mAcm^{-2}$ and 25 $mLmin^{-1}$ of 0.01 M $V(acac)_3$, 0.5 M $TBABF_4$ in DME and b) performance: voltage efficiency (blue upward pointing triangles), coulombic efficiency (red circles), energy efficiency (black squares), energy capacity on charge (purple stars), energy capacity on discharge (green downward pointing triangles). 124

Figure 5.7. Nyquist plots from EIS experiments on flow cell with stagnant 0.01 M $V(acac)_3$, 0.5 M $TBABF_4$ in DME battery solution a) before b) after charge-discharge testing c) and control experiment without any $V(acac)_3$. Insets show the system response at high frequencies. 126

Figure 5.8. Cyclic voltammograms of pristine 0.01 M $V(acac)_3$, $TBABF_4$ in DME (blue, potentials shifted negatively 195 mV and currents increased 9%) and a) negolyte and b) posolyte after charge-discharge cycling (black), glassy carbon, 400 mVs^{-1}, 23 °C. 127

Figure 5.9. Galvanostatic charge-discharge cycling a,b) curves at 2 $mAcm^{-2}$ and 25 $mLmin^{-1}$ of 0.01 M DPA, 0.5 M $TBABF_4$ inDME and c) performance: voltage efficiency (blue upward pointing triangles), coulombic efficiency (red circles), energy efficiency (black squares), energy capacity on charge (purple stars), energy capacity on discharge (green downward pointing triangles). 129

Figure 5.10. Cross-section of 0.01 M DPA, 0.5 M $TBABF_4$ in DME negolyte tubing inner circumference after cycling a) SEM micrograph in 'Analytical' mode and EDS spectra for b) fluorine content and c) carbon content. 130

Figure 5.11. Nyquist plots from EIS experiments on flow cell with stagnant 0.01 M DPA, 0.5 M $TBABF_4$ in DME battery solution a) before and b) after charge-discharge testing. Insets show system response at high frequencies. 131

Figure 5.12. Cyclic voltammograms of 0.01 M DPA, 0.5 M $TBABF_4$ in DME a) negolyte and b) posolyte after charge-discharge cycling, glassy carbon, 400 mVs^{-1}, 23 °C. 132

Figure 5.13. Galvanostatic charge-discharge cycling a,b) curves at 2 $mAcm^{-2}$ and 25 $mLmin^{-1}$ of 0.01 M DdPA, 0.5 M $TBABF_4$ in DME and c) performance: voltage

efficiency (blue upward pointing triangles), coulombic efficiency (red circles), energy efficiency (black squares), energy capacity on charge (purple stars), energy capacity on discharge (green downward pointing triangles). 134

Figure 5.14. Nyquist plots from EIS experiments on flow cell with stagnant 0.01 M DdPA, 0.5 M $TBABF_4$ in DME battery solution a) before and b) after charge-discharge testing. Insets show the system response at high frequencies. 135

Figure 5.15. Cyclic voltammograms of 0.01 M DdPA, 0.5 M $TBABF_4$ in DME a) negolyte and b) posolyte after charge-discharge cycling, glassy carbon, 400 mVs^{-1}, 23 °C. 136

Figure 5.16. Galvanostatic charge-discharge cycling a,b) curves at 5 $mAcm^{-2}$ and 25 $mLmin^{-1}$ of 0.075 M DdPA, 0.5 M $TBABF_4$ in DME and c) performance: voltage efficiency (blue upward pointing triangles), coulombic efficiency (red circles), energy efficiency (black squares), energy capacity on charge (purple stars), energy capacity on discharge (green downward pointing triangles). 138

Figure 5.17. Cross-section of 0.075 M DdPA, 0.5 M $TBABF_4$ inDME negolyte tubing inner circumference after cyclinga) SEM micrograph in 'Analytical' mode and EDS spectra for b) fluorine content and c) carbon content. 140

Figure 5.18. Nyquist plots from EIS experiments on flow cell with stagnant 0.075 M DdPA, 0.5 M $TBABF_4$ in DME battery solution a) before and b) after charge-discharge testing. Insets show the system response at high frequencies. 141

Figure 5.19. Cyclic voltammograms of 0.075 M DdPA, 0.5 M $TBABF_4$, in DME a) negolyte as it stabilized with cycling and b) posolyte (diluted to 0.15 M with solution of 0.5 M $TBABF_4$, DME) after charge-discharge cycling, glassy carbon, 400 mVs^{-1}, 23 °C. 142

Figure 5.20. Galvanostatic charge-discharge cycling a,b) curves at 2 $mAcm^{-2}$ and 25 $mLmin^{-1}$ of 0.01 M DdPA, 0.5 M $TBABF_4$ in ACN and c) performance: voltage efficiency (blue upward pointing triangles), coulombic efficiency (red circles), energy efficiency (black squares), energy capacity on charge (purple stars), energy capacity on discharge (green downward pointing triangles). 143

Figure 5.21. Cross-section of 0.075 M DdPA, 0.5 M $TBABF_4$ in ACN negolyte inner tubing circumference after cycling a) SEM micrograph in 'Analytical' mode and EDS spectra for b) fluorine content and c) carbon content. 144

Figure 5.22. Nyquist plots from EIS experiments on flow cell with stagnant 0.01 M DdPA, 0.5 M $TBABF_4$ in ACN battery solution a) before and b) after charge-discharge testing. Insets show the system response at high frequencies. 145

Figure 5.23. Cyclic voltammograms of 0.01 M DdPA, 0.5 M $TBABF_4$ inACN a) negolyte and b) posolyte after charge-discharge cycling (black), glassy carbon, 400 mVs^{-1}, 23 °C. 146

Figure 5.24. Flow-rate dependence (upward triangle –12.5 $mLmin^{-1}$, square – 25 $mLmin^{-1}$, downward triangle – 50 $mLmin^{-1}$) of 0.1 M $V(acac)_3$, 0.5 M $TEABF_4$ in

ACN on coulombic efficiency (red), energy efficiency (black), discharge energy capacity (green). 148

Figure 5.25. Flow rate dependence (upward triangle –12.5 $mLmin^{-1}$, square – 25 $mLmin^{-1}$, downward triangle – 50 $mLmin^{-1}$) of 0.1 M $V(acac)_3$, 0.5 M $TEABF_4$, ACN on average discharge voltage (blue) and power density (purple). The black dashed line is a best-fit second order polynomial to the power density data according to Equation 5.6. 150

Figure 5.26. Experimental results for first charging step of 0.1 M $V(acac)_3$, 0.5 M $TEABF_4$ in ACN at 100 $mAcm^{-2}$ and 12.5 (red), 25 (blue), and 50(black) $mLmin^{-1}$ and prediction of equilibrium potentials *via* Nernst equilibrium equation and CSTR design equation (purple). 153

Figure 5.27. Experimental results for first charging step of 0.1 M $V(acac)_3$, 0.5 M $TEABF_4$ in ACN at 100 $mAcm^{-2}$ and 12.5 $mLmin^{-1}$. Prediction of cell potentials *via* a Nernst/CSTR model that includes ohmic overpotentials as collected from EIS (green). 155

List of Tables

Table 2.1. LCOSC of 1 MW/ 3.2 MWh AVRFB and Li-ion system. 27

Table 2.2. Breakdown between power and energy related AVRFB costs in 2017 dollars (2% inflation). 29

Table 2.3. Areal Costs ($/m^2) in 2017 dollars (2% inflation). Averages from datasets possessing more than five values are calculated from a subset culled of the two extremes. 30

Table 2.4. Reactor cost breakdown derived from values in Table 2.3..... 30

Table 2.5. Battery solution cost breakdown..... 37

Table 4.1. Solvent screening: bulk solvent properties[132] and screening outcomes..... 84

Table 4.2 Solubility limits (mM) of DPA based molecules in ACN and DME 89

Table 5.1. Properties and parameters of fluid flow, reactor electrodes, and 0.1 M $V(acac)_3$, 0.5 M $TEABF_4$ in ACN battery solution at 22 °C. 156

List of Abbreviations

$acac^-$: acetylacetonate
ACN: acetonitrile
$AgNO_3$: silver nitrate
AVRFB: aqueous vanadium redox flow battery
$B(OH)_2$-Ph-pEG: diethyleneglycoxy ether functionalized phenyl boronic acid
Br-Ph-pEG: diethyleneglycoxy ether functionalized bromo-phenol
CAES: compressed air energy storage
CE: coulombic efficiency
$Co(bpy)_3$: cobalt bipyridyl
$Co(phen)_3$: cobalt phenanthroline
$Cr(acac)_2$: chromous acetylacetonate
$Cr(acac)_3$: chromium acetylacetonate
CSTR: continuous stirred-tank reactor
CV: cyclic voltammetry
DBA: 9,10-dibromoanthracene
DBN: 1,4-dibromonaphthalene
DCM: dichloromethane
DdPA: diethyleneglycoxy ester functionalized DPA
DdPN: diethyleneglycoxy ester functionalized DPN
DePA: ethylene glycoxy ester functionalized DPA
DMBA: methyl ester functionalized DPA
DMBN: methyl ester functionalized DPN
DMC: dimethyl carbonate
DME: 1,2-dimethoxyethane
DMF: *n*,*n*-dimethylformamide
DMOPA: methyl ether functionalized DPA
DMPA: methyl functionalized DPA
DMSO: dimethylsulfoxide
DO: 1,2-dioxolane
DPA: 9,10-diphenylanthracene
DPN:1,4-diphenylnaphthalene
eDdPA: diethyleneglycoxy ether functionalized DPA
EDS: energy dispersive x-ray spectroscopy
EE: energy Efficiency
EES: electrochemical energy storage
EIS: electrochemical impedance spectroscopy
EtOAc: ethyl acetate
FEP: fluorinated ethylene propylene
Fe-Cr: iron chromium redox flow battery
$Fe(acac)_2$: ferrous acetylacetonate
$Fe(acac)_3$: ferric acetylacetonate
$Fe(bpy)_3$: iron bypyridyl
GC-MS: gas chromatography – mass spectrometry
H(acac): acetylacetone
HPLC: high pressure liquid chromotography
IEM: ion-exchange membrance
ID: inner diameter

IR: infrared
LCOE: levelized cost of electricity
LCOS: levelized cost of storage
LCOSC: levelized cost of nameplate storage capacity
LCOSPC: levelized cost of nameplate storage power capability
LSV: linear sweep voltammetry
$M(acac)_3$: metal acetylacetonate complex
$Mn(acac)_3$: manganese acetylacetonate
m-DMBA: methyl ester functionalized DPA (*meta*)
NMR: nuclear magnetic resonance spectroscopy
OCP: open-circuit potential
OD: outer diameter
pAH: polycyclic aromatic hydrocarbon
PC: propylene carbonate
$Pd(OAc)_2$: palladium acetate
$Pd(PPh_3)_4$: palladium *tetrakis* triphenylphosphine
PHS: pumped hydroelectric storage
ppm: parts per million
PTFE: polytetrafluoroethylene
RFB: redox flow battery
RMS: root-mean-squared
$Ru(acac)_3$: ruthenium acetylacetonate
$Ru(bpy)_3$: ruthenium bipyridyl
SEM: scanning electron microscopy
SOC: state of charge
$TBABF_4$: tetrabutylammonium tetrafluoroborate
$TEABF_4$: tetraethylammonium tetrafluoroborate
$TEAClO_4$: tetraethylammonium perchlorate
$TEANO_3$: tetraethylammonium nitrate
THF: tetrahydrofuran
TLC: thin layer chromotography
UV: ultraviolet
$V(acac)_3$: vanadium acetylacetonate
VE: voltage efficiency
Vis: visible
$VO(acac)_2$: vanadyl acetylacetonate
Zn-Br: zinc-bromine redox flow battery

Abstract

Analysis and Performance of Symmetric Nonaqueous Redox Flow Batteries

James Saraidaridis, St. Peter's College, University of Oxford

DPhil in Engineering Science, Trinity 2017

Symmetric nonaqueous redox flow batteries (RFBs) use negative and positive battery solutions of the same solution composition to operate at high cell voltages. This research effort targets these systems since they offer performance improvements derived from using nonaqueous systems and symmetric active species. Nonaqueous solutions permit significantly higher cell voltages than state-of-the-art aqueous RFBs and symmetric active species chemistries reduce the required complexity of cell reactors. Both performance advantages correspond to significant cost improvements beyond already commercially competitive aqueous RFB chemistries.

This document focuses on two classes of symmetric nonaqueous RFB chemistries: coordination complexes such as vanadium acetylacetonate [$V(acac)_3$] or chromium acetylacetonate [$Cr(acac)_3$], and organic active species such as 9,10-diphenylanthracene (DPA). $V(acac)_3$ delivers reversible electrochemistry that supports a 2.2 V equilibrium cell potential, but there are some gaps in the understanding of its degradation mechanisms. $Cr(acac)_3$ supports redox reactions that suggest cell potentials above 4 V, but shows signs of irreversibility in voltammetry experiments and is not yet well understood. Finally, the DPA system could be interesting because it does not use metal active species, and its voltammetry promises cell potentials above 3 V. Yet DPA suffers from low solubility in nonaqueous solvents that limit its practicality. These three systems show promise for symmetric nonaqueous RFBs and offer avenues for further improvement.

Voltammetry and spectroelectrochemical electrolysis experiments on the metal coordination complexes clarify the mechanisms behind the voltammetry on these symmetric chemistries. Ligand dissociation causes the irreversible behavior observed in voltammetry on $Cr(acac)_3$. The same experiments reaffirm the expected cyclability of $V(acac)_3$.

Chemical functionalization of the DPA center is performed to investigate the solubility and reactivity of various derivatives. Functionalizing DPA with ethylene glycol chains to form 'DdPA' significantly increases solubility limits from 0.6 mM and 44 mM for DPA in acetonitrile and 1,2-dimethoxyethane, respectively, to 12 mM and 0.21 M for DdPA in the same solvents. At the same time, DdPA retains redox activity that promises 3 V cell potentials.

Ultimately, a custom, nonaqueous-compatible redox flow reactor was designed and used to test the performance of $V(acac)_3$, DPA, and DdPA under various operating conditions. Contradicting previous reports, $V(acac)_3$ delivers stable cycling over the 21-cycle experimental protocol. Exploration over a range of flow rates and current densities give energy and power densities up to 1.09 WhL^{-1} and 0.16 Wcm^{-2}, respectively, for the battery solution compositions examined. These experiments further predict values up to 28 WhL^{-1} and at least 0.22 Wcm^{-2} for optimized $V(acac)_3$ battery solutions. DPA and DdPA deliver the highest operating potential observed from organic nonaqueous RFBs, discharging at 3 V and 2.9 V, but require further work to understand degradation in the systems.

1 Introduction

1.1 Large-Scale Energy Storage

Energy sectors in countries around the world increasingly look to large-scale energy storage for progress in their economic, environmental and social impact. Aging electrical grid infrastructures require upgrades or remedial maintenance such that industrial stakeholders and governmental policymakers must decide whether to maintain the *status quo* or adopt new strategies enabled by energy storage. Economic development in remote locations increases demand for reliable electricity, which can be supplied less expensively with non-traditional grids that employ energy storage.[1,2] Renewable electrical energy generation is increasing globally and energy storage offers a method for providing reliable electricity from popular intermittent sources like solar and wind generation. Energy storage thus offers opportunities for stakeholders ranging from developed to developing countries and from conventional inter-connected thermal-powered electricity grids to renewably powered microgrids.

Large-scale energy storage can serve many purposes for the different stakeholders in an existing electrical grid. Electricity producers could see benefits like peak flattening, which reduces the need for 'peaker plants': energy storage would compete with the present inventory of peaker plants, which operate infrequently and expensively. Suppliers would also realize benefits from ancillary services provided by energy storage: load following (having electricity supply ready to meet predicted demand), area regulation (adjusting supply to short-time-scale perturbations in demand), electric supply reserve capacity (having electric supply ready to support unexpected losses of other supply resources), and voltage support (maintaining the power quality

delivered across the network), which are presently served by the inefficient operation of thermal plants to allow quick adjustments in generation.[3] Providing these ancillary services with energy storage would avoid using thermal generators at inefficient operating conditions, thereby reducing costs and emissions. Alternatively, system operators, who represent the interests of the physical electrical-grid hardware, could expect transmission support, congestion relief, an ability to defer grid upgrades, and provide sub-station power on site. Finally, consumers with access to energy storage would benefit on an existing grid from enhanced reliability, power quality, and the ability to avoid time of use or demand charges where those apply.[3] Therefore, inexpensive large-scale energy storage would deliver benefits to the largest stakeholders in existing electrical grids.

Energy storage also supports strategies for reliable electrical power in rural or geographically isolated populations by providing an alternative to extending and connecting into existing electrical grids. Pairing lowest-cost electricity generators with storage to develop microgrids can avoid the relatively expensive, resource-intensive connection to existing grids. By facilitating electricity access for new populations, energy storage would support the further development of those communities.

Large-scale energy storage also provides solutions for problems arising from the intermittent nature of renewable electricity generators like wind turbines and solar photovoltaics. Wind and solar generation are subject to relatively unpredictable fluctuating conditions in the natural environment, unlike the human-controlled fuel inputs of thermal generators. Additionally, the nature of these generation resources leads to low capacity factors, which describe the fraction of time the resource operates at full capacity, in comparison to thermal plants. When paired with the inability to control generation, low capacity factors make the electricity output less valuable.

Energy storage can act as a buffer to the whims of natural resources by introducing some control into the disbursement of the generated electricity to allow delivery of smoother supply curves. Additionally, storage can improve the capacity factor of these resources by avoiding curtailment of electricity generation in situations where the resources could produce electricity, but demand is too low. By helping match electricity supply with demand and improving capacity factors, energy storage would facilitate higher penetrations of intermittent renewable generators.

Large-scale energy storage technologies exist to serve all of the roles described above. Most storage comes from pumped hydroelectric storage (PHS) facilities, which accounted for 99% of U. S. storage capacity in 2010.[4] The majority of the remaining storage resources come from compressed air energy storage (CAES) and electrochemical energy storage (EES) technologies.[5] The predominance of PHS systems stems from cost advantages, but other factors, such as reliance on geological features can affect selection or feasibility of a storage resource: PHS requires two large reservoirs at disparate heights and CAES often uses voluminous, air-tight underground caverns to store compressed air. Anything reliant on geological features is necessarily stationary and risks becoming a stranded asset if demand changes. Electrochemical energy storage (EES) systems are not limited to locations with certain geological features and can realistically be moved to multiple locations throughout a system's life. In 2017, the United States Department of Energy (DOE) Global Energy Storage Database had recorded 987 grid-connected EES systems worldwide, with 63% using lithium ion (Li-ion) chemistries and 10% using RFBs, including aqueous all-vanadium RFBs (AVRFBs, 6%) and zinc-bromine systems (Zn-Br, 3.5%).[6] Presently, it seems that Li-ion dominates grid scale EES installations.

Further analysis of EES installations and their rated duration reveal that RFBs are more competitive for long-duration applications, and less competitive for applications demanding shorter durations. When longer duration (≥4 hours) systems are considered exclusively, Li-ion systems only represent a 34% share to RFBs' 26% share. This points to the improved cost-effectiveness of RFBs for longer duration applications, which stems from their very easily scalable energy capacity. The non-uniform distribution of battery chemistries across rated duration highlights the variation in performance characteristics in different EES technologies and shows that grids should expect to employ different battery chemistries depending on the requirement of their intended application.

Demand for electricity storage is expected to increase; some studies propose storage mandates up to 5% of peak electricity demand.[5] If projected across the whole world, demand for EES may require several battery types and chemistries, even beyond current state-of-the-art Li-ion and AVRFB technologies. In this regard, parallels to fossil-fuel consumption can be found: oil resources are predominantly used in transportation rather than electricity generation and *vice versa* for coal and natural gas. This arises partly from the energy density of oil at atmospheric pressure and the ability of its power conversion systems to scale down to smaller applications. Similarly, this would apply for the more energy-dense Li-ion systems, which would be used for electric-powered transportation, while less energy-dense RFB systems would be used for grid applications. With all this in mind, RFBs are well suited to supply the increasing demand for large-scale, semi-permanent energy storage independent of geographical constraints.

1.2 Redox Flow Batteries

As research in the field blossoms, RFBs come in many varieties, but a standard RFB architecture shown in Figure 1.1 consists of: two reservoirs, which each contain an ionically conductive redox-active solution, and a reactor, where electron exchange occurs between the solid inert electrodes and the battery solution. Solutions flow from their tanks through the reactor to contact the inert electrodes and each other ionically, through an ion exchange membrane or separator. Electrical loads or sources connect to the electrodes *via* current collectors to discharge or charge the system, respectively. When an electricity generator delivers power to this archetypal RFB, electrons react heterogeneously with solvated active species at the surface of the inert electrode. Meanwhile, electrodynamic and diffusion driving forces induce travel of dissolved species across the ion-exchange membrane or separator to the opposing electrolyte in order to allow a flow of ionic current that maintains overall electroneutrality.

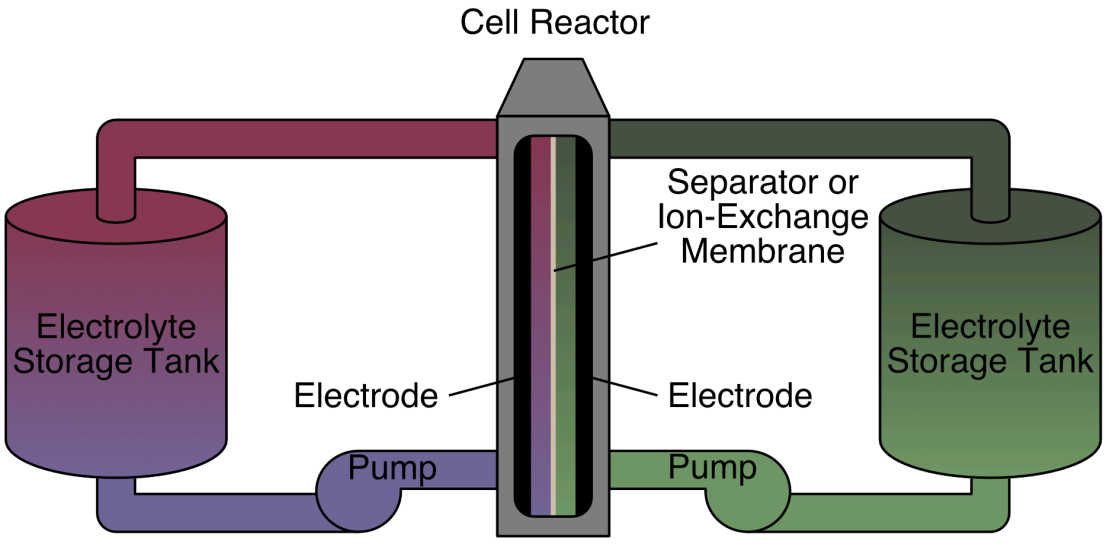

Figure 1.1. RFB Schematic.

This architecture and operation is attractive for large-scale storage since the use of liquid electrolytes and chemically inert electrodes decouple energy from power.

Energy scales with the volume of solution within the storage tanks (and, ultimately their volume), while power scales with the area within the reactor system. This decoupling is an essential difference between RFBs and familiar solid-electrode batteries such as Li-ion. Conventional Li-ion manufacturing techniques require formation of electrodes with uniform, large surface-area-to-volume ratios to permit high-power operation: energy scales with electrode material, which scales with surface area and, thus, power. Manufacturers cannot increase energy capacity without also increasing power capacity or changing their manufacturing procedures. Furthermore, the inert electrodes and dissolved active species of RFBs are resistant to mechanical fatigue or interfacial side reactions that occur in solid electrodes, enabling RFBs to have longer lifetimes. Both of these RFB features lead to less expensive systems: customizable RFBs avoid wasting resources on unnecessary power capacity in high energy-capacity systems and longer operational lives obviate frequent cell or system replacement costs.

NASA developed one of the first RFBs[7] in an effort that birthed the aqueous iron-chromium chemistry (Fe-Cr). Development of this chemistry continued with commercial efforts pursued as recently as 2015;[8] it employs the Cr^{2+}/Cr^{3+} couple in the negative electrolyte, and the Fe^{2+}/Fe^{3+} redox couple in the positive electrolyte.[9] Further research into RFBs has led to a wide variety of chemistries or cell architectures: hybrid flow cells that replace an inert electrode with a metallic electrode such as Zn metal in the Zn-Br system,[10] single-active-species chemistries such as the AVRFB,[11] nonaqueous chemistries using transition metal coordination complexes such as $Ru(acac)_3$,[12] membrane-free laminar flow cells demonstrated with the AVRFB chemistry,[13] or symmetric chemistries such as nonaqueous $V(acac)_3$.[14] Various tradeoffs exist between the types of RFBs: the electrochemical stability of water limits the voltages possible in aqueous systems,[15] dendrite formation on metallic electrode surfaces limits current and

power densities in hybrid systems, nonaqueous systems use more expensive solvents and supporting electrolytes, and membrane-free laminar flow cells require precise cell construction that may not scale cheaply. The variety of relative strengths and weaknesses provides many avenues for further RFB research and development.

With so many chemistries and architectures to choose from, early RFB research targeted certain metrics in the hope of improving performance of these systems. One performance metric, energy density, directly relevant to volume-constrained applications and pumping cost considerations, varies solely on active species concentration, c_{active}, for a given chemistry. The figure of merit for theoretical energy density in this case is

$$\tilde{E}_{\text{solution}}\left(\frac{\text{W}\cdot\text{h}}{\text{L}}\right) \sim nFV_{\text{OCP}}c_{\text{active}}^{\text{sat}} \tag{1.1}$$

where $\tilde{E}$ is the theoretical volumetric energy density (in WhL^{-1}), n is the number of electrons reacting per active species, F is Faraday's constant, and V_{OCP} is the equilibrium cell open circuit potential (OCP) offered by the RFB chemistry. Another vital RFB performance metric is power density, $\tilde{P}$, measured in Wcm^{-2},

$$\tilde{P}\left(\frac{\text{W}}{\text{cm}^2}\right) \sim V_{\text{cell}}i \tag{1.2}$$

where V_{cell} is the cell voltage at i, the current density applied to the cell. Power density describes the amount of power generated per given unit area of the cell reactor as measured by the superficial separator area within the reactor. This directly influences the superficial area of the separator, porous electrodes, and current collectors necessary within a reactor to deliver a rated power. Cells will usually have a single current density that maximizes the power density: this maximum depends on a variety of properties that affect both V_{cell}, which can range from bulk cell resistance to active species diffusivity.

Energy and power density combine with an individual system's volume and reactor area to deliver the system power and duration. Subsequently, system power and duration define a system's capabilities and are key classification parameters in the DOE Global Energy Storage Database referred to earlier.

1.3 Aqueous RFBs

Early research and development of RFBs focused on aqueous chemistries using acid as the supporting electrolyte. Formally, water has an electrochemical stability window of only 1.23 V before either hydrogen or oxygen evolve from the solvent.[16] Wider windows are achieved in practice by using electrodes that have slow reaction kinetics for the hydrogen and oxygen evolution (water splitting). Additionally, the position of the voltage window relative to standard hydrogen shifts with solution pH; more basic solutions access lower potentials and acidic solutions, higher potentials.[15,16]

Early aqueous RFB chemistries generally rely on two different active species for their respective electrolytes. For example the Fe-Cr chemistry involves dissolved salts of iron and chromium. Since this cell accesses an iron half-reaction that operates at a more positive potential than the chromium reaction, the iron electrolytic solution is referred to as the posolyte (positive-electrolyte) or catholyte (cathode-electrolyte) and the chromium electrolytic solution is the negolyte (negative-electrolyte) or anolyte (anode-electrolyte). This dual-active-species paradigm requires a highly selective ion-exchange membrane (IEM) to prevent active species crossover between the two solutions. Alternatively, this paradigm can use bystander active species in the opposing solution to combat diffusion gradients driving crossover so long as the active species are passive at the opposing electrode's operating potentials. Both strategies introduce added

cost and complexity, but they are necessary since any crossover of active species leads to irreversible capacity loss.

As development apparently stalled on aqueous Fe-Cr RFBs, newer aqueous chemistries were discovered and have been studied since.[17] Other metal-based, dual-species chemistries like iron-titanium were explored.[18] Moving away from metallic active species, researchers developed and attempted to commercialize a polysulphide-bromide chemistry; it discharges at 1.4 V and delivers power densities up to 0.64 Wcm^{-2}.[19] Although grid-scale pilot plants were built for this chemistry, they were never commissioned.[20] This plant's failure to gain acceptance may stem from the use of bromide redox chemistry, which requires complexing agents to avoid the safety hazards associated with elemental halogens.[21] Other chemistries kept the bromine pair and swapped out the sulfide-polysulfide reaction, using hydrogen[22] or anthraquinone[23] species instead. In a shift away from both metallic and halogen active species, recent work developed an organic active species chemistry using anthraquinone paired with organometallic ferricyanide in basic aqueous solutions.[15,23] The new organic active species derive from low-cost feedstocks and support molecular customization through functionalization for specific applications. Additionally they offer versatility since the chemistry can operate in acidic, neutral, and basic environments.[15,23] These organic active species are relatively new research demonstrations and still need to be studied further to determine commercial viability.

The most developed of the first-generation aqueous chemistries is the AVRFB chemistry,[24] which has become state-of-the-art. This chemistry relies on four valence states of vanadium, with the negative cell reaction accessing the V^{2+}/V^{3+} valence states[25] and the positive cell reaction accessing VO^{2+}/VO_2^{+},[26] which are the V(IV) and V(V) valence states in aqueous media. Historically, the AVRFB represents a departure

from previous chemistries that use the dual-species paradigm and a first step toward symmetric systems, which use the same active species in the same charge state in both discharged electrolytes.

Flow reactors with the same active metal center on both sides of the cell avoid irreversible efficiency losses from crossover or the added cost of bystander active species. If VO_2^+ crosses the separator in an AVRFB, it meets a V^{2+} or V^{3+} and the two would spontaneously react to oxidize and reduce each other at the expense of coulombic efficiency. Although irreversible crossover is avoided, the negolyte and posolyte lack a common vanadium valence state and this crossover affects the full cell state-of-charge (SOC) and balancing between the negolyte and posolyte half-cell SOCs. After a single converted active species 'contaminant' crosses to the opposing electrolyte it would need to traverse two valence states before achieving the same valence state as the unconverted 'host' active species. Similarly, an unconverted active species 'contaminant' would need to traverse one valence state. These conversions to the valence state of the 'host' solution occur by annihilation of opposing charge on converted or unconverted 'host' molecules. Annihilation of charge on each individual converted 'contaminating' molecule would therefore annihilate a charge on two of the converted 'host' molecules. Similarly for the unconverted 'contaminant', its crossover would return a converted 'host' back down to an unconverted state. Hence, these self-discharge crossover effects deliver asymmetric differences in SOC to the two half-cells. Rebalancing the electrolyte SOC is still possible during cell operation by transferring some posolyte solution to the negolyte side with each pass or extended open circuit holds.[27,28] This requires careful fluid management or system down-time and comes at the expense of further coulombic inefficiency, however.

When the performance metrics described in Equations 1.1 and 1.2 are applied to aqueous systems, the limitations imposed by the relatively small 1.23 V electrochemical window of water become clear. If all other parameters are kept the same, a RFB that operated at 4 V, a voltage which is realized in commercial nonaqueous Li-ion cells, would triple both energy and power density. While voltages slightly higher than 1.23 V are achieved in aqueous RFBs through the use of electrodes with poor water-splitting kinetics, voltages significantly larger than 1.23 V can only be achieved in cells with adapted cell architectures. For instance, an architecture has been proposed where a basic negolyte and an acidic posolyte are used; an extra membrane layer is introduced to provide a channel for a third electrolytic solution that flows between the negolyte and posolyte chambers in the reactor to share ions between and maintain the opposing pHs.[29] Replacing aqueous solutions with more electrochemically stable nonaqueous solutions is a much more straightforward route to permit higher voltage chemistries.[30]

1.4 Nonaqueous RFBs

Aprotic nonaqueous solvents can provide significantly wider electrochemical stability windows than water. Several early nonaqueous chemistries employed acetonitrile (ACN) as a solvent because solutions supported by tetraethylammonium tetrafluoroborate ($TEABF_4$) offer a 6.1 V electrochemical stability window.[30] In the $TEABF_4$-supported ACN solution, researchers demonstrated cyclability of ruthenium bipyridyl ($Ru(bpy)_3$),[12] and various transition-metal acetylacetonate coordination complexes ($M(acac)_3$: M=V, Cr, Mn, Ru).[14,31,32,33] Other nonaqueous solvents offer similarly large stability windows;[30] propylene carbonate (PC, 6.6 V), *n*,*n*-dimethylformamide (DMF, 4.6 V), and dimethylsulfoxide (DMSO, 4.4 V) all saw use

in early nonaqueous chemistries.[34,35] PC and other carbonate solvents are used in commercial Li-ion systems, which deliver operating voltages that reach above 4 V.

For RFB chemistries that show promise from the standpoint of voltage and stability, researchers have looked to evaluate the redox behavior across the space of solvent and supporting salts to increase active species solubility. For instance, $V(acac)_3$, which has electrochemical activity illustrated by the cyclic voltammogram in Figure 1.2, has been tested with solvents including DMF,[36,37] tetrahydrofuran (THF),[36,37] dimethylcarbonate (DMC),[36] gamma-butyrolactone,[38,39] 1,3-dioxolane (DO),[37,38] 1,2-dimethoxyethane (DME),[38,39] methyl acetate,[38,39] and ethyl acetate.[38,39] $V(acac)_3$, as originally studied, has a solubility limit of 0.6 M in neat ACN[40] and delivers a 2.2 V cell potential,[41] which offers a theoretical maximum energy density of 17.7 WhL^{-1}. Solvent studies found solutions that increased solubility first to 0.8 M in DO, then to 1.1 M in a mixture of ACN, DO, and DMSO: increasing the energy density almost twofold from neat ACN, to 32.4 WhL^{-1}. Meanwhile, functionalization of acetylacetonate ligands with an ethylene glycol chain increases $V(acac)_3$ solubility sufficient to offer 38 WhL^{-1} in neat ACN.[42] This compares favorably to the energy densities of commercialized AVRFBs, which offer 36.2 WhL^{-1} at 2 M vanadium concentrations and 1.35 cell voltages.[43] Given the higher voltage of this nonaqueous $V(acac)_3$ system, it offers up to 61% power density improvement over AVRFBs operated at the same current density. These studies demonstrate the importance of active-species solubility on solvent selection in addition to electrochemical stability.

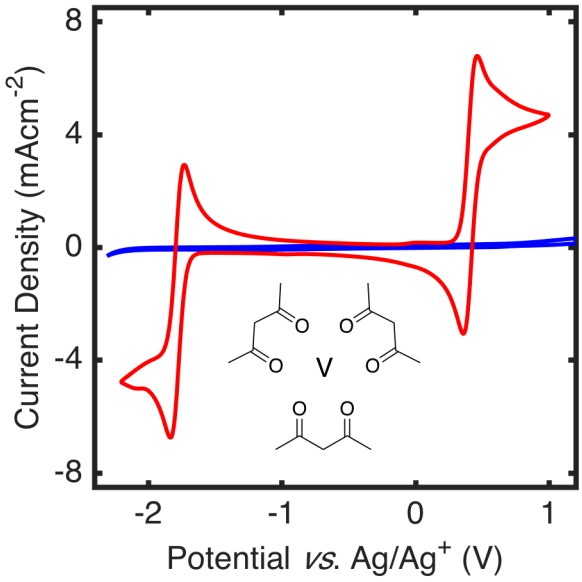

Figure 1.2. Cyclic voltammogram of 0.05 M $TEABF_4$ in ACN with (red) and without (blue) 0.01 M $V(acac)_3$ active species, platinum, 500 mVs^{-1}, 25 °C.

As researchers continue to propose nonaqueous RFBs that compete on first-pass performance metrics, the prime motivation for RFBs must be remembered: their comparative advantage over other EES technologies for long-duration, long-term grid installations. While a nonaqueous RFB chemistry may offer comparable energy density and improved power density over an AVRFB, the chemistry must support the long operational lifetimes achieved with AVRFB systems. This introduces a less easily parameterized performance criterion that largely determines whether these systems are useful for grid applications: cost-effectiveness, which improves with longer-lived systems. From a practical standpoint, the long operational lifetime of an AVRFB can justify an increased capital cost compared to shorter-lived systems.

Cost effectiveness further motivates improvements in the energy density performance metric. Whereas AVRFB active species are supported by solutions of sulfuric or hydrochloric acid in water, which are all abundant and inexpensive, nonaqueous solutions and high-voltage compatible supporting salts are relatively expensive. These components will contribute significantly to the cost of nonaqueous

RFBs in a way that water and simple acids do not. These cost factors introduce an alternative significance to the energy density performance metric: rather than indicating that the sizes of storage tanks or pumping specifications can be reduced, higher energy density indicates that smaller amounts of expensive supporting solution can be used to achieve a particular battery capacity.

Nonaqueous solvents are composed of larger, less polar molecules than water, physical features that correlate with lower solution conductivity and power capabilities in RFBs.[44] The ionic conductivity achievable in nonaqueous support solutions is limited by lower solubility limits and disassociation levels of supporting salts, and lower ionic mobilities, all of which imply that a lower conductivity will be achieved at a given salt concentration. Lower conductivity corresponds to higher overpotentials, η_{cell}, during operation, which lowers the maximum power density of a cell. If the losses in a liquid are purely ohmic, the associated overpotential is

$$\eta_{\text{cell}} = IR = i \cdot \text{ASR} = \frac{il}{\sigma} \tag{1.3}$$

where I is the total applied current through the cell, R is the internal cell resistance, ASR is the area-specific resistance, l is the length in the direction through which current is driven, and σ is the conductivity of the electrolytic solution. In selecting a nonaqueous solvent and corresponding supporting salt, conductivity must receive consideration along with electrochemical stability.

Nonaqueous systems can access chemistries with additional benefits, besides increased cell voltage, which may counteract cost and conductivity downsides, however. While some early nonaqueous chemistries followed the dual-species paradigm, wider stability windows allowed the use of high-voltage chemistries that employ the same active species in both the negolyte and posolyte. Early coordination complex chemistries used iron or nickel metal centers, which only offered one redox

couple and functioned in dual-active-species cells.[35] Replacing iron or nickel with other transition-metal centers offers chemistries, such as $V(acac)_3$, with multiple redox couples that allow switching to single active species systems. Complexes of transition metals like ruthenium,[31] vanadium,[14] chromium,[32] manganese,[33] and cobalt[45,46] all have been observed to offer multiple redox events and could be used to construct single-active-species RFBs. These metal centers are bound covalently to organic molecules, or ligands, which form the outer shell of the coordination complex. Additionally, ligands can either be ancillary, like acetylacetonate, merely serving to stabilize the metal centers, or non-innocent, like bipyridyl, which contributes its own reversible redox activity.

Acetylacetonate ligands stabilize the Ru, V, Cr, or Mn centers through octahedral bidentate bonds, but don't provide reversible electrochemistry themselves.[14,31,32,33] The $V(acac)_3$ chemistry, which offers two redox couples, improves upon the single-active-species AVRFB not only by increasing the open-circuit voltage, but also by reducing the number of charge states the cell needs to span: three states ($[V(acac)_3]^-$, $[V(acac)_3]^0$, $[V(acac)_3]^+$) to access two reactions and operate symmetrically, rather than four states in the AVRFB (V^{2+}, V^{3+}, VO^{2+}, VO_2^+) to access two reactions and operate asymmetrically. Furthermore, the $Cr(acac)_3$ chemistry shows another advantage since it accesses 4 different redox couples as shown in Figure 1.3, which are also separated by as much as 4.1 V in ACN.[32] This increases not only V_{cell} in Equation 1.1, but n as well.

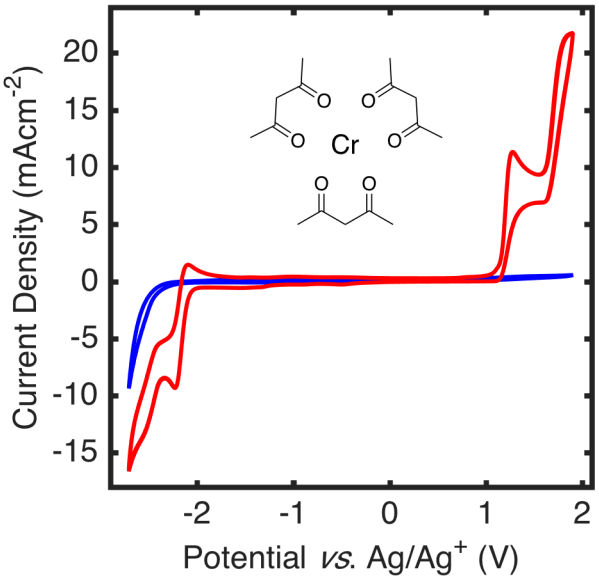

Figure 1.3. Cyclic voltammogram of 0.05 M $TEABF_4$ in ACN support solution with (red) and without (blue) 0.01 M $Cr(acac)_3$ active species, platinum, 500 mVs^{-1}, 25 °C.

Non-innocent ligands, like those based on bipyridyl, can further increase the number of redox couples accessed by an active species complex. Although they may not improve voltage, non-innocent ligands can further improve energy density by increasing *n*. For example, a functionalized $Cr(bpy)_3$ system offers 5 different redox couples, although these are only separated by as much as 1.6 V in ACN.[47]

Rather than coordinating non-innocent ligands, which are often purely organic structures, to metal centers, another strategy focuses on using organic active species alone for RFBs. Organic molecules would avoid the use of transition-metal resources that rely on mining operations, which make them susceptible to resource scarcity. Additionally, there is a vast library of organic molecules with different physical and electrochemical properties. One organic active species, rubrene, a polycyclic aromatic hydrocarbon, was proposed early in the field of nonaqueous RFB research, but the chemistry was abandoned because of low solubility in acetonitrile.[31] Other researchers have paired organics based on other polycyclic aromatic hydrocarbons,[48] phenothiazine,[49] quinones,[49] quinoxalines,[49] TEMPO radicals,[50] and viologens

(specifically, a bipyridyl with its nitrogens at the 4-positions)[50] to demonstrate all-organic RFBs using the dual-species paradigm. Other systems pair organics based on quinones[51] or quinoxalines[52] with lithium metal to create hybrid RFB systems. Even with this library of redox-active organic molecule classes, individual molecules can be functionalized to customize their physical and electrochemical properties to deliver better performance.[53,54,55]

Research into redox active organics recently produced a quinone-based organic chemistry that can range over multiple organic redox states, which has been used to form a single-active-species, symmetric organic nonaqueous RFB.[56] This paradigm was recently demonstrated again with a nitronyl nitroxide radical (similar to TEMPO) active species.[57] Also, pairing the two promising features of organic active species – the large library of redox-active molecule classes and the ability to customize them through functionalization – researchers tethered viologen moieties, which have half-reaction potentials suitable for aqueous negolytes, to nitroxide TEMPO radicals, which have half-reaction potentials suitable for aqueous posolytes. This viologen-TEMPO compound can operate symmetrically with redox reactions for both the negolyte and posolyte.[58]

1.5 Symmetric RFBs

Symmetric RFBs are systems where the negolyte and posolyte have identical chemical compositions in the fully discharged state. This symmetry offers performance and cost benefits because it simplifies reactor design. In symmetric RFBs, the consequences of crossover between electrolyte chambers are limited: crossover can only lead to losses in coulombic efficiency and electrolyte imbalancing, which can be easily rectified by mixing or polarity switches. In dual-species RFBs, crossover is irreversible

and must be prevented by expensive, highly selective IEM or bystander species. Symmetric chemistries even offer advantages over asymmetric single-active-species chemistries like the AVRFB: crossover delivering a charged 'contaminant' species to an opposing electrolyte only annihilates one charged 'host' species in the opposing electrolyte of a symmetric system, compared to two in the asymmetric AVRFB. This reduces coulombic losses compared to AVRFBs and eliminates a source of electrolyte imbalance from unbalanced changes in half-cell SOCs. Lowering the deviations between charge states should also reduce any migration-induced imbalancing. More palatable consequences of crossover in symmetric RFBs suggest that expensive IEMs used in many systems can be replaced with less expensive and less selective IEMs – or even porous, inert separators.

In order to achieve a symmetric chemistry, the active species must stably undergo two redox reactions that traverse three consecutive redox states. Ideally, these redox couples have widely separated voltages, as demonstrated in Figures 1.2 and 1.3 with even numbers of redox couples on each side of the voltage gap. If there are an odd number of redox couples, or they are not evenly balanced between positive and negative potentials, a system can be designed with different storage-tank and reactor volumes to account for the expected coulombic imbalance between the electrolytes.

Although not vast, a healthy number of symmetric nonaqueous RFB chemistries have been demonstrated. In addition to the $V(acac)_3$ and $Cr(acac)_3$ chemistries already described, there are other demonstrations of symmetric chemistries provided by coordination complexes: $Ru(bpy)_3$,[12] $Ru(acac)_3$,[31] $Mn(acac)_3$,[33] Co(bpy),[59] $Co(phen)_3$,[46] $Fe(bpy)_3$,[60] as well as several β-diketonate uranium complexes.[34] These systems all involve a transition metal center octahedrally coordinated with bidentate ligands, which seems to support their reversible redox behavior.

Alternatively, there are also demonstrations of organic active species potentially useful for symmetric RFBs, including rubrene,[31] diaminoanthraquinone-based molecules,[56] and nitronyl-nitroxide-radical-based PTIO.[57] PTIO spans three redox states from the aminoxyl anion, the neutral nitroxide radical, and oxammonium cation to deliver two stable redox reactions separated by 1.7 V. The diaminoanthraquinone chemistries offer as many as five redox states separated by up to 2.7 V.

Several classes of redox chemistries, both organometallic and organic, are capable of powering symmetric RFBs. As more chemistries are demonstrated, it becomes increasingly important to quantify the performance of these systems.

1.6 Cost-Effective Symmetric Nonaqueous RFBs

In studying symmetric nonaqueous RFB chemistries, the effort must focus on systems that match or improve upon the performance characteristics of state-of-the-art AVRFB while achieving lower cost. Nonaqueous symmetric chemistries can offer cost improvements via higher cell voltages and simpler reactors, but the chemistries must still provide the extremely long system lives (20 years) of AVRFBs.[61]

This thesis first uses a cost analysis to identify promising areas for cost reductions. Consequently, promising nonaqueous symmetric $V(acac)_3$ and $Cr(acac)_3$ are studied further to examine their cost, performance, and limitations. Whereas nonaqueous $V(acac)_3$ offers very promising electrochemical behavior, (Figure 1.2), using $Cr(acac)_3$ (Figure 1.3) offers more electrons at higher voltages, but has less well understood electrochemistry. $Cr(acac)_3$ uses a cheaper metal center, chromium, and provides four redox couples (n=1 or 2), rather than the two provided by $V(acac)_3$ (n=1 at most); $Cr(acac)_3$ also has more widely separated redox couples (voltammetry of $Cr(acac)_3$ suggests OCPs of 3.4 V for the cell reaction between the first electron

transfers and 4.1 V between the second *vs*. 2.2 V for $V(acac)_3$ with n=1). Therefore, the redox behavior of $Cr(acac)_3$ is studied further using both electrochemical and spectroscopic techniques.

Alternatively, as described, organic active species can replace transition-metal organometallic active species. Polycyclic aromatic hydrocarbon active species derived from waste products of highly scaled production processes for oil, coal, plastics *etc*. would offer extremely inexpensive feedstocks. Therefore, active species that can be derived from these inexpensive feedstocks are considered. A nonaqueous RFB chemistry employing 9,10-diphenylanthracene (DPA) could support symmetric operation using its radical oxidation and reduction reactions.

$$DPA + e^- \rightleftharpoons DPA^{\bullet -} \tag{1.4}$$

$$DPA \rightleftharpoons DPA^{\bullet +} + e^- \tag{1.5}$$

DPA was studied originally for its ability to deliver electrogenerated chemiluminescence.[62,63] It can offer cell voltages above 3 V between the two reactions and charged solutions of DPA at the millimolar scale have been observed to be stable on the time scale of hours.[64,65] Consequently, it is an ideal chemistry to study for nonaqueous symmetric RFB applications.

Finally, the performance of these chemistries in actual laboratory-scale flow cells is considered. Early demonstrations often used batch reactor electrolysis cells, which convolute the performance of the chemistry with inefficiencies arising from cell design.[31,41] Laboratory-scale flow cells can provide more realistic energy and power density performance metrics.[66] Cell performance metrics can be paired with cost estimates to allow decision-making on the overall cost-effectiveness. To this end, other metrics, such as cyclability, efficiency, and degradation pathways are all quantified for the chemistries studied in the following chapters.

2 Cost Considerations

As research on nonaqueous RFBs has developed, the focus has begun to shift from discovery and demonstration of early chemistries to evaluating developed chemistries for their utility and competitiveness in the intended large-scale EES applications. RFB cost analysis can vary from accurate depictions of near-commercial aqueous systems (Fe-Cr,[67] AVRFB,[68] Zn-Br[21]) to more general guiding directives for research into new chemistries, cell architectures, and performance features. Some of these predictive cost models identified nonaqueous RFBs as a promising low-cost EES technology.[69]

The various sources of revenue and avoided cost provided by energy storage underpin any motivation for installing EES. Some reports aggregate both cost and revenue data to demonstrate a cost-benefit analysis: these conclude that EES provides a net benefit.[5,70] Market failures stemming from absent regulatory frameworks or diffuse public benefits still hinder action on the clear cost-benefit results, however. These policy and social issues need to be resolved for EES to realize its full promise. The revenue streams available to EES are a complicated topic highly dependent on regional energy resources and can be expected to evolve with time. Rather than convolute an analysis with uncertainty derived from both revenue and expense estimations, only the cost of EES systems will be assessed in this study. Though this analysis may not solve policy shortcomings, it can identify means to decrease the cost of EES, which will make the technologies even more economically compelling and mitigate external factors dampening their widespread use. By avoiding uncertainty associated with value calculations for EES systems, competing EES technologies can be compared fairly within the uncertainty of the system's cost components.

With only costs in mind, comparisons can be made between state-of-the-art EES Li-ion and AVRFB systems with similar performance parameters. Furthermore, the cost structure of RFB technology is considered in search of 'low-hanging fruit' to reduce cost. This analysis reveals advantages provided by symmetric nonaqueous RFB chemistries in both power-related and energy-related costs. These areas of possible cost mitigation motivate further study of already discovered nonaqueous symmetric RFB chemistries as well as the search for new chemistries.

2.1 Large-Scale EES Analysis

EES can be based on many chemistries, each of which has a different vector of performance strengths and weaknesses, making it hard to compare across systems. Yet, all EES systems are delivered with a rated power and duration. These parameters are found in archives such as the DOE Global Energy Storage Database. Power ratings are available in the units of watts (W) and duration in the units of hours (hr), which can be combined to deliver an energy content of a system in watt-hours (Wh). Duration is another way of describing the energy-to-power ratio. By selecting a given duration and power, EES systems based on different chemistries can be compared fairly; disparate systems parameterized by the same duration and power should offer equivalent service in a first-pass analysis. In focusing on systems with equal power and duration, system cost, P_{system}, can be compared. Three primary contributions comprise system cost:

$$P_{system} = P_{capex} + P_{opex} + P_{disposal}. \tag{2.1}$$

Here P_{capex} is the capital expenditure at the start of the system's lifetime, P_{opex} is the cost of operating the system throughout its lifetime, and $P_{disposal}$ is the end-of-life cost (if positive) or revenue (if negative). Values for P_{capex} are well-established for many battery types and have received modeling attention for RFBs. Advantages can be found

between P_{opex} and $P_{disposal}$ values for different EES technologies. Advantages for one technology in P_{opex} may be counterbalanced by disadvantages in $P_{disposal}$, however. Li-ion systems with higher energy efficiencies than AVRFBs would expect a lower P_{opex} in models that include electricity charging costs into operating expenses (arguably these costs should appear as negated revenue in a value/benefit calculation). Yet, RFBs are expected to significantly outperform Li-ion systems in respect to $P_{disposal}$ owing to the comparative ease of separating RFB recycling streams. Nevertheless these costs are expected to be a minor fraction of P_{system};[71] only P_{capex} is considered in this analysis.

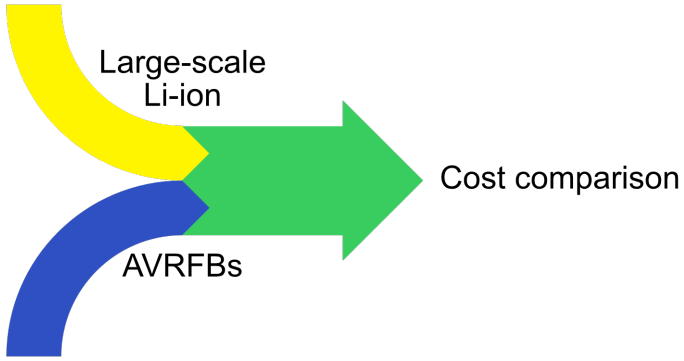

Figure 2.1. Analysis flow chart – cost comparison between commercial Li-ion and AVRFBs for large-scale energy storage.

Although this analysis neglects expenses after initial capital expenditure, the time period over which the system operates and before its eventual disposal is still relevant. P_{capex} must be amortized over the lifetimes associated with different EES systems and chemistries while accounting for the time value of that capital expenditure: the absence of stress and strain in redox-active solid electrodes allows RFBs to sustain more cycles, last longer temporally, and justify a higher P_{capex}, than shorter-lived solid-electrode system chemistries like Li-ion. Thus, in addition to comparing systems of

similar power and duration, levelized analysis must be performed to account for the difference in system lifetimes and the time value of money.

Even when using levelized comparisons, the different lifetimes of these systems and the systems they might displace – *e.g.* a thermal power plant – entail a variety of discount rates. Projects with shorter lifetimes like Li-ion EES systems, which range from 5 – 15 years,[72] are often subjected to discount rates of 7-13%.[70] Longer-lived systems, which accurately describe RFBs with 20-year warranties,[61] have recommended discount rates of 4%.[73] Meanwhile, peaker plants, which generate energy only when demand is extremely high and could be displaced by EES, can have even longer lifetimes, suggesting the use of lower discount rates. Both the Bush and Obama administrations recommended performing cost-benefit analyses with discount rates of 7%, 3%, or below 3% for long-term calculations meant to account for health and environmental impacts of future generations (often referred to as 'intergenerational equity').[73] Thus, the time scales associated with different EES technologies, and the thermal generators they might replace, require the use of long-term-project discount rates, which are much lower than those used in previous studies.

Building off of previous work with power plant economics and the levelized cost of electricity (LCOE), researchers suggested developing a levelized cost of storage (LCOS) framework for comparing EES technology. There still is no consensus about how this value might be calculated, however. Some researchers calculate the cost of the system and apply generic use scenarios to produce a LCOS, in cost per unit energy discharged from the storage device.[72] These calculations of LCOS are highly dependent on generic use scenarios and discount rates. Other models present LCOS as a function of discharged energy per given year, E_{out},[71]

$$\mathrm{LCOS}=\frac{P_{capex}+\sum_{t=1}^{t=N}\frac{A_t}{(1+r)^t}}{\sum_{t=1}^{t=N}\frac{E_{out}}{(1+r)^t}} \tag{2.2}$$

where N is the system lifetime in years. The yearly cost A_t, which amortizes P_{opex} and $P_{disposal}$ from Equation 2.1 *via* a discount rate, r, is assumed to be the same across Li-ion, RFB, and lead-acid chemistries in that report, with the exception of additional charging costs for more inefficient systems. Equation 2.2 may appear to provide a fair comparison on capital cost normalized by its energy output that also includes second-pass EES metrics like round-trip efficiency, but it implies an assumption that EES systems only provide value through delivered energy. This assumption is both invalid and favors higher efficiency systems more than they deserve. Other researchers describe how EES can provide value without actually needing to deliver energy: for example, an owner of a storage system can negotiate a capacity contract, which agrees to deliver electricity at a certain power whenever called upon.[74] Thus, a model that accurately depicts lifetime cost while avoiding value assumptions has yet to be formulated. Instead of making any value assumptions, an accurate, use-agnostic cost metric needs to be available to stakeholders looking to procure EES who better know their specific value proposition.

The present analysis proposes the use of an LCOS-like calculation providing levelized cost in $/kWh-yr, or the levelized cost of nameplate energy storage capacity for a given year, LCOSC,

$$\mathrm{LCOSC}=\frac{P_{capex}}{E_{np}\sum_{t=1}^{t=N}\frac{1}{(1+r)^t}} \tag{2.3}$$

where E_{np} is the nameplate energy storage capacity of the EES system in question. The

energy LCOSC metric serves as a good comparison method for systems with durations significantly greater than 1 hour. An alternative to this LCOSC value is LCOSPC, or the levelized cost of nameplate energy storage power capability, which instead uses the systems nameplate power capability, $\dot{E}_{np}$, rather than E_{np}, in Equation 2.3 to deliver a LCOSPC in $/kW-yr. This would be more suitable for applications with durations significantly shorter than an hour and will not be discussed further. Development of both energy and power LCOSC formulations are motivated by the fundamental step in life-cycle assessment procedures of defining a functional unit: in this case the unit is the annualized capital cost of available energy (or power) capacity. This functional unit has no bias towards certain EES uses. Second-pass EES metrics such as efficiency or self-discharge show up in value calculations: whether it is frequency regulation with multiple cycles in a day or capacity contracts with multiple cycles in a year. Armed with a suitable functional unit describing cost, stakeholders now can assess the benefit they would realize from storage, as measured by this functional unit, and make a decision.

Comparison of commercial AVRFBs and Li-ion systems are made using LCOSC. Table 2.1 shows that commercial UniEnergy AVRFBs[61] offer better or comparable LCOSC to commercial Li-ion systems from Tesla Energy.[75] Tesla Energy systems, quoted in April 2017, were adjusted with an installation multiplier of 1.3 to provide fair comparison against the UniEnergy system commissioned in June 2015. UniEnergy AVRFB systems have warranties of 20 years[61] compared to 10 years modeled for the Tesla Energy Li-ion systems. As expected with these long system lifetimes, the comparison depends strongly on selection of discount rate.

Table 2.1. LCOSC of 1 MW/ 3.2 MWh AVRFB and Li-ion system.

	LCOSC ($/kWh-yr) at relevant discount rates		
Discount Rate	1%	4%	7%
AVRFB (UniEnergy)	51.95	68.98	88.49
Li-ion (Tesla)	62.01	72.41	83.61

AVRFBs are an especially compelling choice in the 1% discount-rate scenario that properly accounts for intergenerational equity and the long lifetime of thermal peaker plants they could replace. At a higher discount rate, 4%, the results still indicate that the commercial AVRFBs offer less expensive long-duration storage than Li-ion. Even at the highest recommended discount rate associated with the shorter lifetime Li-ion systems, AVRFBs are competitive.

As Li-ion and AVRFB systems achieve more commercial installations, these battery systems become the benchmark against which to measure new EES technologies. Therefore, the cost considerations from these technologies, specifically AVRFBs, will be applied to symmetric nonaqueous RFBs.

2.2 RFB Cost Models

Li-ion systems are self-contained, hermetically sealed cells using well-established chemistries that achieve lower cost in part through vast economies of scale and incremental technological improvements. RFB systems, including AVRFBs, have more nebulous economics and require thorough cost analysis.[69,76] RFBs offer customizable power and duration capabilities by allowing adjustment between reactor power capabilities and reservoir energy-storage sizes. The customizable balance of energy and power is not available in typical solid-electrode batteries whose power generally scales linearly in proportion to energy.

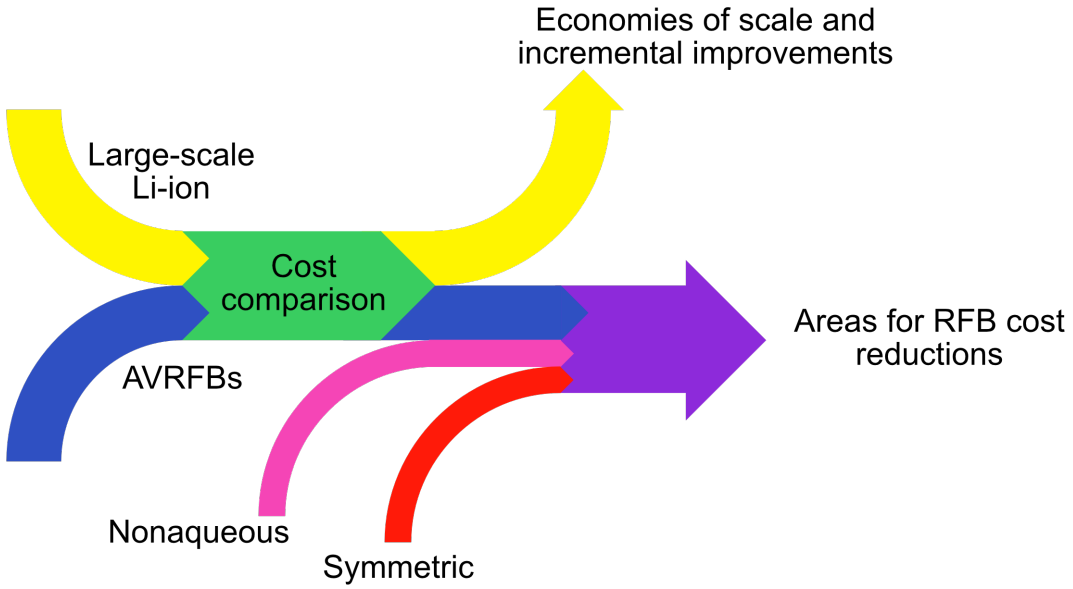

Figure 2.2. Analysis flow chart – identifying the cost components of RFBs.

Capital costs in RFBs are attributed separately to power capability of the reactor, P_{power}, and energy capacity of the storage tanks or battery solution, P_{energy},

$$P_{capex} = P_{power} + P_{energy} + P_{BOP}; \quad (2.4)$$

the additional factor P_{BOP} accounts for the balance-of-plant cost that are not associated with power or energy performance. Unlike Li-ion technology where increasing energy capacity requires increasing the number of hermetically sealed cells in a system such that power capabilities correspondingly increase (or *vice versa*) along with their associated expense, energy and power metrics (and their expense) scale independently for RFBs. Researchers have offered estimates of the power and energy related capital cost for AVRFBs, which are shown in Table 2.2 and inform targets for cost reductions. For instance, reducing power-related expenses may not improve cost effectiveness of extremely long duration systems where energy-related expenses dominate.

Table 2.2. Breakdown between power and energy related AVRFB costs in 2017 dollars (2% inflation).

	Eckroad[68]	Schoenung[77]	Viswanathan[78]	Keoleian[79]
Year	2007	2011	2014	2015
Power ($/kW)	2804	450	1062	1156
Energy ($/kWh)	366	676	208	224
P_{power}=P_{energy} duration (hrs)	7.7	0.7	5.1	5.2

Together the energy- and power-related capital expense estimates can combine to give a breakeven duration, after which the energy costs for AVRFBs begin to outweigh power costs. The cost estimates for AVRFBs from these studies vary significantly and suggest some inherent uncertainty in these studies. The most recent two reports give durations of equal power and energy expense just over 5 hours. Reducing the energy-related costs would make a larger impact on systems with durations longer than 5-hours as indicated from the last two studies. Alternatively, reduced power costs would achieve greater impact for durations shorter than 5 hours and shift the competitiveness of RFBs into shorter durations (*i.e.* the breakeven duration would decrease). When contextualized with the increased prevalence of AVRFBs and other RFBs in the DOE Global Energy Storage Database at durations longer than 4 hours, shrinking either power- or energy-related costs could impart significant cost reductions for RFBs in their commercial niche since they incur similar fractions of total cost. Further analysis of the expenditures associated with both P_{power} and P_{energy} can find areas to improve RFB cost-effectiveness.

For a given RFB chemistry, P_{power} scales linearly with reactor area, just as P_{capex} for Li-ion systems scales with electrode area. P_{power} arises from areal costs of the reactor components such as the reactor separator/membrane, porous electrodes, and current collectors, and non-areal costs like the power conversion system:

$$P_{power} = P_{separator} + P_{electrodes} + P_{currentcollector} + P_{pcs} + P_{other} \quad (2.5)$$

where P_{other} represents costs otherwise not accounted for. Since power conversion systems are expected to be agnostic to cell structure and chemistry, these costs, along with P_{other}, are not considered further. Using areal cost estimates from a comprehensive review of RFB cost-modeling (and some fuel cell cost-modeling) sources, reactor components most suitable for cost improvement are identified. Though more reports than cited in Table 2.3 exist, areal costs that clearly cited an already included value were removed to avoid double counting. Furthermore, owing to the uncertainty behind the source for these values, areal costs with a sufficiently large set of values were culled of the two extremes. Since these models, in most cases, gave predictive cost-values, this culling procedure is acceptable, but should be avoided when supplier-provided, scaled-up costs are compiled. When each component is factored into actual reactor cost, only porous electrode costs double as a result a bipolar reactor construction.

Table 2.3. Areal Costs ($/m^2) in 2017 dollars (2% inflation). Averages from datasets possessing more than five values are calculated from a subset culled of the two extremes.

Year	Porous electrodes	Bipolar plates	Architecture	IEM	Separator
1980[9]	36	3	3	67	
2004[80]	81	105	703		40
2007[68]	61	98		305	
2012[81]	99	92	66		5
2014[78]	74	58	6	531	11
2016[82]	20	52		26	
Average	63	75	36	233	19
Reactor cost	126	~75	36	233	19

Table 2.4. Reactor cost breakdown derived from values in Table 2.3.

	Porous electrodes	Bipolar plates	Architecture	IEM	Separator
IEM system	27%	16%	8%	50%	
Separator system	49%	29%	14%		7%

Table 2.3 shows that IEMs are the highest areal cost for IEM-reliant RFBs. Whereas IEMs account for 50% of the power-associated areal cost in RFB reactors that use them, porous separators only represent 7% of the cost in porous-separator-compatible RFBs. Systems requiring IEMs can achieve the highest cost reductions by developing inexpensive IEMs or eliminating their use in favor of porous separators. One study recently quoted a low areal price for an IEM,[82] though it is unclear where this value originates from and it conflicts with values for the same IEM in other reports.[78] In systems that merely use porous separators, the porous electrodes and bipolar plates account for nearly 80% of power related costs and should receive focus for further improvements.

Power also depends on the voltage provided by the RFB chemistry, as described in Equation 1.2. Whereas finding inexpensive components can reduce the costs of individual sources of power, changing to higher voltage chemistries will reduce the necessary area to provide the same power. Higher voltages reduce costs of all areal components through this mechanism.

Alternatively, energy costs are slightly more complicated to estimate. P_{energy} can be broken into two components representing the hardware cost, P_{tanks}, and solution cost, $P_{solution}$,

$$P_{energy} = P_{tanks} + P_{solution}. \quad (2.6)$$

Whereas many components of P_{power} scale linearly with reactor area, P_{tanks}, which describes the costs of the electrolytic solution reservoirs, is expected to scale with volumes as a power law with an exponent below unity (i.e. storing larger volumes becomes less expensive per additional unit volume).[69] One reason RFBs have been touted for grid storage is that this scaling leads to cost savings for very-long duration applications when compared against typical secondary batteries such as Li-ion or lead-

acid whose power-laws relation between volume and energy are nearly unity and linear. These savings begin to explain the increased prevalence of RFBs at longer durations in the DOE Global Energy Database and justify the recommendations for their use in applications with durations longer than 2 hours.[5]

Meanwhile $P_{solution}$ for a single active species chemistry, like the AVRFB or any symmetric chemistry, scales with the cost of battery solution as indicated:

$$P_{solution}\left(\frac{\$}{kWh}\right)=\frac{7.2\times10^{6}}{nFV_{OCP}}\left(P_{active}+\frac{P_{solvent}c_{solvent}}{c_{active}}+\frac{P_{support}c_{support}}{c_{active}}\right) \quad (2.7)$$

where P_i is the molar cost and c_i is molar concentration of active-liquid component *i*. In commercial AVRFBs, $P_{active} >> (P_{solvent} + P_{support})$, *i.e.* solution costs are completely dominated by the vanadium active species, whose cost significantly outweighs that of water and sulfuric or hydrochloric acid used in the supporting electrolyte.[68] Thus, for AVRFBs, Equation 2.7 simplifies to

$$P_{solution}\left(\frac{\$}{kWh}\right)=\frac{7.2\times10^{6}P_{active}}{nFV_{OCP}}. \quad (2.8)$$

Even with the price of the vanadium pentoxide precursor recently falling to $7.17/kg,[83] the active species used for commercial aqueous vanadium RFB equate to at least $36/kWh capital expense at commodity pricing, before any additional purification or conditioning. High purity resources and preconditioning can be expected to at least double or triple the cost of the vanadium active species. When vanadium pentoxide costs were 78% higher in 2014,[84] researchers reported that active-species cost accounted for $200/kWh in 4-hour duration systems (greater than triple the cost of the precursor in this instance).[78] Equation. 2.8 reveals little room for cost improvement in $P_{solution}$ since the 1.35 V AVRFB cell voltage is already above the maximum voltage of 1.23 V sustained by aqueous support without detrimental side reactions. The only means to

reduce $P_{solution}$ in aqueous systems would be to find new active-species with lower chemical cost or more available redox couples within the voltage window allowed by water (so that n >1). By contrast, using a nonaqueous system that permits higher cell voltages provides an alternative avenue to reduce P_{energy} *via* $P_{solution}$ so long as peripheral costs associated with solvent and support can be kept low; P_{power} would also shrink with increased cell voltage *via* reductions in areal cost components: $P_{separator}$, $P_{electrodes}$, $P_{currentcollector}$.

2.3 Nonaqueous RFBs

Whereas aqueous systems are limited to low voltages by water's electrochemical stability window, aprotic nonaqueous solutions offer significantly higher stability. For instance, switching to a nonaqueous vanadium RFB chemistry using the $V(acac)_3$ coordination complex in principle allows use of the same vanadium pentoxide precursor to produce the active species, but delivers an OCP of 2.2 V – a 63% voltage increase over AVRFB systems. According to Equation 2.8, this reduces active species cost by nearly 40% to achieve the same energy density as an AVRFB. If active species cost for vanadium is assumed to be \$200/kWh, the nonaqueous $V(acac)_3$ chemistry avoids \$78/kWh in costs. Yet in nonaqueous systems, the costs of nonaqueous solvents and support cannot be neglected as they are in Equation 2.7. A new question arises: can the cost savings from using less active species justify the more costly solvent and support?

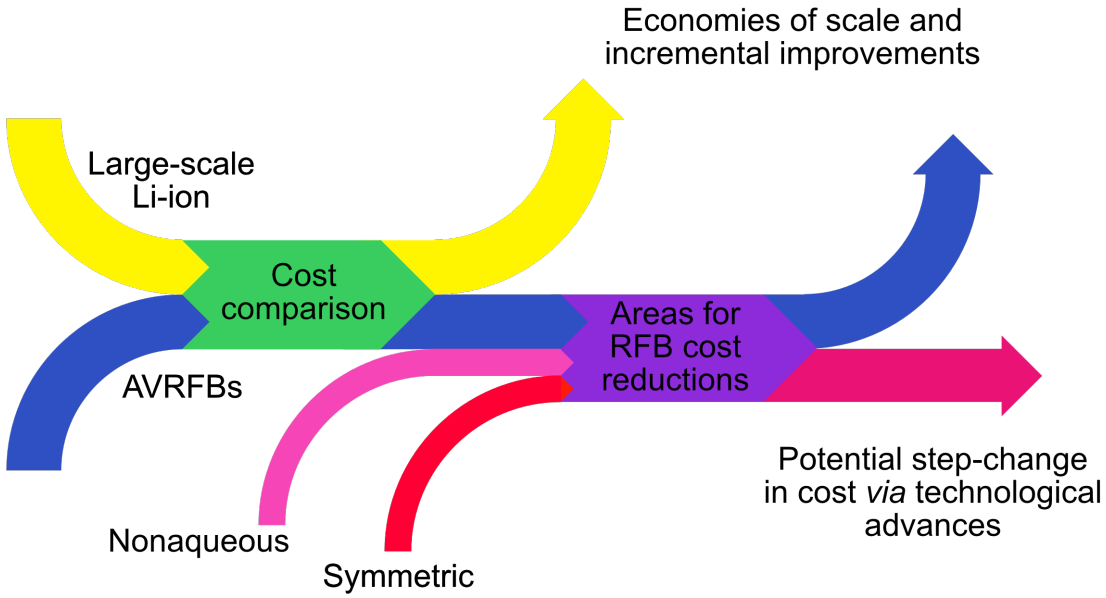

Figure 2.3. Analysis flow chart – cost implications of RFB technology step-changes.

While nonaqueous solvents inarguably cost more than water, there are many aprotic nonaqueous solvents that are both produced at industrial scale and useful for RFBs. Carbonate solvents including PC, ethylene carbonate, and DMC are already used in for Li-ion systems. Carbonate solvents could previously be found as low as \$6-\$10/L in 2002, well before Li-ion systems achieved the large-scale use in EES applications that they have achieved today.[85] Other solvents are waste products of large production scale commercial processes; ACN is a by-product of acrylonitrile production, which is a monomer used in synthetic rubbers.[86] The ACN by-product is largely combusted to fuel acrylonitrile synthesis,[86] which roughly indicates the value of ACN, as perceived by acrylonitrile producers. Laboratory suppliers offer ACN at \$8.05/L for the HPLC-grade solvent.[87] Assuming a system with an energy density of 35 WhL^{-1}, ACN would account for \$230/kWh of energy-related capital expenditure, even larger than the AVRFB active species cost.

At this price point, solvent costs significantly outweigh the cost savings from the high voltage nonaqueous RFB chemistries. Laboratory-supplier prices do not accurately

reflect the cost of solvents at large scales, however. A nonaqueous solvent such as fuel ethanol can be considered as a model solvent to describe the cost of human-produced organic solvents at large scales: fuel ethanol costs only \$0.56/L.[88] Large-scale nonaqueous RFBs using ACN can hope to target this solvent cost, which would lead system solvent cost to drop from \$230/kWh to below \$16/kWh. This price point leaves another \$64/kWh for supporting electrolytes. As a sanity check, the laboratory-supplier markup on commodity organic solvents can be assessed. If the markup on the price for hexanes, quoted before taxes at \$3.12/L,[87] compared to gasoline prices, at \$0.50/L before fuel tax,[88] are indicative of the markup on laboratory-supplier acetonitrile, \$230/kWh drops to \$36/kWh. This value is similar in magnitude to the target derived from fuel ethanol. Both costs leave room for additional expenditure on supporting electrolytes. Thus, it appears that solvents at commodity pricing could support nonaqueous systems while still leaving room for cost savings relative to AVRFBs.

Supporting electrolyte costs are also significant in nonaqueous systems. Many of the chemistries discussed here use salts with tetraalkylammonium cations and fluorinated anionic compounds as supports, which are expensive at lab supply scales. Lithium- and fluorine-containing salts that are used in Li-ion systems, which have a similar expense at laboratory-supplier prices, can be used as a cost target for nonaqueous symmetric RFB supporting electrolytes. Large-scale production delivers solutions of 1.2 M $LiPF_6$ in a mixed carbonate solvent for Li-ion battery electrolytes at a cost of \$20/L.[89] Subtracting out carbonate solvent cost from this value delivers a supporting electrolyte costing \$10/L, or \$285/kWh for a system with an energy density of 35 WhL^{-1}. A 1.2 M supporting electrolyte concentration is unnecessary for an RFB where support ions are redox-inactive and a system that only used 0.5 M solutions would spend \$119/kWh. Again this price point appears to outweigh the savings

provided by the high voltage active species, but, similarly to the case for solvents, there is room for improvement.

Appropriately designed nonaqueous RFB chemistries could use chemistries that sit above the voltage for lithium reduction, allowing lithium electrolytes to be used as supports and to benefit from extended economies of scale above those that have already been achieved. Alternatively, tetraalkylammonium salts produced at large scales could reach lower price points than those using a lithium cation since tetraalkylammonium cations comprise only carbon, hydrogen, and nitrogen molecules, all of which are abundant.

The issues of solvent and support costs identify the strongest motivation for improving energy density in symmetric nonaqueous RFBs. Higher energy densities reduce the necessary volume of supporting solution, and therefore supporting salt and solvent cost. Therefore, further development of nonaqueous RFB chemistries should target more energy dense battery solutions, even above the 35 WhL^{-1} target.

Clearly, additional cost savings must be found to make nonaqueous systems cost effective. This work explores two other symmetric nonaqueous chemistries that could significantly reduce cost: $Cr(acac)_3$ and DPA. Chromium is a less expensive transition-metal than vanadium since ferrochromium costs \$1.54/kg by chromium content.[90] This corresponds to an exceptionally low cost of \$0.80/kWh based off a system that reversibly undergoes two single-electron, full-cell reactions at 3.4 V and 4.1 V, as suggested by voltammetry from Figure 1.3. Another inexpensive alternative uses anthracene oil, a derivative of coal tar, as the base moiety of DPA, and delivers a precursor cost of \$0.50/kg.[91] Paired with its 3.1 V cell potential, this would enable another low active species precursor cost of \$2.15/kWh, still an order of magnitude smaller than the aqueous or nonaqueous vanadium precursor cost. Both of these

promising active species offer significant savings to counterbalance the additional cost of nonaqueous supporting electrolyte solutions. Assuming a 35 WhL^{-1} energy density and the solvent and supporting electrolyte values derived earlier, both $Cr(acac)_3$ and DPA precursor costs would reduce battery solution expense by nearly a third compared to AVRFBs, though some of that avoided expense would necessarily get used towards purification and treatment of the quoted precursors.

Table 2.5. Battery solution cost breakdown.

	Cost ($/kWh)			
Chemistry	Active Species	Solvent	Supporting Electrolyte	Total
AVRFB[78]	200	~0	1	201
$V(acac)_3$[§]	122	16	119	257
$Cr(acac)_3$[§]	1[*]	16	119	136[*]
DPA[§]	2[*]	16	119	137[*]

[§]assuming 35 WhL^{-1} energy density
[*]does not include purification or synthetic cost assumptions

These savings only reflect the avoided cost in P_{energy}, but do not include the savings in P_{power} offered by their higher OCPs. The power capabilities of these systems will ultimately depend on both cell voltage and rate capability. Higher voltages provided by these chemistries reduce the current density needed to achieve a given power. For example, a $V(acac)_3$ system would only need to deliver a current density that is 61% of the corresponding AVRFB current density to deliver the same power. $Cr(acac)_3$ operating at an average cell voltage of 3.75 V would similarly only require 36% of the AVRFB maximum power current density, and DPA, at 3.1 V, would need only 44%.

The rate capabilities of nonaqueous systems, which also involve losses from ohmic drops and interfacial reaction kinetics, need to be understood to inform the cost implications – a question that motivates the study presented in Chapter 5 of this document. Coupled to these power savings are the power-related savings offered by

employing symmetric chemistries, which requires further investigations into reactor design.

2.4 Symmetric RFBs

In addition to saving on reactor cost by using high voltage nonaqueous systems, employment of a symmetric RFB chemistry can further reduce reactor costs. Symmetric systems can use inexpensive porous separators rather than the expensive IEMs needed for dual-species RFBs or asymmetric single-active-species systems like the AVRFB. As shown in Table 2.3, porous separators can offer over 90% cost savings from IEMs and reduce the separator/membrane percentage of P_{power} from 50% to 7%. Given that P_{power} equals P_{energy} at AVRFB durations of 5 hours, these savings would still significantly improve the cost effectiveness of RFBs at long durations.

Using the AVRFB as a model, a breakeven current density corresponding to maximum power density can be identified between IEM-reliant AVRFBs and symmetric nonaqueous RFBs using porous separators. Since RFBs with separators have a total areal cost of \$256/m^2 and RFBs with IEMs cost \$470/m^2, separators offer a 45% cost savings. Pair these savings with the impact of higher cell voltages described in Equation 1.2 and, at a given current density, $V(acac)_3$ offers a 67% discount in reactor areal costs, DPA offers a 76% discount, and $Cr(acac)_3$ offers 80%. Yet, nonaqueous electrolytic solutions are less conductive than aqueous acid solutions and it is unclear if they will support the same magnitude of current density.

This data can instead predict the lowest current density necessary in a symmetric nonaqueous RFB to maintain the same reactor cost as an IEM-separated AVRFB. Since the symmetric nonaqueous reactor with a porous separator is less expensive than the aqueous IEM-separated reactor, a larger symmetric reactor could be built at the same

cost of a smaller IEM-separated reactor. Thus, the symmetric nonaqueous reactor would not require as high of a power density to deliver the same power and cost: A RFB using a porous separator needs a maximum power density of only 0.7 Wcm^{-2} to match the reactor cost of a power-maximizing AVRFB cell design that delivers 1.3 Wcm^{-2}, achieved *via* a non-archetypal cell that employs a single-pass reactor and four electrolyte storage tanks (a design that overestimates AVRFB's practical capabilities).[44,78] If the only losses in this power-maximized cell are ohmic, then the 1.35 V AVRFB requires a 1,926 $mAcm^{-2}$ current density to deliver this power. For the nonaqueous chemistries with nominal voltages as described earlier, any rates above breakeven current densities of 322 $mAcm^{-2}$, 228 $mAcm^{-2}$, and 189 $mAcm^{-2}$ for $V(acac)_3$, DPA, and $Cr(acac)_3$, respectively, would correspond to reduced reactor costs. Chapter 5 assesses the practicality of these peak-power current densities in symmetric nonaqueous RFBs.

2.5 Summary and Discussion

This chapter focuses on cost effectiveness to motivate further research into RFBs, specifically nonaqueous symmetric RFBs. In considering cost-effectiveness, this chapter aims to provide an amortized cost figure for EES systems with similar power and duration performance parameters; making any assumptions about the value of the resources is avoided since it convolutes the decision-making process for stakeholders who better understand the value provided to them by an EES system. LCOSC, or the levelized cost of nameplate energy storage capacity, offers a cost metric capable of fairly comparing RFB technologies or competitive conventional battery technologies such as Li-ion. RFBs are attractive because of their long lifetimes, good cyclability, and cost advantages for long duration systems. Large-scale AVRFBs commissioned in 2015

offer lower LCOSC than commercial large-scale Li-ion systems quoted in 2017, despite the recent rapid drop in Li-ion battery prices. This suggests that AVRFBs should have achieved more installations than Li-ion in the past two years and in the future. The DOE Global Energy Storage Database still shows more Li-ion systems at durations greater than 4 hours, however. This likely stems from ubiquity and familiarity of Li-ion systems and the nascent stage of AVRFB commercialization and supply chain.

LCOSC, as defined here, only uses capital expense and seeks a use-case agnostic description of cost. Once accurate data exists, disposal expenses (or revenue), maintenance expenses, or age-dependent nameplate capacity degradation can be incorporated into this metric. Obviously, stakeholders looking to procure EES must consider the value these system's provide them. This value can depend on secondary or tertiary EES performance metrics not incorporated into LCOSC; these include efficiency, self-discharge, or cycle-dependent degradation rate. For instance, Li-ion systems have higher AC round-trip efficiency, which would affect any arbitrage (purchasing electricity at low prices to sell subsequently at a higher price) value calculation: Tesla energy stated an 80% AC round-trip efficiency, while UniEnergy, 65 – 70%.[75,61] Thus, the examination of flow reactor experiments in Chapter 5 with symmetric nonaqueous chemistries will also discuss their energy efficiencies.

Although both technologies are expected to continue reducing costs incrementally, new RFB technologies, which offer possible step-changes in cost-effectiveness, are also considered. Symmetric nonaqueous RFBs are one such strategy for RFBs. Nonaqueous systems can access higher voltages than the 1.23 V accessible by aqueous systems; higher voltages reduce both energy and power costs for RFBs. Symmetric cells avoid using expensive IEMs in favor of inexpensive porous separators to further diminish power costs. This cost study focuses on three symmetric nonaqueous

RFB chemistries: $V(acac)_3$, $Cr(acac)_3$, and DPA. Two-electron $Cr(acac)_3$ and metal-free DPA both discount active species cost by 1-2 orders of magnitude compared to vanadium pentoxide used in symmetric nonaqueous $V(acac)_3$ or aqueous vanadium – the component that overwhelmingly dominates energy costs for AVRFBs. After introducing solvent and supporting electrolyte costs, both $Cr(acac)_3$ and DPA offer a 32% discount on battery solution cost compared to AVRFBs. All three nonaqueous chemistries offer the possibility of greatly reduced reactor costs compared to AVRFBs – as low as one-fifth for $Cr(acac)_3$. These compelling cost arguments warrant further study of the three chemistries to understand their limitations and to quantify their performance.

3 Coordination-Complex Active Species

Researchers have identified several coordination complex active species capable of supporting symmetric nonaqueous RFB operation.[12,14,31,32,33] The cost analysis in Chapter 2 suggests that these chemistries, specifically $V(acac)_3$ and $Cr(acac)_3$, could offer significant improvements in cost effectiveness. Both complexes stabilize transition-metal centers with three bidentate acetylacetonate ligands bound octahedrally. These complexes deliver high cell voltages that necessitate nonaqueous solutions and can support symmetric operation. $V(acac)_3$ provides almost ideal electrochemical behavior, but lacks the transformative cost impact offered by $Cr(acac)_3$, whose electrochemistry needs further study.

$Cr(acac)_3$ appears especially promising as a symmetric nonaqueous RFB active species: it has five accessible redox states in $TEABF_4$ supported ACN, which would deliver cell OCPs of 3.4 V for first oxidation and reduction reactions and 4.1 V for the subsequent reactions. The $Cr(acac)_3$ complex has also been used for catalysis[92] and as a standard for atomic absorption spectra.[93] Whereas $V(acac)_3$ appears to support outer-sphere electron transfer for both single-electron addition and withdrawal in certain nonaqueous electrolytes, and to undergo both charge exchanges with relatively facile kinetics,[94] the voltammetric response of $Cr(acac)_3$ is harder to interpret. Experimental efforts to clarify the electrochemistry of $Cr(acac)_3$ have been challenging because the reaction mechanism apparently varies with the choices of solvent, working electrode, and supporting electrolyte.[95,96,97,98,99]

The literature describing nonaqueous $Cr(acac)_3$ electrochemistry fails to provide a consensus about the mechanisms for either the first reduction or first oxidation of the neutral complex. The electrochemical response during reduction depends heavily upon solvent, with different responses observed in DMSO,[95,97,100,101] DMF,[97] DCM,[96] ACN,

[97, 99,102] and others.[97] Consequently, various mechanisms have been proposed for the first reduction. The first oxidation mechanism only received significant attention after $Cr(acac)_3$ was proposed for nonaqueous RFB applications.[32,103]

Most reports of $Cr(acac)_3$ electrochemistry describe experiments performed with mercury electrodes, which have been observed to form complexes with $acac^-$ ions.[104] When the nonaqueous electrochemistry of $Cr(acac)_3$ is compared between mercury and platinum working electrodes, experiments using mercury suggest the presence of three distinct reduction events, whereas those with platinum only indicate one.[99] $Cr(acac)_3$ oxidizes at relatively high potentials, which are beyond the oxidation potentials of mercury, so $Cr(acac)_3$ oxidation has only been probed with solid electrodes.[32,103] Most of the studies characterizing $Cr(acac)_3$ electrochemistry do not illustrate its behavior at surfaces similar to those of the porous electrodes in RFBs.

The choice of supporting electrolyte is also known to affect the electrochemical response of β-diketonate coordination complexes. When supported by alkali and alkaline-earth-metal salts, the salt cations coordinate with $acac^-$ ligands harvested from the $M(acac)_3$ and shift reaction potentials; this coordination does not occur in the presence of TEA^+ cations, however.[98,105,106] Consequently, tetraalkylammonium salts have been preferred as supporting electrolytes for nonaqueous RFB using these coordination chemistries.

Symmetric nonaqueous RFB cells based on several metal-organic coordination complexes are hypothesized to charge and discharge *via* single-electron disproportionation and comproportionation mechanisms, respectively,[12,14,31,32,33,] but the chromium system exhibits unexpected charge-discharge behavior in light of this proposed electrochemistry. The present study intends to illuminate the chemical or electrochemical processes that cause the unusual cycling responses of $Cr(acac)_3$ cells.

Linear-sweep voltammetry (LSV) experiments with microelectrodes, similar to those performed by Shinkle *et al.* with $V(acac)_3$ solutions,[94] show that the redox activity of $Cr(acac)_3$ is inconsistent with a single-electron disproportionation mechanism: there appears to be a charge imbalance between the first oxidation and the first reduction half-reactions.[32] Spectroelectrochemistry supports the previously proposed simple outer-sphere mechanism for $V(acac)_3$ and conflicts with reports of ligand dissociation degradation pathways in $V(acac)_3$ flow cells.[66] By contrast, experiments with $Cr(acac)_3$ provide evidence of a ligand dissociation mechanism during the first reduction, further contradicting the proposed simple single-electron outer-sphere electron exchange.

A new mechanism for $Cr(acac)_3$ reduction is proposed that is consistent with the voltammetric (Section 3.2) and spectroelectrochemical (Section 3.3) observations. The alternative mechanism suggests a different overall cell reaction than previously proposed for RFBs involving $Cr(acac)_3$, which affects expectations for charge-discharge performance (Section 3.4) and solution metrics such as theoretical maximum energy density. Clarification of the reduction mechanism informs the uses of $Cr(acac)_3$ as an electrocatalyst or standard as well. Ultimately, a different solvent system is tested with both $V(acac)_3$ and $Cr(acac)_3$ in an effort to understand the chemistries' dependence on solvent systems and to inform the search for a solvent system that supports reversible $Cr(acac)_3$ electrochemistry.

3.1 Experimental

Vanadium acetylacetonate (98%, Strem Chemicals, USA), chromium acetylacetonate (99.99%, Sigma-Aldrich, USA) and tetrabutylammonium tetrafluoroborate ($TBABF_4$, Sigma-Aldrich, UK) were used as delivered. $TEABF_4$

(99%, Alfa Aesar, USA) was recrystallized in methanol following the procedure of Rolfe *et al.*[107] and dried under a nitrogen atmosphere. All solutions were prepared in an argon-filled glove box (OMNI series, Vacuum Atmospheres, USA or PureLab, Inert Technologies, USA) with oxygen and water contents less than 1 ppm. Anhydrous ACN (99.8%, Sigma-Aldrich, USA) and anhydrous DME (99.5%, Sigma-Aldrich, USA) were dried over molecular sieves (3Å, Sigma-Aldrich, US) in the glovebox for more than a day before being used to prepare solutions.

Fabrication of metal microelectrodes for voltammetry entailed encapsulating platinum wires (99.9%, 100 μm diameter, Alfa Aesar, USA) in molten soda-lime-glass tubing and then grinding the ends of the cooled glass bulb to expose a circular cross-section of the metal wire. The area of the disk electrodes were verified using voltammetry in aqueous potassium ferricyanide solutions, as described by Kucernak *et al.*[108]

3.1.1 Linear Sweep Voltammetry and Cyclic Voltammetry

Voltammetry is a workhorse experimental technique for electrochemists, and two versions of the technique are used heavily in this chapter: linear sweep voltammetry and cyclic voltammetry. Experiments presented here illustrate results from voltammetry performed on three-electrode cells comprising a working electrode, counter electrode, and reference electrode. The intended purpose of the three-electrode setup is to allow study of the electrochemical phenomena that occur at a single electrode. One circuit connects the working electrode to the counter electrode, providing a path along which current flow can be driven. The working electrode is connected through a second, high-impedance circuit to the reference electrode, which is used to measure the voltage. Both circuits are connected electrically through the potentiostat and ionically through the solution being tested; experiments typically measure the relationships between the

working-to-counter current and the working-to-reference voltage. This differs from a traditional battery where there are only two electrodes and the current and resistance between the two electrodes convolutes the voltage measured across the cell.

In a practical three-electrode cell, the counter electrode needs to be large compared to the working electrode so that the working electrode provides the dominant series resistance. The counter electrode also must be placed sufficiently far from the working electrode to avoid contamination of the working electrode's immediate environment with reaction products formed at the counter.[109] The reference electrode ideally samples a solution with nearly identical composition to the working electrode, a goal that is usually achieved by physical proximity. The reference electrode must also undergo a half-reaction that involves one of the molecular or ionic species comprising the working solution under analysis in order to deliver thermodynamically meaningful potential measurements.[109] When using the three-electrode setup, CV delivers information on half-reaction potentials, electrochemical reversibility, and reactant mass transport; LSV can deliver additional information in the form of diffusion limited reaction rates, often referred to as limiting currents. Both CV and LSV are important first steps in most electrochemical characterization efforts.

Voltammetry delivers information about redox reactions by monitoring current response as a function of applied voltage. Voltage is swept at a constant scan rate between a starting voltage and stopping voltage in LSV or cycled between these two extremes (as a triangular wave) in CV. The convention used in this report plots more negative voltages on the left and more positive voltages on the right (with relatively negative voltages being more reducing). Additionally, positive current corresponds to oxidation reactions at the working electrode (*i.e.* anodic currents are positive) and negative currents to reduction reactions (cathodic currents are negative). Peaks during

CV, like those observed in Figure 1.2, occur as a result of the balance between reaction kinetics and mass transfer: before reaching a peak current the reaction rate is controlled by kinetics; after the peak, active-species diffusion limits transport of reactant to the electrode surface. Running CV at a variety of scan rates can capitalize on these disparate time-scales to provide information on kinetics and mass transfer.

The data in Figure 1.2 illustrate the archetypal CV phenomenon of 'redox couples', or the close proximity in voltage between the peaks of a redox half-reaction and its reverse reaction; this signature corresponds to a reversible half-reaction. Various analyses can be performed to deliver quantitative and qualitative information about such half-reactions. Averaging the reduction and oxidation peak potentials yields the equilibrium reaction potential; the dependence of peak heights on scan rate delivers qualitative information on mass transfer mechanisms and, for diffusion-controlled systems, quantitative values for reactant diffusivity. Qualitative information about reaction kinetics can be gathered by inspecting the voltage separation between peaks of a couple; reversibility, in this case defined as the ability of a species produced by oxidation or reduction to return to its original state, can be assessed by inspecting the ratio of redox-peak currents relative to the current at equilibrium potential. Reversibility metrics are not quantitative without deep understanding of the reaction mechanisms and various other system parameters, but are good indicators.

Whereas redox activity produces current peaks in CV, it manifests as current steps in microelectrode LSV; the currents achieved when voltages are swept far past the equilibrium potential are referred to as limiting currents. These current plateaus deliver information about active species diffusivity. Additional modeling can exploit the shape of the LSV response to deliver reaction rate constants, and has been demonstrated previously with $V(acac)_3$.[40] Both LSV and CV provide experimental results capable of

identifying promising redox active materials and further characterize the electrochemical behavior of nonaqueous RFB chemistries.

Voltammetry was performed using three-electrode electrochemical cells in the glovebox, which were connected to an Autolab PGStat 302N potentiostat (Metrohm, Ecochemie, Netherlands) *via* electrical feed-throughs in the glovebox wall. Experiments were performed in a three-electrode cell with the counter electrode separated from the chamber containing the reference and working electrodes by a glass frit. All working electrodes were polished wet with alumina slurry (5 μm, then 0.05 μm, Pine Instruments, USA) and dried between experiments. A coiled 0.3 m length of Pt wire (99.99%, 0.3 mm diameter, Alfa Aesar USA) was used as the counterelectrode in all cases. Voltammetry was performed relative to a nonaqueous Ag/Ag^+ reference electrode (BASi Inc., USA) comprising a silver wire immersed in a solution of 0.01 M $AgNO_3$ (99%, Basi Inc., USA) and 0.1 M tetraethylammonium perchlorate ($TEAClO_4$, 90%, Alfa Aesar, USA) in the working solvent (ACN or DME). The reference electrode was ionically connected with the working solution through a fritted junction involving an intervening solution of 0.05 M tetraethylammonium nitrate ($TEANO_3$, 97%, Fluka, USA) in the working solvent. After running a LSV experiment in the negative (for reduction) or positive (for oxidation) direction toward potentials increasing in magnitude, the voltage was swept back across the same range, but in the reverse direction, to look for hysteresis in the current response. All linear-sweep voltammograms showed minimal hysteresis when reversed; results presented graphically here show both the forward and reverse voltage sweeps for every experiment.

3.1.2 Spectroelectrochemical Methods

Reduction and oxidation of electrolytic solutions can be monitored using metrics

beyond current and voltage. Pairing electrochemical experiments with spectroscopic techniques can deliver physical properties of electrolytic solutions and their redox-active constituents. So-called spectroelectrochemical techniques pair electrochemical experiments like voltammetry, electrolysis, or impedance spectroscopy with spectroscopic measurements such as ultraviolet-visible-infrared light (UV-vis-IR) absorbance or nuclear magnetic resonance (NMR). In this study, spectroelectrochemical analysis pairs bulk electrolysis with UV-vis-IR absorbance.

Spectroelectrochemical experiments were performed in a custom cell, which was fabricated in-house and is depicted in Figure 3.1. A 1-mm pathlength quartz cuvette was fused to an airtight glass cell body *via* a quartz-glass gradient. A Pt-mesh working electrode accessed the electrolytic solution occupying the quartz cuvette while a Pt-disk (3 mm diameter) counterelectrode completed the circuit from a sidearm in the glass cell body. Another sidearm allowed access for the nonaqueous Ag/Ag^+ reference electrode. To clean the Pt mesh, it was rinsed with ultrapure water, then with acetone, and dried; the Pt disk was cleaned using the aforementioned polishing procedure.

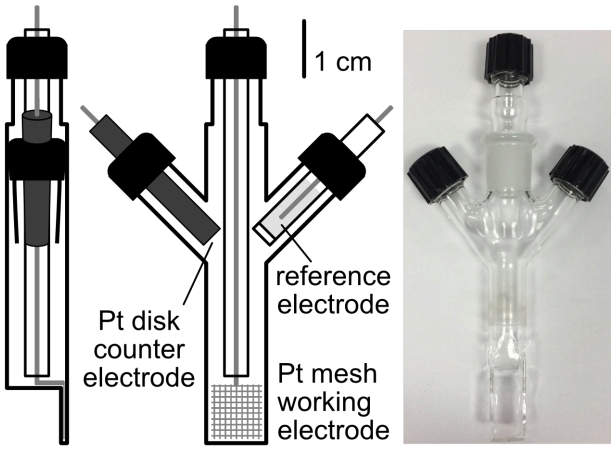

Figure 3.1. Schematic diagram and photograph of the spectroelectrochemical cell.

Chronoamperometric – also referred to as potentiostatic – bulk electrolysis was performed using a Ag/Ag^+ reference electrode containing a solution of 0.01 M $AgNO_3$

and 0.1 M $TEAClO_4$ in ACN. The spectroelectrochemical cell was assembled and filled with the test solution in the glovebox; the electrode ports were then sealed using screw tops containing o-rings before being transferred out of the glovebox and into a spectrophotometer for experiments. Prior to exiting the glovebox and beginning chronoamperometry, a cyclic voltammogram was collected to reaffirm the suitable range of applied potentials. Spectra were gathered using ThermoFisher Genesys 10S UV-Vis (Fisher, USA) and Cary 40 (Agilent, USA) spectrophotometers to quantify UV-vis and near-IR absorption, respectively. The general procedure involved observing the absorbance spectrum of the pristine solution at its OCP, followed by collection of spectra after applied chronoamperometric electrolysis for 30, 60, 120, 240, and 480-second intervals. Unless otherwise specified, the spectra reported here illustrate absorbance data collected after the last electrolysis interval (after 930 total seconds of applied potential). The baseline spectrum obtained from a 0.025 M solution of $TEABF_4$ in ACN has been subtracted from all the data reported here to isolate effects due to the electrochemistry of the metal complexes.

3.1.3 Charge-Discharge Cycling

Cells optimized for battery operation deliver quantitative results about the performance of coordination complexes as an RFB active species and differ substantially in their design from spectroelectrochemical cells. Charge-discharge experiments perform bulk electrolysis galvanostatically (or potentiostatically) and allow observation of the cell potential (or current) with time. The current-voltage-time relationships measured during charge-discharge cycling allow further analysis to characterize efficiency and cyclability.

There are additional performance characteristics that can influence system cost that lie outside the scope of the discussion in Chapter 2. Commercial battery suppliers for Li-ion systems often report maximum C-rate, which is defined as

$$\text{C-rate} = \frac{I_{\text{appl}}}{I_{\text{1hr}}} \tag{3.1}$$

where I_{appl} is the maximum applied current and I_{1hr} is the current obtained by dividing a battery's total available charge capacity by one hour. A similar quantity can be used for RFB systems: although the community has yet to agree on a suitable convention to determine total available capacity, which is constrained in practice by operating-voltage limits. The theoretical maximum capacity associated with complete reactant conversion will be used here as the basis for C-rates. In commercial RFB applications, reactors are designed for lowest cost in what are generally long-duration applications, corresponding to low C-rates: a system designed for 4-hour durations should not pay for reactor power capacity capable of C-rates significantly larger than C/4. Still, understanding the C-rate capabilities of these systems becomes important if short-duration RFB applications become viable. This would only occur if cost-effectiveness of reactor components improves significantly, which might be possible in systems where IEMs can be replaced with porous separators.

The efficiency of batteries is quantified with three metrics: coulombic, voltage and energy efficiency. Coulombic efficiency, CE, is the ratio of coulombs output in a discharge step, Q_{out}, against the coulombs input during the preceding charge step, Q_{in}.

$$\text{CE} = \frac{Q_{\text{out}}}{Q_{\text{in}}} \tag{3.2}$$

Whereas coulombic efficiencies below 100% are usually associated with cell degradation in conventional Li-ion systems, coulombic efficiencies below 100% do not necessarily represent irreversible capacity losses in RFBs. Lower coulombic efficiencies

can stem from multiple causes to which the system is relatively resilient, including shunt currents in piping, reactant crossover across the separator, poor mixing in solution reservoirs, and accumulated imbalances in compositions and volumes between the negolyte and posolyte. Voltage efficiency, VE, is the ratio of the average voltage delivered on discharge, V_{disch}, against the average voltage on charge, V_{charge}.

$$\text{VE} = \frac{\langle V_{\text{disch}} \rangle}{\langle V_{\text{charge}} \rangle} = \frac{\left(\frac{1}{Q_{\text{out}}}\right)\int_0^{Q_{\text{out}}} V_{\text{disch}}\, dQ}{\left(\frac{1}{Q_{\text{in}}}\right)\int_0^{Q_{\text{in}}} V_{\text{charge}}\, dQ} \tag{3.3}$$

Voltage inefficiencies are a reality for any non-equilibrium process and its sources are further discussed later in this chapter and in Chapter 5. Energy efficiency, EE, combines information about voltage and charge, expressing the energy dispensed during discharging against the energy accepted during charging:

$$\text{EE} = \frac{\int_0^{Q_{\text{out}}} V_{\text{disch}}\, dQ}{\int_0^{Q_{\text{in}}} V_{\text{charge}}\, dQ} \tag{3.4}$$

For cells cycling at constant currents (galvanostatically), energy efficiency can be obtained from the product of coulombic and voltage efficiency. Energy efficiency becomes important for cost considerations at any nonzero electricity prices – a factor not considered in Chapter 2. There are other performance characteristics such as self-discharge, which will influence cost effectiveness, but these can be mitigated with cell or stack optimization, and, consequently, are not studied in this chapter.

Batch-reactor charge-discharge experiments were performed in a one-dimensional, two-chamber, 10 cm long cylindrical glass cell, similar to the one described earlier by Shinkle *et al*.[40] Electrolytic solutions were contained within the two 12.5 mL chambers, which were continuously stirred by Teflon-coated magnetic stir-bars. A Celgard 4560 membrane was used to separate the positive and negative cell

chambers. The separator was rinsed with ACN before use and allowed to soak within the loaded cell for 24 hours before beginning experiments. The electrodes employed in the charge-discharge experiments were graphite slabs (GraphiteStore, U.S.), offering 2.54 cm^2 of superficial contact surface to each solution. Galvanostatic charge-discharge experiments were performed using a solution of 0.05 M $Cr(acac)_3$ and 0.5 M $TEABF_4$ in ACN. The charge-discharge scheme entailed a 0.39 $mAcm^{-2}$ charging current density to deliver 30% of the theoretical maximum state of charge (SOC) assuming a single-electron disproportionation or 4.1 V cutoff – whichever came first – and a 0.039 $mAcm^{-2}$ discharging current density down to a 0.5 V cutoff. All charge-discharge experiments were performed in the argon-filled glovebox.

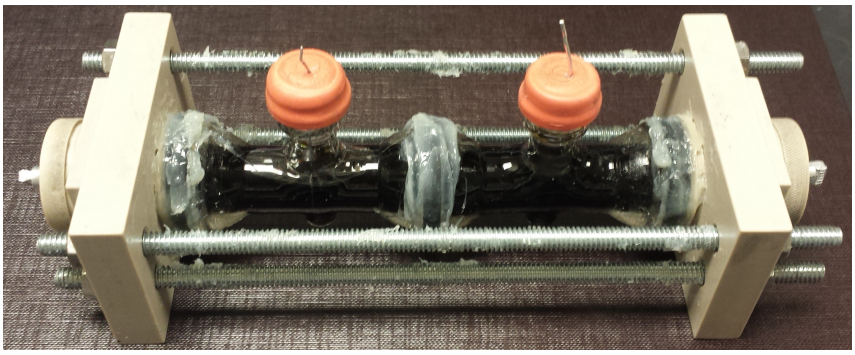

Figure 3.2. Batch-reactor charge-discharge cell.

3.2 Voltammetry

Whereas $V(acac)_3$ displays facile electrochemical kinetics for both oxidation and reduction,[14, 94] the redox behavior of $Cr(acac)_3$ appears less reversible, as illustrated by the cyclic voltammogram in Figure 1.3. For the oxidation reaction occurring at 1.20 V *vs*. Ag/Ag^+, no significant reduction peak is visible, whereas the corresponding oxidation peak is sharply defined. In an effort to clarify the cyclic voltammetry, LSV was performed using disk microelectrodes at a 1 mVs^{-1} scan rate. Use of

microelectrodes makes diffusion transients very short, so that liquid-phase mass transport can be taken to reside in a pseudo-steady-state at all times. An ancillary benefit of the small electrode area is that the overall conversion of the active species is small during a voltage sweep; solution properties change minimally over the course of procedures whose scan rates demand long experimental time-scales more consistent with electrolysis.

Microelectrode LSV data for $V(acac)_3$ was gathered in the past by Shinkle *et al.*, who used it to determine kinetic parameters such as exchange-current density and symmetry factor for the two redox couples flanking the OCP of freshly prepared $TEABF_4$-supported $V(acac)_3$ solutions in acetonitrile.[94] The model from that study is based on an assumption that the metal complex undergoes an outer-sphere, single-electron disproportionation; it characterizes the redox events on either side of the OCP with a $[V(acac)_3]^{0/+1}$ couple (at 0.45 V *vs.* Ag/Ag^+) and a $[V(acac)_3]^{-1/0}$ couple (at –1.77 V *vs.* Ag/Ag^+).

As discussed by Shinkle *et al.,*[94] the microelectrode LSV response of a complex that disproportionates electrochemically differs from traditional LSV experiments that probe single half-reactions. During microelectrode LSV of disproportionation complexes, current is expected to be near zero at the OCP of the pristine solution, and nonzero currents are observed at the equilibrium potentials of the positive and negative couples involved in the disproportionation. Generally the current falls (or rises) to a negative (positive) limiting current as the potential traverses past the first redox couple below (above) the OCP. If the pristine complex is the limiting reactant and the number of electrons involved is identical in both the positive and negative half-reactions, then the limiting currents achieved at low and high potentials during LSV are expected to be equal and opposite. Consistent with the hypothesized outer-sphere single-electron

electrochemical disproportionation, microelectrode LSV experiments with solutions of 0.01 M $V(acac)_3$ and 0.05 M $TEABF_4$ in ACN exhibited approximately equal and opposite limiting currents for the first positive and negative couples adjacent to the OCP of the pristine solution.

Reduction and oxidation LSV data for solutions of 0.01 M $Cr(acac)_3$ supported by 0.05 M $TEABF_4$ in ACN are shown in Figure 3.3. Figures 3.3a and 3.3b each present three voltammograms of freshly prepared solutions using three different platinum microelectrodes in independent experiments. The $Cr(acac)_3$ voltammograms are non-hysteretic and show appreciable currents at the equilibrium potentials of both the first negative and first positive redox couples, at –2.17 V and 1.20 V *vs*. Ag/Ag+, respectively. The current reaches a limiting value of $i_L^- = -4.2$ mAcm^{-2} when sweeping past the first reduction couple and $i_L^+ = 6.3$ mAcm^{-2} when sweeping past the first oxidation. Instead of the similar magnitudes one would expect based on theory and observed in the $V(acac)_3$ LSV,[32] these limiting currents differ substantially, having an approximately 2:3 ratio (4.2/6.3 = 0.67) between the first negative and first positive couple.

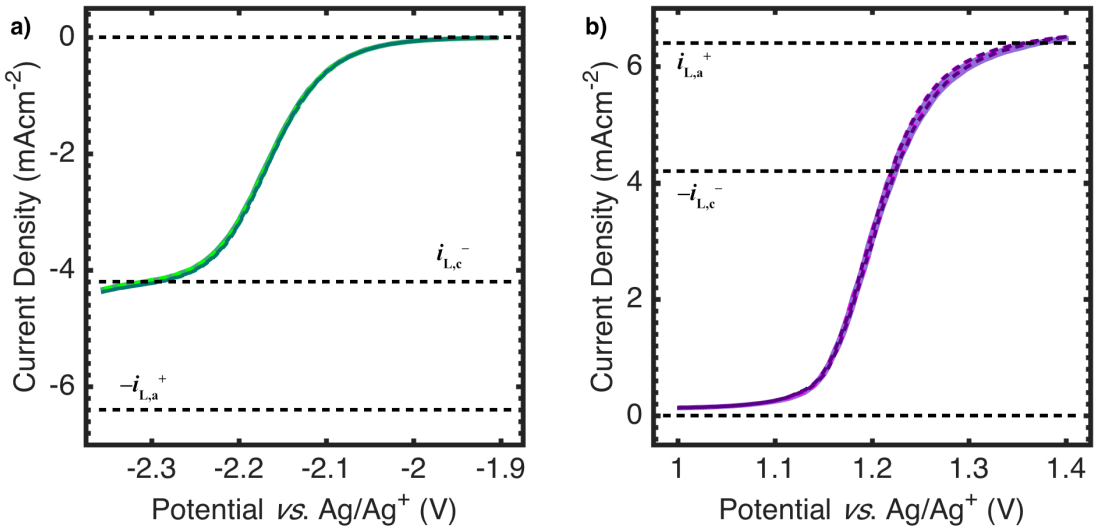

Figure 3.3. Linear-sweep voltammograms at 1 mVs^{-1} probing a) the first reduction and b) the first oxidation of 0.01 M $Cr(acac)_3$, 0.05 M $TEABF_4$ in ACN on Pt at 25 °C under an Ar atmosphere. Each panel presents three data sets; each data set includes both a forward and reverse voltage sweep. Horizontal dashed lines indicate zero current, and magnitudes of limiting currents, labeled i_L^+ and i_L^-.

On the basis that tetraethylammonium salts have been observed to be passive in other $M(acac)_3$ redox reactions,[98,105,106] it is appropriate to work under the assumption that only changes to the active species are responsible for deviations from the simple outer-sphere electron exchange pathway. In that case general reaction mechanisms can be proposed for the first negative and first positive couples,

$$a\mathrm{Cr}\left(\mathrm{acac}\right)_3 + b\mathrm{e}^- \rightleftharpoons \text{reduction products} \tag{3.5}$$

$$c\mathrm{Cr}\left(\mathrm{acac}\right)_3 \rightleftharpoons \text{oxidation products} + d\mathrm{e}^- \tag{3.6}$$

where a, b, c, and d are positive integers. Since the reacting molecule is the same in both half-reactions, the maximum diffusion-limited reactant fluxes have the same magnitudes. Thus the limiting currents relate through the stoichiometric constants in Reactions 3.5 and 3.6,

$$\frac{c}{d}\left|i_{\mathrm{L}}^+\right| = \frac{a}{b}\left|i_{\mathrm{L}}^-\right|, \quad \text{or} \quad \frac{\left|i_{\mathrm{L}}^-\right|}{\left|i_{\mathrm{L}}^+\right|} = \frac{bc}{ad} \tag{3.7}$$

Given the observation that $\left|i_L^-\right| = \frac{2}{3}\left|i_L^+\right|$ from the LSV results, this constraint affords four possibilities for the half-reaction stoichiometries: a=b and c/d=2/3; a=c and b/d = 2/3; c=d and b/a=2/3; or b=d and c/a=2/3.

One mechanism consistent with the observed limiting currents – and perhaps the simplest – is a disproportionation in which both the reduction and oxidation involve the exchange of multiple electrons with a single $Cr(acac)_3$ molecule (a=c=1, b=2, and d=3). This would entail reducing a Cr[III] complex to Cr[I] while oxidizing another Cr[III] complex to Cr[VI], which is unlikely: examinations of the first reduction of $Cr(acac)_3$ on various electrodes and in various supporting solutions fail to report any multiple-electron first reductions.[95,97,99,100,101,102] Additionally, a mechanism where the Cr[III] complex oxidized to Cr[VI] would be anomalous in light of the responses of other $M(acac)_3$ complexes, which appear consistent with single-electron oxidations.[14,33,110]

Both dimerization of the complex or the chromium within it and ligand-dissociation processes allow mechanisms consistent with Equation 3.7 in which $b/d \neq 2/3$. UV-vis-IR spectrophotometry was used to explore these possibilities.

3.3 Spectroelectrochemistry

The spectroelectrochemical cell was first used to probe the hypothesis that the products in Reactions 3.5 and 3.6 involve species with bonds between two chromium atoms. Literature regarding other transition-metal dimers suggests that absorption signatures of dimerization would be expected in the near-IR region.[111,112] Solutions with active-species concentrations ranging from 0.001 M to 0.05 M were electrolyzed chronoamperometrically at –2.40 and 1.50 V *vs.* Ag/Ag^+ following the procedure described in the Section 3.2. No changes in absorbance were observed in the 1000-3500 nm IR spectrum; chromium dimerization was therefore excluded as a possibility in

further study.

An alternative series of spectroelectrochemical experiments was executed to assess the possibility of ligand dissociation. Several reports have suggested that ligand dissociation may be involved in the electrochemical response of $Cr(acac)_3$ redox couples.[32,97,103,113] Spectroscopic absorbance signatures of acetylacetonate were collected from a solution of 0.003 M acetylacetone – abbreviated as H(acac) – and 0.025 M $TEABF_4$ in acetonitrile by electrochemically inducing hydrogen evolution on the spectroelectrochemical cell's platinum working electrode. That is, an applied potential was used to drive electrolysis, shifting the H(acac)/$(acac)^-$ equilibrium according to the cell reaction

$$\mathrm{H(acac)} \rightleftharpoons \mathrm{H^+ + (acac)^-} \tag{3.8}$$

which follows from the two half-reactions[114]

$$\mathrm{2H^+ + 2e^- \rightleftharpoons H_2} \tag{3.9}$$

$$\mathrm{2H(acac) + 2e^- \rightleftharpoons H_2 + 2(acac)^-} \tag{3.10}$$

As Figure 3.4 shows, absorption associated with $(acac)^-$ is centered in the UV region around 285 nm, whereas H(acac) absorbs near 270 nm. Additionally, bubble formation was observed at the platinum working electrode when held at reducing potentials, consistent with the hypothesis that H_2 gas is evolved during electrolysis. Even at the low concentrations used for the experiment, absorbance at some wavelengths reached the maximum measurable limits of the spectrophotometer (>3): the detection of H(acac) absorption appears saturated from 260-280 nm, while $acac^-$ detection appears saturated from 275-295 nm. Despite the saturation, the absorbance wavelengths are consistent with previous literature regarding the electrochemical formation and UV analysis of $acac^-$.[114,115,116]

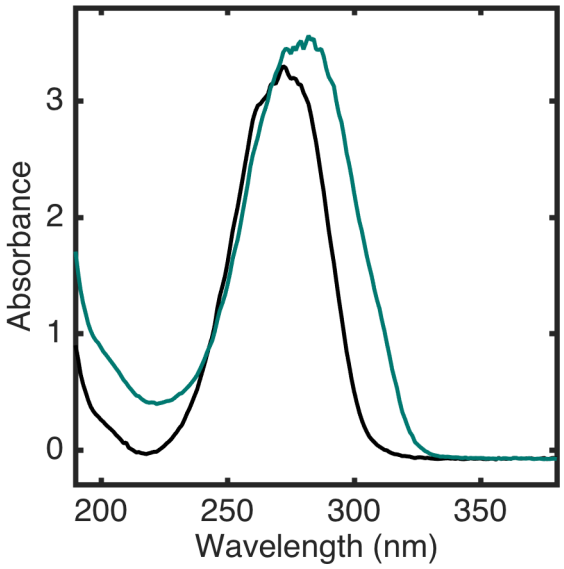

Figure 3.4. UV spectrogram of 0.003 M H(acac), 0.025 M $TEABF_4$ in ACN before (black) and after (green) chronoamperometric reduction at –2.40 V vs. Ag/Ag^+ for 450 seconds.

Solutions of $V(acac)_3$ or $Cr(acac)_3$ supported by 0.025M $TEABF_4$ in ACN were subjected to chronoamperometric electrolysis to illustrate how the absorbance varies during the first reduction or oxidation of the pristine complexes. Experiments with 0.005 M active-species concentrations in the support, shown in Figure 3.5, revealed absorbance shifts in the visible spectrum, which were consistent with the perceptible color changes observed for both solutions as electrolysis progressed. Figure 3.5a shows brown solutions of vanadium species reducing to black and oxidizing to blue, whereas Figure 3.5b depicts violet solutions of chromium species reducing and oxidizing to deeper violet colors.

The absorption peak associated with the vanadium center, whose spectroscopic behavior is known to vary substantially with charge state in aqueous solutions,[117] shows significantly larger changes in visible absorbance with the duration of applied potential than the chromium solution does. For the pristine solutions of neutral complexes, both visible absorbance profiles were found to be consistent with those reported in literature.[66,116] Experiments with 0.001 M solutions allowed spectroscopic behavior in

the UV-region to be analyzed, providing insight into ligand dissociation.

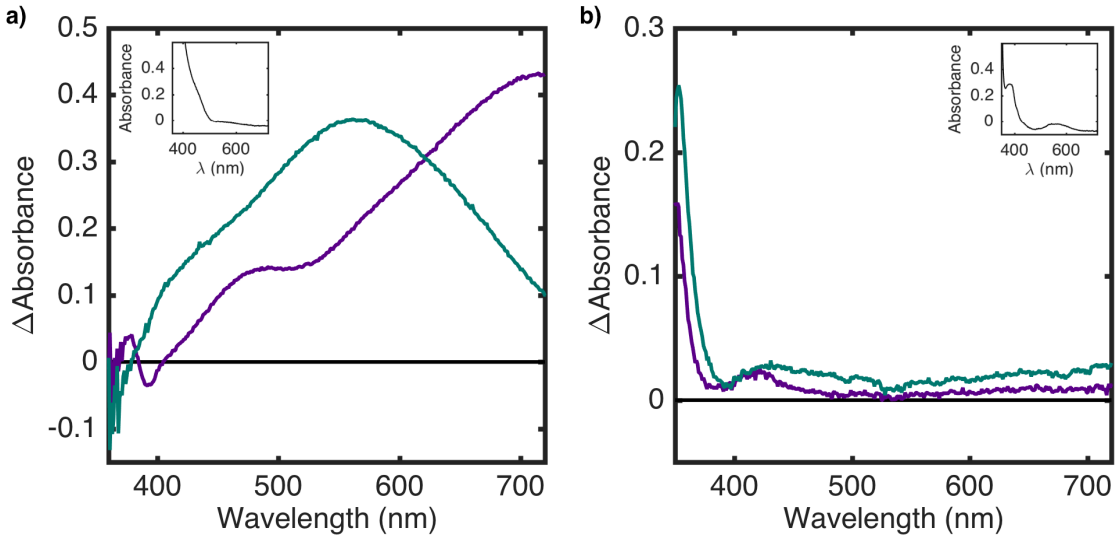

Figure 3.5. Change in visible absorbance of 0.005 M a) $V(acac)_3$ and b) $Cr(acac)_3$ supported by 0.025 M $TEABF_4$ in ACN upon reduction (green) and oxidation (purple). The inset shows a baseline absorbance spectrum collected before the application of potential.

Change in the absorbance of $V(acac)_3$ in the UV spectrum is illustrated in Figure 3.6. There is a strong absorbance plateau centered at 285 nm for the neutral $V(acac)_3$ complex shown in the inset of Figure 3.6, which is associated with the coordinated $acac^-$ moiety; coordination with vanadium reduces the absorbance of a solution containing 0.003 M $acac^-$ ligands to reliably measurable absorbance values. The absorbance shifts little after either electrolysis step. Since there are no significant increases in absorbance in the free $acac^-$ region of both electrolyzed spectra, $V(acac)_3$ yields no evidence of ligand dissociation. This observation is consistent with previous hypotheses:[40] the reaction mechanisms for both the positive and negative couples associated with $V(acac)_3$ are probably simple outer-sphere single-electron transfers. However, this contradicts flow cell studies of the $V(acac)_3$ chemistry that suggested that degradation to $VO(acac)_2$ (which must correspond to dissociation of the third $acac^-$ ligand) was responsible for capacity fade they observed in the cells.[66] The combination of significant visible spectroscopic shifts and lack of change in absorbance associated

with free acac$^-$ during electrolysis provide a few insights: exchanged electrons originate from vanadium in the V(acac)$_3$ chemistry; the acac ligand in V(acac)$_3$ maintains a similar atomic spacing as free acac$^-$ ions; and electrons can be added or removed from the stabilized vanadium center without stressing the octahedral ligand configuration.

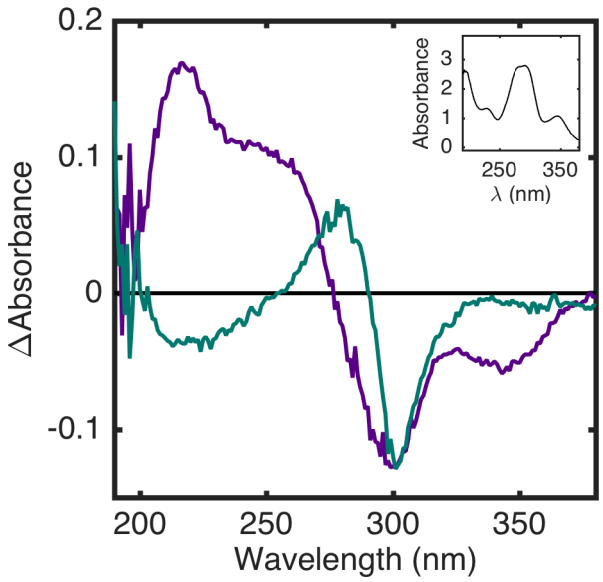

Figure 3.6. Change in UV absorbance of 0.001 M V(acac)$_3$, 0.025 M TEABF$_4$ in ACN after reduction at –2.05 V vs. Ag/Ag$^+$ for 930 seconds (green) and oxidation at 0.65 V vs. Ag/Ag$^+$ for 930 seconds (purple). The inset shows a baseline absorbance spectrum collected before the application of potential.

By contrast, Figure 3.7 shows that the UV absorbance spectrum of Cr(acac)$_3$ undergoes substantial changes as electrolysis of the complex progresses. Absorbance saturation was observed from 200-220 nm, but data outside that region is informative. As the inset in Figure 3.7 shows, the Cr(acac)$_3$ spectrum before electrolysis differs from that of V(acac)$_3$ because it lacks the strong absorbance peak at 285 nm associated with the acac$^-$ moiety. This absorption spectrum in the UV region is consistent with the previous report by Barnum, with peak locations at 255 nm, 270 nm, and 332 nm; all three peaks also exhibit extinction coefficients, ε, consistent with Barnum's reported range of log_{10}(ε * 1 cmM) between 4.0 and 4.5.[116] The lack of absorbance at 285 nm in the spectrum gathered for the pristine solution held at its OCP implies that the metal-

ligand bond constrains the structure of the $acac^-$ ligand more in $Cr(acac)_3$ than in $V(acac)_3$, so that it delivers absorbance maxima at different wavelengths.

Upon reductive electrolysis, the $Cr(acac)_3$ spectrum shows insightful changes. The reduction reaction produces a large absorbance increase from 260-310 nm, with a peak at 285 nm, suggesting the increased concentration of free ligand in the solution. The oxidation reaction has a lower-magnitude, mixed-polarity absorbance differential over the same window. This is consistent with reorganization after a change in redox state and exhibits absorbance changes similar in magnitude to those in the electrolyzed $V(acac)_3$ solution. Additionally, both the positive and negative couples exhibit decreased absorbance near 330 nm. This suggests that the absorbance peak at 330 nm is associated with the Cr[III] in the $Cr(acac)_3$ molecule, since it decreases in both instances of conversion to different redox states. Previous studies of neutral $Cr(acac)_3$ UV absorption attributed the peak at 330 nm to the Cr[III]-to-$acac^-$ charge-transfer band.[116] The observed decrease of absorbance at 330 nm in the present experiments corroborates that attribution: redox reactions, which either change the valence state of Cr or alter the energetics of the Cr–$acac^-$ bond, eliminate the absorbance at 330 nm.

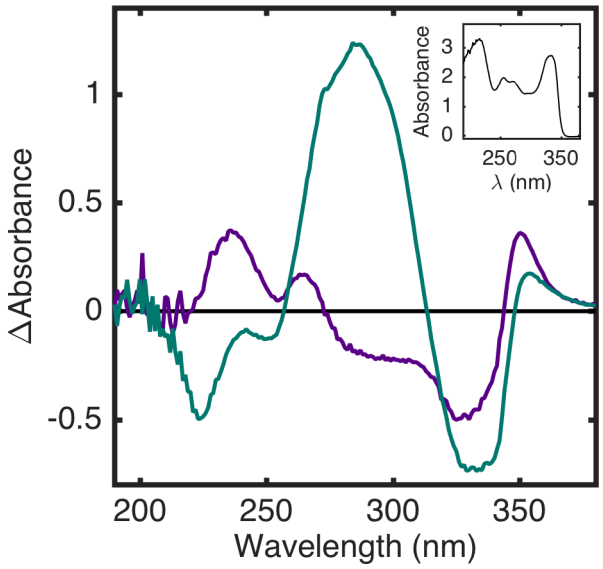

Figure 3.7. Change in UV absorbance of 0.001 M $Cr(acac)_3$, 0.025 M $TEABF_4$ in ACN after reduction at –2.4 V vs. Ag/Ag^+ for 930 seconds (green) and oxidation at 1.5 V vs. Ag/Ag^+ for 930 seconds (purple). The inset shows a baseline absorbance spectrum collected before the application of potential.

To test whether the changes in absorbance observed during both reduction and oxidation of the pristine $Cr(acac)_3$ complex arose from intrusion of ambient air or reference-electrode electrolyte leaking into the working-electrode chamber, two experiments were performed, the results of which are shown in Figure 3.8. For one experiment, the cell's OCP, which was identified to be –0.12 V *vs*. Ag/Ag^+ during a galvanostatic hold at 0 mA, was applied as the chronoamperometric potential. For the other, a completely electrically disconnected cell was assembled, in which the reference electrode was replaced by a glass rod. These time-lapse controls suggest that the influences of time held at OCP or time in contact with the reference electrode are minimal. Both the cell held at OCP and the fully disconnected cell show relatively small increases in absorbance in comparison to both the experimental noise and the changes found to accompany electrolysis.

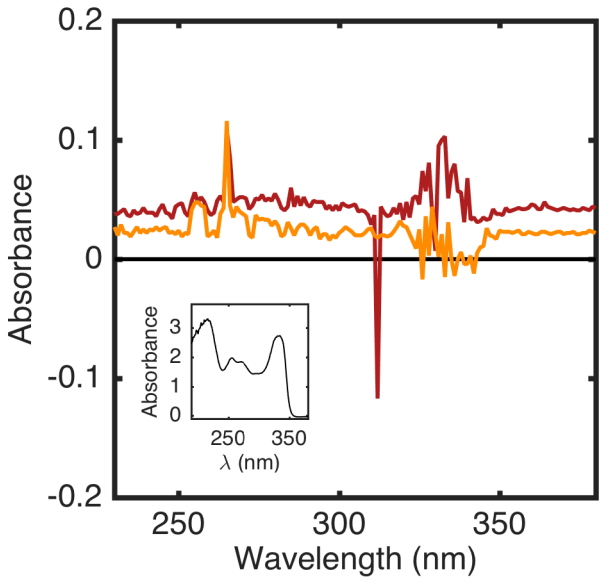

Figure 3.8. Change in UV absorbance of 0.001 M $Cr(acac)_3$, 0.025 M $TEABF_4$ in ACN after being held at OCP (–0.12 V vs. Ag/Ag^+) for 930 seconds (dark red) and when left disconnected, with reference electrode replaced by glass plug, for 930 seconds (orange). The inset shows a baseline absorbance spectrum collected before the application of potential.

The spectroelectrochemical observations suggest that ligand dissociation occurs during the reduction of $Cr(acac)_3$. Upon reduction $[Cr(acac)_3]^-$ has a d^4 electron configuration, isoelectronic with $Mn(acac)_3$, which is known to have lower symmetry due to its first-order Jahn–Teller distortion.[118] This symmetry-lowering molecular distortion likely gives rise to the dissociation. Consequently, these results indicate that Reaction 3.5 involves the formation of free acetylacetonate as a reaction product. The increased complexity of this electrochemical reaction renders examination of microelectrode LSV data by the method used for $V(acac)_3$ LSV[94] uninformative, since the model for vanadium redox kinetics assumes that the first oxidation and first reduction are both single-electron outer-sphere reactions. Additionally, the formation of acetylacetonate products during Reaction 3.5 suggests that the reverse reaction involves several species, which could include the electrode, chromium coordination complexes in various forms with various redox states, and the free ligand. A reverse reaction during discharge would require that two liquid-phase species, at the very least, come

together at the electrode, rather than the single liquid-phase species that performs electron exchange in the $V(acac)_3$ system.

In light of evidence that the electrolytic reduction of $Cr(acac)_3$ appears to drive ligand dissociation, tethering ligands together chemically might improve reversibility of its disproportionation reaction. As well as maintaining physical proximity of the ligand, this 'caging' of the chromium center may decrease the propensity for geometric reorganization of the complex and inhibit ligand substitutions by the solvent.

The observed spectroelectrochemical response combines with the LSV results to suggest a more refined mechanism for the cell reaction in a flow battery based on $Cr(acac)_3$. Ligand dissociation in the negative couple (Reaction 3.5), confirmed by spectroelectrochemistry, and the 2:3 electron stoichiometry suggested by microelectrode LSV are consistent with the half-reactions

$$3\mathrm{Cr}\left(\mathrm{acac}\right)_3 + 2\mathrm{e}^- \rightleftharpoons \mathrm{Cr}\left(\mathrm{acac}\right)_2^+ + 2\left[\mathrm{Cr}\left(\mathrm{acac}\right)_3\right]^- + (\mathrm{acac})^- \tag{3.11}$$

$$\mathrm{Cr}\left(\mathrm{acac}\right)_3 \rightleftharpoons \left[\mathrm{Cr}\left(\mathrm{acac}\right)_3\right]^+ + \mathrm{e}^- \tag{3.12}$$

Reaction 3.12 is a simple outer-sphere mechanism, but Reaction 3.11 involves three molecules of the neutral complex, which participate in a two-electron transfer. Although some products of Reaction 3.11 involve a reduced form of the complex, others leave the metal in an unchanged oxidation state with a different ligand configuration. The oxidation of iron(II) acetylacetonate, where three $Fe(acac)_2$ molecules combine to form two $Fe(acac)_3$ molecules and a free Fe^{2+} cation,[119] provides a precedent for a redox phenomenon like the one proposed in Reaction 3.11. A diffusion coefficient, D_0, of 2.5 x 10^{-5} cm^2s^{-1} can be calculated for $Cr(acac)_3$ using the stoichiometry of Reaction 3.12 and the familiar expression for the limiting current at a disk microelectrode

$$i_\mathrm{L} = 4nFD_0Cr_0 \tag{3.13}$$

where r_0 is the disk microelectrode radius. Urbanczyk *et al.* calculated a value of 1.8 x 10^{-5} cm^2s^{-1} in their polarographic studies of the first reduction of $Cr(acac)_3$ solutions in ACN, assuming a mechanism for Reaction 3.1 with $a=b=1$.[97] If a reaction with $b/a=2/3$ is assumed when processing the data, consistent with Reaction 3.11, the diffusivity of Urbancyzyk *et al*. would become 2.7 x 10^{-5} cm^2s^{-1}, in close agreement with the present result.

Given the evidence of ligand dissociation and the mechanistic complications arising from the presence of more than one reduction product, LSV and UV-vis absorbance measurements cannot eliminate the possibility that more than one $acac^-$ ligand dissociates from the Cr[III] center in Reaction 3.11. Additionally, with the observation of ligand dissociation, evidence against a disproportionation mechanism in which both the reduction and oxidation involve multiple electrons ($a=c=1$, $b=2$, and $d=3$) is less decisive. It would still be anomalous among $M(acac)_3$ complexes for $Cr(acac)_3$ to support a first oxidation involving a three-electron exchange or a reduction involving two electrons, but further study is needed to corroborate the details of Reactions 3.11 and 3.12.

Previous studies of chromous acetylacetonate, $Cr(acac)_2$, report that the complex has a planar structure and is yellow in color.[120,121] However, the visible absorption spectrum of the reduced $Cr(acac)_3$ solution does not shift toward yellow transmittance: this suggests that if a $[Cr(acac)_2]^+$ species is present, the ligands within it retain the same octahedral geometry as in $Cr(acac)_3$. It is possible that $acac^-$, dissociated from the chromium complex as described in Reaction 3.11, could be replaced by two ACN solvent molecules to retain the octahedral coordination of Cr. The reduction mechanism (*e.g.* Reaction 3.11) would consequently depend strongly on solvent choice, which could explain the widely varied reduction responses of $Cr(acac)_3$ observed in

literature.[95,96,97,99,100,101,102] Studies of solvent compatibility for RFB applications similar to those performed by others for $V(acac)_3$[36,37] would therefore be fruitful.

3.4 Batch Reactor Charge-Discharge

As a consequence of Reactions 3.11 and 3.12, the overall expected cell reaction for a symmetric RFB based on $Cr(acac)_3$ would be

$$5Cr(acac)_3 \rightleftharpoons 2\left[Cr(acac)_3\right]^+ + Cr(acac)_2^+ + 2\left[Cr(acac)_3\right]^- + (acac)^-. \quad (3.14)$$

Ligand dissociation leads to a more complicated cell reaction for $Cr(acac)_3$ than expected for disproportion complexes undergoing simple outer-shell electron exchange: charging of a flow battery using the $Cr(acac)_3$ active species would entail the generation of three species in the negative electrolyte, which would have to be brought together during recharge to attain reasonable round-trip efficiency. Reaction 3.14 provides a lens through which to understand the charge-discharge behavior observed earlier for the symmetric nonaqueous $Cr(acac)_3$ RFB. Previous reports[32] show later cycles using a Neosepta AHA membrane, but do not illustrate the voltage response during the initial cycles of the cell. Figure 3.9 demonstrates initial cycles along with later, more developed cycles of a $Cr(acac)_3$-based batch reactor cell using a Celgard 4560 membrane separator. Initial cycles, shown in Figure 3.9a, demonstrate minimal discharge capacity. Later cycles shown in Figure 3.9b are consistent with previous reports,[32] showing increased capacity and discharge potentials beginning from 2.2 V and decreasing toward the 0.5 V cutoff. Coulombic and energy efficiency for these cycles are 26% and 9%, respectively. These efficiencies are lower than in the Neosepta-AHA-separated cells and owe to crossover through the porous Celgard, which is far more permeable to the active species than the anion-exchange membrane.[32] Despite the less selective separator, the Celgard-separated cells continue to operate after hundreds

of hours. Crossover resilience is a major advantage of 'symmetric' RFB configurations.

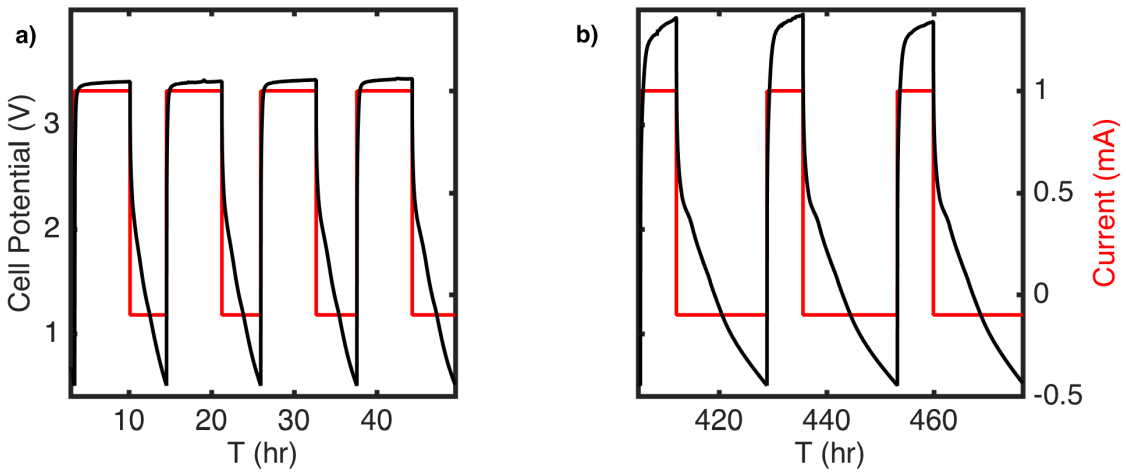

Figure 3.9. Charge-discharge of a cell with Celgard 4560 separator and graphite electrodes containing 0.05 M $Cr(acac)_3$, 0.5 M $TEABF_4$ in ACN, cycled in a glovebox under an Ar atmosphere at 25 °C. a) Cycles 1-4; b) Cycles 23-25.

The low efficiencies of the $Cr(acac)_3$ chemistry in a batch reactor cell separated with Neosepta AHA[32] or Celgard 4560 may result from the complicated nature of the cell reaction. Considering otherwise identical cells with Neosepta AHA separators, the coulombic efficiency drops from 70% for $V(acac)_3$ to 50% for $Cr(acac)_3$ and energy efficiency from 35% to 22%.[32,40] The cell reaction proposed here may help explain the relatively low cycling efficiency of $Cr(acac)_3$. Achieving full discharge capacity would entail capturing and recombining all the Cr-containing reduction products of $Cr(acac)_3$, along with free ligand. Additionally, Reaction 3.14 explains the need for many cycles before performance achieves repeatable efficiency – the free ligand unreacted from initial cycles becomes distributed throughout the cell as time passes, facilitating the reverse reaction in later cycles and altering the Nernstian response of cell voltage. Charge-discharge experiments performed on ethylene-glycol-functionalized $Cr(acac)_3$, with ethylene glycol chains bound to the acetylacetonate ligands, led to an improved steady-state coulombic efficiency of 55% and energy efficiency of 25% at similar rates.[42] A ligand-dissociation mechanism where the ligand diffusivity drops, which

would be the case for these bulkier ligands, may play a role in this improvement.

3.5 Alternative Solvent Chemistry

With the spectroelectrochemical and charge-discharge results in mind, alternative supporting solutions were considered for the $V(acac)_3$ and $Cr(acac)_3$ chemistries. DME, a solvent frequently used for lithium-containing batteries, is reported to have a similar solubility limit for $V(acac)_3$ as ACN (0.6 M),[36,37] and is therefore worth investigating as a solvent for coordination-complex chemistries. The use of DME entails changing the supporting electrolyte from $TEABF_4$ to $TBABF_4$ because $TEABF_4$ cannot sustain the 0.5 M concentration in DME that is required for experiments. Conductivity in DME is much lower for solutions of $TBABF_4$ (2.3 $mScm^{-1}$) than in ACN at the same concentration (31.0 $mScm^{-1}$), explaining the need for high salt concentrations. $TBABF_4$ can be considered a good substitute for $TEABF_4$ because the anions remain the same and the cations only differ with respect to the length of their alkyl chains. Despite the differences in cation structure, the conductivity of 0.5 M $TBABF_4$ concentrations in ACN is comparable to the same concentration of $TEABF_4$ in ACN (42.9 $mScm^{-1}$).

As seen in Figure 3.10, neither the use of DME, nor the switch to $TBABF_4$, substantially influences the redox behavior of $V(acac)_3$, which still shows two reversible redox couples. While the new $V(acac)_3$ solution shows the same general redox activity, the redox couples shift to –1.75 V and 0.60 V *vs.* Ag/Ag^+, which in principle increases the cell OCP to 2.35 V. This small increase will improve performance, but is unlikely to counterbalance the conductivity losses from using DME. This still suggests that solvents may provide a key to incremental voltage and energy density improvements in the future.[40]

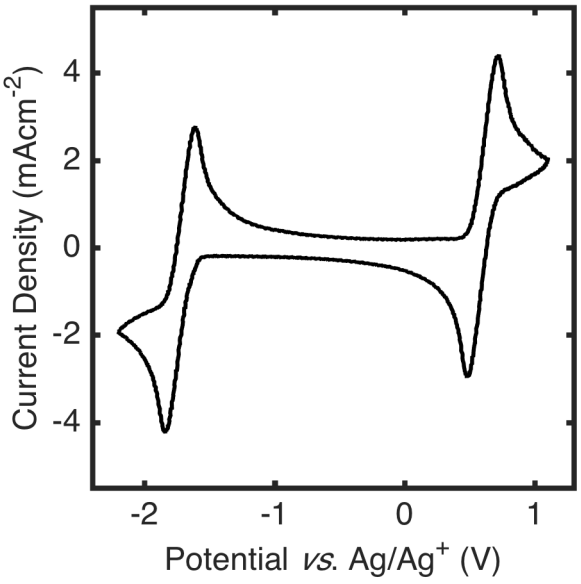

Figure 3.10. Cyclic voltammogram of 0.01 M $V(acac)_3$, 0.5 M $TBABF_4$ in DME, glassy carbon, 400 mVs^{-1}, 25 °C.

Whereas the DME support solution delivers modest improvement to the $V(acac)_3$ OCP, it does not improve the performance of $Cr(acac)_3$ active species. Voltammetry shown in Figure 3.11 reveals an oxidation reaction that still appears irreversible, with a lone oxidation peak at 1.35 V *vs.* Ag/Ag^+. The change of solvent also negatively impacts the reversibility of the first reduction reaction. Whereas $Cr(acac)_3$ in ACN displays an oxidation peak corresponding to the first reduction couple at a reaction potential of –2.16 V *vs.* Ag/Ag^+, the active species shows no oxidation peak corresponding to the first reduction peak at –2.46 V *vs.* Ag/Ag^+. Second and third reduction events accessed in DME both show corresponding oxidation peaks delivering reaction potentials of –2.64 V and –3.13 V *vs.* Ag/Ag^+. Notably, the third reduction event occurs in the DME solution at potentials beyond the apparent breakdown of the ACN support solution tested. While the second and third reductions may appear reversible, there is an oxidation peak at 0.07 V *vs.* Ag/Ag^+, which has been attributed to free ligand in other studies:[40] these two reactions therefore appear to fail to return a product wherein all three ligands remain bound. Although a system using $Cr(acac)_3$ in

DME that only employed the second and third reductions might be possible, it would reintroduce the disadvantages of asymmetric single-active-species RFBs. $Cr(acac)_3$ still offers several redox couples and such large cell potentials that any research breakthroughs to prevent ligand dissociation would produce a cost-effective system.

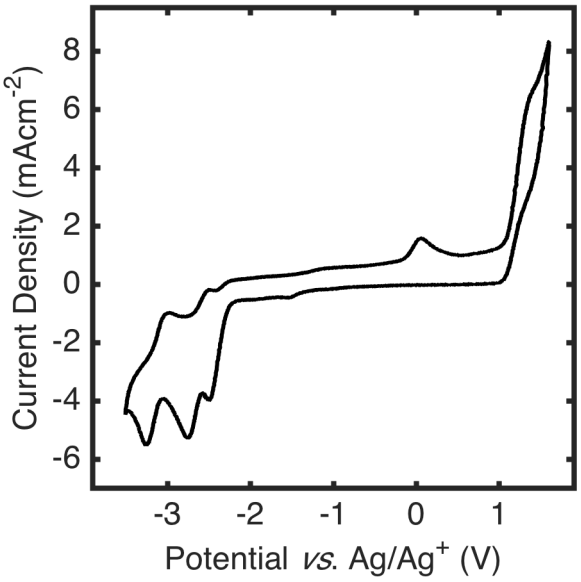

Figure 3.11. Cyclic voltammogram of 0.01 M $Cr(acac)_3$, 0.5 M $TBABF_4$ in DME, glassy carbon, 400 mVs^{-1}, 25 °C.

3.6 Summary and Discussion

CV results gathered from $Cr(acac)_3$ and $V(acac)_3$ solutions reveal more irreversible electrochemical behavior in the $Cr(acac)_3$ system than $V(acac)_3$, which is highly reversible. The electrochemical behavior of $Cr(acac)_3$ was studied further to better understand the chemistry, motivated by the favorable cost advantages of a chromium-based chemistry. Microelectrode LSV experiments further identify discrepancies in the previously proposed single-electron outer-sphere disproportionation reaction mechanism for $Cr(acac)_3$ redox. Spectroelectrochemical experiments performed with $V(acac)_3$ and $Cr(acac)_3$ reveal substantial differences between the redox activity of vanadium and chromium coordination complexes in nonaqueous electrolytes: the vanadium species appears to bind the acetylacetonate such that the ligand maintains

a similar absorption signature after joining the complex, whereas the chromium species constrains the molecular structure of acetylacetonate and eliminates its signature at 285 nm. Chronoamperometric reduction of $Cr(acac)_3$ produces an absorbance peak in a domain of wavelengths indicative of the presence of free acetylacetonate, consistent with ligand dissociation. The same experiment with $V(acac)_3$ shows no increase in absorption in the free ligand region and suggests that ligand-dissociating degradation mechanisms may be misdiagnosed. A new mechanism for the $Cr(acac)_3$ negative half-reaction is proposed and appears consistent with the charge-discharge behavior seen in a batch reactor cell. Furthermore, examination of the two coordination complex chemistries in an alternative DME solvent system reveal small improvements in the OCP offered by the two reversible $V(acac)_3$ reactions, but a less reversible $Cr(acac)_3$ first reduction reaction. For $Cr(acac)_3$, DME also allows access to a third reduction event.

This study shows that $Cr(acac)_3$ is unlikely to deliver a cyclable RFB chemistry in nonaqueous systems using ACN or DME. However, the chemistry is revealed to be extremely solvent dependent and research into different nonaqueous solvents may deliver stable, cyclable $Cr(acac)_3$. Alternatively, the $V(acac)_3$ chemistry looks well-suited for a highly cyclable symmetric nonaqueous RFB in both ACN and DME. While switching to DME seemingly improves the chemistry's performance by increasing its OCP, it may also affect long-term metal-ligand bond stability. Switching to any other solvent system should include study by methods such as UV-vis spectroelectrochemistry to confirm maintenance of its reversible electrochemical behavior.

4 Organic Active Species

The use of organic compounds in place of metal-based RFBs could significantly reduce active species cost. New organic-based aqueous RFB chemistries, such as the anthraquinone-bromine system,[23] look to supplant aqueous AVRFBs,[11] but are still limited by the electrochemical stability of water, which constrains practical cell operating voltages to near the 1.23 V window. The acidic anthraquinone-bromine[23] and alkaline anthraquinone-ferrocyanide[15] chemistries only offer cell voltages under 1.3 V and operate in a dual-species paradigm. An organic active species that can exploit the higher voltages available in nonaqueous systems would likely improve energy and power density metrics compared to these aqueous organic systems. Moving from a dual-species paradigm to a symmetric paradigm would also offer cost savings. Ultimately, 9,10-diphenylanthracene (DPA), which has been studied for its properties in electrogenerated chemiluminescence,[62,63,64,65,122,123,124,125] is selected for further focus because it delivers high voltages in nonaqueous systems, permits symmetric operation, derives from inexpensive organic precursors, and allows the customization and flexibility of organic active species.

DPA, whose structure is illustrated in Figure 4.1, is a molecule in the class of polycyclic aromatic hydrocarbons (pAHs). pAHs support electrochemical activity through their highly conjugated structures. Stable radical-formation mechanisms have been proposed for both the DPA oxidation[65] and reduction[63] reactions described in Equations 1.4 and 1.5. In ACN solutions, the equilibrium redox potentials of these half-reactions are 3.1 V apart. Additionally, charged solutions of DPA with concentrations at the millimolar scale were demonstrated to be stable on the time scale of hours.[64,65] Thus, DPA delivers redox behavior well-suited for symmetric nonaqueous RFBs.

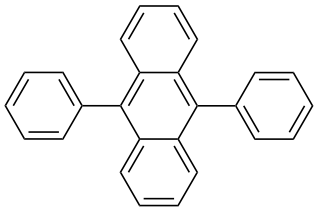

Figure 4.1. Chemical structure of DPA.

In addition to allowing higher cell voltages, nonaqueous solvents are more compatible with pAHs and often substantially raise pAH solubility over aqueous supporting solutions.[126] Researchers previously pursued the use of rubrene, another pAH, in symmetric nonaqueous RFBs, but were discouraged by its 'poor' solubility in ACN.[31] DPA possesses sufficient solubility in various nonaqueous solutions to allow analysis of its electrochemical properties, as demonstrated in work studying the molecule for electrogenerated chemiluminescence,[62,65] but the solubility for RFB applications is still quite low from a practical standpoint.

Although its solubility needs improvement, the extraordinarily low cost of the active-species precursors make the chemistry worthwhile to pursue. The cost of the anthracene oil precursor to DPA paired with an expected OCP above 3 V suggests an active species cost starting at $2.17/kWh,[91] more than an order of magnitude lower than the cost of vanadium in AVRFBs. Additionally, anthracene oil is a waste product of petroleum and coal production that is often part of the mixture used for pavement sealing.[127] Thus, DPA could offer both a higher-value use for extracted fossil fuel resources and an inexpensive active species for nonaqueous symmetric RFBs.

This chapter describes initial studies of symmetric, metal-free, nonaqueous RFBs based on DPA and more soluble functionalized DPA species, which are synthesized (Section 4.2 and Appendix A.2), characterized, and their suitability for RFBs examined. The synthetic effort produces many functionalized versions of DPA, and eventually delivers promising DPA analogues with diethyleneglycoxy-ester moieties appended to

the DPA center (Section 4.3 and 4.4). As the sequence of syntheses proceeded, the process identified synthetic strategies that may be useful for other DPA analogues and even analogues of other pAHs, such as the naphthalene center in 1,4-diphenylnaphthalene (DPN).

4.1 Experimental

4.1.1 Solvent Selection

Solutions were prepared at 0.5 mM DPA loading levels in a variety of solvents to assess whether solubility was sufficient to permit electrochemical analysis *via* CV. If the 0.5 mM DPA loading did not dissolve completely in a solvent, the solvent was eliminated from further analysis.

DPA (98%, Sigma-Aldrich, USA), PC (99.7%, Sigma-Aldrich, USA), and DMC (99%, Sigma-Aldrich, USA), were used as received. ACN (99.8%, Sigma-Aldrich, USA), DMSO (99.5%, Sigma-Aldrich, USA), DMF (99.5%, Sigma-Aldrich, USA), DME (99.5%, Sigma-Aldrich, USA), and THF (99.5%, Sigma-Aldrich, USA) were dried over molecular sieves (3 Å, Sigma-Aldrich, USA) before use. All electrochemical solutions were prepared under argon in a glovebox (OMNI-lab, Vacuum Atmospheres, USA) containing less than 1 ppm water and less than 1 ppm oxygen.

4.1.2 Cyclic Voltammetry

Solutions of 0.5 M $TBABF_4$ in nonaqueous solvents were loaded with 1 mM DPA. $TBABF_4$ (electrochemical grade, 99.9%, Sigma-Aldrich, USA) was used as received. Cyclic voltammetry was performed on a three-electrode cell using an Autolab PGSTAT302N potentiostat (Ecochemie, Netherlands). A 1 mm diameter glassy carbon

disk was used as the working electrode (Basi Inc., USA). A 30 cm long, 0.3 mm diameter coiled platinum wire (99.99%, Alfa Aesar, USA) was used as the counter electrode and separated from the other electrodes by a glass frit. All potentials were referenced against a Ag/Ag^+ reference electrode consisting of a silver wire immersed in 0.01 M $AgNO_3$ (Basi Inc., USA) and 0.1 M $TEAClO_4$ (90%, Alfa Aesar, USA) dissolved in whatever working solvent was used for the CV experiment. This reference electrode connected ionically through a fritted junction with 0.05 M $TBANO_3$ (99%, Fluka, USA) dissolved in the same working solvent. Scan rates for voltammetry were 400 mVs^{-1} unless stated otherwise. All cyclic voltammograms were collected at ambient temperature in an argon-filled glovebox containing less than 1 ppm water and less than 1 ppm oxygen.

4.1.3 Synthesis

Various DPA derivatives were functionalized through Suzuki-Miyaura cross-coupling reactions as illustrated in the reaction scheme shown in Figure 4.2. 9,10-dibromoanthracene was used as received (DBA, 98%, Sigma-Aldrich, USA). Boronic acids were used as received (Oakwood Chemicals, USA). Palladium *tetrakis* triphenylphosphine ($Pd(PPh_3)_4$) was synthesized as reported in literature.[128]

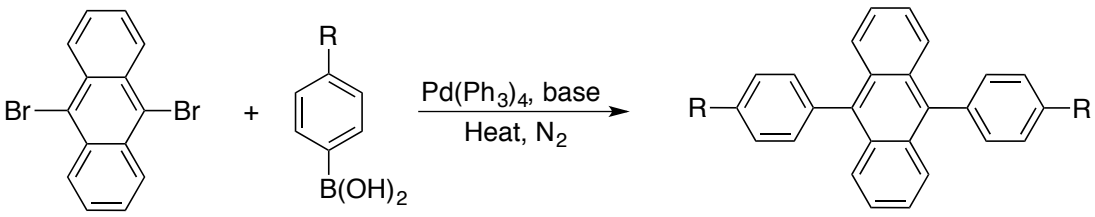

Figure 4.2. Suzuki-Miyaura cross-coupling reaction scheme to produce *para*-functionalized DPA.

Initial efforts focused on functionalizing the DPA molecule at the 4th carbon of the molecule's two phenyl rings to provide *para*-functionalization. 9,10-Bis(4-

methylphenyl)anthracene (DMPA, Figure 4.3) was synthesized as described by Kotha *et al.*[129] using 4-methylphenyl boronic acid. 9,10-Bis(4-methoxyphenyl)anthracene (DMOPA, Figure 4.4) was synthesized as described by the same authors,[129] using 4-methoxyphenyl boronic acid. 9,10-Bis(4-methoxycarbonylphenyl)anthracene (DMBA, Figure 4.5) was synthesized as described by Hauptvogel *et al.*[130] using 4-methoxycarbonylphenyl boronic acid. All structures were corroborated using ^{1}H NMR spectroscopy, the results of which can be found in Appendix A.2, along with detailed synthetic procedures and characterization.

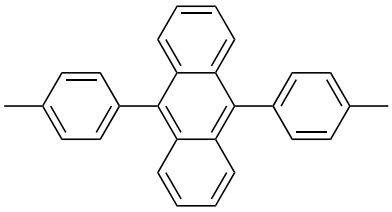

Figure 4.3. Chemical structure of DMPA.

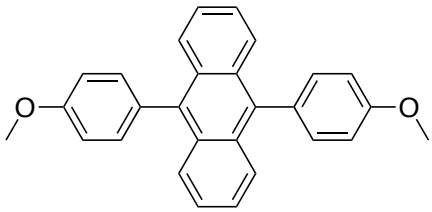

Figure 4.4 Chemical structure of DMOPA.

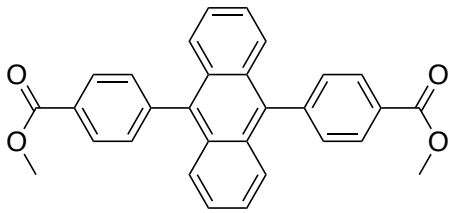

Figure 4.5. Chemical structure of DMBA.

These simple cross-coupling reactions – specifically the synthesis of DMBA – develop a molecular handle that allows one to functionalize DPA with larger functional groups. Ethylene glycol functionalized DPA moieties were prepared through trans-

esterification reactions of DMBA as shown in Figure 4.6. Reaction flasks were loaded with DMBA, a Lewis acid, and the desired ethylene glycol alcohol to replace the methyl group in DMBA's two methyl esters; this alcohol serves as both a reactant and solvent.

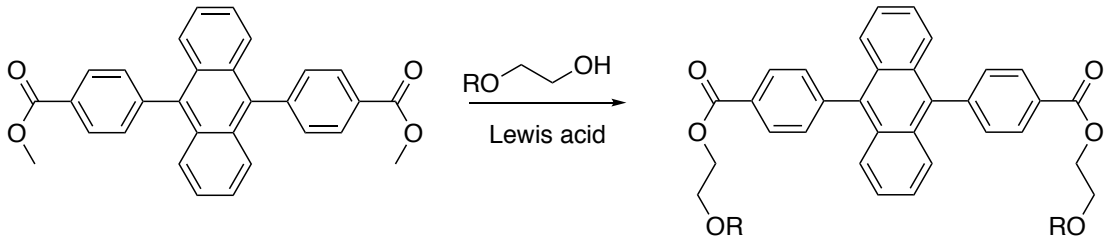

Figure 4.6. Trans-esterification reaction scheme to produce long-chain ester functionalized DPA.

Ethylene glycoxy ester functionalized DPA, 9,10-Bis(4-(2-methoxyethoxy)carbonylphenyl)anthracene (DePA, Figure 4.7), was produced from a mixture of DMBA (0.35 g, 0.785 mmol), $MgBr_2$-Et_2O (0.45 g, 1.74 mmol), and 2-methoxyethanol (7 mL) stirred in an oil bath at 130 °C for 48 hours. Upon cooling to room temperature, DePA crystallized out of solution. The crystals were filtered and rinsed with ethanol and any residual solvent was removed under vacuum (20 mTorr) yielding DePA as yellow crystals (0.32 g, 75%, R_f = 0.6, 50% ethyl acetate in hexanes). The product was characterized by ^{1}H NMR and mass spectroscopy. Further details of synthesis and characterization are included in Appendix A.2.

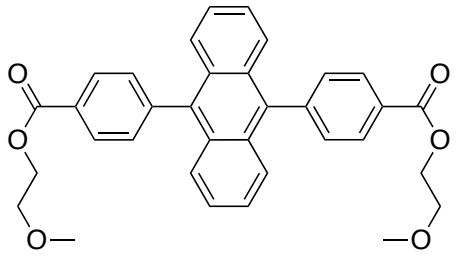

Figure 4.7. Chemical structure of DePA.

Diethyleneglycoxy ester functionalized DPA, bis(2-(2-methoxyethoxy)ethyl) 4,4'-(anthracene-9,10-diyl)dibenzoate (DdPA, Figure 4.8), was produced from a mixture of DMBA (0.2 g, 0.45 mmol), $MgBr_2$-Et_2O (0.11 g, 0.45 mmol), and 2-(2-

methoxyethoxy)ethanol (4 mL) stirred in an oil bath at 150 °C for 48 hours under nitrogen. The solvent was removed by distillation (100 °C, 100 mTorr) using a short-path distillation column. The resulting solid was dissolved in dichloromethane and purified by column chromatography with 40% ethyl acetate in hexanes as eluent. After removal of the solvent by rotary evaporation, DdPA was isolated as a pale yellow solid (129 mg, 46% yield, R_f= 0.2, 50% ethyl acetate in hexanes). The product was characterized by ^{1}H NMR and mass spectroscopy. Further details of synthesis and characterization are included in Appendix A.2.

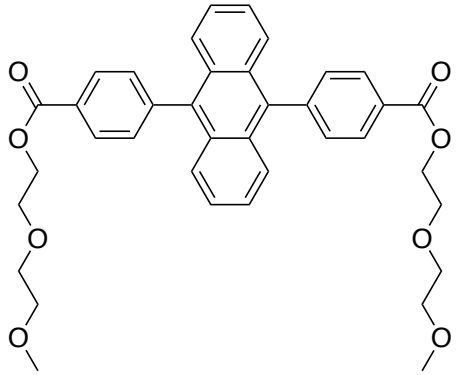

Figure 4.8. Chemical Structure of DdPA.

Deviations from these two functionalization strategies were also considered. A *meta*-functionalized version of DMBA, dimethyl 3,3'-(anthracene-9,10-diyl)dibenzoate, (*m*-DMBA, Figure 4.9) was produced following the same procedure as DMBA, but using a 3-methoxycarbonylphenyl boronic acid. Additionally, a diethyleneglycoxy ether functionalized DPA with ethylene glycol chains linked *via* an ether, rather than an ester form 9,10-bis(4-(2-(2-methoxyethoxy)ethoxy)phenyl)anthracene (eDdPA, Figure 4.10.). First, 1-bromo-4-(2-(2-methoxyethoxy)ethoxy)benzene (Br-Ph-dEG) was synthesized according to reports[131] and its structure was corroborated via ^{1}H NMR and GC-MS included in Appendix A.2. Br-Ph-dEG was then converted to a boronic acid by reaction with butyl lithium for 30 minutes at –78.5 °C and subsequent addition of triisopropyl

borate, left to react for 12 hours. After treatment with acid and purification the (4-(2-(2-methoxyethoxy)ethoxy)phenyl)boronic acid ($B(OH)_2$-Ph-dEG), was washed and filtered. The boronic acid was then cross-coupled with DBA according to the procedure used with DMOPA[129] to form eDdPA (52% yield, R_f= 0.1, 30% ethyl acetate in hexanes). The product was characterized by ^{1}H NMR and mass spectroscopy. Further details on synthesis and characterization are included in Appendix A.2.

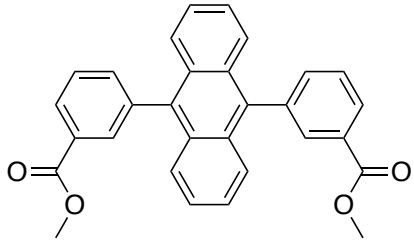

Figure 4.9. Chemical structure of m-DMBA.

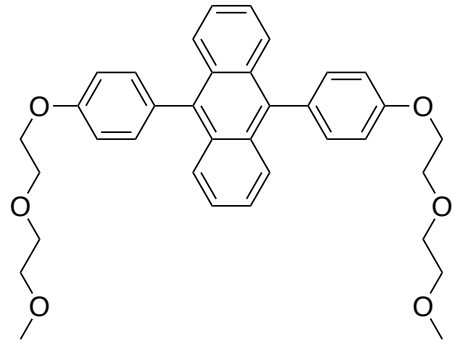

Figure 4.10. Chemical structure of eDdPA.

Another synthetic strategy focused on a naphthalene center, rather than anthracene. Mirroring the initial steps with DPA, 1,4-dibromonaphthalene (DBN, Accela Chem, 97+%, USA) replaced DBA and reacted with 4-methoxycarbonylphenyl boronic acid according to the anthracene procedure described by Hauptvogel *et al.*[130] The resulting product 1,4-Bis(4-methoxycarbonylphenyl)naphthalene (DMBN, 69% yield, R_f= 0.2, dichloromethane, Figure 4.11) was characterized and prepared for further reaction. DMBN reacted with 2-(2-methoxyethoxy)ethanol to form bis(2-(2-methoxyethoxy)ethyl) 4,4'-(naphthalene-1,4-diyl)dibenzoate (DdPN, 67% yield, R_f =

0.2, 33% ethyl acetate in hexanes, Figure 4.12) according to the trans-esterification reaction scheme described in Figure 4.6. The product was characterized using ^{1}H NMR and mass spectroscopy. Further synthetic and characterization details are included in Appendix A.2.

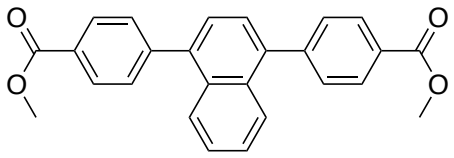

Figure 4.11. Chemical Structure of DMBN.

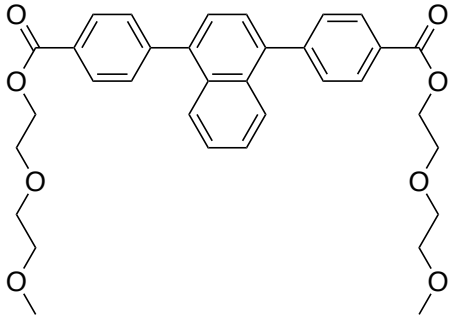

Figure 4.12. Chemical structure of DdPN.

4.1.4 Solubility Limits

Samples of saturated and non-saturated binary solutions comprising of solvent and active species were mixed to determine the solubility limits *via* the densitometric method proposed by Shinkle *et al*.[36] For solutions in which the DPA solute is below its solubility limit in the solvent, such that it dissolves completely, the density varies approximately linearly with concentration. Above the solubility limit, the solution density of the supernatant remains constant. If the liquid solution density is plotted against the loading concentration, the curve fit to the data changes from a sloped line to horizontal after the solution reaches saturation. The intersection of the line established by the unsaturated solutions with the horizontal line formed by the saturated supernatants indicates the binary solubility limit in the solvent. Densities of the solution

samples were measured with an Anton Paar DMA 4100M densitometer. Since all the solutions had relatively low levels of absorbance in the visible spectrum, it was possible to observe the presence of undissolved solutes with the naked eye, helping to corroborate the more quantitative densitometry results.

4.1.5 Batch Reactor Charge-Discharge

Charge-discharge experiments were performed in the 10 cm long, one-dimensional glass cell shown in Figure 3.2. The battery solutions contacted each other through a Neosepta AHA anion-exchange membrane. Neosepta membranes were preconditioned by soaking in 0.075 M $TBABF_4$ in ACN or DME solutions for at least 48 hours. Membranes were further allowed to soak within the loaded, electrically disconnected cell for 24 hours before beginning charge-discharge experiments. The electrodes employed for charge-discharge were graphite plates (GraphiteStore, USA); 2.54 cm^2 of superficial area was exposed to each solution. Charge-discharge experiments were performed with 10 mM DPA, 0.5 M $TBABF_4$, DME solutions and 10 mM DdPA, 0.1 M $TBABF_4$, ACN solutions. The galvanostatic charge-discharge scheme for DPA in DME entailed an 8 μAcm^{-2} charging current density to deliver 4% of the theoretical maximum SOC as estimated assuming single-electron redox reactions involving only the active molecule, or reaching a 3.9 V cutoff, whichever came first. A 4-hour rest at open circuit followed the charge step before the discharge step applied a 2 μAcm^{-2} discharging current density down to a 0.5 V cutoff. The DdPA in ACN cycling scheme entailed a 60 μAcm^{-2} charging current density to deliver 30% theoretical SOC or 3.9 V, whichever came first. A 4-hour rest at open circuit followed, and then a discharge step at a 10 μAcm^{-2} discharging current density down to the 0.5 V cutoff. The first charge step in both procedures extended the SOC limit 150% further than the limit laid out earlier for all subsequent steps such that burn-in effects are sequestered to the

first cycle (increasing the first charge's SOC limit to 10% for DPA in DME and 75% for DdPA in ACN). All charge-discharge experiments were performed under an argon atmosphere in the glovebox.

4.2 Solvent Selection

Development of the proposed symmetric organic RFB chemistries began with investigations of nonaqueous solvent and supporting electrolyte systems. These studies set out to identify support solutions with sufficient electrochemical stability, ionic conductivity, active-species solubility, and which facilitate reversible active species redox behavior.

Various nonaqueous solvents were examined to support the RFB cell reactions based on DPA using $TBABF_4$ as a supporting electrolyte. The solvent selection process began with a test to screen against a lowest limit on DPA solubility: at least 0.5 mM in the neat solvent. Table 4.1 shows the results for several electrolytes typically used for nonaqueous electrochemistry: PC,[39] DMSO,[37,39,]ACN,[36,39] DMF,[36,39] THF,[36] DME,[39] and dimethyl carbonate (DMC).[36] Both the cyclic and linear carbonate solvents were found to be incapable of dissolving 0.5 mM DPA loadings and were therefore eliminated from further study. These observations agree with the notion that favorable molecular complexation, or lack thereof, between the solute and solvent classes drives solubility: both propylene carbonate and dimethyl carbonate failed to dissolve small amounts of the pAH. Electronic permittivity or neat solvent molarity, which have been reported to drive solubility,[36] appear to be less important: high and low permittivity ACN and DME both dissolve 0.5 mM DPA, while high and low permittivity carbonates both fail to dissolve it.

Table 4.1. Solvent screening: bulk solvent properties[132] and screening outcomes.

	PC	DMSO	DMF	ACN	THF	DME	DMC
Permittivity	66.1	47.2	38.3	36.6	7.5	7.3	3.1
Solvent Molarity	11.8	14.1	12.9	19.1	12.3	9.3	11.8
Supports CV analysis*	–	+	+	+	+	+	–
Reversible		–	±	+	–	+	

+/– indicates success of screening analysis *dissolves 0.5 mM active species loading

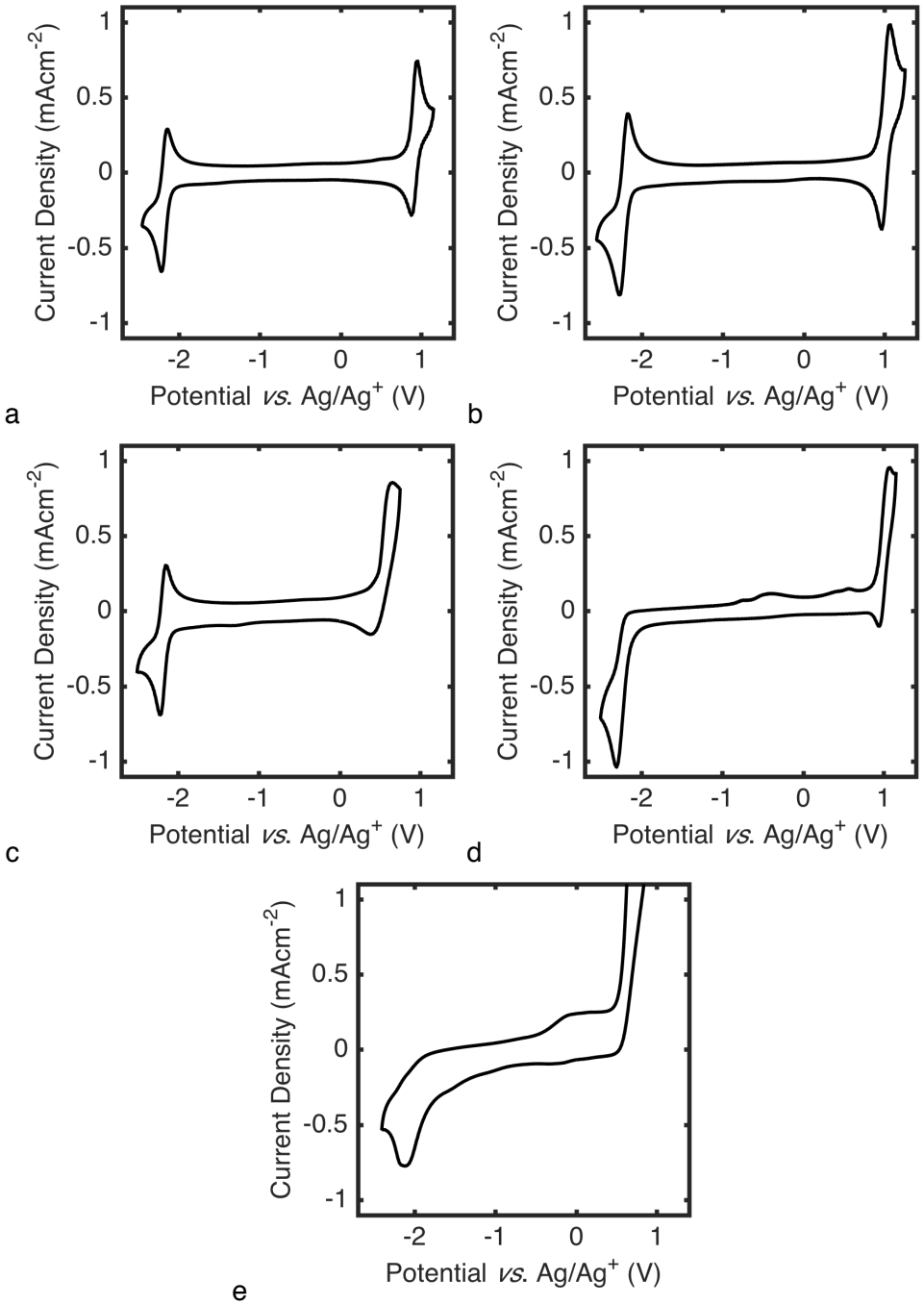

Figure 4.13. Cyclic voltammogram of 1 mM DPA loading, 0.5 M $TBABF_4$ in a)ACN, b) DME, c)DMF, d) THF, e)DMSO glassy carbon, 400 mVs^{-1}, 23 °C.

Cyclic voltammograms of DPA in supporting solutions using solvents that met the minimum solubility criterion are shown in Figure 4.13. These experiments use $TBABF_4$ as the supporting electrolyte because of its high solubility in all the solvents and its ability to imbue the solutions with sufficient ionic conductivity. Both ACN and DME solvated solutions show promising electrochemistry, with first reduction couples at –2.19 V and –2.23 V *vs.* Ag/Ag^+, respectively, and first oxidation couples at 0.90 V and 1.00 V *vs.* Ag/Ag^+; the voltammetry with both solvent systems suggests that a full cell based on DPA would achieve an OCP above 3 V in a symmetric configuration.

Figure 4.13a shows that in ACN, the peak-to-peak separation is 66 mV for the first reduction half-reaction and 56 mV for the first oxidation; both peak separations reasonably match the Nernstian reversibility criterion of 57 mV separation (for experiments run at 25 °C). Peak separation below 57 mV may indicate formation of a surface film, but more likely owes to the lower temperature conditions for the experiment (23 °C). Peak-height ratios at the 400 mVs^{-1} scan rate – measured from chords connecting the limiting baseline currents before and after the peaks – are 0.94 and 0.81 for the negative and positive reactions, respectively. 0.81 is not a large deviation from unity for this type of measurement, but may suggest that the positive reaction suffers from slow kinetics or possible chemical irreversibility. Physical modifications, such as a drop in active-species diffusivity upon change in charge state, could also cause the non-unity oxidation couple peak height ratio.

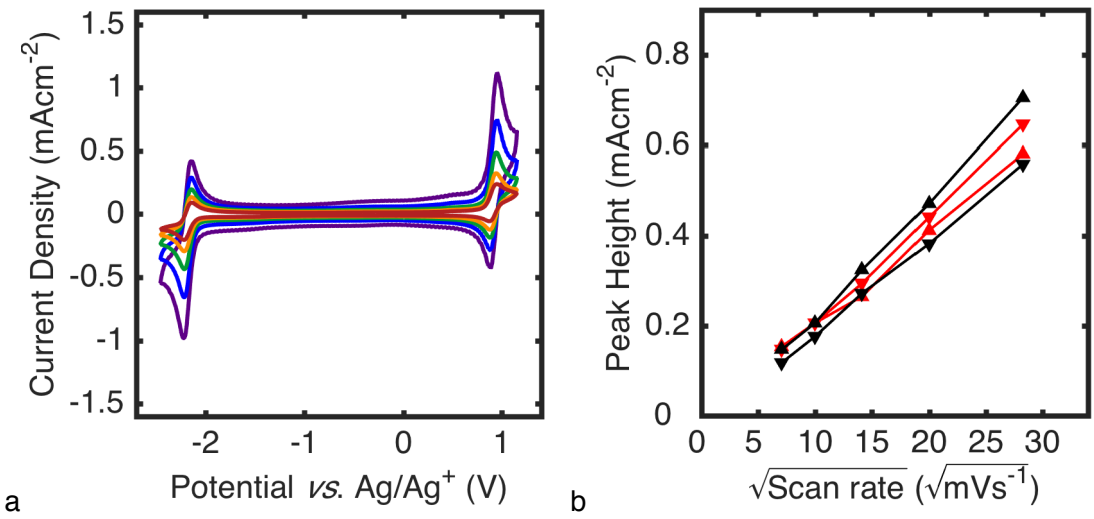

Figure 4.14. Cyclic voltammogram of 1 mM DPA loading, 0.5 M $TBABF_4$ in ACN, glassy carbon run at a) 50 (red), 100 (orange), 200 (green), 400 (blue), 800 (purple) mVs^{-1} and b) influence of scan rate on peak height for the reduction (downward triangle) and oxidation (upward triangle) peaks in the reduction couple (red) and oxidation couple (black).

Analysis of DPA in ACN voltammetry results at multiple scan rates, shown in Figure 4.14a tests whether reaction products form a surface layer on the electrode during operation. Formation of a surface film would correspond to linear dependence of current-density peak height with respect to scan rate. Instead, Figure 4.14b indicates that the peak height depends linearly on the square root of scan rate. This is consistent with the typical assumption of a diffusion-limited heterogeneous reaction.

Scan-rate studies also suggest quantitative values of the neutral active species diffusivity through the Randles-Sevcik equation for a electrochemically reversible reaction:

$$i_p = \left(2.69 \times 10^5\right) n^{3/2} D_0^{1/2} C_0 v^{1/2}. \qquad (4.1)$$

Here i_p is the peak current density (Acm^{-2}), v is the scan rate in (Vs^{-1}), and C_0 is neutral species concentration ($molmL^{-1}$). Assuming a single-electron reaction (n=1) gives a diffusion coefficient of 7.8 x 10^{-6} cm^2s^{-1} for the reduction reaction and 9.7 x 10^{-6} cm^2s^{-1} for the oxidation. The reactant is the same DPA molecule for both reactions, so the diffusivity value should be the same. It can be assumed that, within the error of the

method, the diffusivity is somewhere around the average of these two values – about 9 x 10^{-6} cm^2s^{-1}.

In DME, the peak separation at 400 mVs^{-1} is 93 mV for the reduction half-reaction and 85 mV for the oxidation (Figure 4.13b), both of which deviate sufficiently from 57 mV to suggest quasi-reversible redox kinetics. Alternatively, the increased peak separation could result from the support solution since more resistive solutions with lower $TBABF_4$ concentrations offer even higher peak separation. Peak height ratios are 0.95 for both redox couples. This indicates that DME supports chemically reversible DPA redox reactions.

Analysis of the scan-rate dependence of DPA voltammetry in the DME solution shown in Figure 4.15b also points to better redox behavior. Assuming a single-electron reaction in Equation 4.1 (n=1) gives a diffusion coefficient of 9.2 x 10^{-6} cm^2s^{-1} for the reduction half-reaction and 9.1 x 10^{-6} cm^2s^{-1} for the oxidation. These two values agree with each other and the notion that they represent a property of the same reactant.

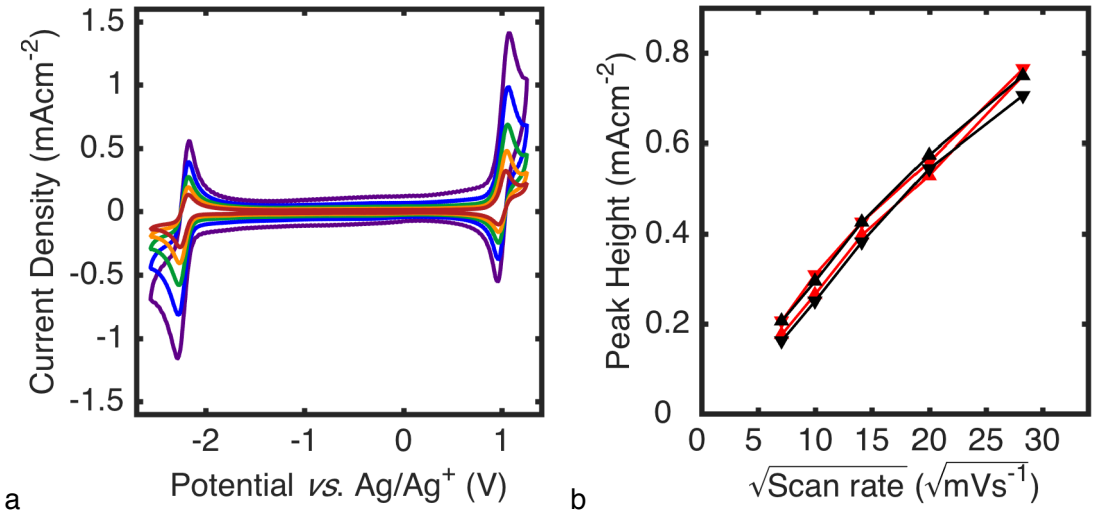

Figure 4.15. Cyclic voltammograms of 1 mM DPA loading, 0.5 M $TBABF_4$ in DME, glassy carbon, run at a) 50 (red), 100 (orange), 200 (green), 400 (blue), 800 (purple) mVs^{-1} and b) influence of scan rate on peak height for the reduction (downward triangle) and oxidation (upward triangle) peaks in the reduction couple (red) and oxidation couple (black).

DPA in DMF produces broad peaks at the oxidation couple, seen in Figure 4.13c, suggesting sluggish redox kinetics, especially when the oxidized species reduces back to the neutral molecule. DPA in THF displays evidence of chemical side reactions (*cf*. Figure 4.13d) because reverse reaction peaks are muted or absent for both redox couples, being replaced with oxidative activity across –1.0 V to 0.5 V *vs.* Ag/Ag^{+}. Alternatively, voltammetry with DMSO, shown in Figure 4.13e, suggests entirely irreversible electrochemistry for DPA. For the present analysis, these preliminary voltammetric measurements disqualify less promising solvent systems: study of DPA-based RFB electrochemistry continues only with ACN and DME. Further study of the synergistic and detrimental effects of solvents and support on DPA should be pursued, however, since these phenomena are observed with other RFB chemistries.

Solubility limits of DPA in both solvents were determined by densitometry, summarized in Figure 4.16. The solubility limit of DPA is 0.6 mM in ACN and 44 mM in DME. A cell built using this chemistry would achieve active-species cost savings, but the low active-species solubility corresponds to an energy density below 2 WhL^{-1} in the DME solutions. Consequently, this low active species solubility, and resultant low energy density, would require large solvent and supporting-electrolyte expenditure as described in Equation. 2.7.

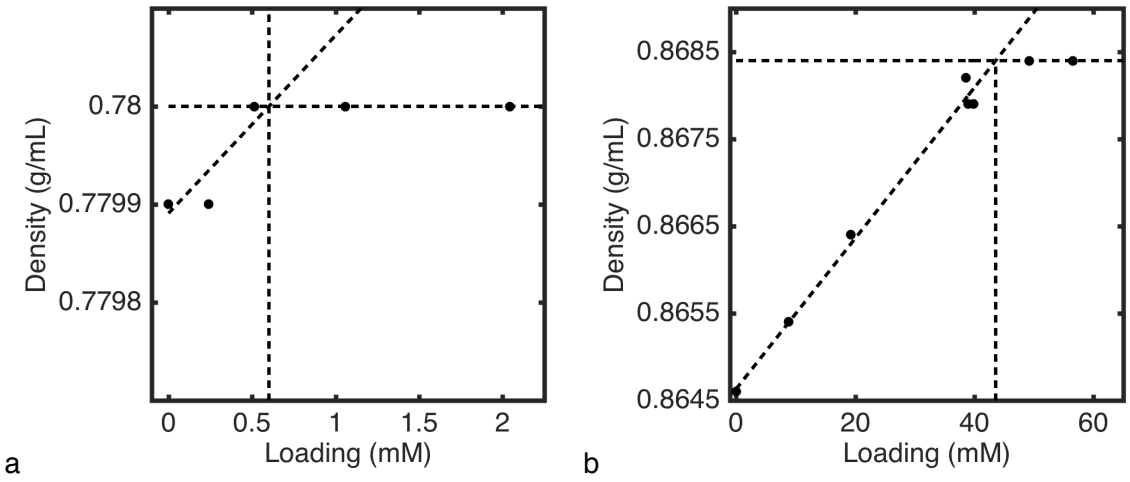

Figure 4.16. Densitometric solubility limit determination of DPA in (a) ACN and (b) DME.

4.3 Functionalized DPA Analogues

Various functional groups were incorporated at the 4-position of the phenyl groups in DPA to investigate their impact on active species solubility. This strategy aimed to improve the solubility of the derivatives without significantly altering the electrochemical activity of the polycyclic aromatic center.

4.3.1 Solubility and Voltammetry of Functionalized DPA

Suzuki cross-coupling reactions, described in Figure 4.2, produced several preliminary DPA analogues with electron-donating/withdrawing groups in a single step. These functional groups ranged from moderately donating methoxy, to weakly donating methyl, to moderately withdrawing methyl ester functional groups. These preliminary derivatives all exhibit decreased solubility, listed in columns 3-5 of Table 4.2, relative to unmodified DPA.

Table 4.2 Solubility limits (mM) of DPA based molecules in ACN and DME

	DPA	DMPA	DMOPA	DMBA	DePA	DdPA
ACN	0.6	0.5	<0.3	<0.3	0.3	12
DME	44	19	7.5	0.5	12	210

The DPA analogues were also tested with CV to observe the influence of functionalization on redox behavior. Functionalization with methyl groups to form DMPA delivers a voltammogram in ACN, shown in Figure 4.17, qualitatively similar to DPA. Both half-reactions show clear oxidation and reduction couples centered at –2.23 V and 0.87 V *vs.* Ag/Ag^+, corresponding to a negative shift of 30-40 mV for both reaction potentials relative to DPA. DMOPA and DMBA have especially low solubilities in ACN and double-layer capacitance obscures full interpretation of the redox activity in the voltammetric response. Voltammetry of DMOPA, shown in Figure 4.18, seems to reveal three redox couples compared to DPA's two: there are two reduction couples and a lone oxidation peak at positive potentials. Of the reduction couples, the first occurs at –2.25 V *vs.* Ag/Ag^+, 60 mV lower than the DPA reduction event and the second reduction occurs at –2.45 V *vs.* Ag/Ag^+. The lone oxidation peak occurs at 0.76 V *vs.* Ag/Ag^+, 140 mV lower than the DPA oxidation couple. The signals from redox events in the voltammetry of DMBA in Figure 4.19 are even less distinct, but reveal at least one couple, a reduction couple at –2.07 V *vs.* Ag/Ag^+, which is 120 mV higher than the DPA reduction potential. Functionalization affects the redox potential of these DPA analogues as expected based on the electron-withdrawing or donating nature of the functional groups. Electron-donating methoxy groups and methyl groups (less so) in DMOPA and DMPA lead to less extreme potentials necessary to induce loss of an electron (oxidation) and more extreme potentials to add an extra electron (reduction). Correspondingly, the electron-withdrawing methyl makes a compound for which less extreme potentials are needed to accept an electron.

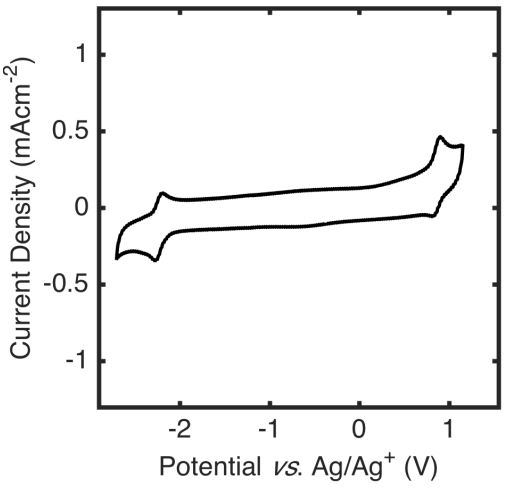

Figure 4.17. Cyclic voltammogram of 1 mM DMPA, 0.5 M $TBABF_4$ in ACN, glassy carbon, 400 mVs^{-1}, 23 °C.

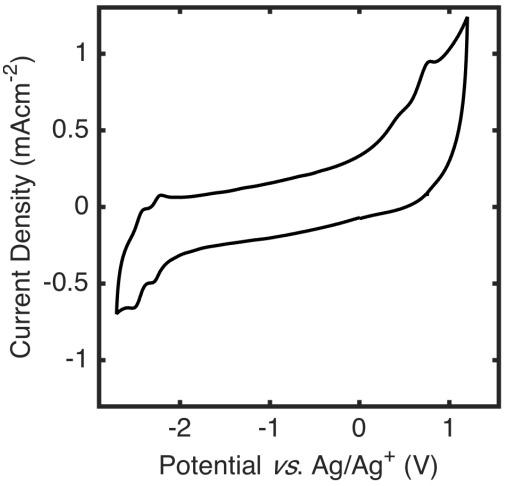

Figure 4.18. Cyclic voltammogram of 1 mM DMOPA, 0.5 M $TBABF_4$ in ACN, glassy carbon, 400 mVs^{-1}, 23 °C.

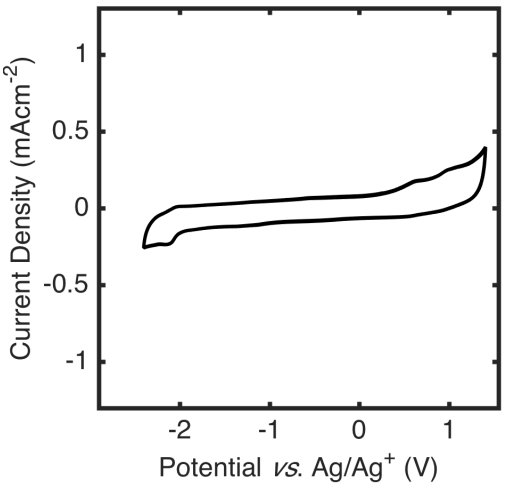

Figure 4.19. Cyclic voltammogram of 1 mM DMBA, 0.5 M $TBABF_4$ in ACN, glassy carbon, 400 mVs^{-1}, 23 °C.

Although unsuccessful in improving solubility, the preliminary study of these DPA analogues produced a reliable method to synthesize DMBA, which is a useful precursor for further functionalization. The methyl-ester functional group of DMBA provides a synthetic handle that can be used to incorporate pendant ethylene glycol chains, which have been demonstrated to drastically improve solubilities of organometallic complexes in nonaqueous environments.[47,42] Using DMBA as a starting material, the methyl from the ester functionalization is exchanged with a single ethylene glycol unit (to form DePA) or a double unit (to form DdPA) according to the reaction scheme shown in Figure 4.6. The solubility of DePA is higher than DMBA – 0.3 mM in neat ACN and 12 mM in DME – and allows full interpretation of CV experiments. Voltammetry on DePA, shown in Figure 4.20, reveals the presence of an oxidation couple for the ester-functionalized analogue of DPA, which was unclear from CV on DMBA. The equilibrium reaction potential of both redox couples shift positively: 130 mV to –2.06 V, for the reduction couple, and by 60 mV for the oxidation to 0.96 V, both *vs.* Ag/Ag^{+}. Again, this is consistent with the addition of an electron-withdrawing group: less electron density in the aryl structure makes removing an electron more energetically unfavorable, and *vice versa*.

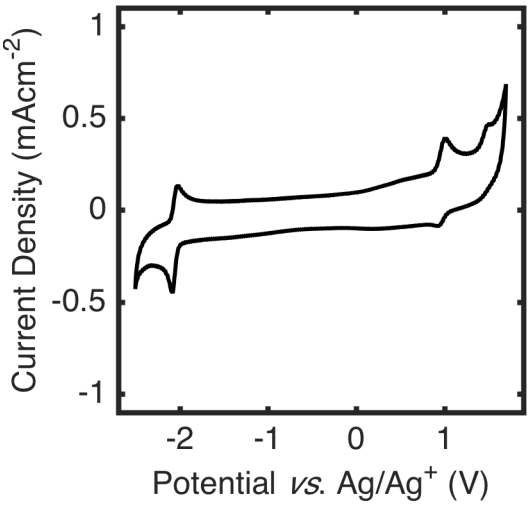

Figure 4.20. Cyclic voltammogram of 1 mM DePA, 0.05 M $TEABF_4$ in ACN, glassy carbon, 500 mVs^{-1}, 23 °C.

Increasing the ethylene glycol chain length from one in DePA to two in the diethyleneglycoxy esters present in DdPA delivers drastic solubility improvements. DdPA can dissolve up to 12 mM concentrations in neat ACN and 0.21 M in DME, as shown in Figure 4.21, representing 20x and nearly 5x improvements over DPA, respectively. The DdPA solubility in DME corresponds to a theoretical maximum energy density greater than 8 WhL^{-1} for the 3.2 V OCP chemistry. This is roughly one-fourth of the 35 WhL^{-1} energy density target proposed in Chapter 2, which outperforms AVRFBs energy costs by reining in supporting electrolyte material costs. DdPA shows that improvements of this magnitude (*i.e.* 5x) are possible and provides an energy density that begins to approach the value used in cost-competitiveness analysis from Chapter 2. Certainly, these synthetic procedures will increase active species cost above the precursor cost used in that analysis. Further development of the synthetic chemistry should consider other criteria, such as the cost of the synthesis, now that the compounds have been demonstrated and tested.

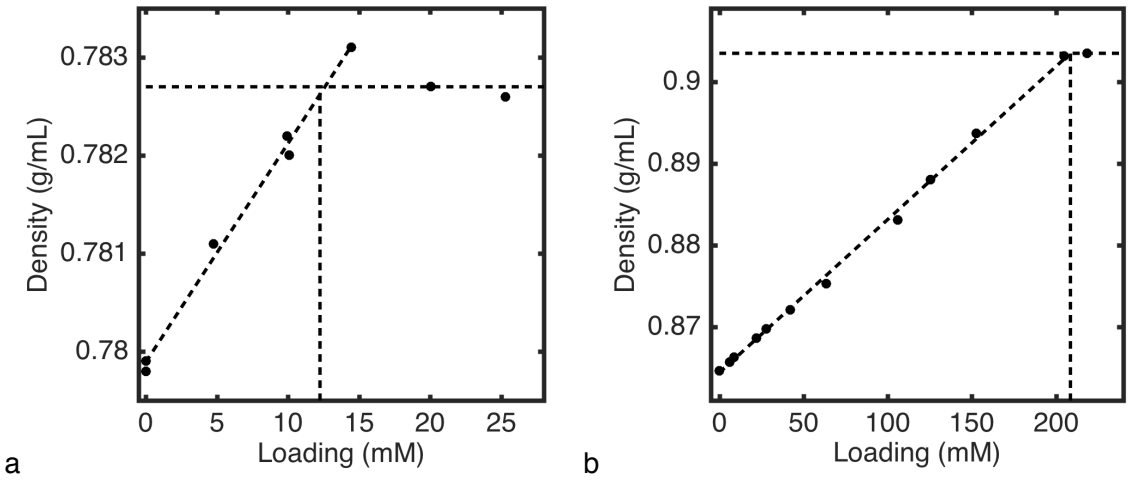

Figure 4.21. Densitometric solubility limit determination of DPA in (a) ACN and (b) DME.

DdPA shows some deviation from the reversible electrochemistry of the non-functionalized DPA. The oxidation couple still appears reversible, occurring 90 mV higher at 0.99 V and 1.09 V *vs.* Ag/Ag^+ in ACN and DME, respectively. The oxidation couple has peak separation of 78 mV and 97 mV and peak-height ratios of 0.83 and 1.22, respectively in the two solvents. Sluggish reaction kinetics is evident for the reduction couple in both solvents, visible from the voltammograms in Figure 4.22a-b. Both solvent systems exhibit a sharp reduction peak at –2.07 V and –2.09 V *vs.* Ag/Ag^+ in ACN and DME, respectively, but the corresponding oxidation peaks are broad and include a second, small oxidation feature at –1.17 V *vs.* Ag/Ag^+.

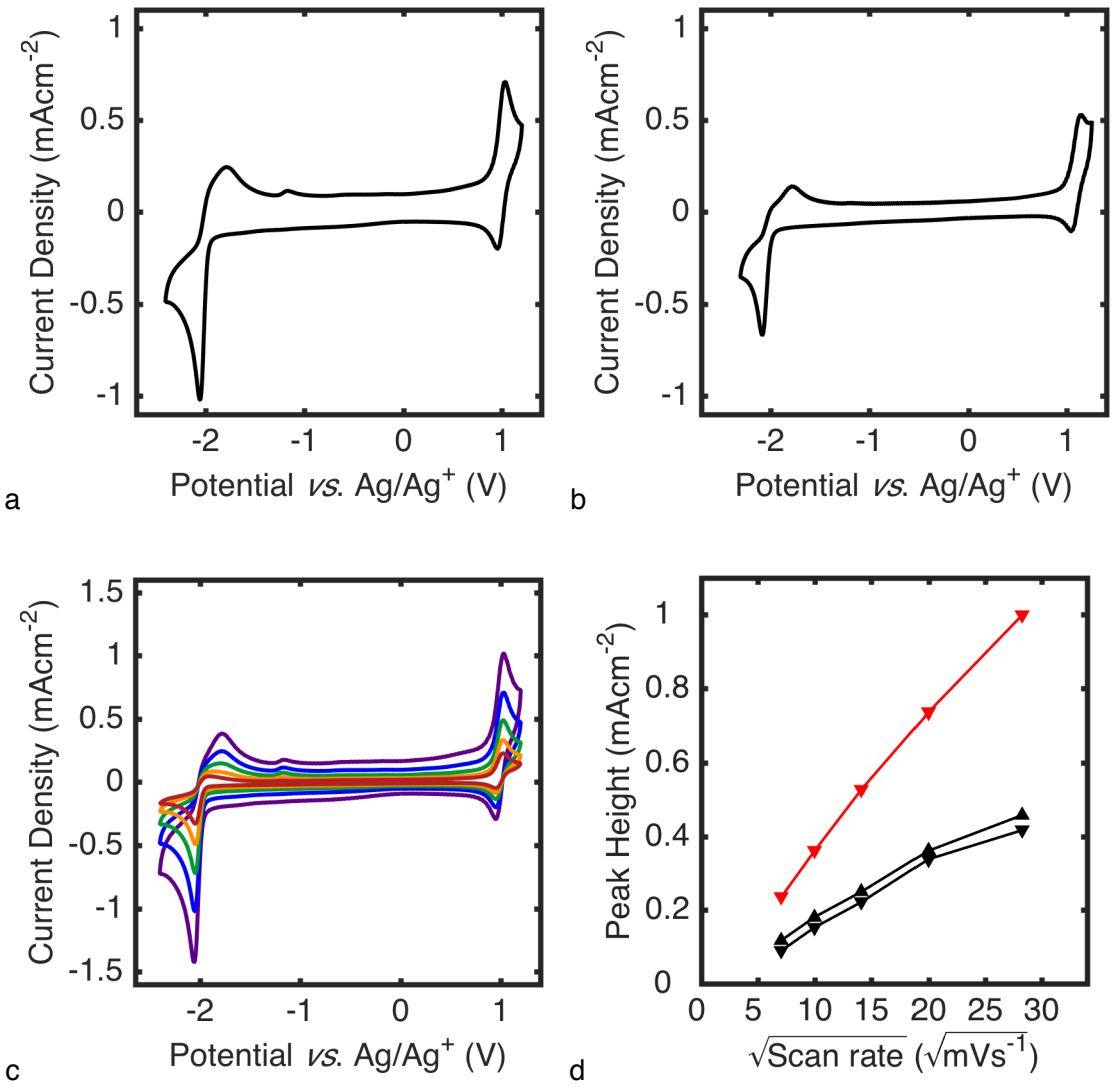

Figure 4.22. Cyclic voltammogram of 1 mM DdPA, 0.5 M $TBABF_4$ in (a) ACN (b) DME, glassy carbon, 400 mVs^{-1}, 23 °C. Voltammograms in ACN run at c) 50 (red), 100 (orange), 200 (green), 400 (blue), 800 (purple) mVs^{-1} and d) influence of scan rate on peak height for the reduction (downward triangle) and oxidation (upward triangle) peaks in the reduction couple (red) and oxidation couple (black).

Examination of DdPA in ACN by CV at multiple scan rates in Figure 4.22c-d allows estimation of the neutral active species' diffusivity. Assuming a single-electron exchange in Equation 4.1 (n=1) for the oxidation reaction gives a diffusion coefficient of 4.8 x 10^{-6} cm^2s^{-1} for DdPA in ACN. This is about half the diffusivity value calculated for DPA in ACN, which is a diminishment consistent with the addition of long side-chains to the base molecule.

While DdPA offers significantly improved solubility and retains redox couples that still offer high cell voltages, the synthetic procedure to produce DdPA has some limitations. Efforts to scale the procedure above the 100 mg scale were unsuccessful. Even at this small scale, the yields from the trans-esterification reaction are low (maximum of 46%). Whereas the molecule has physical properties that allow experiments employing larger amounts of material, the synthetic procedure still limited experiments to small scales.

Building from the success at improving solubility with diethyleneglycoxy ester functionalizations, an alternate DdPA is pursued. Instead of tethering the ethylene glycol chain *via* an ester, eDdPA uses an ether. Production of eDdPA involves preparing a diethyleneglycoxy ether functionalized boronic acid and following the cross-coupling reaction scheme in Figure 4.2. This eliminates the troublesome DMBA trans-esterification reaction. The cross-coupling scheme in Figure 4.2 offers higher yields than the trans-esterification reaction and circumvents the DdPA scale-up issue.

The voltammetry of eDdPA shows promise. As shown in Figure 4.23, eDdPA offers cleaner electrochemistry than DdPA. The reduction couple returns to the reversible appearance of DPA, at a more negative potential than DPA, –2.20 V *vs.* Ag/Ag^+. The suggested second reduction half-reaction observed for DMOPA appears to be an artifact of the low concentration since this is absent for eDdPA. Instead, there are two oxidation couples, apparently reversible, with the first reaction potential at 0.83 V, 70 mV lower than the DPA oxidation half-reaction, and the second couple higher at 1.03 V *vs.* Ag/Ag^+. Although eDdPA offers advantages for synthesis and redox activity its solubility in the nonaqueous battery solvents makes it less compelling. ACN could not fully dissolve 2 mM loadings of eDdPA Consequently, subsequent experiments focused on DdPA, which offered the highest solubility of the synthesized compounds.

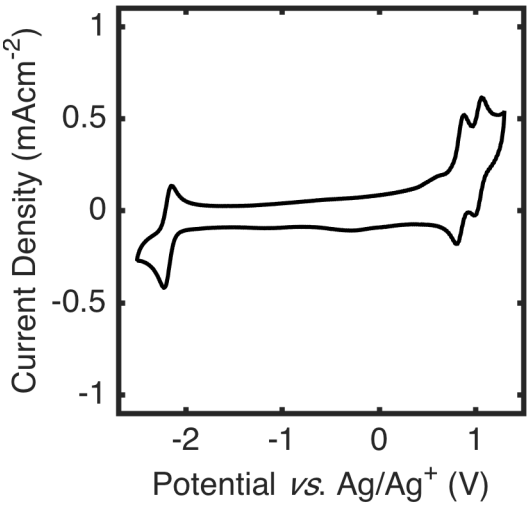

Figure 4.23. Cyclic voltammogram of 1 mM eDdPA, 0.1 M $TBABF_4$ in ACN, glassy carbon, 400 mVs^{-1}, 23 °C.

Other strategies focus on improving solubility by functionalizing at the *meta*-position using a *meta*-functionalized version of DMBA, *m*-DMBA, or even *ortho* functionalizations. These functionalizations still require the trans-esterification reaction, which will not avoid synthetic inefficiencies, but may further improve solubility by breaking up molecular symmetry. These efforts are ongoing.

4.3.2 Batch Reactor Charge-Discharge

Batch reactor charge-discharge experiments on DPA in DME within the continuously stirred electrolysis cell are presented in Figure 4.24. Although its 44 mM solubility limit in DME means than DPA is unlikely to produce a commercially relevant cell in DME solutions, this provided an opportunity to observe the cyclability of the DPA chemistry. Capacity is retained after 25 cycles, with coulombic and energy efficiencies stabilizing at 63% and 20%, respectively. The relatively low conductivity of 0.5 M $TBABF_4$ in DME supporting solution (2.3 $mScm^{-1}$) restricts the tests to low current densities of 8 μAcm^{-2} on charge and 2 μAcm^{-2} on discharge.

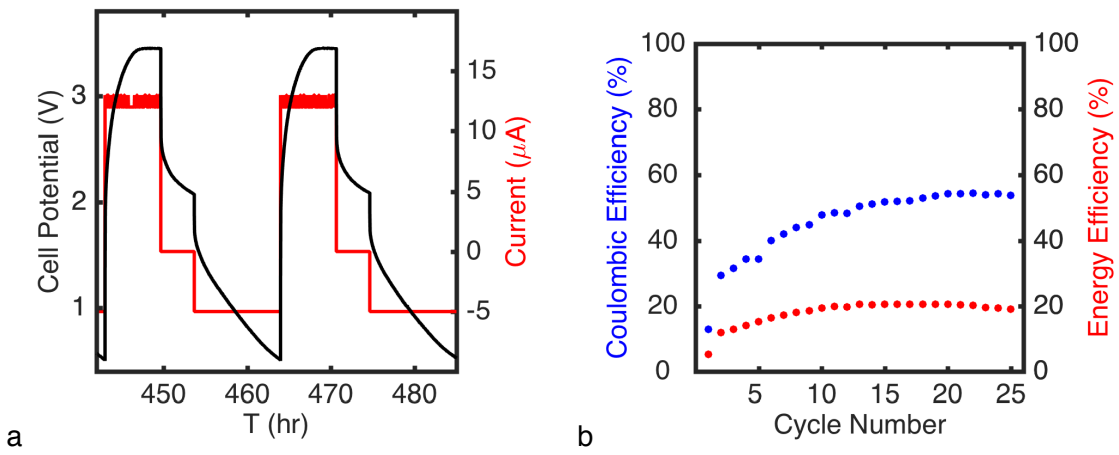

Figure 4.24. Charge/discharge performance of 10 mM DPA, 0.5 M $TBABF_4$ in DME: (a) cycling behavior, (b) coulombic (blue) and energy (red) efficiency performance over 25 cycles.

DdPA in ACN delivers substantially improved rate capability over DPA in DME; charge-discharge data are presented in Figure 4.25. The comparatively high conductivity of the 0.1 M $TBABF_4$ in ACN supporting solution (10.9 $mScm^{-1}$, *vs.* 2.3 $mScm^{-1}$ for 0.5 M $TBABF_4$ in DME) permits higher current densities of 60 μAcm^{-2} on charge and 10 μAcm^{-2} on discharge. Coulombic efficiency and energy efficiency stabilize to 55% and 20%, until capacity begins to fade after 15 cycles. This capacity fade stems from charging potentials hitting the 3.9 V potential cutoff before the designated 30% theoretical SOC is delivered: as capacity fades, coulombic efficiency increases toward 100%, but energy efficiency only increases moderately to 25%. It is unclear what is responsible for this response, but overcharging due to positive average SOC drift is a likely possibility since the discharge voltage cutoff may prevent complete coulombic reversal of the cell reaction. 3.9 V may provide sufficiently high voltage to drive the apparently irreversible redox activity observed in Figure 4.20 at 1.40 V, which is also observed ~0.4 V above the first oxidation of the other DPA-based moieties. Further studies in flow cells, discussed in Chapter 5, may help illustrate the mechanism behind capacity fade.

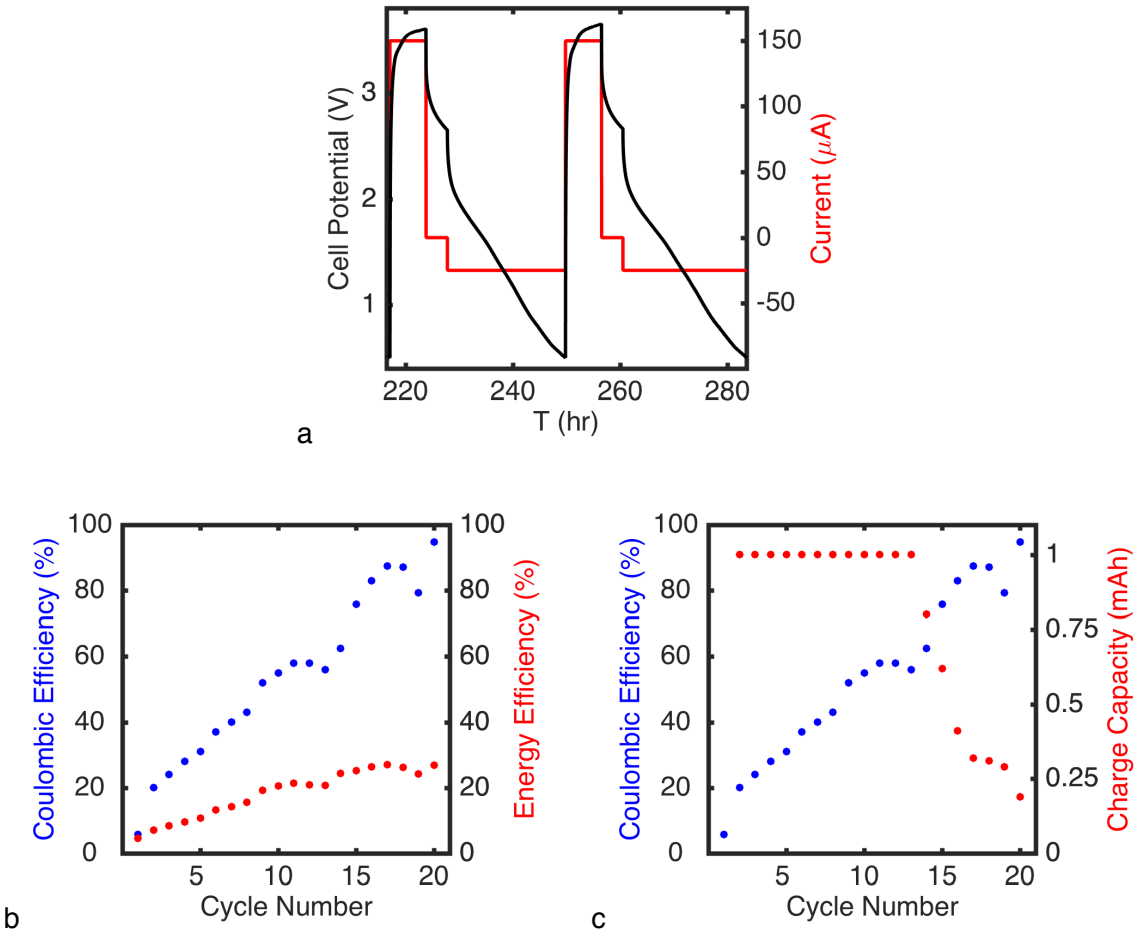

Figure 4.25. Charge/discharge performance of 10 mM DdPA, 0.1 M $TBABF_4$ in ACN: (a) cycling behavior, (b) coulombic (blue) and energy (red) efficiency performance over 25 cycles (c) coulombic efficiency (blue) and charge capacity (red) over 25 cycles.

Although the efficiencies appear low, experiments with nonaqueous $V(acac)_3$ demonstrate that this owes in large part to the cell geometry. Nonaqueous $V(acac)_3$ charge-discharge experiments performed in a similar batch reactor electrolysis cell achieved comparable coulombic and energy efficiencies, of 70% and 35%, respectively.[40] With the same chemistry in a flow cell, these efficiencies can reach 91% and 80% (albeit, with a different membrane).[66] Similar improvements are expected for the organic symmetric nonaqueous RFB chemistries upon implementation in the flow cell experiments described in Chapter 5.

Analysis of OCP data show that the voltage relaxes over the course of the 4-hour OCP hold. The cell potential should relax initially as concentration gradients in the cell

dissipate. Further cell potential drop might arise as a consequence of radical comproportionation accompanying crossover, chemical reaction with the membrane, or radical decomposition. Previous work has reported radical stability over a scale of at least several hours,[64,65] suggesting that other mechanisms might be at play. Membrane compatibility is an important consideration because the Neosepta AHA membrane used here is not designed for nonaqueous environments; chemical compatibility should receive close attention for any porous separators sought to replace ion-exchange membranes.

4.4 Alternative Aromatic Centers

With the demonstrated success of DPA and its analogues, another aromatic moiety is considered: naphthalene-centered 1,4-diphenylnaphthalene (DPN). Using the results from DPA analogues as a guide, the functionalization that induced the highest solubility limits is targeted for DPN: diethyleneglycoxy chains tethered *via* an ester. First, the methyl ester functionalized DPN was synthesized (DMBN, Figure 4.9) and, subsequently, trans-esterified with diethylene glycol alcohol to form DdPN.

DdPN shows immediate promise for use in a nonaqueous symmetric RFB since it is a liquid at room temperature. Addition of ACN or DME to neat DdPN reveals that the liquid is miscible with both solvents. The density of the neat DdPN liquid would determine the theoretical limit on energy density for a chemistry based on this active species.

Voltammetry further emphasizes the promise of the DdPN active species for RFBs. As shown in Figure 4.26a, DdPN in ACN has two widely separated redox couples. The reduction couple, located at –2.14 V *vs.* Ag/Ag^+, and oxidation couple, located at 1.47 V *vs.* Ag/Ag^+, promise a cell voltage over 3.6 V. The reduction couple is

very stable with cycling and produces 46 mV of peak separation and a 0.84 peak-height ratio. The oxidation couple gives 106 mV of peak separation and a 0.76 peak-height ratio. Both peak-height ratios are less than unity, though not too significantly, and may point to irreversibility issues. The peak separation for the reduction couple is significantly smaller than 57 mV, which indicates that an adsorption layer may be forming or a multi-electron reaction occurring. Voltammograms produced with DME solvent, shown in Figure 4.28b, reveal similar behavior to the ACN-based system at the reduction couple: –2.14 V *vs.* Ag/Ag^+ with a peak-height ratio of 0.98 and a peak separation of 72 mV. The oxidation reaction appears completely irreversible, however. This emphasizes the importance of solvent selection for nonaqueous systems and any further studies of DdPN for symmetric RFBs must start with ACN based solutions.

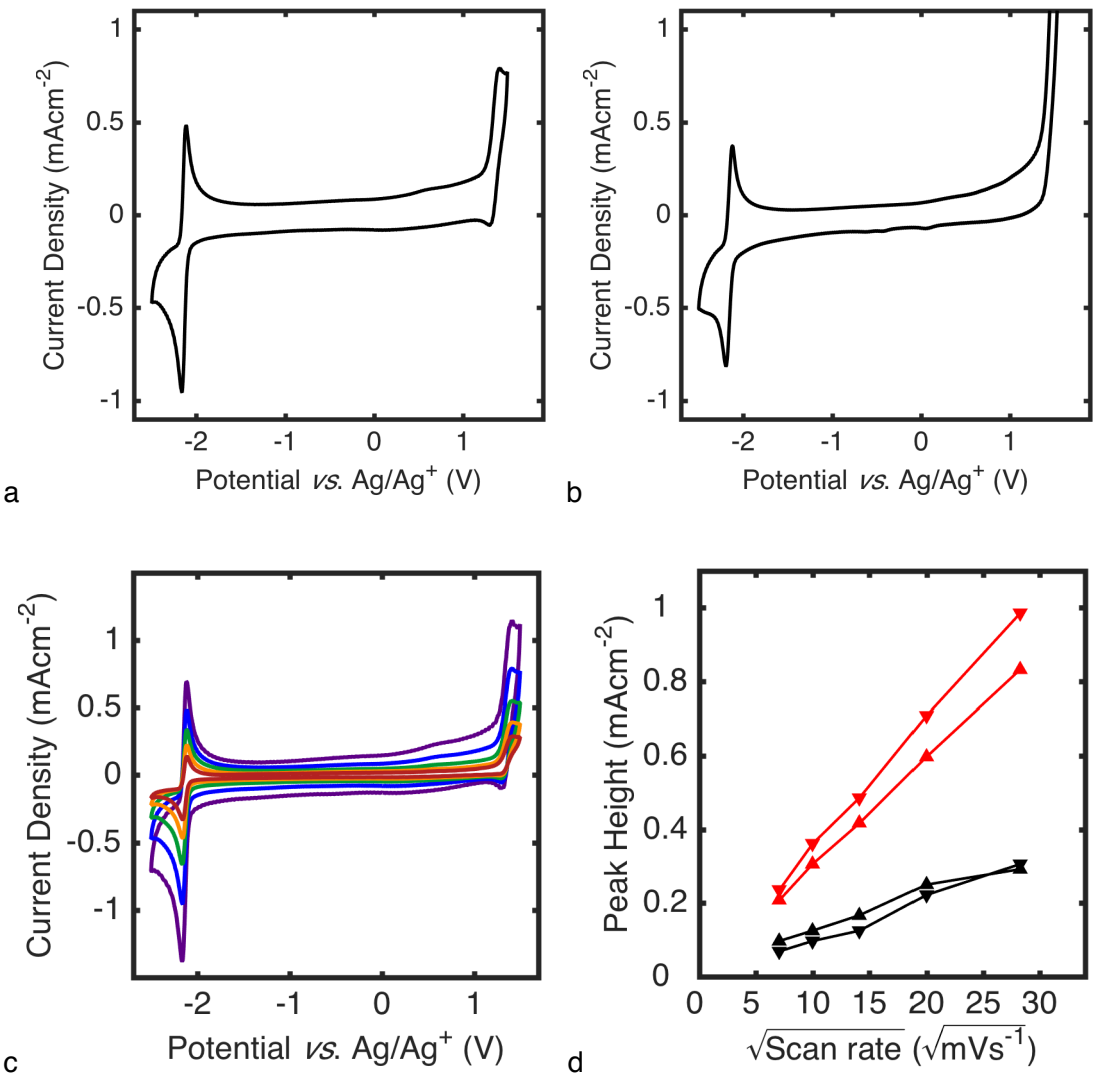

Figure 4.26. Cyclic voltammogram of 1 mM DdPN, 0.5 M $TBABF_4$ in a)ACN and b) DME, glassy carbon, 400mVs^{-1} 23 °C. Voltammograms run at c) 50 (red), 100 (orange), 200 (green), 400 (blue), 800 (purple) mVs^{-1} and d) influence of scan rate on peak height for the reduction (downward triangle) and oxidation (upward triangle) peaks in the reduction couple (red) and oxidation couple (black).

Voltammetry at various scan rates can shed light on possible underlying causes for small peak separation across the DdPN reduction couple in ACN. Adsorption reaction mechanisms are likely when peak separations are below 57 mV. Figures 4.26d indicates, however, that the peak height depends linearly on the square-root of scan rate. This is consistent with voltammograms for diffusion-limited heterogeneous half-reactions and suggests other mechanisms, possibly a multi-electron reaction, are responsible for the small peak separation. A multi-electron electron reaction would

further improve the practicality of DdPN and further motivate development of this active material for symmetric nonaqueous RFBs.

Calculation of DdPN diffusivity from the scan-rate dependence of peak heights also suggests that multi-electron reactions may be occurring. Assuming a single-electron reaction in Equation 4.1 (n=1) gives a diffusion coefficient of 1.7 x 10^{-5} cm^2s^{-1} for the reduction reaction and 1.3 x 10^{-6} cm^2s^{-1} for the oxidation. Even though these diffusivities should describe the same DdPN molecule, they differ by an order of magnitude. This comparison is convoluted by the fact that the oxidation reaction occurs just before an irreversible reaction and prevents reliable comparison of current peaks for the reversible oxidation couple. Furthermore, the diffusivity calculated from the reduction reaction is more than three times larger than that found for DdPA; some improvement in diffusivity is expected from the smaller naphthalene-centered moiety, but this seems exceptionally large. Scan-rate studies indicate that the DdPN reduction reaction likely involve more than a single electron.

4.5 Synthesis Scale-Up

Having demonstrated the promise of functionalized DPA using both CV and batch reactor charge-discharge experiments, a synthetic procedure that reliably produced larger laboratory-scale quantities of active-species material was necessary. All previous synthetic procedures described in this chapter were performed under the guidance of post-doctoral chemistry researchers, Dr. James A. Suttil and, subsequently, Dr. Christo S. Sevov, from Prof. Melanie Sanford's laboratory at the University of Michigan. The imminent need for reliable larger scale synthesis also coincided with a move from the University of Michigan to the University of Oxford. Consequently, a new collaboration began with Prof. Michael C. Willis and his post-doctoral researcher,

Dr. Robert Straker, in the Oxford chemistry department. This collaboration identified synthetic strategies for the scale-up effort and Dr. Straker executed the scale-up synthetic procedures.

The scale-up effort initially focused on larger scale preparation of DdPA from its precursor DMBA, but a slight alteration to the DMBA synthetic procedure eased production of that material too. The reaction scheme still employs a Suzuki-Miyaura cross-coupling reaction scheme, but the reaction conditions were modified: palladium acetate ($PdOAc_2$) (as a palladium source) paired with (2-biphenyl)dicyclohexylphosphine-2'-(*N,N*-dimethylamino)biphenyl ('DavePhos') free ligand replaced $Pd(PPh_3)_4$. Additionally, the reaction is run in THF (at lower temperatures), which allows easier isolation and purification of the DMBA product. Other palladium ligands were examined, (2-biphenyl)di-*tert*-butylphosphine and (2-biphenyl)dicyclohexylbutylphosphine ('JohnPhos' and 'CyJohnPhos'), but delivered worse reaction specificity. This synthetic procedure led to production of DMBA at a 10-gram scale with yields up to 75%. Further synthetic and characterization details are in Appendix A.3.

Scaling up the trans-esterification reaction entailed more significant changes to its procedure. The new scheme adds a co-solvent, *ortho*-dichlorobenzene, in addition to the liquid 2-methoxy(ethoxyethanol) reagent, and switched to a different Lewis acid, titanium isopropoxide (TiO-*i*-Pr). The co-solvent helps combat the low solubility of DMBA in the alcohol reactant/solvent. Although this does not significantly improve the reaction yield (48%), the reaction scaled up significantly, and has produced 5 gram batches of the DdPA active material.

As with the initial synthetic effort, lessons learned with DPA were applied to DPN. DdPN was produced at large scales using the same reaction scheme. DMBN's

improved solubility in the liquid 2-methoxy(ethoxyethanol) trans-esterification reagent eliminated the need for a co-solvent. These results indicate that an underlying cause of the limited scale of the original DdPA synthesis stemmed from the low DMBA solubilities. Further synthetic and characterization details are provided in Appendix A.3.

4.6 Summary and Discussion

This chapter concerns preliminary investigations of metal-free symmetric RFB chemistries based on polycyclic aromatic hydrocarbon chemistries. It provides evidence that both nonaqueous-solvent variation and active-species functionalization are useful strategies by which to enhance the theoretical maximum energy density of an organic symmetric nonaqueous RFB. Nonaqueous solvents were investigated with the dual aims of realizing the high voltage offered by DPA and maximizing DPA solubility. DME offers higher active species solubility, but is limited to lower rates due to the lower conductivities of DME solutions. ACN produces supporting solutions with higher conductivity, but yields lower active-species solubility.

Chemical functionalization of DPA centers allows active-species solubility to be changed without substantially altering the 3.1 V separation between the negative and positive half-reactions associated with its electrochemical disproportionation. Functionalization of DPA with diethyleneglycoxy esters to form DdPA significantly increases solubility in both DME and ACN, by factors of 5x and 20x, respectively. The 0.21 M maximum concentration of DdPA in DME suggests an energy density of 8 WhL^{-1}, which approaches the energy density value used in Chapter 2's cost-competitiveness analysis that indicates cells built using the inexpensive DPA could be viable. Batch electrolysis cells separated by Neosepta AHA membranes were used to demonstrate charge-discharge of the metal-free, symmetric, nonaqueous RFB

chemistries based on DPA in DME and DdPA in ACN. Although the DdPA cell experienced capacity fade after 15 cycles, the DPA cell retained capacity after 25 cycles. Efficiencies for DPA in DME and DdPA in ACN are similar to those of nonaqueous $V(acac)_3$ in cells with the same construction. This demonstrates the promise of inexpensive polycyclic aromatic hydrocarbon active species for nonaqueous RFBs. Furthermore, scale-up efforts have reliably produced quantities need for laboratory-scale experiments with the DdPA and DdPN active species.

The dramatic reduction in active-species cost can offset the increased expense of nonaqueous solvents and supporting electrolytes, but improvements in energy density are necessary to manage these costs. Signs of capacity fade in the DdPA cycling experiments indicate that some degradation may occur, which should receive attention in the future. The spectroelectrochemical experimental procedure described in Chapter 3 offers a means to study possible degradation in these active species Future work to identify compatible inexpensive nonaqueous supporting solutions could help to reduce the cost of nonaqueous, symmetric redox flow batteries even further.

5 Symmetric Nonaqueous Redox Flow Cells

As nonaqueous RFB technology matures research focus increasingly needs to reflect intended applications. The increased interest in nonaqueous RFBs will lead to discovery of new chemistries and it is critical that performance be evaluated in flow reactors to allow clear comparison with the dominant aqueous alternatives. Whereas laboratory-scale aqueous RFB cells are readily available from various battery and fuel cell suppliers, these systems often employ materials that are chemically incompatible with nonaqueous systems. This chapter describes experiments in a custom flow cell designed specifically for chemical compatibility with nonaqueous solutions and resilience against corrosive high-voltage battery solutions. The new design reported in Section 5.1.2-3 improves upon similar cell designs from the RFB literature,[66,133] and further aims to provide simple reproducibility by other researchers using inexpensive commercially available materials and standard machining equipment. Ultimately, the new design allows flow cell demonstrations of promising nonaqueous RFB chemistries.

The nonaqueous flow cell is employed to investigate system control factors that affect the practical performance of the well-understood $V(acac)_3$ RFB chemistry[14] and demonstrate new symmetric organic chemistries based on the metal-free DPA redox center. A previous flow cell demonstration by Escalante-García *et al.* focused on the $V(acac)_3$ chemistry and reported significant capacity loss within 20 cycles, using both ion-exchange membranes and porous separators in the reactor.[66] These results are inconsistent with the spectroelectrochemistry results shown in Chapter 3, which suggest much better stability. Escalante-Garcia *et al.* described a cell that exhibited several material compatibility issues when reproduced with non-proprietary materials such as 'sweating' graphite (ACN solvent seeped through the porous graphite structure, carrying electrolyte salt and active species to the outer surface, where it precipitated)

and poor seals between hard PTFE gaskets; these issues have been resolved in this study and work from other groups.[133] Consequently Escalante-Garcia's experiments are repeated to examine $V(acac)_3$ performance in flow cells in Section 5.2. The flow cell is also used to test the DPA-based RFB chemistry in Section 5.3.

In addition to studying the cyclability of nonaqueous $V(acac)_3$, the power capabilities of this symmetric nonaqueous RFB with a low-cost porous Celgard 4560 separator is explored at various flow rates in Section 5.4. This study was largely motivated by the need to better understand the power-density capabilities of nonaqueous RFB chemistries for cost modeling and to respond to literature that has attacked nonaqueous chemistries on the basis that they cannot support practical current densities.[44] The different flow rates in this study and their associated impact on charge-discharge performance further inform the capabilities of this reactor, specifically, and nonaqueous RFBs, generally.

Chapter 2 focused on the capital cost of RFBs and showed that long-lived RFB systems can be cost-competitive with present commercial Li-ion systems. The development of novel RFB strategies – including high-voltage nonaqueous RFBs, symmetric RFBs, and RFBs with inexpensive active species – could support dramatic improvements to cost-performance metrics. Chapter 2 established that cost metrics can determine whether nonaqueous RFBs perform comparably to commercial aqueous systems and will predict their viability at the commercial scale. Long life is one advantage of RFBs that was presumed in Chapter 2; this stable cyclability must be demonstrated in practice. Additionally, the footprint and capital-cost calculations described in Chapter 2 require knowledge of the system's energy density and power density. Energy density, reported in WhL^{-1} informs the systems volume and volume-associated energy costs. Power density, reported in Wcm^{-2}, informs reactor area, reactor

cost, and power-electronics costs. These metrics also provide a means for comparison with conventional battery systems.

Secondary performance metrics, such as efficiency, which are absent from the cost analysis in Chapter 2, are relevant for models that consider EES value. Chapter 3 introduced three efficiency metrics: coulombic efficiency, voltage efficiency, and energy efficiency. These efficiencies are all quantified for the novel flow cells examined here. Chapter 3 also introduced the notion of a maximum C-rate. Although not relevant to RFBs presently, maximum C-rates could become relevant in systems with drastically reduced power costs, as might be expected from high-voltage symmetric systems that eschew expensive IEMs for inexpensive porous separators. Tertiary performance metrics like self-discharge are relevant and can be assessed with the experimental apparatus developed here, but are not considered in this thesis.

5.1 Experimental

5.1.1 Battery Solutions

Battery solutions were prepared using anhydrous ACN (99.8%, Sigma, UK) and DME (99.5%, Sigma, UK) as received or dried over molecular sieves (4Å, Fisher Scientific, UK) as indicated. $TEABF_4$ (Sigma, 99%, UK) and $TBABF_4$ (99%, Sigma, UK) were used as received. $V(acac)_3$ samples from two suppliers (97%, Sigma, UK or 98%, Strem, UK) were compared and used as indicated. Water content was measured with a C30 Karl Fischer Coulometer (Mettler-Toledo, UK). Solution conductivity was measured using a Thermo Scientific Orion Star A215 pH/conductivity benchtop multiparameter meter. Solution density and viscosity were measured at 22.0 °C using an Anton Paar DMA 4100M densitometer and Lovis 2000 M/ME rolling-ball viscometer.

5.1.2 Cell Design

The cell design employed in this study is illustrated in Figure 5.1. Multipurpose 304 stainless steel (McMaster-Carr, USA) was machined into 110 mm x 110 mm x 17 mm endplates with 6.35 mm diameter bores to allow cell compression *via* 6 mm 316 stainless steel threaded rods. Rigid HDPE polyethylene (McMaster-Carr, USA) was machined into 110 mm x 110 mm x 17 mm tubing manifolds with corresponding bolt-holes, and two 6.35 mm diameter centering-pin guides. Two 4 mm diameter, 8.5 mm deep tubing-outlet bores were connected perpendicularly with two 6.35 mm diameter tubing-inlet bores to provide access through the tubing manifold to the cell reactor *via* PTFE tubing. These manifolds serve three purposes: insulate the cell from an endplates-bolt short-circuit, provide a path for 1/8" OD, 1/16" ID tubing (PTFE from Fisher Scientific, UK or fluorinated ethylene propylene (FEP) coated Teflon from McMaster-Carr, USA), and provide a rigid face for a compression seal *via* o-rings and the rigid face of the graphite flow-plate. Corrosion-resistant 6101 aluminum (McMaster-Carr, USA) was machined into 80 mm x 80 mm x 3.2 mm current collectors with two 6.35 mm guides for centering-pins, two 6.35 mm holes for a tubing-path/compression-fitting, and a 40 mm x 25 mm tab for electrical connection. A 1/32" high-temperature graphite gasket (McMaster-Carr, USA) cut to the size of the current collector and punched with 6.35 mm holes for the centering-pins and tubing-path sits between the aluminum current collector and impervious graphite flow-plates. Impervious bipolar graphite (Graphitestore.com, USA) was machined into 80 mm x 80 mm x 6.35 mm flow-plates with two 6.35 mm guides for centering-pins and two 25 mm x 3.175 mm x 3 mm flow-collector-recesses framing the square 25 mm x 25 mm cell reactor area. A single 3.175 mm tubing-inlet bore was drilled into each flow collector recess such that they oriented diagonally across the reactor area.

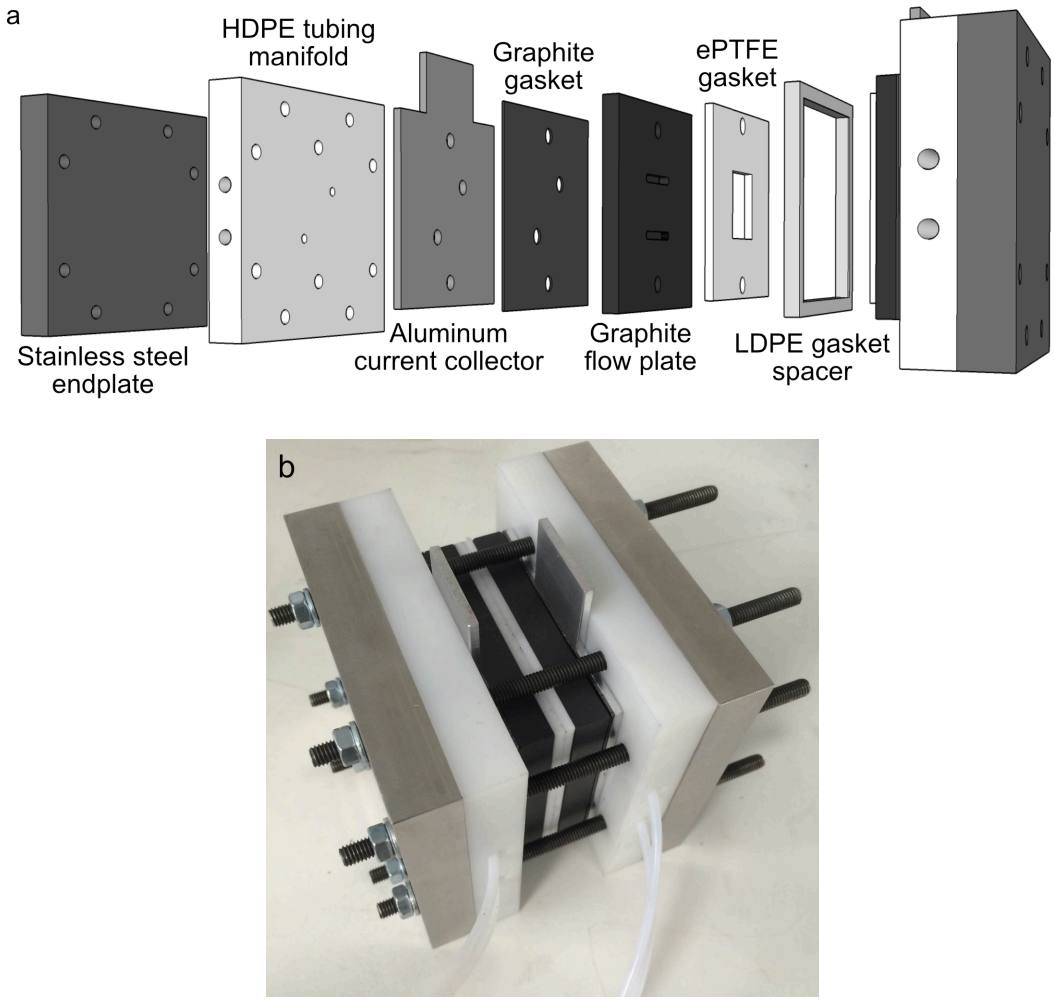

Figure 5.1. Schematic showing individual reactor components of one half of the cell (the other half is a mirror image) and a photograph of the constructed cell.

For assembly, the 1/8" OD PTFE tubing winds through the HDPE flow manifold, current collector, gasket, and ultimately, the flow plate, with 3 o-rings placed between the manifold and flow-plate: two Viton on the manifold side, and one FEP-coated Viton on the flow-plate side (McMaster-Carr, USA). This construction forms a solvent-tight seal under compression. Expanded PTFE gaskets (ePTFE, 3.125 mm thick uncompressed, McMaster-Carr, USA and Polyflon, UK) were cut to 70 mm x 70 mm, with two 6.35 mm guides punched for centering-pins and a 25 mm x 25 mm reactor area cut to fit carbon felt electrodes. Finally, a single 80 mm x 80 mm x 3 mm LDPE spacer (McMaster-Carr, USA) envelops the outer edges of the two ePTFE gaskets and provides a compression guide. Upon construction, the eight bolts are tightened with a torque-

wrench to 50 in-lb in a 4-2-4-3 pattern until all bolts achieve the desired torque. This torque compresses the two ePTFE gaskets sufficiently that they become flush with the single 3 mm LDPE spacer. All construction occurred within an Inert PureLab argon-filled glovebox with <1.0 ppm O_2 and H_2O.

5.1.3 Reactor Components

Cell electrodes consisted of 3.18 mm thick carbon felt (Alfa-Aesar, UK) cut into 25 mm x 25 mm squares. Before use, the carbon felt electrodes were heated to 250 °C for 48 hours under vacuum to remove residual water. During construction, the felt is placed into the void of the ePTFE gasket and subsequently compressed to 1.5 mm thickness – a compression ratio of 53%. The Celgard 4560 separator, which consists of a 25 μm polypropylene membrane laminated onto a 110 μm nonwoven polypropylene support fabric, was cut into 50 mm x 50 mm squares and heated at 75°C for two hours in ambient air before being brought into the glovebox. Before use in the cell, the separator was soaked in ACN or DME for two hours depending on the battery solution solvent used in the experiment. Upon construction, the separator is sandwiched between the two expanded PTFE gaskets.

5.1.4 Flow Rate Calibration Procedure

Electrolyte flows were oriented co-currently and calibrated with battery solution before initiating charge-discharge. Flow meters with sufficient precision and versatility to support nonaqueous solutions of differing compositions were prohibitively expensive and a simple flow calibration procedure was performed before any reactor experiment. Both reactor chambers are loaded with solution before diverting the reactor outlet line to a graduated cylinder for flow calibration. Flow rate calibrations targeted 50 mL total of pumped fluid into the graduated cylinder, leading to 4-minutes, 2-minutes, and 1-minute

calibration test periods for the 12.5, 25 and 50 $mLmin^{-1}$ flow rates, respectively. If flow rates did not achieve the necessary pumped volume, the pump speed of the Masterflex L/S PTFE Tubing Pump (Model 77390, Cole-Parmer, UK) with 6-mm PTFE pump-head tubing (Cole-Parmer, UK) was adjusted and the calibration test rerun. Once both pumps were calibrated, the battery solution was vacated from the cell and the 100 mL battery electrolyte was split between the two battery reservoirs. Subsequently, the pumps were restarted and the cell was prepared for electrochemical testing.

5.1.5 Charge-Discharge Procedure

Charge-discharge experiments with the 0.1 M $V(acac)_3$, 0.5 M $TEABF_4$, ACN battery solution were controlled *via* either an Autolab PGSTAT 302N potentiostat or Maccor 4000 series battery tester. The procedure involved an initial charge to 75% of the theoretical maximum SOC and all subsequent discharges and charges to 50% theoretical SOC as computed via coulomb counting, or until voltage cutoffs were reached, whichever came first. Theoretical SOC was calculated using active-species concentration and assuming a single-electron disproportionation $V(acac)_3$ reaction. Voltage cutoffs of 3.7 V on charging steps or 1.0 V on discharging steps were applied. Either the delivery or removal of 50% theoretical SOC or surpassing the voltage cutoffs triggered a switch to the next cycling step. Experiments were performed at 10, 20, 40 and 100 $mAcm^{-2}$ current densities on cells employing 12.5, 25 and 50 $mLmin^{-1}$ flow rates. Rarely, reservoirs were observed to accumulate volume imbalances; these imbalances were ascribed to imperfect flow calibration and deterioration in pump performance over the course of a cycling experiment. Simply transferring electrolyte directly from the rich reservoir to the poor reservoir was found to rectify the imbalance without any observed effects after the cycle in which the transfer occurred.

Similar procedures were employed for all other chemistries as well. All experiments aimed to deliver 75% theoretical SOC on the first charge and traverse a window of 50% theoretical SOC on subsequent discharge-charge cycles, with the same 3.7 V and 1.0 V voltage cutoffs. The 0.01 M $V(acac)_3$, 0.5 M $TBABF_4$, DME system was operated at 2 $mAcm^{-2}$ and 25 $mLmin^{-1}$. Low-concentration organic experiments, which involved 0.01 M DPA or DdPA supported by 0.5 M $TBABF_4$ in DME or ACN, also operated at the lower 2 $mAcm^{-2}$ current density used for $V(acac)_3$ in DME. The high-concentration 0.075 M DdPA, 0.5 M $TBABF_4$ in DME cycling experiments were operated at 5 $mAcm^{-2}$ to shorten the length of the experiment and minimize the need for reservoir rebalancing.

5.1.6 Electrochemical Impedance Spectroscopy

Electrochemical impedance spectroscopy (EIS) is an electrochemical technique that involves applying a small alternating potential input, E_{appl}, between two electrodes at a variety of frequencies and observing the resultant alternating current output, I, at those frequencies (or *vice versa*). Potentiostats capable of performing EIS often deliver the output as an impedance Z (magnitude Z_0 and phase ϕ).

$$E_{appl}(t) = E_0 \exp(j\omega t) \tag{5.1}$$

$$I(t) = I_o \exp(j\omega t + \phi) \tag{5.2}$$

$$Z = \frac{E(t)}{I(t)} = Z_0 \exp(j\phi) \tag{5.3}$$

Here, ω is frequency and t is time. Two archetypal EIS plots are typically used to present experimental results. A Nyquist plot graphs the negative imaginary component of the impedance against the real component as a parametric function of frequency. A Bode plot consists of two semi-logarithmic charts: one graphs the impedance magnitude

against frequency and the other graphs phase angle against frequency, with both frequency axes on a logarithmic scale. Nyquist plots help to understand the system response but fail to convey information about the frequencies at which measurements were gathered. Despite this shortcoming, Nyquist plots are often preferred over Bode plots because their presentation delivers characteristic shapes that ease interpretation of EIS data from electrochemical systems.

Typical electrochemical systems do not exhibit inductive responses, so EIS data can often be analyzed by fitting impedance spectra to equivalent-circuit models comprising only resistors and capacitors. The impedances of resistors and capacitors are:

$$Z_{\text{resistor}} = R \tag{5.4}$$

$$Z_{\text{capacitor}} = \frac{1}{j\omega C} \tag{5.5}$$

where R is resistance and C is capacitance. One circuit often associated with electrochemical systems is a parallel RC circuit; for example, this circuit is a good description of an electrode interface with double-layer capacitance and charge-transfer resistance. In a Nyquist plot, a parallel RC circuit manifests as a semicircle atop the real axis. EIS spectra are often analyzed by fitting semi-circles, or 'depressed' semi-circles (where a capacitor in the equivalent-circuit model is replaced by a constant-phase element representing an imperfect capacitor) whose radii along the real axis quantify the various resistances in the system; in combination with the frequencies of the measurements, the peaks of the semicircles can be used to gather information about the capacitance.

5.1.7 Degradation Testing

EIS was executed before and after charge-discharge experiments from cells with both stagnant and flowing electrolyte. The signal amplitude was 10 mV RMS, and the spectra were gathered over frequencies ranging from 50 kHz to 0.1 Hz with eight points per decade. EIS was performed using an Autolab PGSTAT 302N potentiostat with the FRA32 module (Metrohm, UK). EIS spectra were analyzed using the 'equivalent circle finder' tool in NOVA software (Metrohm UK). Cyclic voltammograms of the battery solutions were collected for both the negolyte and posolyte after completion of impedance and charge-discharge experiments. The voltage was swept between –2.2 V and 1.0 V *vs.* Ag/Ag^+ at 400 mVs^{-1} for the $V(acac)_3$ in ACN experiments. Larger voltage windows were examined as needed for the DPA and DdPA in DME or ACN solutions. A 1 mm diameter glassy carbon electrode (Basi Inc., USA/UK) served as the working electrode and a frit-separated, coiled 30 cm long, 0.3 mm diameter platinum wire served as counter electrode. The Ag/Ag^+ reference electrode consisted of a silver wire submerged in an ACN or DME solution of 0.01 M $AgNO_3$ and 0.05 M $TEAClO_4$ (or $TBAClO_4$ for TBA^+ supported DME experiments). In addition to atmospheric control, the glovebox provided temperature control for the experiments (21.5 ± 2°C).

5.1.8 Microscopy and Spectroscopy

Reactor componentry was studied *post hoc* using scanning electron microscopy (SEM) and energy dispersive x-ray spectroscopy (EDS). Analysis was performed using a Hitachi TM3000 Tabletop Microscope equipped with a Bruker Quantax 75 for EDS analysis. Samples were rinsed with either ACN or DME and allowed to dry before being adhered to an SEM stage with double-sided carbon or copper tape. Before performing microscopy, samples were sputter-coated (Sputter Coater 208 HR,

Cressington, UK) with platinum until reaching a 3.2 nm thickness (Thickness Controller mtm 20, Cressington, UK). Micrographs were collected in 5 kV, 15 kV, or analytical mode, and EDS spectra in analytical mode.

5.2 $V(acac)_3$ Cyclability

Previous flow cell demonstrations by Escalante-García *et al.* focused on $V(acac)_3$ in ACN solutions and reported significant capacity loss within 20 cycles, using both ion-exchange membranes and porous separators in the reactor.[66] The report identified a degradation pathway of $V(acac)_3$ to $VO(acac)_2$ as the cause of capacity loss in their cells. This capacity fade mechanism necessitates ligand dissociation. Also, these cells used $V(acac)_3$ active species from Sigma, which is demonstrated later to have impurity issues, and in a glovebox with an atmosphere containing 250 ppm of water vapor – a documented source of degradation.[40] The spectroelectrochemistry in Chapter 3 showed that acetylacetonate ligand dissociation does not occur appreciably when the atmospheric conditions, solvent, and supporting salt are water- and oxygen-free and the $V(acac)_3$ precursor is relatively pure. Imposing stricter control of ambient conditions and material compatibility in the reactor design described here produces cycling experiments retaining complete capacity over 20 cycles without the need for the stringent voltage cutoffs used in the Escalante-Garcia *et al*. experiments. These observations are consistent with the results from Chapter 3, which suggested that there is no electrolysis-induced $V(acac)_3$ degradation for either the positive or negative couple.[134]

5.2.1 $V(acac)_3$ in ACN

Since previous reports revealed that the presence of water leads to a degradation pathway for $V(acac)_3$,[40] Karl Fischer titration is used to quantify the water content of solution components. As received anhydrous ACN samples had water contents of 29.2 ± 2.0 ppm. Similarly, solutions of $TEABF_4$ in ACN at various concentrations had similar water contents of 28.3 ± 4.7 ppm, indicating the lack of appreciable moisture in the salt. The conductivity of 0.5 M solutions of $TEABF_4$ in ACN was measured and found to be 43 $mScm^{-1}$. Storage over 4 Å molecular sieves for 24 hours reduced water content in ACN samples by an order of magnitude, to 2.8 ± 0.7 ppm.

The voltammogram of Strem-provided $V(acac)_3$ delivers the expected redox reactions at –1.79 V and 0.41 V *vs.* Ag/Ag^+ as shown by the blue curve in Figure 5.2. Voltammetry on solutions of $V(acac)_3$ received from Sigma, which was used in the Escalante-Garcia study,[66] shows clear evidence of impurity. The voltammogram of Sigma-provided $V(acac)_3$ shown by the red curve in Figure 5.2 produces noticeably smaller redox peak magnitudes and a redox couple at 0.71 V *vs.* Ag/Ag^+ that indicates a $VO(acac)_2$ impurity.[40] The Strem samples are delivered in a wax-sealed, argon-filled, amber screw-top bottle packaged within an airtight tin filled with hygroscopic vermiculite. The Sigma samples are merely sealed in an amber screw-top bottle under ambient atmosphere and packaged in bubble-wrap when shipped. Ambient moisture exposure has been shown to be responsible for degradation of $V(acac)_3$ to $VO(acac)_2$[40] and the different delivery conditions explains the discrepancy in sample quality. Since the prices are comparable between the suppliers, Strem-supplied $V(acac)_3$ is used in all subsequent experiments and recommended for all future studies.

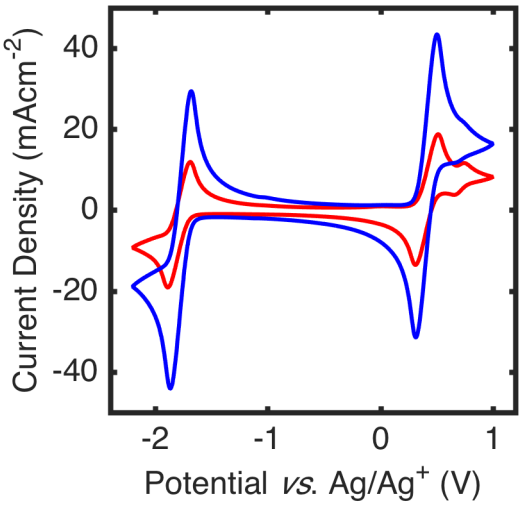

Figure 5.2. Cyclic voltammograms of 0.1 M $V(acac)_3$ from Sigma (red) and Strem (blue), 0.5 M $TEABF_4$ in ACN, glassy carbon, 400 mVs^{-1}, 23 °C.

Charge-discharge experiments using $V(acac)_3$ under the conditions investigated by Escalante-García *et al.*[66] were repeated, with more stringent atmospheric control and using battery solutions dried over molecular sieves and that were tested to be free of observable $VO(acac)_2$ impurity. The procedure also eliminated the strict 2.27 V charging cutoff used in that study. These cells were run using 0.1 M $V(acac)_3$, 0.5 M $TEABF_4$ in ACN with a 10 $mAcm^{-2}$ current density (corresponding to 0.47 C) and 25 $mLmin^{-1}$ flow rates. Immediately apparent from the first cycle in Figure 5.3 is a 'burn-in' inefficiency across the first cycle. Even though the cell is charged to 75% theoretical SOC, the discharge hits 1 V before discharging 50% theoretical SOC, and the first cycle delivers lower coulombic and energy efficiency than subsequent cycles. The rest of the cycles in Figure 5.3 show that batteries using solutions free of vanadyl and significant water impurity do not succumb to capacity fade; the cell cycles reproducibly after burn-in. The system averages 66% coulombic efficiency, 94% voltage efficiency, and 63% energy efficiency, consistent with results from the previous study, agnostic to its observed capacity fade. The cell delivers an energy density of 0.89 WhL^{-1} and an average power density of 20.4 $mWcm^{-2}$. Whereas discharge capacity faded in the

previous experiments by over 80% after ten cycles, the present study produces a decrease of less than 3% over 20 cycles. Additionally, the stringent voltage cutoffs described in the previous report[66] were unnecessary.

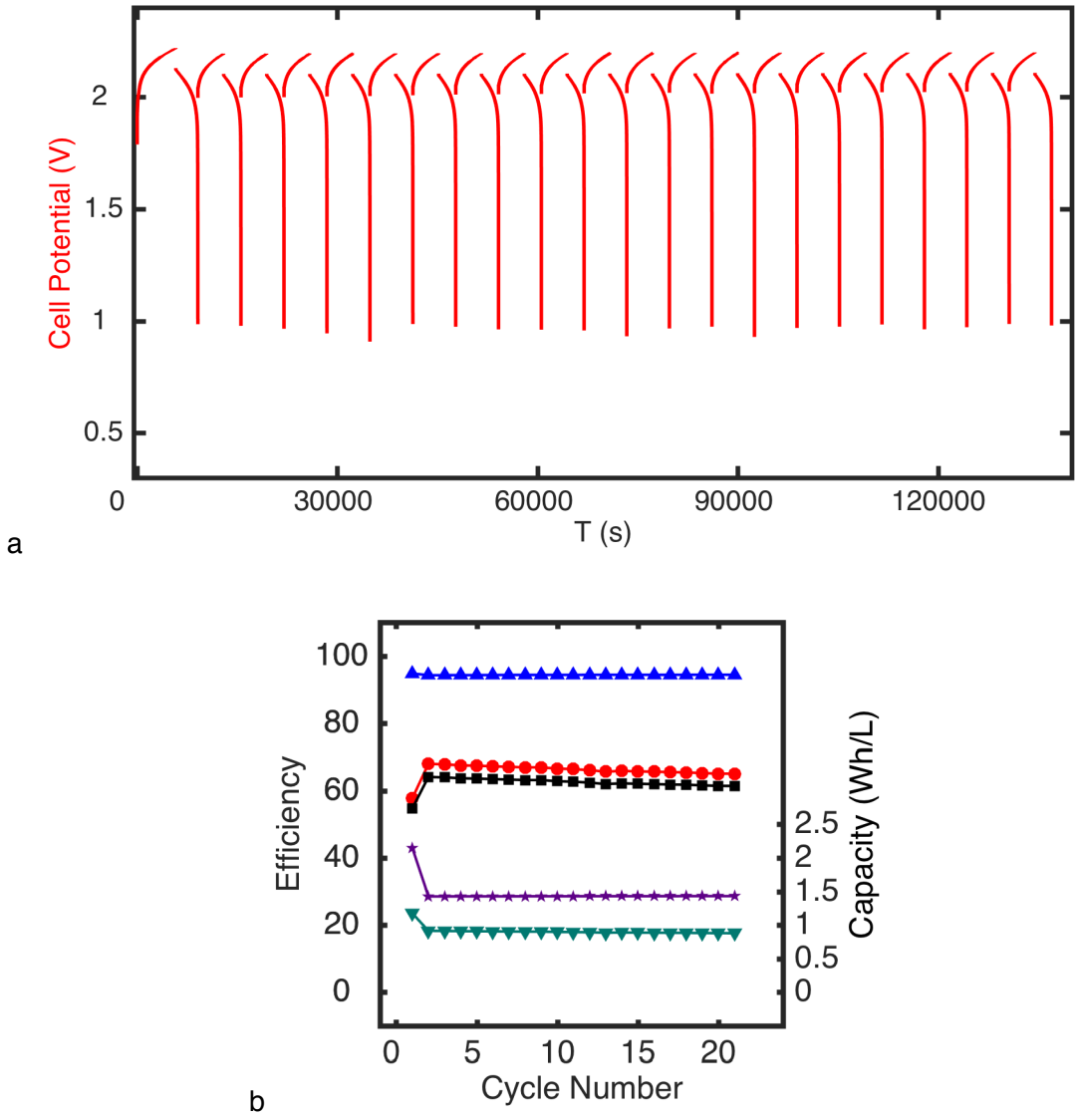

Figure 5.3. Galvanostatic charge-discharge cycling a) curves at 10 $mAcm^{-2}$ and 25 $mLmin^{-1}$ of 0.1 M $V(acac)_3$, 0.5 M $TEABF_4$ in ACN and b) performance: voltage efficiency (blue upward pointing triangles), coulombic efficiency (red circles), energy efficiency (black squares), energy capacity on charge (purple stars), energy capacity on discharge (green downward pointing triangles).

EIS data from before and after cycling, shown in Figure 5.4a-b, reveal little change in the impedance; the low-frequency response changes somewhat, likely because of the difference in OCP between the beginning and end of cycling. The bulk area-specific resistance (ASR), as determined by the intercept with the real axis, is

relatively constant before and after cycling: 4.6 Ωcm^2 and 4.5 Ωcm^2, respectively. A second ASR value, as determined by a semicircle fit to the high frequency data, is 8.1 Ωcm^2 before cycling and 7.4 Ωcm^2 after. The underlying source of this second ASR is unclear since an ASR of that magnitude at the current density applied in the cycling experiments would equate to voltage efficiencies below the 94% observed. Furthermore, control experiments lacking any redox-active solution components shown in Figure 5.4c exhibit the same high frequency behavior. This apparent semicircle results from the support solution and cell architecture, but does not provide information about redox-active species.

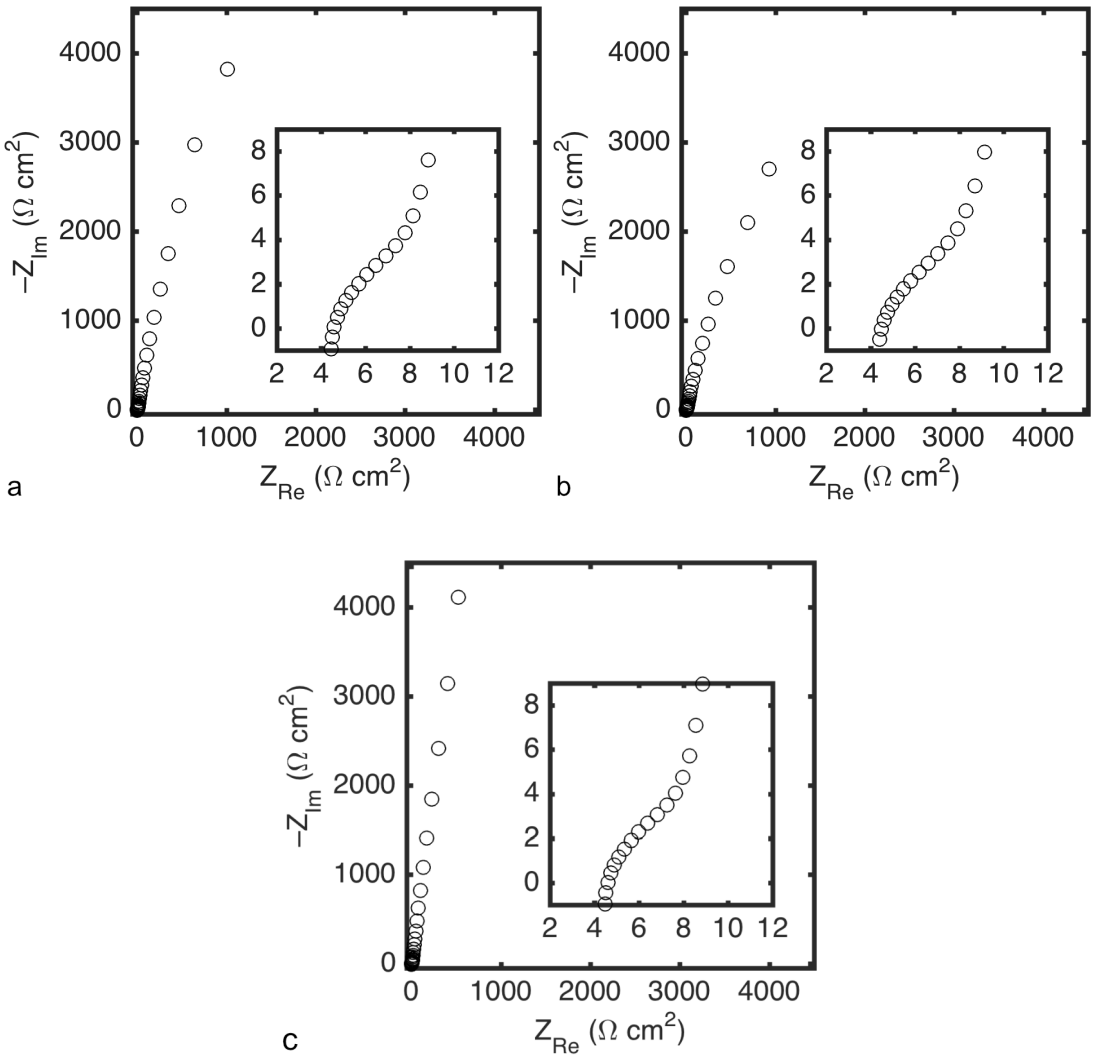

Figure 5.4. Nyquist plots from EIS experiments on flow cell with stagnant 0.1 M $V(acac)_3$, 0.5 M $TEABF_4$ in ACN battery solution a) before b) after charge-discharge testing c) and control experiment without any $V(acac)_3$. Insets show the system response at high frequencies.

Cyclic voltammetry of the electrolyte before and after charge-discharge testing, included in Figure 5.5a-b, shows that the redox behavior after cycling is similar to that of the pristine solution: the reduction and oxidation peaks still dominate at –1.79 and 0.41 V *vs.* Ag/Ag^+.[66] Some small differences are observable after the 21st cycle. The cycled negolyte delivers smaller peak heights for the reduction couple and the reduction peak of that couple is shifted more negatively. The cycled posolyte shows evidence of an extremely dilute $VO(acac)_2$ couple centered at 0.71 V vs. Ag/Ag^+, as well as a

similarly minute oxidative peak at –1.03 V vs. Ag/Ag^+, which has been observed in systems with added acetylacetone.[135] These signatures are barely perceptible, however.

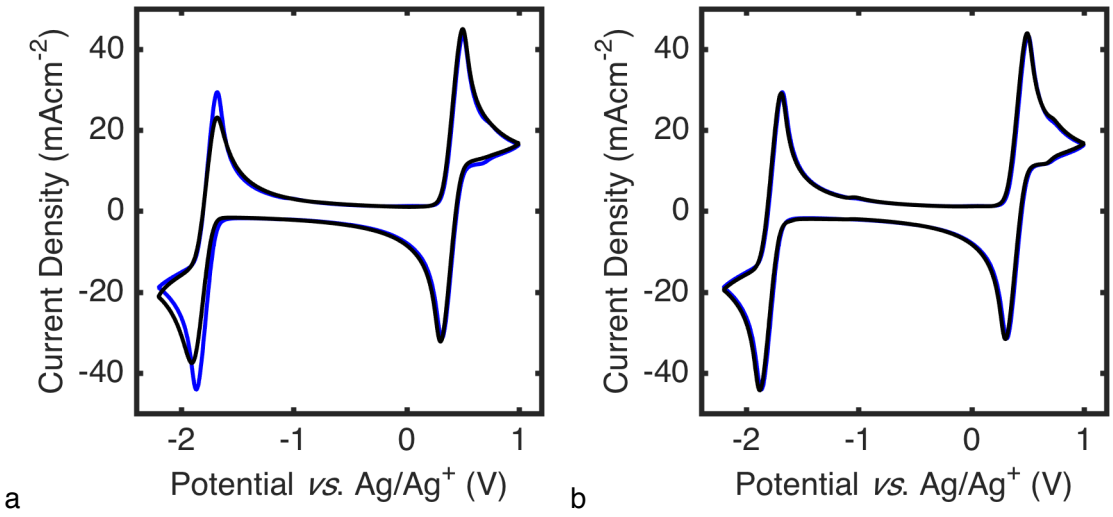

Figure 5.5. Cyclic voltammograms of pristine 0.1 M $V(acac)_3$, $TEABF_4$ in ACN (blue) and a) negolyte and b) posolyte after charge-discharge cycling (black), glassy carbon, 400 mVs^{-1}, 23 °C.

5.2.2 $V(acac)_3$ in DME

As demonstrated in Section 3.5, $V(acac)_3$ in DME could also be promising for a symmetric RFB. Cells using 0.01 M $V(acac)_3$, 0.5 M $TBABF_4$ in DME were run at a 2 $mAcm^{-2}$ current density (0.93 C) with a 25 $mLmin^{-1}$ flow rate, using the same theoretical SOC and voltage cutoffs. Run under these conditions, the cell shows average discharge capacity of 0.123 WhL^{-1} at average voltage and coulombic efficiencies of 90% each over the 21 cycles shown in Figure 5.6. The average discharge capacity comes from cycle capacities that rise from 0.120 WhL^{-1} on the third cycle to 0.125 WhL^{-1} by the 21st cycle. Similarly, efficiencies drift over the course of cycling: upward for coulombic efficiency, from 87% in the third cycle to 93% in the 21st, and downward for voltage efficiency, from 92 % in the third cycle to 84% in the 21st. This behavior can be seen from the charge-discharge curves presented in Figure 5.6a by comparing the

shape of data from the last cycle to early cycles. The average cell discharge voltage is 2.10 V compared to the 2.01 V observed in the ACN experiments, reaffirming the DME system's increased OCP observed in voltammograms from Figure 3.10. Similar to ACN experiments, these experimental conditions avoid the use of stringent voltage cutoffs described in previous reports.

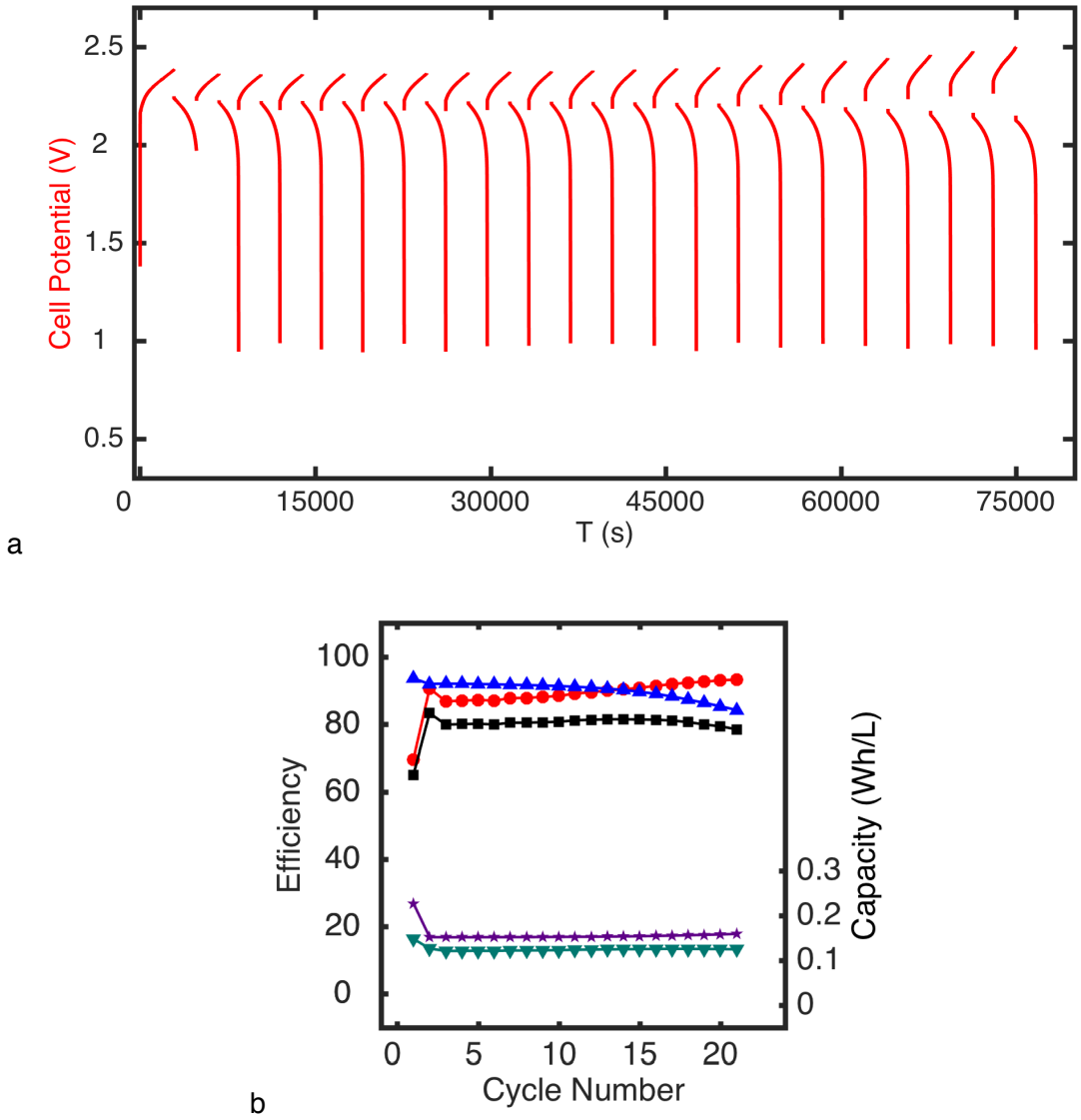

Figure 5.6. Galvanostatic charge-discharge cycling a) curves at 2 $mAcm^{-2}$ and 25 $mLmin^{-1}$ of 0.01 M $V(acac)_3$, 0.5 M $TBABF_4$ in DME and b) performance: voltage efficiency (blue upward pointing triangles), coulombic efficiency (red circles), energy efficiency (black squares), energy capacity on charge (purple stars), energy capacity on discharge (green downward pointing triangles).

Comparison of EIS from before and after cycling, shown in Figure 5.7a and 5.7b, respectively, may explain the observed shifts in efficiency behavior. The post-

cycling Nyquist plot reveals that the bulk ASR increases by 50% over the course of the test, growing from 20 Ωcm^2 before cycling to 31 Ωcm^2 after. A second ASR associated with the first semicircular feature at high frequencies has morphed from a proper semi-circle 18 Ωcm^2 in diameter to a depressed semicircle 50 Ωcm^2 in diameter. Both spectra, especially after cycling, suggest the presence of a second semicircular feature with characteristic ASRs of 330 Ωcm^2 before and 300 Ωcm^2 after cycling. These semi-circular features are also present in the control spectrum depicting EIS collected from a cell containing a solution without $V(acac)_3$ in Figure 5.7c. This is similar to EIS results for cells with ACN solvent and suggests that these features do not reflect properties of the redox-active material.

The increased bulk ASR indicates that extended exposure to DME battery solutions likely affects the performance of cell reactor components: the impervious graphite flow plates, porous separator, or carbon felt electrodes. A separator that becomes less porous, and therefore more resistive, would increase the ohmic overpotentials and slow active-species crossover, which could explain both the decreasing voltage efficiency and improving coulombic efficiency. Another possibility is that ASR increases because DME leaches material out of the ePTFE gaskets, which then adsorbs onto the felt electrodes to form a resistive layer. (Whereas soaking in ACN shows little observable effect on ePTFE, soaking in DME gives ePTFE a translucent appearance.) Regardless of the cause, an increasing bulk resistance helps explains the cycling behavior observed in the DME solvated system. Nonaqueous RFBs using DME may need further work to select reactor materials more resilient to the solvent.

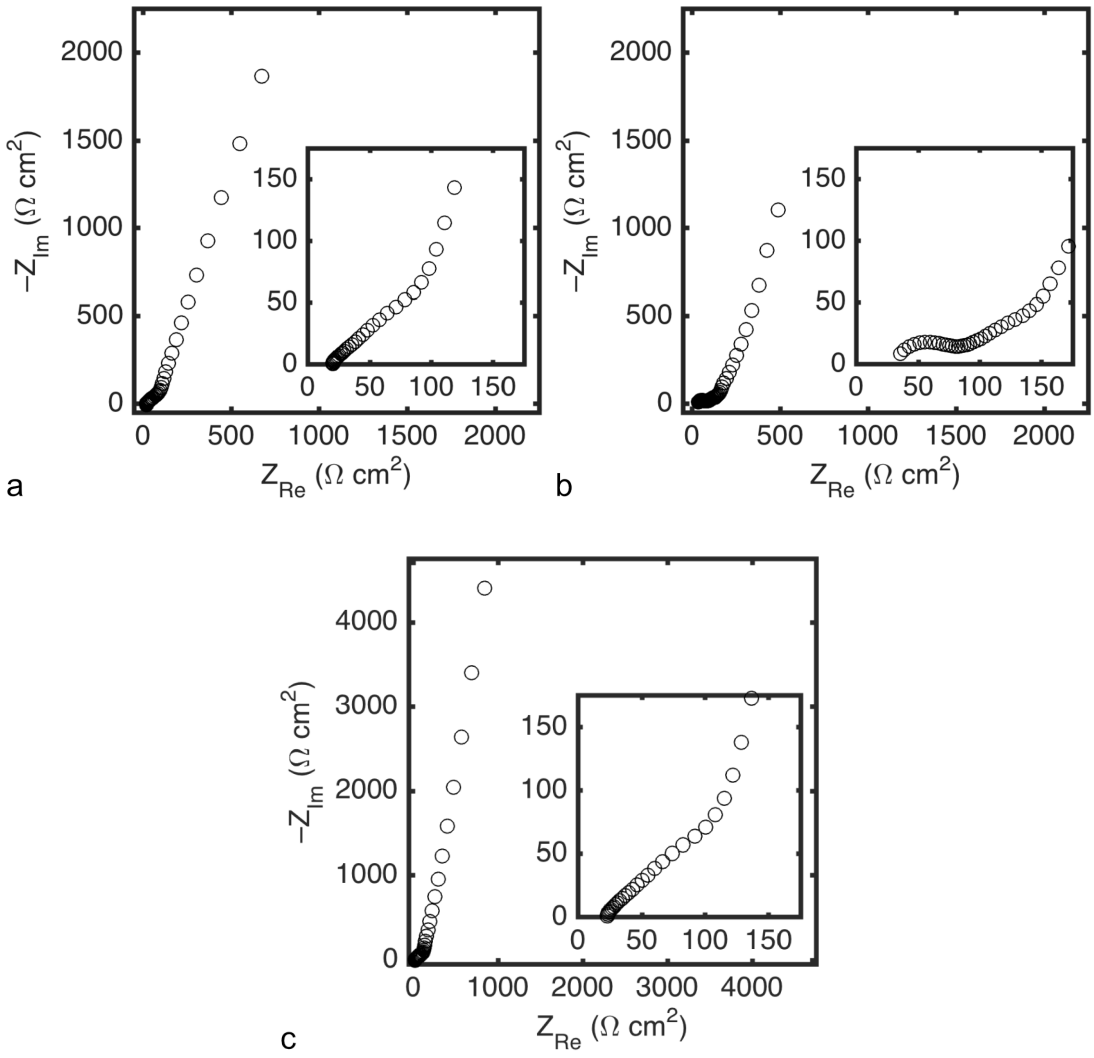

Figure 5.7. Nyquist plots from EIS experiments on flow cell with stagnant 0.01 M $V(acac)_3$, 0.5 M $TBABF_4$ in DME battery solution a) before b) after charge-discharge testing c) and control experiment without any $V(acac)_3$. Insets show the system response at high frequencies.

Cyclic voltammetry of the cycled negolyte and posolyte in Figure 5.8 reveal the same major peaks as the pristine electrolyte observed in Figure 3.10, except both are shifted negatively by 195 mV. The cycled electrolytes also exhibit minor voltammetric behavior inconsistent with the pristine solution. The cycled negolyte shows a dilute couple centered at – 0.14 V *vs*. Ag/Ag^+, which has not been observed in other degradation studies. The cycled posolyte reveals the appearance of a $VO(acac)_2$ couple centered at 0.67 V *vs*. Ag/Ag^+ and a very dilute couple at –1.22 V *vs*. Ag/Ag^+, which has been observed in systems with oxygenated solutions.[135] A small increase in current

density above the capacitive baseline from 0 to 0.5 V *vs*. Ag/Ag^+ appears after cycling, which is consistent with redox behavior of oxygenated solutions. Two possible sources of oxygen in this chemistry are from acetylacetonate ligands and DME solvent. Since oxygenation signatures do not appear in the ACN experiments, which have acetylacetonate as a possible oxygen source, but not an oxygen-containing solvent, DME may act as an oxygen source in these systems. High voltage systems sensitive to oxygen impurity may need to avoid solvents containing oxygen groups that can degrade during operation.

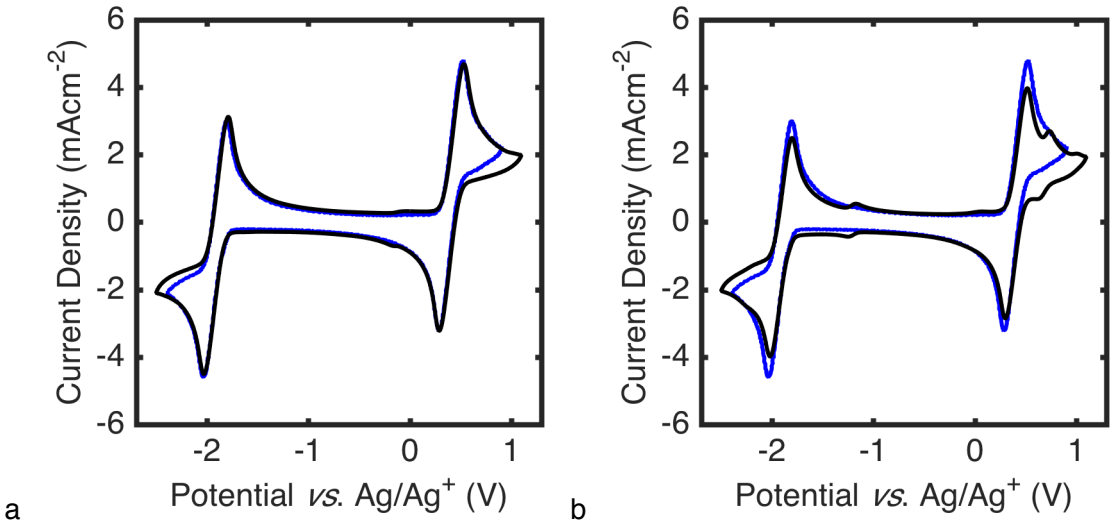

Figure 5.8. Cyclic voltammograms of pristine 0.01 M $V(acac)_3$, $TBABF_4$ in DME (blue, potentials shifted negatively 195 mV and currents increased 9%) and a) negolyte and b) posolyte after charge-discharge cycling (black), glassy carbon, 400 mVs^{-1}, 23 °C.

5.3 Organic Active Species

5.3.1 DPA in DME

Delivering highly cyclable symmetric nonaqueous $V(acac)_3$ experiments in the custom flow cell verified the informative nature of experiments using this design and allowed examination of the organic active species synthesized and studied in Chapter 4.

Since these metal-free chemistries show the best solubilities in DME, cells run with that solvent are examined first and can be compared to the $V(acac)_3$ chemistry in the same supporting solution for reference. As a first step, a baseline DPA charge-discharge performance, shown in Figure 5.9, was established using a solution of 0.01 M DPA, 0.5 M $TBABF_4$ in DME run at 2 $mAcm^{-2}$ (0.93C) and a 25 $mLmin^{-1}$ flow rate. The first five charge cycles exhibit a voltage plateau between 3.1 – 3.4 V, but appreciable discharge capacity is only seen beginning with the second discharge. This lack of capacity on first discharge appears to be an exaggerated equivalent to the burn-in behavior observed on first cycles of the $V(acac)_3$ cells. Subsequent discharges deliver appreciable capacities around 3 V, but the coulombic efficiency hovers around 50%. After these initial cycles, charging begins to access a second plateau at 3.5 V, which corresponds to discharge capacity observed at 2.1 V and shrinking capacity at the 3 V plateau. Coulombic efficiency of the cells stabilizes at 52% over the last ten cycles, while voltage efficiency drops from a high of 85% on the 5th cycle to 69% by the 21st, corresponding to slowly dropping energy efficiencies. Discharge capacity stays above 0.08 WhL^{-1} through the later cycles, although it slowly decreases. This capacity is comparable to that observed in the $V(acac)_3$ system at the same concentration in DME and highlights the benefit of high-voltage systems: even at lower efficiencies, the higher-voltage organic active species offer the same energy density.

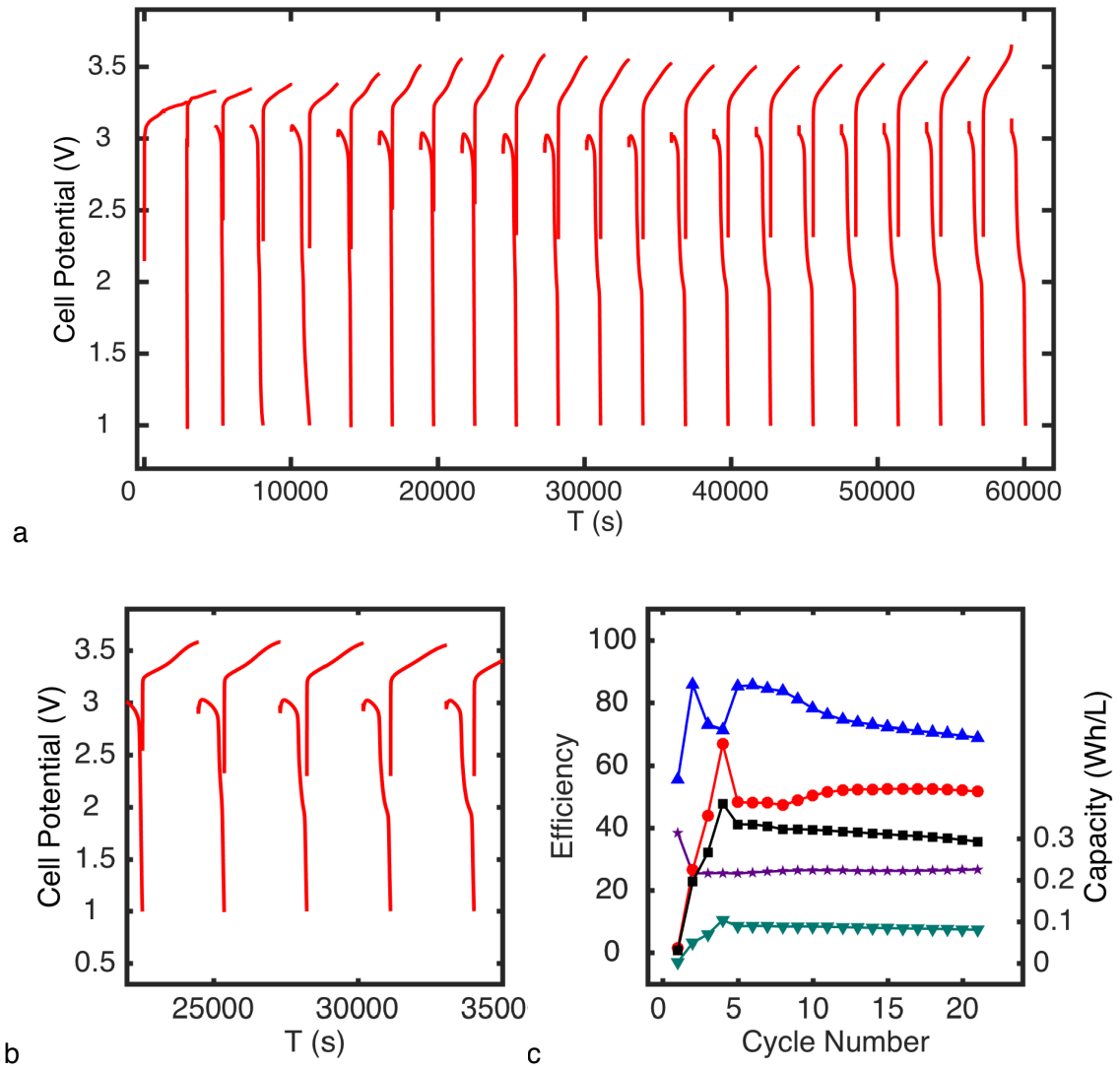

Figure 5.9. Galvanostatic charge-discharge cycling a,b) curves at 2 mAcm^{-2} and 25 mLmin^{-1} of 0.01 M DPA, 0.5 M TBABF$_4$ inDME and c) performance: voltage efficiency (blue upward pointing triangles), coulombic efficiency (red circles), energy efficiency (black squares), energy capacity on charge (purple stars), energy capacity on discharge (green downward pointing triangles).

During cycling the negolyte solution changed from clear pale yellow color to dark, vivid blue. Upon completion of cycling a uniform black deposit was observed on the negolyte tubing and the solution color had become pale brown. This deposit was studied using SEM and EDS, the results of which are shown in Figure 5.10, to better understand its composition and morphology. EDS reveals the deposition of a carbon-containing film within the surface roughness of the PTFE tubing's inner circumference: the PTFE tubing shows fluorine content in EDS, but a film formed from active species or solvent would not. A simple estimate can be made using parameters from the system

components and SEM results: the apparatus contains 30 cm of 4 mm ID pump-head tubing and 210 cm of 1.6 mm ID tubing; the surface roughness region is 33 μm thick with a 0.4 void fraction; and the density of the deposit is likely similar to LDPE at 0.9 g/cm^3. If a film filled the roughness over the entire length of tubing, this would represent 0.167 grams of material, compared to the 0.165 grams of DPA initially dissolved in the 50 mL sample of electrolyte solution. This surface-film formation by the active complex could provide at least one explanation for poor cyclability, capacity fade, and exaggerated burn-in on initial cycles.

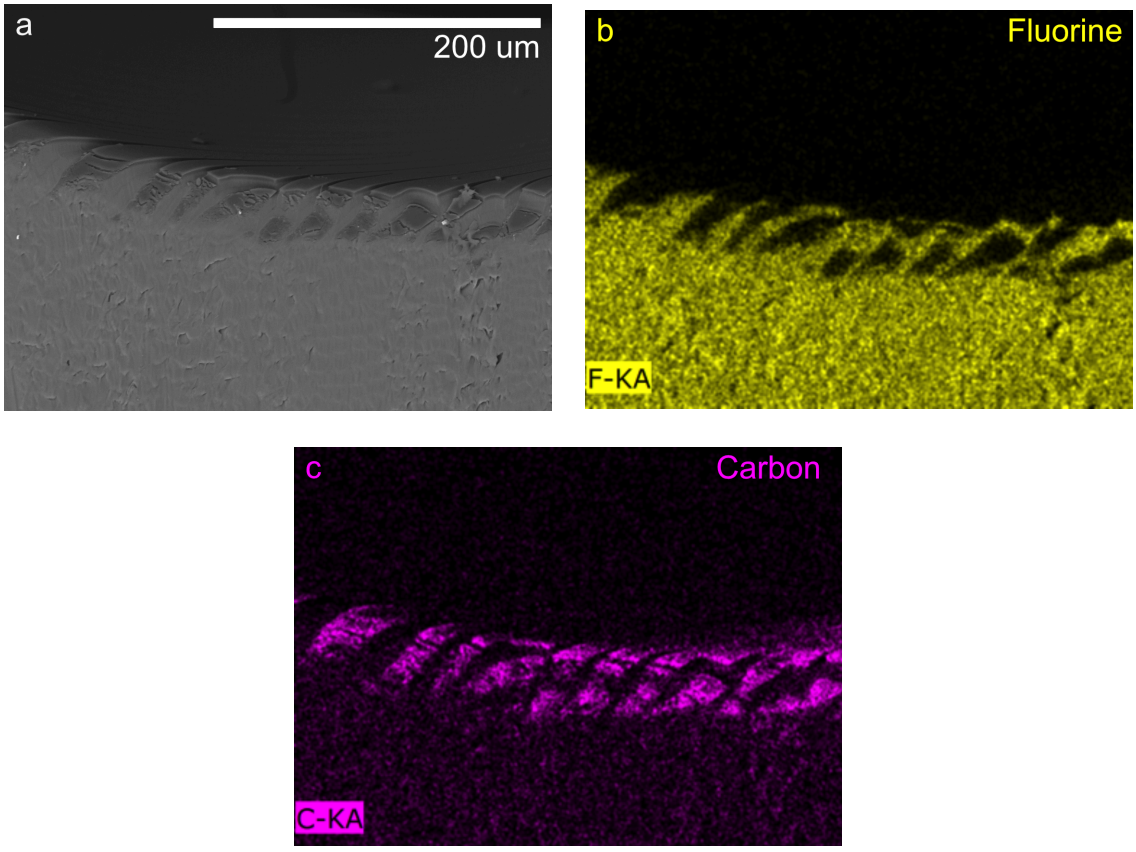

Figure 5.10. Cross-section of 0.01 M DPA, 0.5 M $TBABF_4$ in DME negolyte tubing inner circumference after cycling a) SEM micrograph in 'Analytical' mode and EDS spectra for b) fluorine content and c) carbon content.

The pre-cycling EIS results are similar to those observed in the $V(acac)_3$ system, especially at higher frequencies shown in the inset of Figure 5.11. Compared to the $V(acac)_3$ system, the DPA in DME cell shows higher impedance at low frequencies, but

exhibits similar high-frequency behavior: a bulk ASR of 23 Ωcm^2, a first semicircle indicating an ASR of 26 Ωcm^2, and a second semicircle indicating 300 Ωcm^2. After cycling the DPA cell branches away from the EIS behavior of its $V(acac)_3$ counterpart. The bulk ASR increases to 37 Ωcm^2, the second ASR remains relatively constant at 27 Ωcm^2, but now corresponds to a depressed semicircle, and the third apparent ASR is 130 Ωcm^2, also from a depressed semicircle. This indicates that the DME solution still increases bulk ASR in the system, but that the phenomena associated with second and third ASRs are becoming less resistive. Since these ASRs also arise in reactors without active-species, it is unclear what physical phenomena within a reactor cycled with active battery solutions can contribute to the changes in these two features.

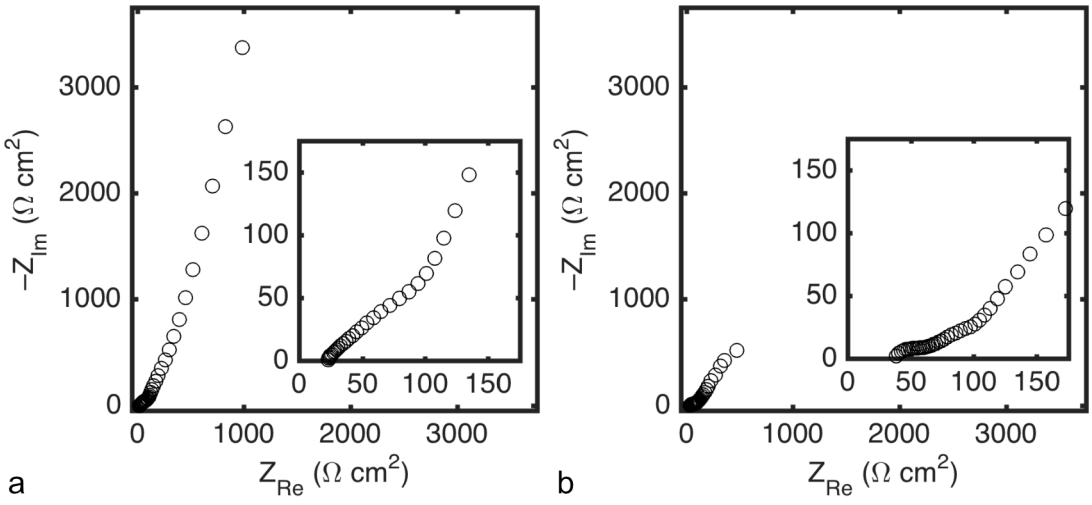

Figure 5.11. Nyquist plots from EIS experiments on flow cell with stagnant 0.01 M DPA, 0.5 M $TBABF_4$ in DME battery solution a) before and b) after charge-discharge testing. Insets show system response at high frequencies.

Finally, voltammetry of the cycled DPA in DME solutions shows redox activity that clearly indicates the presence of degradation products. The cycled negolyte voltammogram shown in Figure 5.12a reveals new peaks inconsistent with the pristine solution: dilute, lone reduction peaks at –1.43 V and – 1.86 V, a dilute couple centered a 0.26 V, and an apparently lone oxidation peak at 0.74 V, all *vs*. Ag/Ag^+. Two reversible redox couples are still present, but the reduction couple now occurs at –2.30 V

compared to –2.23 V *vs*. Ag/Ag^+ in the pristine solution. The cycled posolyte in Figure 5.12b also shows signs of degradation: similar dilute lone reduction peaks at –1.46 V and –1.81 V, and two new peaks at –0.34 and –0.07 V, all *vs*. Ag/Ag^+. Both redox couples that were intended to comprise the cell reaction look less chemically reversible; the oxidation peak of the reduction couple is mostly absent and the oxidation couple seems swamped by broader redox activity in the area, likely consistent with the lone oxidation peak at 0.74 V *vs*. Ag/Ag^+ in the negolyte. The degradation mechanisms that result in this diverse redox activity need to be inspected further.

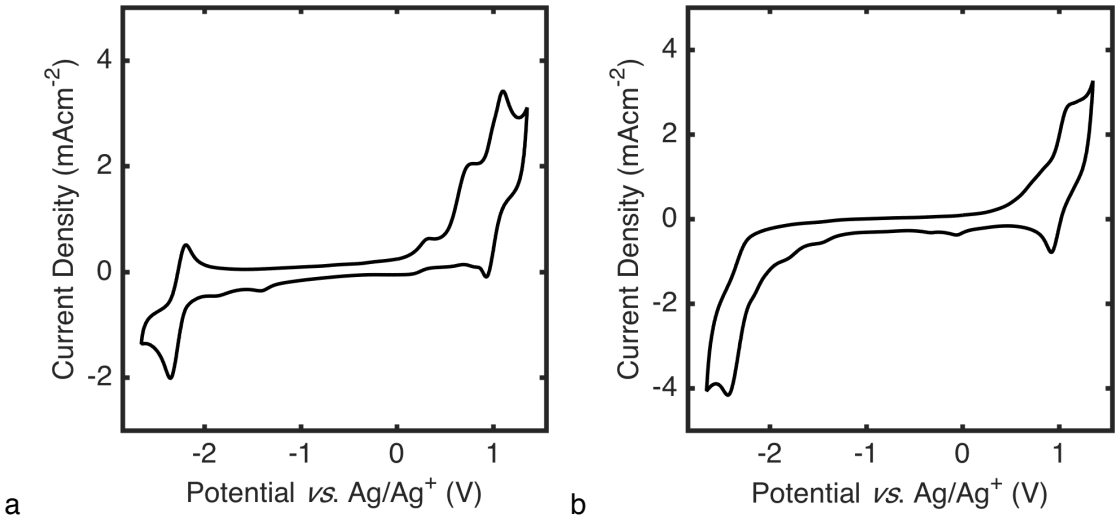

Figure 5.12. Cyclic voltammograms of 0.01 M DPA, 0.5 M $TBABF_4$ in DME a) negolyte and b) posolyte after charge-discharge cycling, glassy carbon, 400 mVs^{-1}, 23 °C.

5.3.2 DdPA in DME

The same charge-discharge cycling procedure was run with a solution of 0.01 M DdPA in place of DPA or $V(acac)_3$; results are shown in Figure 5.13. Initial cycles charge between 3 - 3.1 V, but an appreciable discharge capacity delivering as high as 2.9 V appears only after the third cycle. Beginning in the fifth cycle, as shown in Figure 5.13b, charging periods access a second voltage plateau near 3.6 V, which is

accompanied by the slow disappearance of the discharging plateau at 2.9 V and the appearance of discharge capacity at 1.1 V. Similar to experiments run with DPA, coulombic efficiency stabilizes in later cycles, which exhibit both voltage plateaus, although this efficiency begins to decrease in the last few cycles. Voltage efficiency drifts lower than in the DPA experiments, from 74% in the fifth cycle to 38% in the 21st, as expected by the second charging plateau occurring at 3.6 V and corresponding to a discharging plateau at 1.1 V. Discharge capacity for the DdPA system drops to 0.04 WhL^{-1} with cycling, half the energy density of the DPA cycling experiments.

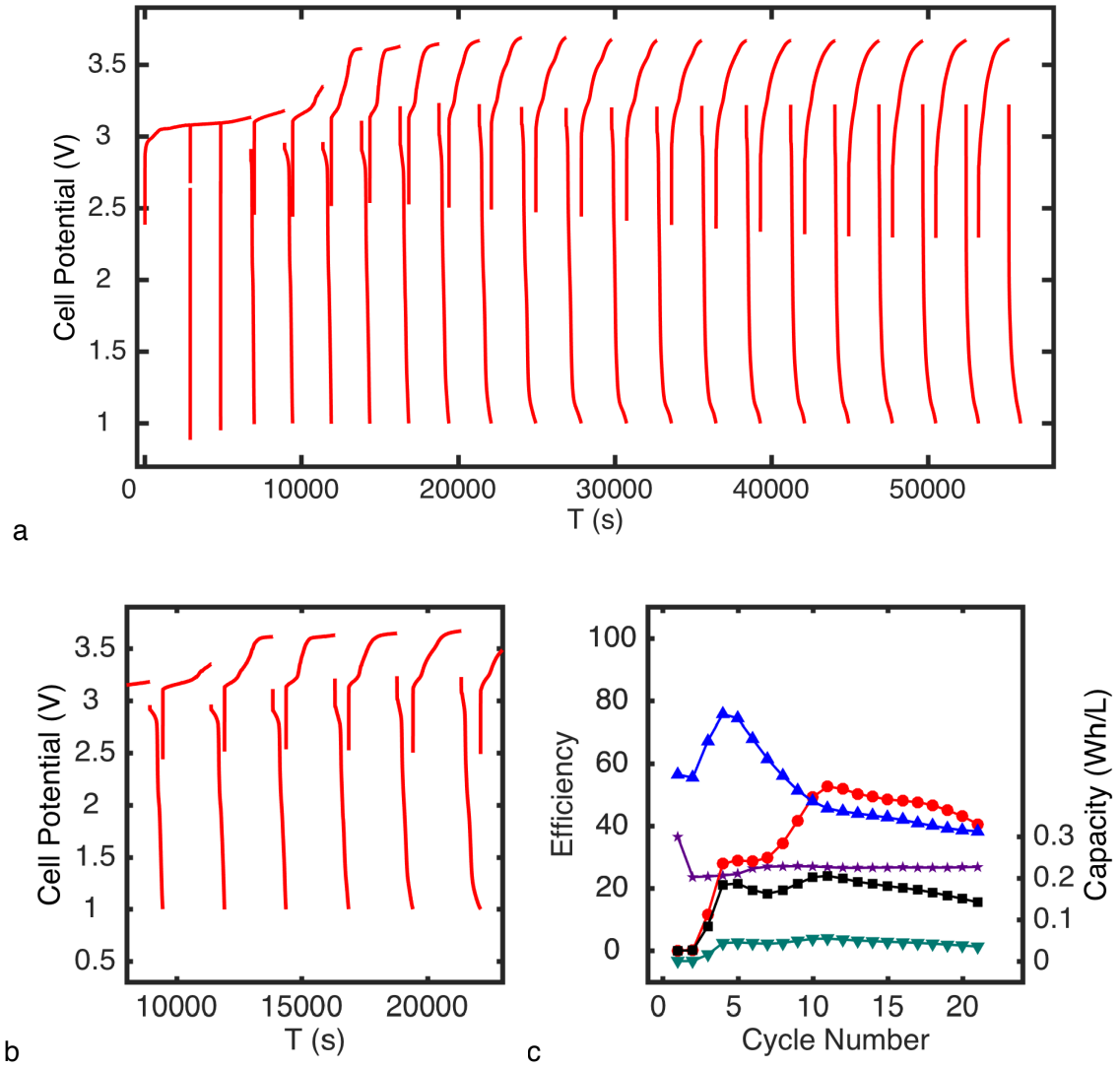

Figure 5.13. Galvanostatic charge-discharge cycling a,b) curves at 2 mAcm^{-2} and 25 mLmin^{-1} of 0.01 M DdPA, 0.5 M TBABF$_4$ in DME and c) performance: voltage efficiency (blue upward pointing triangles), coulombic efficiency (red circles), energy efficiency (black squares), energy capacity on charge (purple stars), energy capacity on discharge (green downward pointing triangles).

During the first cycle, the negolyte solution changes color from pale yellow to pale orange-pink after 400 seconds and to deep magenta after 1000 seconds. As cycling progresses further, this color shifts from deep magenta to brown upon completion of cycling. The posolyte solution changes from pale yellow to greenish yellow by the end of the first cycle and more intense green in subsequent cycles, before progressing to brown at the end of cycling. After disassembly it became clear that a black film had again deposited on the negolyte tubing surface (and that the solution was now brown)

similar to the DPA experiments. SEM and EDS analysis of this film is discussed in the concentrated DdPA in DME degradation analysis.

The pre-cycling EIS results agree with the $V(acac)_3$ and DPA comparators, especially at high frequencies, for which the Nyquist plot is shown in the inset of Figure 5.14a. The high frequency results indicate three characteristic resistances: a bulk ASR of 24 Ωcm^2, an ASR of 27 Ωcm^2 from the first semicircle, and 430 Ωcm^2 from the second. Lower frequencies show higher impedances, which increasingly stem from real values. Upon completion of cycling, EIS of the DdPA cell reveals similar drops in low-frequency impedance as seen with DPA. More so than DPA, the low frequency response has shifted away from a 90° phase angle, corresponding to capacitive behavior, to 45°, which is associated with diffusion processes. Impedance at high frequencies in the inset of Figure 5.14b deviate from the behaviors observed with both $V(acac)_3$ and DPA: the bulk ASR remains relatively constant at 25 Ωcm^2, the second ASR, still from a semi-circle drops to 21 Ωcm^2, and the third ASR, from a depressed semi-circle shrinks, similar to observations with the DPA cell, to 220 Ωcm^2.

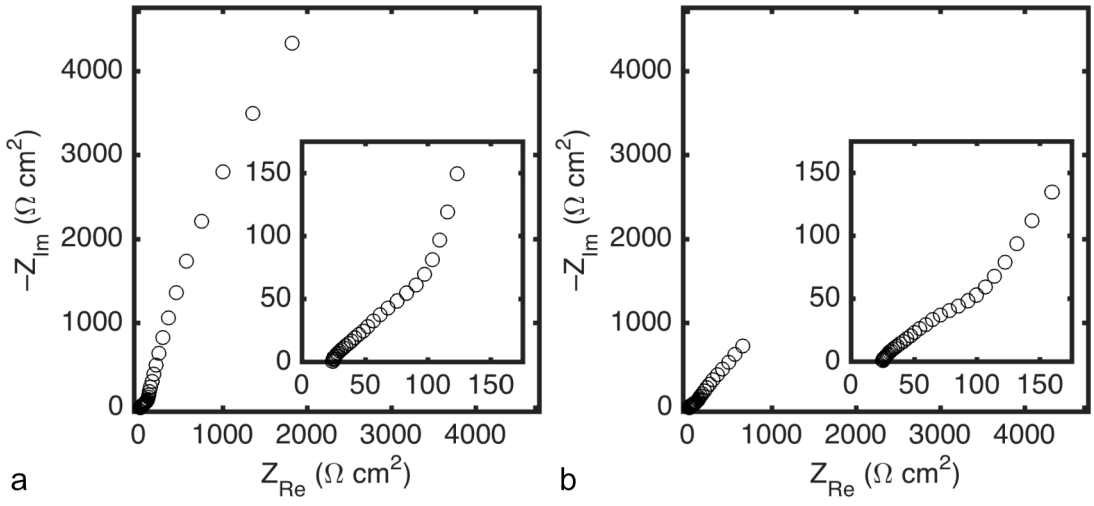

Figure 5.14. Nyquist plots from EIS experiments on flow cell with stagnant 0.01 M DdPA, 0.5 M $TBABF_4$ in DME battery solution a) before and b) after charge-discharge testing. Insets show the system response at high frequencies.

Voltammetry of the cycled DdPA in DME solutions show additional redox activity that indicates degradation. The voltammogram of the cycled negolyte shown in Figure 5.15a reveals two new redox couples with similar peak magnitudes at –2.11 V and another slightly more negative at –2.32 V *vs*. Ag/Ag^+. Another large reduction peak is observed at –2.78 V *vs*. Ag/Ag^+, which has no clear oxidation peak associated with it. All signs of the reversible oxidation reaction have disappeared and new reactions appear: an apparently lone oxidation peak at 0.66 V and another slight, lone oxidation shoulder at 1.00 V *vs*. Ag/Ag^+ before irreversible side reactions begin. The voltammogram of the cycled posolyte in Figure 5.15b also shows some additional activity compared to the pristine battery solution: a lone oxidation peak appears at –1.25 *vs*. Ag/Ag^+ and an oxidation shoulder occurs at 1.36 V *vs*. Ag/Ag^+ before irreversible side reactions begin. Neither the negolyte nor the posolyte retains a voltammetric response that suggest utility for a symmetric RFB.

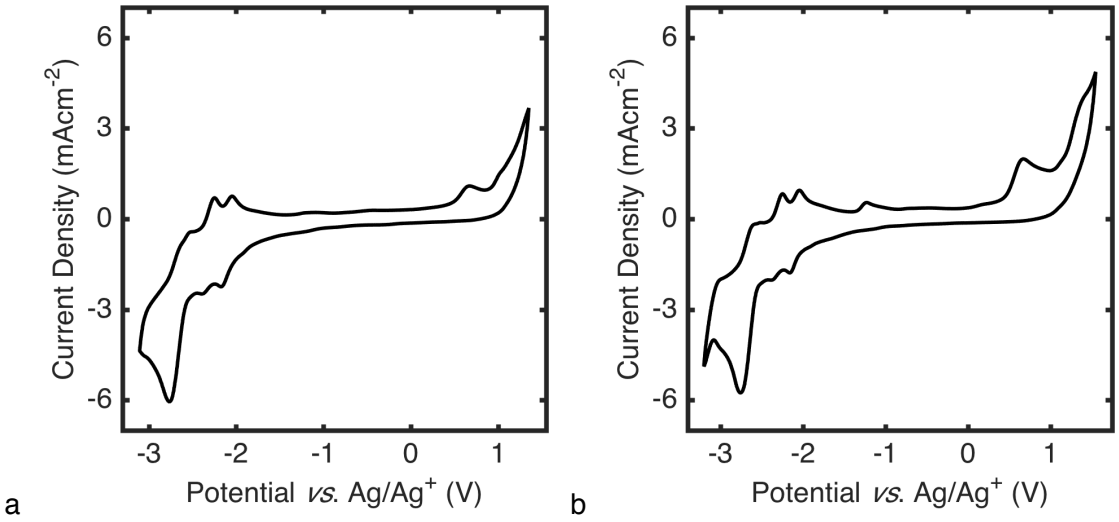

Figure 5.15. Cyclic voltammograms of 0.01 M DdPA, 0.5 M $TBABF_4$ in DME a) negolyte and b) posolyte after charge-discharge cycling, glassy carbon, 400 mVs^{-1}, 23 °C.

Cycling of a more concentrated solution of DdPA in DME solution, made possible by the significantly improved solubility of DdPA in DME and a synthetic procedure improved to allow larger-scale production, was also performed. The cycling

experiment, shown in Figure 5.16, uses a solution of 0.075 M DPA, 0.5 M $TBABF_4$ in DME run at 5 $mAcm^{-2}$ (0.47 C) and a 25 $mLmin^{-1}$ flow rate. The higher current density completes the experiment on a timescale less susceptible to small differences in pump calibration, which can lead to reservoir imbalances during long experiments. Similar to low-concentration experiments, the initial cycles charge at a voltage plateau between 3.1V and 3.4 V. The higher-concentration experiments deliver discharge capacity on the first cycles, however, as Figure 5.16b illustrates. This indicates that the lack of capacity during initial cycles in the dilute DdPA experiments arose from the low concentration and mass transport limitations on the dilute active species. The first discharge cycle shows voltage plateaus at 2.6 V and 2.1 V. The plateau at 2.6 V is slightly lower than the 2.9 V observed in the dilute solutions, but the increase in charging potentials is similar in magnitude and this agreement indicates that the higher rate applied to the concentration solution is responsible. This does not explain the presence of a second plateau, however. Subsequent cycles show reduced capacity at the 2.6 V plateau and the appearance of another discharge plateau at 1.1 V. Later cycles show a second charging plateau centered at 3.6 V, which eventually leads to repeated triggering of the 3.7 V potential cutoff with each charging cycle. Upon reaching this cutoff during charging, cell capacity dropped significantly since the charging step no longer delivered 50% theoretical SOC. Discharge capacities are stable around 0.22 WhL^{-1} before charging cycles begin consistently hitting the voltage cutoff, an almost six-fold increase from the low concentration experiments. This increase in magnitude scales roughly with concentration and suggests that concentration does not affect the reaction mechanism.

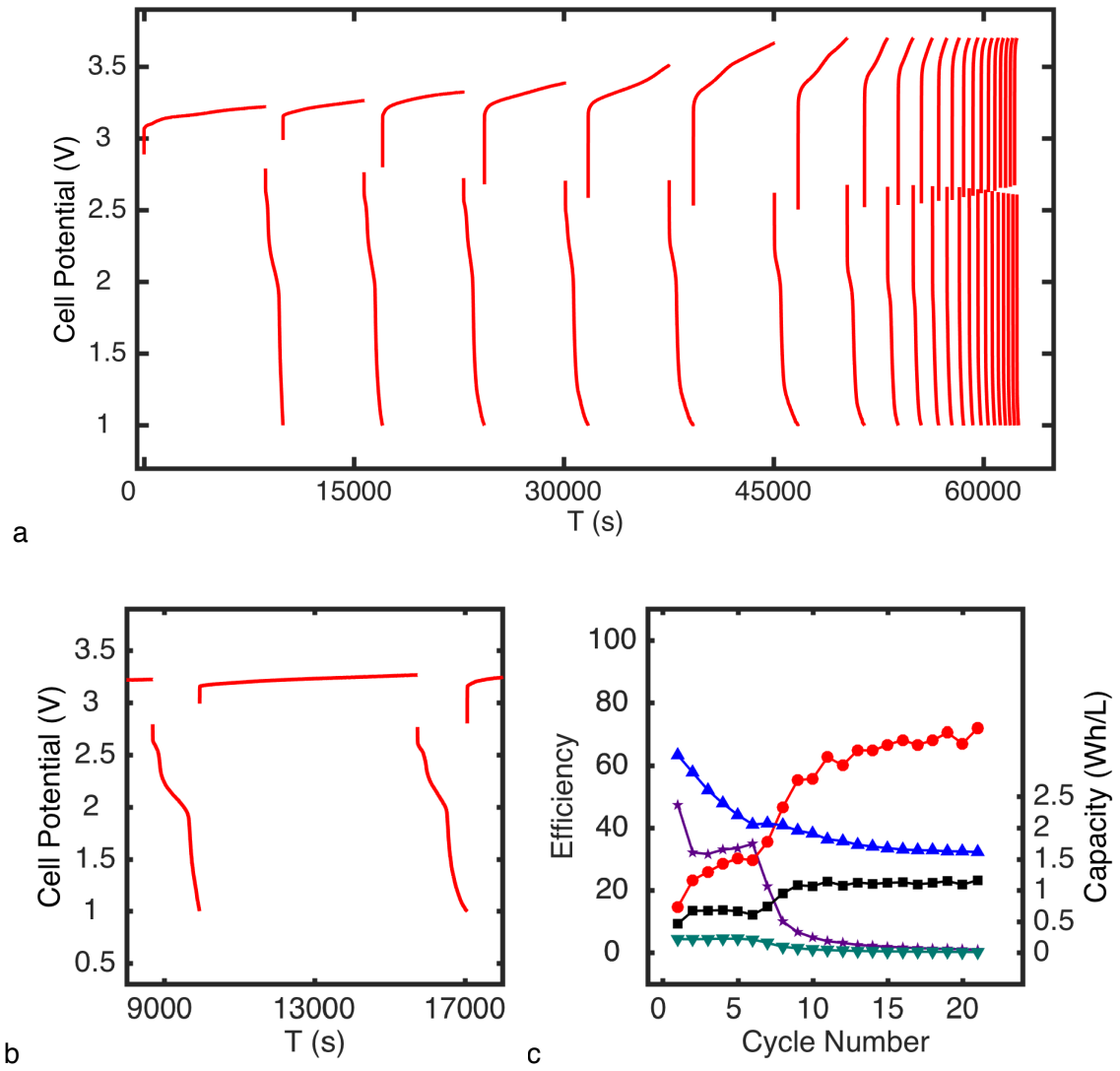

Figure 5.16. Galvanostatic charge-discharge cycling a,b) curves at 5 mAcm^{-2} and 25 mLmin^{-1} of 0.075 M DdPA, 0.5 M TBABF$_4$ in DME and c) performance: voltage efficiency (blue upward pointing triangles), coulombic efficiency (red circles), energy efficiency (black squares), energy capacity on charge (purple stars), energy capacity on discharge (green downward pointing triangles).

The progression of color change during the first charge is similar between the concentrated DdPA solution and the dilute DdPA solution. The negolyte changes from pale yellow to pale orange-pink to deep magenta. The posolyte changes from pale yellow to green and eventually to blue. As cycling progresses, the negolyte remains a deep magenta while the posolyte becomes a blue-green mixture. The retention of the electrolyte colors from the first cycle instead of an ultimate degradation to brown colors is attributed to the limited amount of current passed at cell voltages significantly above

the intended reaction potentials. Strict voltage controls may improve efficiency by preventing degradation, but will also lead to severe capacity fade as observed in the later cycles of this experiment.

Despite the relatively tight voltage limits at the higher current densities, a black film on the negolyte tubing was still visible to the naked eye. PTFE tubing from a different supplier was used for these experiments (Teflon-FEP, McMaster-Carr, USA), which avoided the rough surface present in the tubing used for the DPA experiments. SEM and EDS analysis shown in Figure 5.17 reveal a much thinner film, approximately 4 μm in thickness. This film represents only 0.015 grams of active material compared to the 2.2993 grams of organic DdPA active species dissolved in the negolyte solution. Thus, accumulation of active species on the tubing walls cannot explain the inefficiency of the DdPA system.

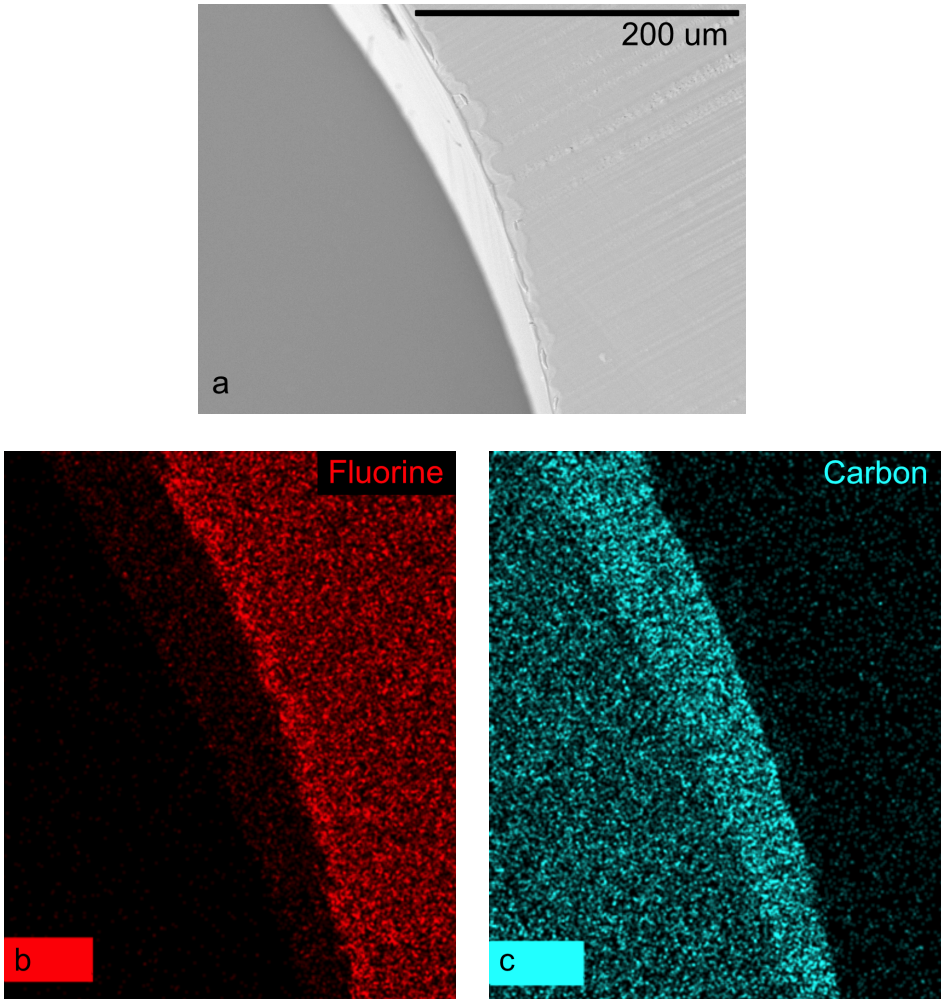

Figure 5.17. Cross-section of 0.075 M DdPA, 0.5 M $TBABF_4$ inDME negolyte tubing inner circumference after cyclinga) SEM micrograph in 'Analytical' mode and EDS spectra for b) fluorine content and c) carbon content.

EIS of the concentrated DdPA solution before cycling is similar to that of the pre-cycling dilute DdPA. Results at high frequencies, shown in the inset of Figure 5.18a, reveal three similar characteristic ASRs: a 23 Ωcm^2 bulk ASR, 28 Ωcm^2 from the first semicircle, and 400 Ωcm^2 from the second. If either semicircle arose from active species mass transfer, then the ASR would be expected to shrink when switching from the dilute to concentrated experiments because the more concentrated solutions would be expected to have larger permeability. Upon completion of cycling, EIS of the high-concentration DdPA, presented in Figure 5.18b, shows similarly shaped, more exaggerated changes to those observed between the two dilute DdPA spectra. The high-

frequency data reveal a bulk ASR increased to 44 Ωcm^2 and exhibit two depressed semicircles with ASRs of 14 Ωcm^2 and 85 Ωcm^2 for the first and second, respectively. Impedances at low frequencies dropped to even lower magnitudes than the dilute system and also approach a 45° phase, but appear erratic at the lowest applied frequencies.

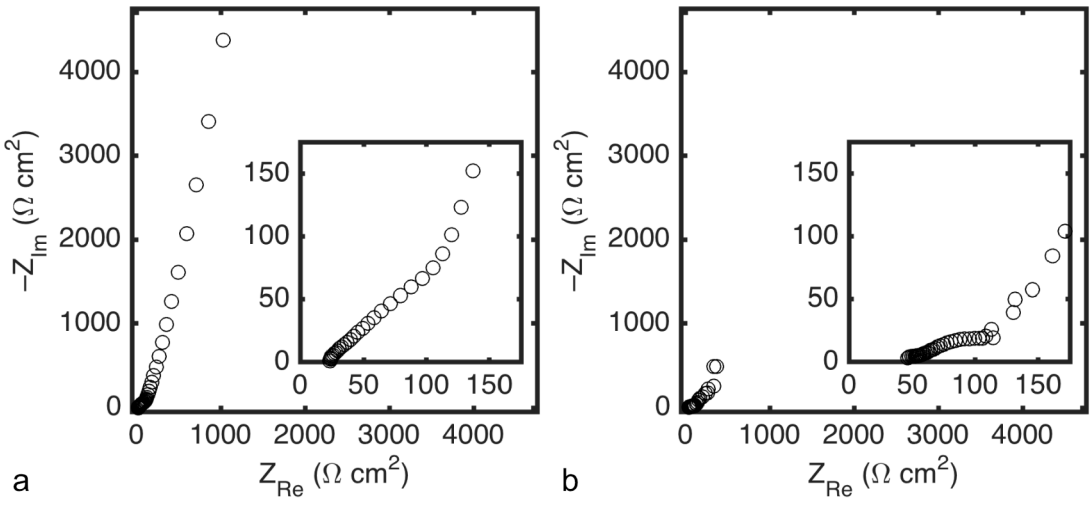

Figure 5.18. Nyquist plots from EIS experiments on flow cell with stagnant 0.075 M DdPA, 0.5 M $TBABF_4$ in DME battery solution a) before and b) after charge-discharge testing. Insets show the system response at high frequencies.

Voltammetry of the cycled concentrated DdPA in DME solutions show stark differences from the cycled dilute solutions. The voltammograms of the cycled negolyte shown in Figure 5.19a suggest a few redox events in early cycles: a lone reduction peak at –2.11 V and three clear oxidation peaks 0.10 V, 0.66 V and 1.08 V *vs.* Ag/Ag^+. This activity disappears with cycling, eventually stabilizing upon a voltammogram that shows little redox activity. The voltammogram of the cycled posolyte in Figure 5.19b, which appears to have lost the reversible reduction couple, still shows a reversible oxidation couple at 0.82 *vs*. Ag/Ag^+ after a small shoulder beginning at 0.37 V *vs*. Ag/Ag^+. Neither the negolyte nor the posolyte retain the voltammetric signatures of reversible activity for the reduction couple, which explains the decay in cycling performance, but the posolyte has retained reversible oxidation electrochemistry. This

suggests that decaying cell performance stems largely from the negolyte and its reduction couple. Further study of DdPA's degradation pathways will help understand this mechanism and provide strategies to combat it. These voltammetric results, paired with a stricter voltage cutoff suggest that stable cycling may be possible, especially for the positive couple.

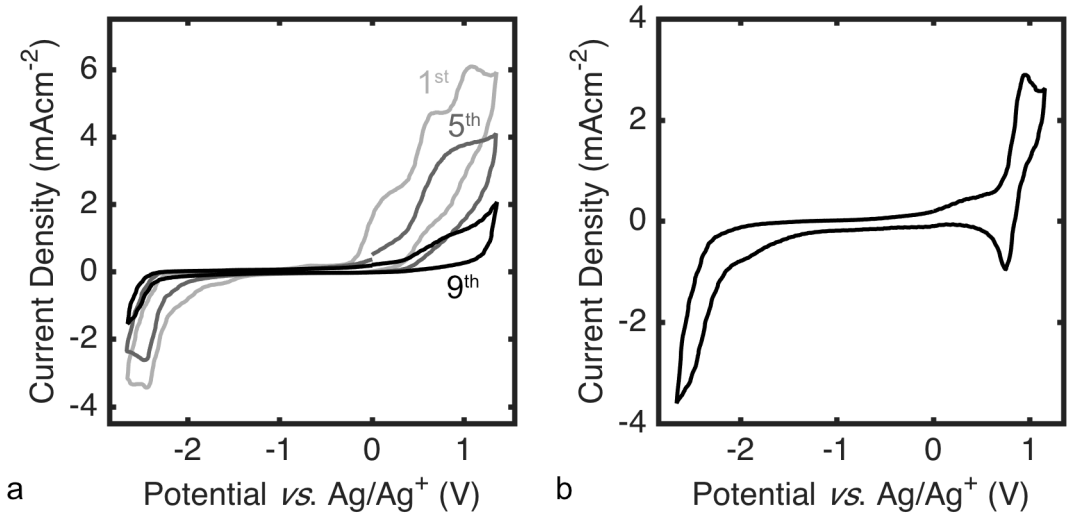

Figure 5.19. Cyclic voltammograms of 0.075 M DdPA, 0.5 M $TBABF_4$, in DME a) negolyte as it stabilized with cycling and b) posolyte (diluted to 0.15 M with solution of 0.5 M $TBABF_4$, DME) after charge-discharge cycling, glassy carbon, 400 mVs^{-1}, 23 °C.

5.3.3 DdPA in ACN

The improved solubility of DdPA in ACN also allowed charge-discharge cycling of dilute battery solutions in ACN, for which the results are shown in Figure 5.20. Using the same cycling procedure as the other low-concentration experiments, charge-discharge experiments were run with a solution of 0.01 M DdPA, 0.5 M $TBABF_4$ in ACN. The initial three cycles charged at a 3 V plateau before reaching a second plateau at 3.25 V. Discharge capacity is observable at 2.3 V only after the third cycle, when the charging reaches the second plateau, and the efficiencies during these cycles are low. Subsequent charging cycles accessed a third charging plateau at 3.45 V,

then another at 3.55 V, before hitting the 3.7 V cutoffs in later cycles. Upon accessing these third and fourth charging plateaus, discharge capacity presented at 1.8 V and 2.7 V, respectively. Once charging cycles began hitting the voltage cutoff, cell capacity dropped precipitously.

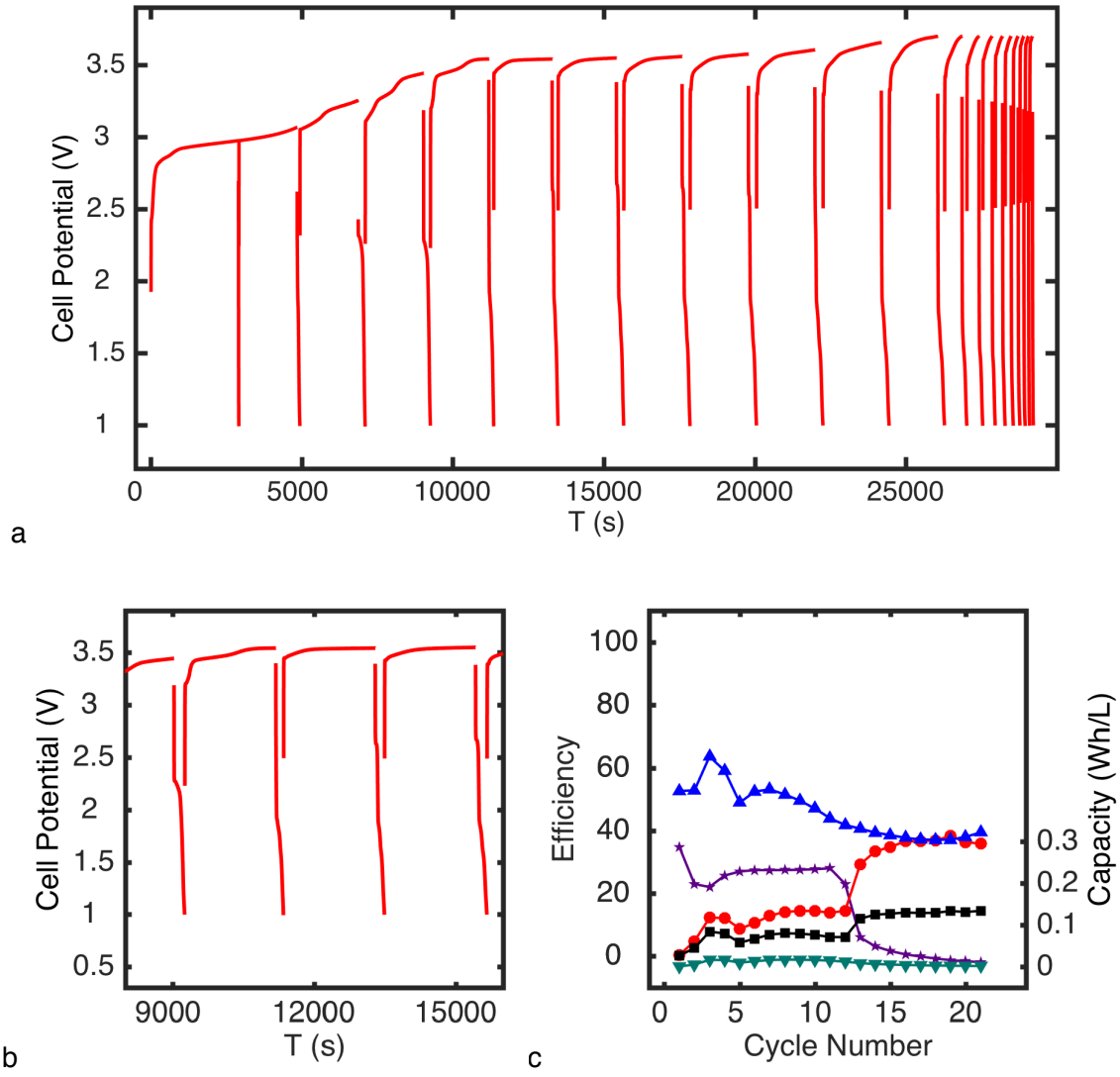

Figure 5.20. Galvanostatic charge-discharge cycling a,b) curves at 2 mAcm^{-2} and 25 mLmin^{-1} of 0.01 M DdPA, 0.5 M $TBABF_4$ in ACN and c) performance: voltage efficiency (blue upward pointing triangles), coulombic efficiency (red circles), energy efficiency (black squares), energy capacity on charge (purple stars), energy capacity on discharge (green downward pointing triangles).

Cycling in ACN brought on similar color changes as the DME cell. The negolyte changed from pale yellow to yellow-orange before reaching deep magenta. The posolyte changed from pale yellow to blue early in the first cycle, turning darker

blue with cycling, and eventually brown. Ultimately, the negolyte also became a brown solution and a light brown film could be seen on the negative tubing. Analysis with SEM and EDS (see Figure 5.21) did not show evidence of a significant film on the inner circumference of the tubing, however. Other degradation mechanisms must be responsible for the poor performance.

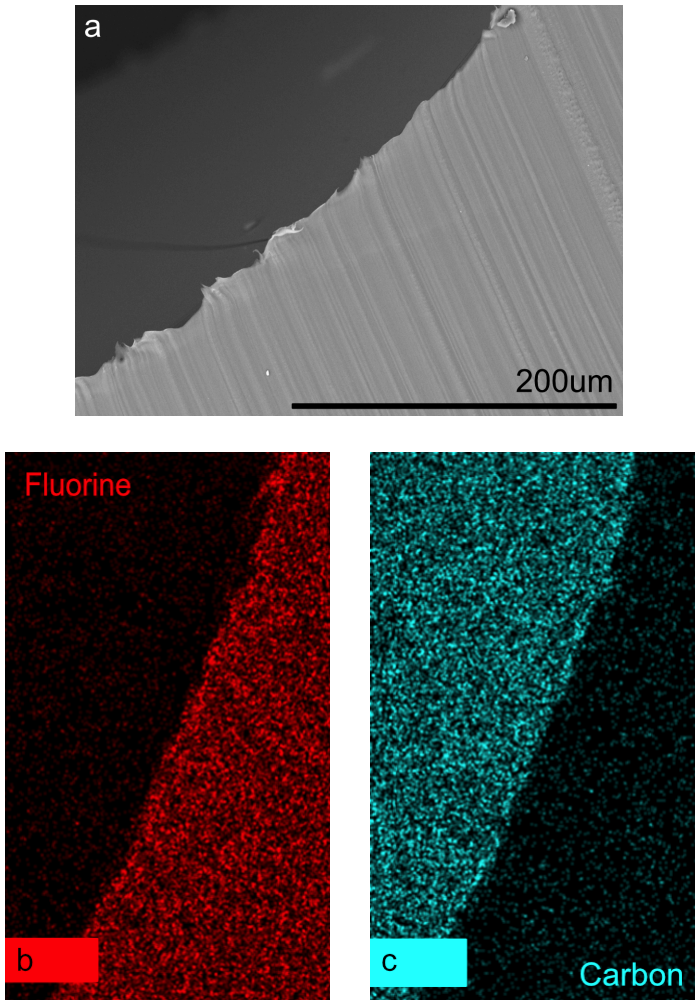

Figure 5.21. Cross-section of 0.075 M DdPA, 0.5 M $TBABF_4$ in ACN negolyte inner tubing circumference after cycling a) SEM micrograph in 'Analytical' mode and EDS spectra for b) fluorine content and c) carbon content.

EIS results for the DdPA in ACN before cycling, shown in Figure 5.22a, resemble the high concentration $V(acac)_3$ experiments in ACN due to the higher conductivity of the supporting solvent. While this experiment uses $TBABF_4$ as a support, instead of $TEABF_4$ used in the $V(acac)_3$ experiments, the bulk ASR is similar

at 5.0 Ωcm^2. A lone semicircle fit indicates another ASR of 8.5 Ωcm^2, similar with the $V(acac)_3$ experiments. After cycling, EIS, shown in Figure 5.22b, reveals changes similar to those observed after cycling in DME. Impedance at low frequencies drops significantly. The spectrum at high frequencies shows a bulk ASR that increases to 9.1 Ωcm^2, but an ASR from the first semicircle that maintains a similar magnitude of 7.6 Ωcm^2. Since $V(acac)_3$ in ACN shows no increase in bulk ASR with cycling, this increase can be attributed to the DdPA active material and is consistent with the experiments run in DME solutions.

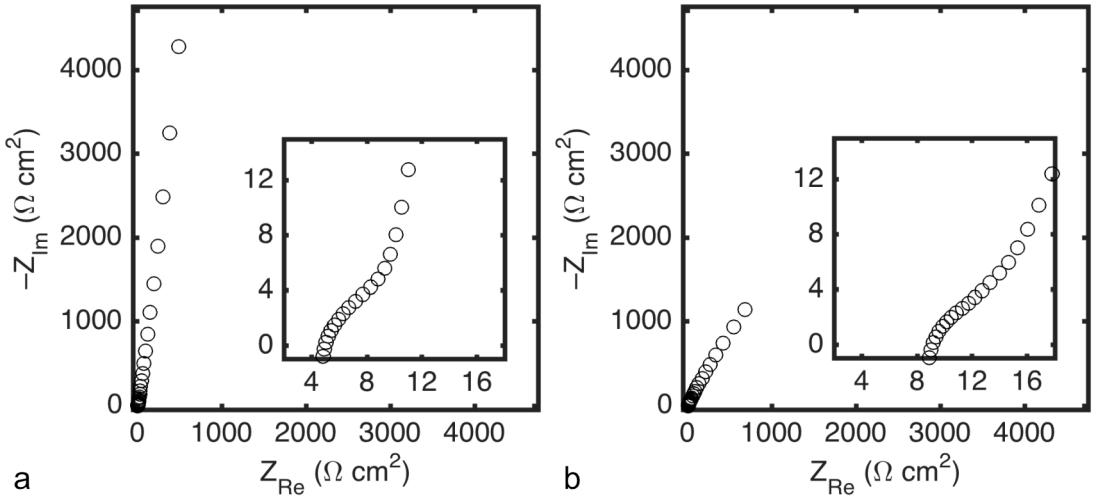

Figure 5.22. Nyquist plots from EIS experiments on flow cell with stagnant 0.01 M DdPA, 0.5 M $TBABF_4$ in ACN battery solution a) before and b) after charge-discharge testing. Insets show the system response at high frequencies.

Voltammetry of the DdPA in ACN solutions clearly revealed degradation, illustrated by the absence of the original, promising redox activity. The cycled negolyte shown in Figure 5.23a reveals only a lone reduction peak at –2.22 V *vs.* Ag/Ag^+ along with one oxidation shoulder at 0.26 V *vs.* Ag/Ag^+ and indistinct unpaired oxidation activity from 0.5 to 1.35 V *vs*. Ag/Ag^+. All signs of the reversible reactions are gone. The cycled posolyte in Figure 5.23b shows voltammetry more consistent with the starting material. While the reduction couple disappeared, replaced with two lone reduction peaks at –1.32 vs. Ag/Ag^+ and –2.30 V vs. Ag/Ag^+, the oxidation couple

seems to have survived cycling somewhat. The oxidation reaction still shows both an oxidation and reduction peak, centered at 0.98 V vs. Ag/Ag^+. This is consistent with oxidation reaction observed before cycling and with the results observed in the concentrated DdPA in DME cycling experiment. The negative redox couple is a limiting factor and strategies to prevent its degradation would be necessary to deliver a highly cyclable symmetric nonaqueous DdPA-based RFB.

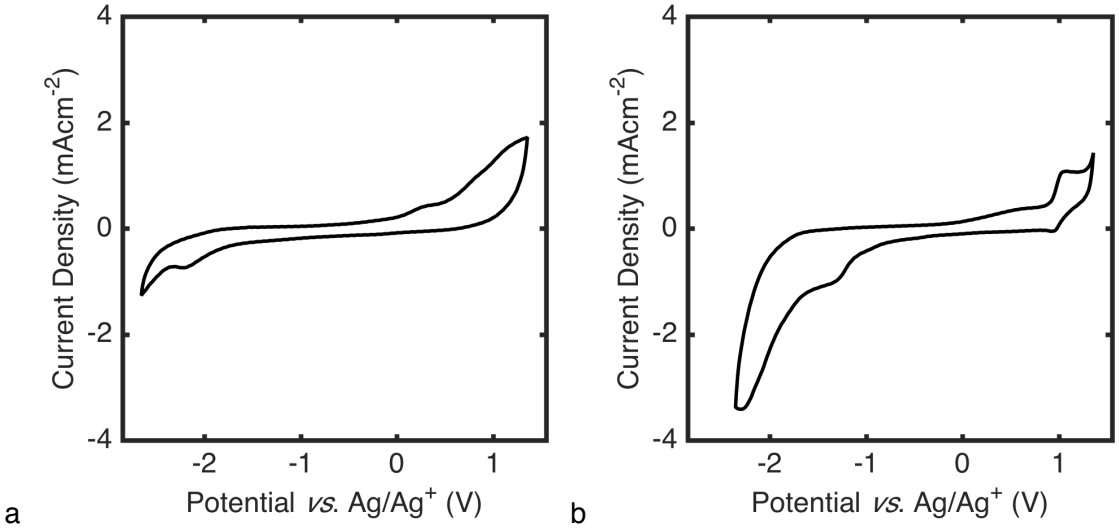

Figure 5.23. Cyclic voltammograms of 0.01 M DdPA, 0.5 M $TBABF_4$ inACN a) negolyte and b) posolyte after charge-discharge cycling (black), glassy carbon, 400 mVs^{-1}, 23 °C.

These demonstrations of symmetric nonaqueous RFBs are among the first of their kind. DPA-based organic chemistries are able to deliver 3 V cell potentials in flow cells. Despite relatively low-efficiency performance, the DPA system offered a comparable energy capacity to the more efficient $V(acac)_3$ system, largely due to this high cell potential. Still, DPA and its functionalized analogues suffer from degradation during cycling, accompanied by observable deposition of active material on inert surfaces within the RFB system. Specifically, the negative cell reaction in the DdPA electrochemistry appears to have the greatest instability during cycling. Alternative functionalizations that do not compromise the negative couple's reversibility (*e.g.* eDdPA), but maintain or further improve solubility might address performance

limitations imposed by negolyte decomposition. Alternative solvents and supporting electrolytes impact the performance of other nonaqueous RFB chemistries and provide another avenue to improve negolyte cyclability as well.

5.4 $V(acac)_3$ Flow-Rate and Current Study

5.4.1 Experimental Results

Having demonstrated the stable cyclability of the $V(acac)_3$ disproportionation chemistry, the system was used to explore two more general questions. First, how does changing cell operating parameters such as flow rate affect performance metrics like energy density, power density, and efficiencies of symmetric nonaqueous RFBs? Second, are nonaqueous RFBs subject to transport limitations that will severely handicap them compared to aqueous systems, as suggested by Sun *et al.*?[44] This experimental protocol entailed cycling cells across a procedural matrix formed by charge-discharge experiments run at 12.5, 25, and 50 $mLmin^{-1}$ and 10, 20, 40, and 100 $mAcm^{-2}$. This allows comparison of system performance metrics identified at the beginning of this chapter and plotted in Figure 5.24 across a range of liquid flow rates and electric current densities.

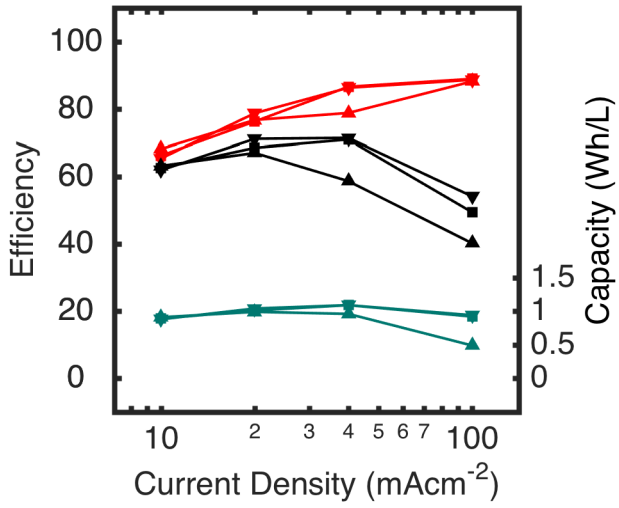

Figure 5.24. Flow-rate dependence (upward triangle –12.5 mLmin^{-1}, square – 25 mLmin^{-1}, downward triangle – 50 mLmin^{-1}) of 0.1 M V(acac)$_3$, 0.5 M TEABF$_4$ in ACN on coulombic efficiency (red), energy efficiency (black), discharge energy capacity (green).

Cells run at 25 or 50 mLmin^{-1} provide a maximum energy density at 40 mAcm^{-2} of 1.09 WhL^{-1} as shown in Figure 5.24 from cells operating with 87% (86%) coulombic efficiency, 82% (83%) voltage efficiency, and 71% energy efficiency at 25 mLmin^{-1} (50 mLmin^{-1}). These are also the most energy efficient procedures. Extrapolated to cells run across 100% SOC at the solubility limit of 0.6 M,[40] unmodified V(acac)$_3$ in neat ACN offers a maximum energy density of 13 WhL^{-1}. Unmodified V(acac)$_3$ in mixed nonaqueous solvents have realized even higher solubility limits of 1.1 M[39] and would deliver a maximum energy density of 24 WhL^{-1}. V(acac)$_3$ with modified acac$^-$ ligands have achieved concentrations as high as 1.3 M in neat ACN and would provide energy densities of 28 WhL^{-1}.[42] This is 80% of the 35 WhL^{-1} target suggested in Chapter 2.

Cells run at the highest current density, 100 mAcm^{-2}, with 25 and 50 mLmin^{-1} flow rates suffer from low voltage efficiencies (56% and 61%, respectively), yet deliver comparable discharge capacities of 0.92 and 0.94 WhL^{-1}, respectively; the higher current densities improve coulombic efficiencies to 89% at both flow rates. These results demonstrate the predictable tradeoff that arises due to the use of porous separator: higher current densities improve coulombic efficiency by shortening the time

for crossover to occur and counteract voltage efficiency losses from increased ohmic overpotentials at higher currents.

These results also reveal diminishing energy-capacity returns with respect to flow rates above 25 $mLmin^{-1}$. A more optimal flow rate for the current densities examined may exist between 12.5 and 25 $mLmin^{-1}$. Cells run at current densities corresponding to peak power may benefit from the high flow rate, however. Lower flow rates require less pumping energy and should be targeted so long as they do not introduce additional overpotentials. Nonaqueous RFBs using ACN already promise lower pumping losses than aqueous systems due to the solutions lower viscosity.

Whereas this matrix of experiments reveals a combination of parameters that maximizes energy density, a power density maximum is not reached. The polarization curve in Figure 5.25 is still trending upwards even for the 100 $mAcm^{-2}$ trials, which delivers 0.16 Wcm^{-2} at the highest flow rate. Following a model proposed by Sun *et al*. to predict the maximum power capability of these systems using ohmic resistances,[44] the losses for the 50 $mLmin^{-1}$ flow rate can be fit to a parabola under the assumption that all losses are linearly-resistive.

$$P = IV_{OCP} - I^2R \tag{5.6}$$

The power trend fits a second-order polynomial that predicts a maximum power of 0.22 Wcm^{-2} would be reached in cells run at 206 $mAcm^{-2}$. Although 206 $mAcm^{-2}$ is lower than the 322 $mAcm^{-2}$ break-even current density suggested for nonaqueous $V(acac)_3$ in Chapter 2, it indicates that other nonaqueous chemistries with swift kinetics will meet their targets. Recall that the breakeven current densities for $Cr(acac)_3$ and DPA are 189 and 228 $mAcm^{-2}$. This extrapolation is valid assuming that the kinetics of the higher-voltage chemistries are sufficiently rapid that they do not introduce large kinetic

overpotentials. Additionally, more concentrated battery solutions and cell optimization should improve the maximum power density for these systems.

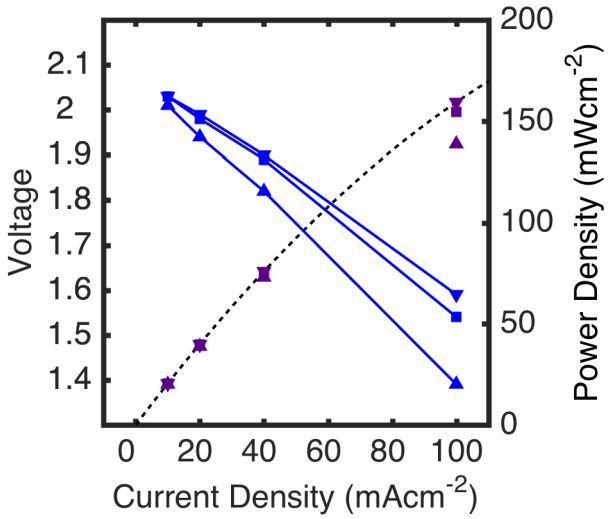

Figure 5.25. Flow rate dependence (upward triangle –12.5 mLmin^{-1}, square – 25 mLmin^{-1}, downward triangle – 50 mLmin^{-1}) of 0.1 M V(acac)$_3$, 0.5 M TEABF$_4$, ACN on average discharge voltage (blue) and power density (purple). The black dashed line is a best-fit second order polynomial to the power density data according to Equation 5.6.

Whereas the cells run at 25 and 50 mLmin^{-1} deliver similar cell performance, the cells run at 12.5 mLmin^{-1}, especially above the lowest current density, deviate from the high flow rate performance levels. Specifically, cells run at 100 mAcm^{-2} present impractical decreases in discharge capacity as evident in evident in Figure 5.24, while cells run at 20 mAcm^{-2} begin to show significantly lower average cell discharge voltage in Figure 5.25. These phenomena of significantly decreased discharge capacity and voltage at low flow rates likely result from concentration overpotentials at pseudo-steady state conditions. Concentration overpotentials can arise because reactants in the electrolytes become depleted during their residence time in the reactor. Since residence time in the RFB cell increases at lower flow rates, reactors will deliver higher bulk conversion of active species and cause substantial concentration overpotentials in low flow rate systems.

5.4.2 Modeling Results

Assuming that the reactants in the cell are well mixed, and otherwise making the assumptions that would hold valid for a continuous stirred-tank reactor (CSTR), concentration overpotentials can be calculated using a model based on the Nernst equation. Two applications of the Nernst equation are employed to determine cell voltage: the theoretical equilibrium potential of the whole system is controlled by the compositions of the liquid reservoirs and the observable equilibrium cell voltage is determined by the compositions of the solutions within the reactor volume. The concentration in the reactor will differ from the reservoirs due to bulk conversion occurring in the reactor. Assuming that the reactor and pipe volumes are small in comparison to the reservoirs, and that the chambers within the cell are well mixed, the fractional SOC based on the initial amount of neutral active species is defined as

$$SOC = 1 - \frac{C^0_{inlet}}{C^0_0} \tag{5.7}$$

where C^0 is the concentration of neutral species, then the open-circuit voltage that would be measured between the two solutions in the reservoirs is

$$E_{\text{reservoir}} = E^0_{\text{cell}} + \frac{2RT}{F}\ln\left(\frac{SOC}{1-SOC}\right). \tag{5.8}$$

Here, E^0_{cell} is the standard cell potential, R is the gas constant, T is the absolute temperature.

While concentration overpotentials stemming from conversion of bulk solution stored in the reservoirs will affect apparent voltages, conversion of active species in the reactor will also affect the open-circuit cell voltage.

$$E_{\text{cell}} = E^0_{\text{cell}} + \frac{2RT}{F}\ln\left(\frac{SOC+\Delta SOC}{1-SOC-\Delta SOC}\right) \tag{5.9}$$

where E_{cell} is the equilibrium cell potential and the variable ΔSOC expresses the difference in conversion between the solution composition exiting the reactor and that entering it. Charging procedures correspond to positive values for ΔSOC and discharging corresponds to negative values, which will lead to greater equilibrium overpotentials in E_{cell} than $E_{reservoir}$. This behavior will lead to voltage efficiency losses in any real system and motivates another trade-off between higher pumping costs at higher flow rates and higher voltage efficiency in systems with shorter residence times.

Modeling the cell reactor as a continuous stirred-tank reactor (CSTR) allows use of the design equation for these systems and calculation of ΔSOC,

$$\varepsilon V C^0_{reactor} \frac{dSOC}{dt} = \dot{V} C^0_{inlet} - \dot{V} C^0_{outlet} - \frac{iA}{F}, \tag{5.10}$$

where V is the reactor volume for a single electrolyte, $\dot{V}$ is the volumetric flow rate, i is the current density, A is the reactor area, F is Faraday's constant, and ε is the electrode porosity. The Damköhler number for this system,

$$Da = \frac{iA}{\dot{V} C^0_{inlet} F}, \tag{5.11}$$

indicates the relative speed of the electrochemical reaction rate compared to the convective transport of reactant species into the reactor volume. Damköhler numbers less than unity allow use of a pseudo-steady state approximation and eliminate the differential term in Equation 5.10 delivering a simple formula for ΔSOC:

$$\frac{iA\varepsilon}{\dot{V} F C^0_0} = \Delta SOC \tag{5.12}$$

This ΔSOC is expected to remain constant for any operating condition with a small Damköhler number. That assumption breaks down for the 12.5 $mLmin^{-1}$, 100 $mAcm^{-2}$ procedure after the SOC, as related to the inlet concentration in Equation 5.6, reaches

69%: as the cell approaches 69% *SOC* the model will struggle to accurately predict cell potential.

The model can be used with equations describing the expected SOC in the reservoirs during charge-discharge cycling to predict cell voltage behavior. The SOC is modeled using the reaction rate delivered by the current only:

$$SOC = SOC_0 + \frac{iAt}{V_{\text{electrolyte}} C_0^0 F} \tag{5.13}$$

where SOC_0 is the SOC at the beginning of a charge or discharge step and $V_{\text{electrolyte}}$ is the volume of one electrolytic solution. This ignores crossover through the porous separator as a means to regenerate reactant species. Equations 5.9, 5.12, and 5.13 allow prediction of charging and discharging cell potentials under equilibrium conditions as shown by the purple curve in Figure 5.26.

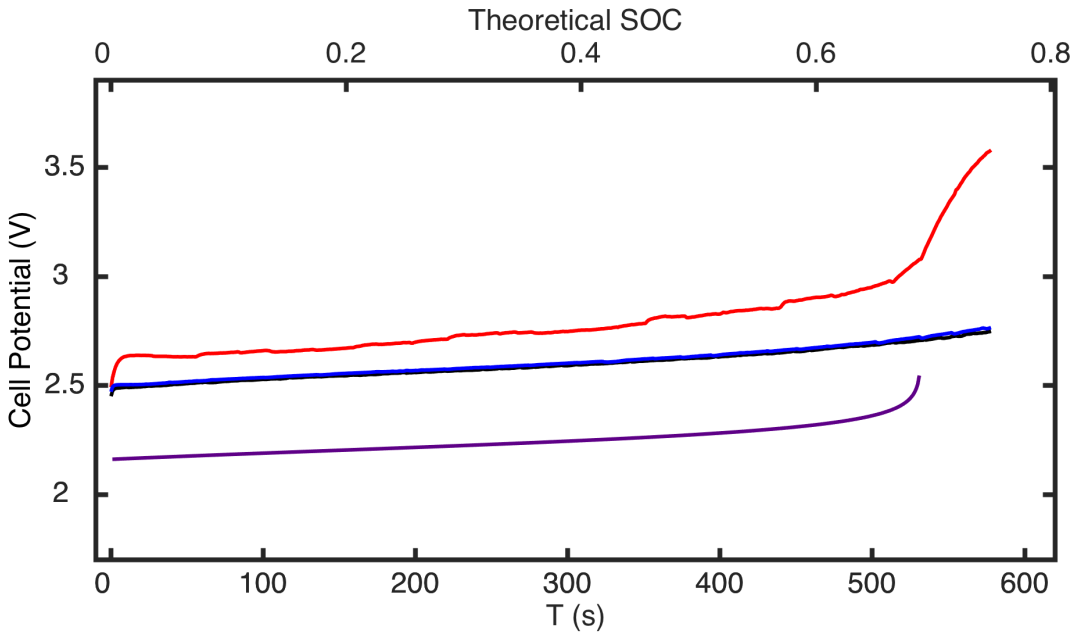

Figure 5.26. Experimental results for first charging step of 0.1 M $V(acac)_3$, 0.5 M $TEABF_4$ in ACN at 100 $mAcm^{-2}$ and 12.5 (red), 25 (blue), and 50(black) $mLmin^{-1}$ and prediction of equilibrium potentials *via* Nernst equilibrium equation and CSTR design equation (purple).

The model predicts that upon reaching any SOC above 70% the 12.5 $mLmin^{-1}$, 100 $mAcm^{-2}$ experiment, shown by the red curve in Figure 5.26, the reactor should

exhaust the neutral active species before exiting the outlet. This would correspond to a rapid increase in potential and triggering the experimental voltage cutoff. These predictions agree with experimental results as the cell potential increases rapidly in that region and nearly triggers the voltage safety cutoff in the approach to the prescribed 75% theoretical SOC. While the model predicts the point of neutral species exhaustion well, comparison of the first charges at all three flow rates indicate an additional source of overpotential at the lowest flow rate, which appears constant across the full duration of the charging step. The equilibrium model cannot explain the difference in overpotentials between the low flow rate and higher flow rates.

Other sources of overpotential stemming from reaction dynamics such as ohmic overpotentials and kinetic overpotentials can account for the difference in equilibrium model voltage and experimental data, which could also explain the increased overpotential at the lowest flow rate. Ohmic overpotentials are expected to be constant across the three flow rates as they are run at the same current density. Kinetic overpotentials across experiments run at the same current density would be expected to remain constant as well, so long as mass transport does not limit active species concentration at electrode surfaces and surface area remains constant across flow rates. These dynamic overpotentials can be further analyzed to assess what causes the increased overpotential at low flow rates.

One source of overpotential is ohmic resistance. This resistance can be calculated several ways: two options used here are either using the conductivity of the solution paired with separator properties or by using the bulk ASR values captured from EIS data. The resistance of the separator can be calculated using the conductivity of the support solution, 43 $mScm^{-1}$, and the Bruggeman correction: [136,137]

$$\kappa_{separator} = \kappa_{electrolyte} f^{1.5} \tag{5.14}$$

where κ_i is the conductivity across the separator or bulk electrolyte and f is the volume fraction of the electrolyte, taken as the porosity (0.55) of the Celgard 4560 separator. Paired with the separator dimensions, the bulk ASR across the separator is calculated to be 0.63 Ωcm^2. This value is significantly lower than the 4.6 Ωcm^2 measured with EIS and suggests that this cell design has significant room for improvement in reducing ohmic losses. When operated at 100 $mAcm^{-2}$ these resistances suggest an ohmic overpotential of 460 mV, with as little as 63 mV of the overpotential coming across the separator. Including ohmic overpotential into the model produces strong agreement between the model output for cell voltage and experimental results as shown in Figure 5.27. As the cell approaches larger SOC values the experimental results and model diverge slightly, which may be due to the increasingly inaccurate assumption of a low Dahmköhler number as SOC approaches and passes 69%.

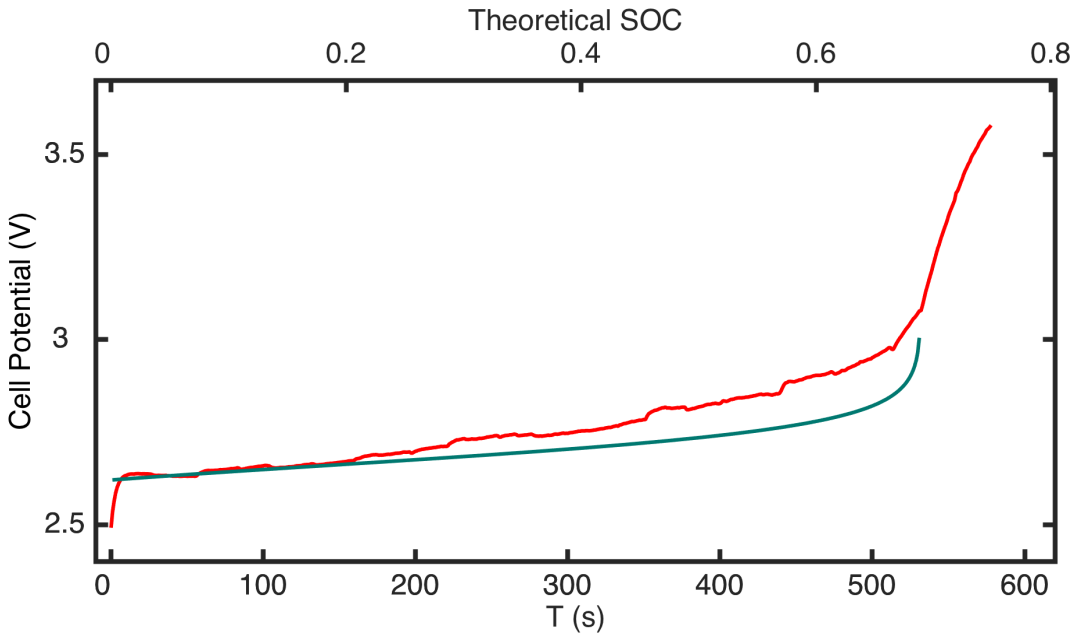

Figure 5.27. Experimental results for first charging step of 0.1 M $V(acac)_3$, 0.5 M $TEABF_4$ in ACN at 100 $mAcm^{-2}$ and 12.5 $mLmin^{-1}$. Prediction of cell potentials *via* a Nernst/CSTR model that includes ohmic overpotentials as collected from EIS (green).

This ohmic overpotential explains a large majority of the discrepancy in cell voltage between the equilibrium model and experimental data at 100 $mAcm^{-2}$ at the highest flow rate. Additionally, the difference in average charging and discharging voltage is 1.02 V, indicating that 0.10 V of overpotential, at most, arises from non-ohmic losses. Most of the remaining voltage losses must come from other dynamic overpotentials like kinetic or mass transport limitations.

RFBs can be expected to be kinetically limited only when mass transport limitations are avoided. Systems with Peclet and Schmidt numbers much larger than unity will not have mass transport limitations. The Peclet number describes the relative speed of reactant transport *via* bulk electrolyte flow compared to diffusional means:

$$\mathrm{Pe} = \frac{uL}{\varepsilon D} \tag{5.15}$$

where u is the superficial fluid velocity, L is the length scale of the carbon felt fibers, ε is the porosity, and D is the neutral active species diffusivity. Given a high Peclet number, indicating transport dominated by bulk flow, the Schmidt number describes the relative speed of transport *via* viscous diffusion compared to mass diffusion:

$$\mathrm{Sc} = \frac{\mu}{\rho D} \tag{5.16}$$

where ρ is the solution density and μ is the dynamic viscosity. Using values listed in Table 5.1, the Peclet number is 529 at the lowest flow rate and the Schmidt number is 1630, indicating that the system should not be mass-transfer limited.

Table 5.1. Properties and parameters of fluid flow, reactor electrodes, and 0.1 M $V(acac)_3$, 0.5 M $TEABF_4$ in ACN battery solution at 22 °C.

D[94]	ρ	u	L	μ	ε
$\frac{cm^2}{s}$	$\frac{g}{cm^3}$	$\frac{cm}{s}$	cm	$\frac{g}{s \bullet cm}$	
3.93 x 10^{-6}	0.8335	1.1, 2.1,4.2	0.002	0.535	0.98

This also gives an indication toward the source of additional overpotential in this system at low flow rates. While the higher flow rates reveal similar kinetic overpotentials while charging, a system parameter that affects kinetics in the lowest flow rate experiments is likely responsible for the additional charging overpotential in that system. As there is no evidence of different reaction pathways or products at the low flow rate, the likely explanation is that lower flow rates reduce the effective wetting of the carbon felts. This will increase the kinetic overpotentials due to the reduced electrochemical surface area compared to higher flow rates. The lack of difference between flow rates 25 and 50 $mLmin^{-1}$ would indicate no further improvement in electrode wetting after 25 $mLmin^{-1}$. This reflects the importance of electrode wetting properties for the felts used in nonaqueous symmetric RFBs, which is still a heavily researched topic for AVRFB systems.[138]

5.5 Summary and Discussion

The nonaqueous symmetric $V(acac)_3$ RFB chemistry is demonstrably cyclable without appreciable capacity loss in a co-current, flow-through flow cell. This both reaffirms results of the spectroelectrochemical study of $V(acac)_3$ from Chapter 3 and verifies the capabilities of the custom flow cell design to produce cyclable RFBs. The cells run at 10 $mAcm^{-2}$ with a porous Celgard separator deliver good performance with 66%, 94%, and 63% coulombic, voltage, and energy efficiencies, respectively. These are comparable to other flow cell studies,[66] and also improve substantially upon H-cell RFB studies.[40]

Having demonstrated stable cycling with this flow cell design, other chemistries are also tested. DPA-based molecules promising for symmetric nonaqueous RFBs, discovered and synthesized as described in Chapter 4, are studied in flow cells. DPA-

based chemistries were mostly run in DME solutions, the solvent that sustained their highest solubility limits. In order to provide a good comparator, $V(acac)_3$ in DME, which is demonstrated to have reversible electrochemistry using CV in Chapter 3, is cycled using similar procedures to those used in the ACN system. $V(acac)_3$ in DME shows good capacity retention over the course of cycling, but presents signs of increasing voltage inefficiency, which may indicate some material incompatibility between DME and cell componentry. Nevertheless, the organic systems were tested in the flow cell.

The demonstrations of organic-powered symmetric nonaqueous flow cells are some of the first attempts at implementing this RFB strategy. The 3 V discharge potentials for the DPA system, and nearly 3 V for the DdPA system, are the highest voltages delivered from an organic nonaqueous RFB to date. Still, the metal-free chemistries suffer from degradation issues, especially in the negolyte. Performance declined as a result of active-species precipitation on the inert tubing surfaces and through an observed disappearance of the reversible reduction couple in the negolyte after cycling. Alternative functionalization of the active DPA center or the use of different solvent and support systems may combat these sources of degradation.

Flow rate and current density studies are performed with the cyclable $V(acac)_3$ in ACN battery solution. These studies indicate a maximum energy density at 40 $mAcm^{-2}$ for flow rates of 25 and 50 $mLmin^{-1}$. The study suggests a peak power above 0.2 Wcm^{-2} would be achieved at a 206 $mAcm^{-2}$, which was outside the range of current densities studied. This current density outperforms the break-even peak power metrics identified for symmetric nonaqueous RFB chemistries in Chapter 2.

Experiments at high current densities with low flow rates allowed analysis of some flow cell limitations associated with the reactor design. Residence time within the

cell proves important because it correlates with a differential conversion between the reactor feed and exit, and manifests as a concentration overpotential. Modeling the reactor as a CSTR with a small Damköhler number successfully predicts the stark increase in voltage for experimental charge-discharge curves by using this equilibrium concentration overpotential model. The equilibrium model fails to explain increased overpotentials observed during high current density, low flow rate experiments, compared to the same current density at high flow rates: this may indicate poor electrode wetting at low flow rates. Still, in this non-optimized cell, power densities are demonstrated to be comparable to aqueous systems,[44] which should allay fears that nonaqueous RFB power capabilities are impractical for cost-effective applications.

6 Conclusions

Chemistries for symmetric nonaqueous RFBs were studied from a variety of perspectives. Symmetric nonaqueous RFBs, which represent a fraction of the chemistries available for use in nonaqueous systems, are a nascent field and have not matured to the commercial stage. This contrasts aqueous RFBs, for which several chemistries have been employed in commercial installations, with most systems based on the AVRFB chemistry. Aqueous chemistries, such as AVRFBs, already offer cheaper alternatives to ubiquitous Li-ion systems for long-duration applications. Symmetric nonaqueous RFBs further offer unique performance advantages over the commercial aqueous systems. These performance advantages suggest possible step-changes in cost-effectiveness and motivate the study of nonaqueous RFB chemistries generally, and symmetric nonaqueous chemistries specifically.

At this nascent stage of research into nonaqueous RFBs, there is an overabundance of topics to investigate. These range from identifying new chemistries, characterizing the performance of redox couples within a given chemistry, studying and developing membrane materials, performing laboratory-scale flow cell demonstrations, optimizing flow cells, and designing flow cell stacks. As the nonaqueous RFB field has received more interest and funding, the standard of research has improved significantly and extended across most of these areas, with the exception of stack development.

The research effort described herein first focuses on characterizing the redox activity of $V(acac)_3$ and $Cr(acac)_3$, which have been identified as promising symmetric nonaqueous RFB chemistries. It also recognizes promising new organic chemistries based on DPA and functionalized versions of DPA. Ultimately, a bespoke flow cell, fabricated in-house with common milling facilities, demonstrates laboratory-scale full cell cycling of the $V(acac)_3$ and organic chemistries. The test cell can also support half-

reaction studies on these, or other, chemistries in the future. Thus, the research presented here spans three of the many directions in which nonaqueous RFB researchers presently focus.

The economic analysis in Chapter 2 distinguishes symmetric nonaqueous RFBs as a technological opportunity to impart a step change in RFB cost-effectiveness. RFBs, specifically AVRFBs, already offer a lower-cost alternative to Li-ion systems for longer-duration applications, yet RFBs trail Li-ion in terms of the number of commissioned long-duration installations around the world. Whatever the reason for this market failure, developing a lower cost RFB chemistry would combat this underrepresentation by widening the cost difference between the competitive EES systems. Nonaqueous RFBs are a promising alternative to aqueous RFBs because they permit higher cell voltages. Higher voltages can significantly reduce active species cost and areal power costs, which make up a majority of state-of-the-art AVRFB system costs. Nonaqueous solutions, however, also introduce additional costs from the nonaqueous solvent and nonaqueous or high-voltage-compatible supporting salts that can cut into the savings from higher cell voltages. This trade-off is an important design consideration that motivates maximizing the energy density of nonaqueous systems to reduce solvent and supporting electrolyte costs.

Symmetric RFB chemistries, which mitigate the negative impacts of crossover more than single-active-species chemistries such as AVRFBs, offer further drastic reductions in cost by avoiding the need for costly IEMs. Symmetric systems do not necessitate nonaqueous environments, but, until recently, there had been no active species capable of delivering feasible voltages under symmetric operation in aqueous conditions.[58] This motivated the research focus on high-voltage symmetric nonaqueous systems using $V(acac)_3$, $Cr(acac)_3$, and DPA.

The coordination complexes $V(acac)_3$ and $Cr(acac)_3$ are compelling for contrasting reasons. Researchers thoroughly investigated $V(acac)_3$ for use in nonaqueous RFBs and reported on the discovery of the chemistry,[14] degradation pathways,[40] alternative solvents and supports,[36,37,39] ligand functionalization,[42] and attempts at laboratory scale flow cell testing.[66] Yet, some of these early reports conflict with each other, indicating that there are still some gaps in the understanding of this chemistry. Also, the $V(acac)_3$ RFB only offers a cell OCP of 2.2 V, which does not take full advantage of the wide electrochemical stability windows of nonaqueous solutions. Alternatively, a symmetric nonaqueous $Cr(acac)_3$ RFB chemistry offers redox behavior capable of delivering over 4 V cell operation, but researchers have not studied it as thoroughly.[32,42] Consequently, the fundamental electrochemistry is poorly understood. Further study of both coordination complexes aims to improve the state of symmetric nonaqueous RFB research.

Electrochemical and spectroelectrochemical studies of both chemistries close knowledge gaps in the $V(acac)_3$ system and improve the basic understanding of the $Cr(acac)_3$ electrochemistry. Linear sweep voltammetry of $Cr(acac)_3$ solutions immediately reveals that at least one of the electrochemical reactions deviates from the previously proposed single-electron outer-sphere exchange: limiting currents have a 2:3 ratio between the first reduction reaction and first oxidation reaction. Spectroelectrochemical bulk electrolysis experiments performed on $Cr(acac)_3$ elucidate possible mechanisms for this behavior. UV-vis-IR absorbance spectroscopy performed on oxidized, neutral, and reduced $Cr(acac)_3$ solutions provide evidence of ligand dissociation in the reduction reaction: the reduced solution develops drastic absorbance increases in the region consistent with the presence of free $acac^-$ ligand. A reduction mechanism that involves ligand dissociation would negatively impact half and full cell

reaction schemes as is observed in batch reactor cell cycling. The same spectroelectrochemical studies with $V(acac)_3$ lack any evidence of ligand disassociation. This conflicts with previous flow cell studies of the $V(acac)_3$ chemistry, which attributed capacity fade to degradation mechanisms that necessitated ligand disassociation.[66] The spectroelectrochemical study instead suggests that the prior capacity fade likely stemmed from side reactions involving system impurities, rather than the resilience, or lack thereof, to cycling of pure active species. Thus, the voltammetry and spectroelectrochemistry work described here furthered the mechanistic understanding of both coordination complex chemistries.

The results suggested another avenue by which $Cr(acac)_3$ performance could be improved. Ligand disassociation is known to depend on solvent and support conditions for these transition metal complexes. An alternative solvent system using DME, instead of ACN, is studied for both $V(acac)_3$ and $Cr(acac)_3$ to examine how strongly solvent choice can impact the electrochemistry of these complexes. DME shows little impact on the $V(acac)_3$ redox behavior other than a slight increase in the potential between the two redox couples. This presents a strategy to incrementally improve energy and power density, but is not studied further. Although $Cr(acac)_3$ in DME displays irreversibility indicative of ligand disassociation in the first reduction reaction, it made accessible a third apparently reversible reduction couple too. While the DME solutions fail to prevent ligand disassociation in $Cr(acac)_3$ and, instead, seem to exacerbate the problem, the influence of the solvent system, even if deleterious, corroborates the original hypothesis. Solvent systems significantly affect ligand disassociation behavior and alternative solvent systems capable of delivering a more stable metal-ligand bonds may exist.

Ultimately, these studies provide two actionable results. Neutral and electrolyzed $V(acac)_3$ solutions are stable under sufficiently pure conditions: flow cell studies with this chemistry need to be repeated to assess the systems' cyclabilities. The $Cr(acac)_3$ electrochemistry, specifically the first reduction reaction, destroys the coordination complex in both ACN and DME solutions: further voltammetric, and eventually bulk electrolysis, screening should be performed on $Cr(acac)_3$ in alternative solvents to search for a reversible system that can allow progression to half or full cell studies.

These conclusions motivated the study of another symmetric nonaqueous active species, DPA, that delivers higher voltages than $V(acac)_3$, but with better electrochemical behavior than $Cr(acac)_3$. DPA has not been studied for RFBs previously, but it is a polycyclic aromatic hydrocarbon like rubrene, which has. Researchers previously considered rubrene for RFBs because of its promising redox behavior, but stopped after categorizing its solubility limit in ACN as too low.[31] The first steps for establishing a DPA-based symmetric nonaqueous RFB entailed finding a solvent that provided sufficient DPA solubility and delivered reversible electrochemistry. This solvent screening procedure identifies ACN and DME as solvents that sustain reversible DPA electrochemistry, but DPA suffers from similar solubility concerns since it has limits of 0.6 mM and 44 mM in the solvents, respectively. Higher solubility limits are necessary to deliver practical RFBs using this organic chemistry.

Functionalization offers a strategy to improve the solubility of the DPA moiety. Early functionalization featured the addition of small functional groups like methyl, methoxy and methyl esters at the 4-position of the phenyl rings *via* Suzuki-Miyaura cross-coupling reactions. Rather than improve solubility, these functionalizations

lowered the solubility limits in ACN and DME. This reaction scheme still provides the methyl ester functionalized unit, DMBA, which serves as a handle for further functionalization. Additionally, the methyl-functionalized unit, DMPA, shows that functionalized versions of DPA retain the desired redox activity. DMBA allows further functionalization *via* trans-esterification reactions with single-unit and double-unit ethylene glycoxy esters to form DePA and DdPA, respectively. Both ethylene glycol functionalizations improve solubility and DdPA achieves solubility limits of 12 mM in ACN and 0.21 M in DME. DdPA retained redox activity that promises to deliver cell voltages greater than 3 V despite apparent sluggishness of the reduction reaction.

The lessons learned from this progression through different DPA functionalizations guide strategies for other organic active species. One promising alternative involves replacing the anthracene moiety (in DMBA) with naphthalene, which produces a more soluble methyl ester functionalized polycyclic aromatic hydrocarbon, DMBN, that can participate in the trans-esterification reaction to form DdPN. DdPN is liquid at room temperature and has redox activity that offers cell OCPs above 3.6 V. Alternatively, another strategy sought to retain the anthracene center, but links ethylene glycol chains *via* an ether rather than an ester. This requires synthesizing a boronic acid reagent with an ethylene glycol chain for use in the cross-coupling reaction, but avoids the troublesome trans-esterification reaction. This initial synthesis successfully produces the boronic acid for the cross-coupling reaction and delivers the intended molecule, eDdPA. While eDdPA retains the rapid DPA kinetics and offers a second oxidation couple, its solubility limit is lower than DdPA. Both of these systems warrant further study.

Besides designing other active species, the original DdPA trans-esterification synthetic procedure needed reconsideration because it struggled to deliver high yields

and failed to deliver product above a 100 mg scale. An alternative reaction scheme that introduces a co-solvent into the trans-esterification reaction provides a procedure that delivers DdPA product at scales up to 10 grams. This scale-up procedure delivers sufficient DdPA product to enable laboratory-scale flow cell testing.

Both Chapter 3 and 4 offer symmetric nonaqueous RFB chemistries that merit flow cell testing: $V(acac)_3$, DPA, and DdPA. A laboratory-scale, nonaqueous-compatible flow cell was designed and fabricated to allow full cell tests of these chemistries. The design allows easy modification to deliver larger or smaller reactor areas without the need to machine all new components and can also support half cell experiments.

Cycling experiments with $V(acac)_3$ showed stable performance despite relying on similar procedures as previous demonstrations that produced capacity fade.[66] The cycling experiments identify and avoid two likely culprits behind capacity fade in the original study: low purity $V(acac)_3$ and atmospheric moisture. Studies of the cycled electrolytes revealed little degradation of the reactor's EIS spectra or the battery solution's voltammetric response with cycling. These degradation checks reaffirm the results from Chapter 3 suggesting that $V(acac)_3$ should cycle well in full cells and confirm the cell design's capability to deliver stable cycling with a model chemistry.

Equipped with a validated nonaqueous flow cell, symmetric organic nonaqueous flow cells using dilute DPA, dilute DdPA, and concentrated DdPA solutions are examined. Both dilute DPA and DdPA in DME deliver discharge voltages at or near 3 V, which are first-of-their-kind demonstrations. Still, both chemistries have significant burn-in periods, low efficiencies, and degradation pathways that lead to capacity fade. Dilute DdPA in ACN had worse cycling performance than the DME system. Cycling experiments of concentrated DdPA in DME solutions eliminated the significant burn-in

period observed in the dilute cycling experiments. Still, the concentrated system suffers from low efficiency and degradation pathways leading to capacity fade. Degradation studies identify unstable negolyte reaction products as the likely culprit in the DdPA systems. Voltammetry of the cycled negolyte shows few signs of the original reduction reaction and thin organic films are observed to deposit on the negolyte tubing. Spectroelectrochemical bulk electrolysis studies of DdPA, similar to those performed on $Cr(acac)_3$ and $V(acac)_3$, should provide insight into the degradation mechanisms occurring in these systems. Nevertheless, these cycling experiments led to the highest voltage delivered by a symmetric nonaqueous RFB flow cell yet observed and use exceptionally inexpensive organic active species.

A study to characterize the general performance of symmetric nonaqueous RFB cells used the demonstrably cyclable $V(acac)_3$ in ACN system as a model chemistry. Flow cell experiments in which the liquid flow rates and electrical current were varied illustrate the influence of these parameters on important system metrics outlined in Chapter 2 and 3. These studies inform future cycling experiments to evaluate other symmetric nonaqueous chemistries, to implement nonaqueous flow cell engineering, and more generally, to illustrate the power capabilities of nonaqueous RFBs. The flow cell experiments identified and predicted the peak performance metrics of symmetric nonaqueous $V(acac)_3$ system using a matrix composed of flow rates and imposed electrical currents. Peak energy density occurs at 40 $mAcm^{-2}$ and 25 or 50 $mLmin^{-1}$: delivering 1.09 WhL^{-1} for these specific experiments. This predicts maximum energy densities of 13 WhL^{-1} for neat ACN systems and 24 WhL^{-1} for mixed ACN/DMSO/DO solvent systems based on the maximum $V(acac)_3$ solubility.[39,40] Furthermore, functionalized acetylacetonate ligands would offer 28 WhL^{-1} in neat ACN.[42] Cells run at 100 $mAcm^{-2}$ and 50 $mLmin^{-1}$ realize a power density of 0.16 Wcm^{-2} and predicts a

peak power density of 0.22 Wcm^{-2} for this solution composition, separator, and cell design. Higher cell voltages and optimized cell design promise significant improvements in this peak power, which are of the same order of magnitude as AVRFB systems. These metrics suggest that the performance of symmetric nonaqueous RFBs can be competitive with state-of-the-art aqueous RFB systems. Realistically, further cost improvements to deliver a step change in cost-effectiveness may be necessary to warrant commercial development of this specific symmetric nonaqueous $V(acac)_3$ chemistry.

6.1 Future Work

The research in this thesis suggests many avenues for further exploration. Solvent and support studies with $Cr(acac)_3$ should be pursued further to find compositions that hinder ligand disassociation in the troublesome first reduction reaction. Additionally, degradation studies in solvent and support systems that offer high $V(acac)_3$ solubility and energy density are necessary to understand the cyclability of the chemistry in these solutions. Assuming stable bulk electrolysis, these battery solutions should undergo examination in full cells at concentrations closer to their solubility limit. This study largely avoided discussion of membranes and separators since symmetric chemistries can operate with commercially available porous separators, but the topic is important for nonaqueous systems due to the dearth of nonaqueous-compatible membranes. Further exploration into the new inexpensive symmetric high-voltage DPA-based chemistries should continue as well. Spectroelectrochemical electrolysis methods provide a toolkit for identifying degradation pathways and can be used on the DPA chemistries. Identification of the degradation mechanisms can inform future functionalization efforts to provide better cyclability in the DPA-based

symmetric nonaqueous RFBs. Alternatively, symmetric chemistries capable of operating in aqueous supporting solutions could also offer compelling cost-effectiveness improvements and some of the first aqueous-compatible chemistries have been demonstrated recently.[58] Research into new membranes and active species would be best suited by collaboration between chemical synthesis experts capable of versatile, high throughput chemical production and electrochemical engineering experts capable of reliably quantifying performance through a variety of experimental metrics. Symmetric nonaqueous RFBs are promising new EES systems that should provide interesting multi-disciplinary research topics as the technology continues to develop.

The modeling research pertaining to the nonaqueous symmetric flow reactor discovered that modeling the reactor as a continuous stirred-tank reactor accurately predicted high overpotentials at low flow rates. This is an interesting result since physical consideration of the flow through the reactor would suggest a plug-flow or packed-bed reactor. While the CSTR model accurately predicts the stark voltage increase observed in experimental work, the model does could fit more closely to the early data and some reactor behavior is not included in the model: for example, active species crossover across the membrane. Introducing an SOC-dependent crossover term to could provide a parameter, which should be experimentally examinable, that can provide a model that better fits early data, but at the expense of model simplicity.

References

1. Kaldellis, J. K.; Zafirakis, D.; Kaldelli, E. L.; Kavadias, K., Cost benefit analysis of a photovoltaic-energy storage electrification solution for remote islands. *Renewable Energy* **2009,** *34* (5), 1299-1311.

2. Katti, P. K.; Khedkar, M. E., Alternative energy facilities based on site matching and generation unit sizing for remote area power supply. *Renewable Energy* **2007,** *32* (8), 1346-1362.

3. Eyer, J.; Corey, G., Energy Storage for the Electrical Grid: Benefits and Market Potential Assessment Guide. *Sandia Report* **2010,** *SAND0810-2010*.

4. Rastler, D., Electricity Energy Storage Technology Options-A White Paper Primer on Applications, Costs and Benefits. EPRI: 2010.

5. Jenson, J.; Pike, S., State of Charge Massachusetts Energy Storage Initiative Study. 2016.

6. DOE Global Energy Storage Database. U.S. Department of Energy: 2016.

7. Thaller, L. H. In *Electrically rechargeable redox flow cells*, 9th Intersociety energy conversion engineering conference, 1974; pp 924-928.

8. Zeng, Y. K.; Zhao, T. S.; An, L.; Zhou, X. L.; Wei, L., A comparative study of all-vanadium and iron-chromium redox flow batteries for large-scale energy storage. *Journal of Power Sources* **2015,** *300*, 438-443.

9. Michaels, K.; Hall, G., Cost Projections for Redox Energy System. DOE/NASA, Ed. 1980.

10. S. Barnartt, D. F., Bromine-Zinc Secondary Cells. *Journal of the Electrochemical Society* **1964,** *111* (11), 1201-1204.

11. M. Skyllas-Kazacos, M. R., R. Robins, A. Fane, M Green, New All-Vanadium Redox Flow Cell. *Journal of the Electrochemical Society* **1986,** *133*, 1057-1058.

12. Matsuda, Y.; Tanaka, K.; Okada, M.; Takasu, Y.; Morita, M.; Matsumurainoue, T., A rechargeable redox battery utilizing ruthenium complexes with non-aqueous organic electrolyte. *Journal of Applied Electrochemistry* **1988,** *18* (6), 909-914.

13. R. Ferrigno, A. S., T. Clark, M. Mayer, G. Whitesides, Membraneless Vanadium Redox Fuel Cell Using Laminar Flow. *Journal of the American Chemical Society* **2002,** *124*, 12930-12931.

14. Liu, Q. H.; Sleightholme, A. E. S.; Shinkle, A. A.; Li, Y. D.; Thompson, L. T., Non-aqueous vanadium acetylacetonate electrolyte for redox flow batteries. *Electrochemistry Communications* **2009,** *11* (12), 2312-2315.

15. Lin, K.; Chen, Q.; Gerhardt, M. R.; Tong, L.; Kim, S. B.; Eisenach, L.; Valle, A. W.; Hardee, D.; Gordon, R. G.; Aziz, M. J.; Marshak, M. P., Alkaline Quinone Flow Battery. *Science* **2015,** *349* (6255), 1529-1532.

16. Bard, A. J.; Faulkner, L. R., *Electrochemical Methods Fundamentals and Applications*. 2nd ed.; John Wiley & Sons, Inc.: New York, 2001.

17. Bartolozzi, M., Development of redox flow batteries. a historical bibliography. *Journal of Power Sources* **1989,** *27*, 219-234.

18. R. Savinell, C. L., R. Galasco, S. Chiang, Discharge Characteristics of a Soluble Iron-Titanium Battery System. *Journal of the Electrochemical Society* **1979,** *126* (3), 357-360.

19. Ge, S.; Yi, B.; Zhang, H., Study of a high power density sodium polysulfide/bromine energy storage cell. *Journal of Applied Electrochemistry* **2004,** *34*, 181-185.

20. Leon, C. P. d.; Frias-Ferrer, A.; Gonzales-Garcia, J.; Santo, D.; Walsh, F., Redox Flow Cells for Energy Conversion. *Journal of Power Sources* **2006,** *160*, 716-732.

21. Lex, P.; Jonshagen, B., The zinc/bromine battery system for utility and remote area applications. *Power Engineering Journal* **1999**, 7.

22. Kreutzer, H.; Yarlagadda, V.; Van Nguyen, T., Performance Evaluation of a Regenerative Hydrogen-Bromine Fuel Cell. *Journal of The Electrochemical Society* **2012,** *159* (7), F331-F337.

23. B. Huskinson, M. M., C. Suh, S. Er, M. Gerhardt, C. Galvin, X. Chen, A. Aspuru-Guzik, R. Gordon, M. Aziz, A metal-free organic-inorganic aqueous flow battery. *Nature* **2014,** *505*, 195-198.

24. Rychcik, M.; Skyllas-Kazacos, M., Evaluation of electrode materials for vanadium redox cell. *Journal of Power Sources* **1987,** *19* (1), 45-54.

25. Sum, E.; Skyllas-Kazacos, M., A study of the V(II)/V(III) redox couple for redox flow cell applications. *Journal of Power Sources* **1985,** *15* (2), 179-190.

26. Sum, E.; Rychcik, M.; Skyllas-kazacos, M., Investigation of the V(V)/V(IV) system for use in the positive half-cell of a redox battery. *Journal of Power Sources* **1985,** *16* (2), 85-95.

27. X. Wei, B. L., W. Wang, Porous Polymeric Composite Separators for Redox Flow Batteries. *Polymer Reviews* **2015,** *55*, 247-272.

28. Luo, Q.; Li, L.; Wang, W.; Nie, Z.; Wei, X.; Li, B.; Chen, B.; Yang, Z.; Sprenkle, V., Capacity Decay and Remediation of Nafion-based All-Vanadium Redox Flow Batteries. *ChemSusChem* **2013,** *6* (2), 268-274.

29. Gu, S.; Gong, K.; Yan, E. Z.; Yan, Y., A multiple ion-exchange membrane design for redox flow batteries. *Energy & Environmental Science* **2014,** *7* (9), 2986-2998.

30. Ue, M.; Ida, K.; Mori, S., Electrochemical Properties of Organic Liquid Electrolytes Based on Quaternary Onium Salts for Electrical Double-Layer Capacitors. *Journal of The Electrochemical Society* **1994,** *141* (11), 2989-2996.

31. Chakrabarti, M. H.; Dryfe, R. A. W.; Roberts, E. P. L., Evaluation of electrolytes for redox flow battery applications. *Electrochimica Acta* **2007,** *52* (5), 2189-2195.

32. Liu, Q. H.; Shinkle, A. A.; Li, Y. D.; Monroe, C. W.; Thompson, L. T.; Sleightholme, A. E. S., Non-aqueous chromium acetylacetonate electrolyte for redox flow batteries. *Electrochemistry Communications* **2010,** *12* (11), 1634-1637.

33. Sleightholme, A. E. S.; Shinkle, A. A.; Liu, Q. H.; Li, Y. D.; Monroe, C. W.; Thompson, L. T., Non-aqueous manganese acetylacetonate electrolyte for redox flow batteries. *Journal of Power Sources* **2011,** *196* (13), 5742-5745.

34. Yamamura, T.; Shiokawa, Y.; Yamana, H.; Moriyama, H., Electrochemical investigation of uranium β-diketonates for all-uranium redox flow battery. *Electrochimica Acta* **2002,** *48* (1), 43-50.

35. Mun, J.; Lee, M.-J.; Park, J.-W.; Oh, D.-J.; Lee, D.-Y.; Doo, S.-G., Non-Aqueous Redox Flow Batteries with Nickel and Iron Tris(2,2'-bipyridine) Complex Electrolyte. *Electrochemical and Solid-State Letters* **2012,** *15* (6), A80-A82.

36. Shinkle, A. A.; Pomaville, T. J.; Sleightholme, A. E. S.; Thompson, L. T.; Monroe, C. W., Solvents and supporting electrolytes for vanadium acetylacetonate flow batteries. *Journal of Power Sources* **2014,** *248*, 1299-1305.

37. Herr, T.; Noack, J.; Fischer, P.; Tübke, J., 1,3-Dioxolane, tetrahydrofuran, acetylacetone and dimethyl sulfoxide as solvents for non-aqueous vanadium acetylacetonate redox-flow-batteries. *Electrochimica Acta* **2013,** *113*, 127-133.

38. Herr, T.; Fischer, P.; Tübke, J.; Pinkwart, K.; Elsner, P., Low-Temperature, High Energy Density Non-Aqueous Redox Flow Battery. *Meeting Abstracts* **2014,** *MA2014-02* (1), 28.

39. T. Herr, P. F., J. Tubke, K. Pinkwart, P. Elsner, Increasing the energy density of the non-aqueous vanadium redox flow battery with the acetonitrile-1,3-dioxolane-dimethyl sulfoxide mixture. *Journal of Power Sources* **2014,** *265*, 317-324.

40. Shinkle, A. A.; Sleightholme, A. E. S.; Griffith, L. D.; Thompson, L. T.; Monroe, C. W., Degradation mechanisms in the non-aqueous vanadium acetylacetonate redox flow battery. *Journal of Power Sources* **2012,** *206*, 490-496.

41. Q. Liu, A. S., A. Shinkle, Y. Li, L. Thompson, Non-aqueous vanadium acetylacetonate electrolyte for redox flow batteries. *Electrochemistry Communications* **2009,** *11*, 2312-2315.

42. Suttil, J. A.; Kucharyson, J. F.; Escalante-Garcia, I. L.; Cabrera, P. J.; James, B. R.; Savinell, R. F.; Sanford, M. S.; Thompson, L. T., Metal acetylacetonate complexes for high energy density non-aqueous redox flow batteries. *Journal of Materials Chemistry A* **2015,** *3* (15), 7929-7938.

43. Li, L.; Kim, S.; Wang, W.; Vijayakumar, M.; Nie, Z.; Chen, B.; Zhang, J.; Xia, G.; Hu, J.; Graff, G.; Liu, J.; Yang, Z., A Stable Vanadium Redox-Flow Battery with High Energy Density for Large-Scale Energy Storage. *Advanced Energy Materials* **2011,** *1* (3), 394-400.

44. Sun, C. N.; Mench, M. M.; Zawodzinski, T. A., High Performance Redox Flow Batteries: An Analysis of the Upper Performance Limits of Flow Batteries Using Non-aqueous Solvents. *Electrochimica Acta* **2017,** *237*, 199-206.

45. Zhang, D.; Lan, H.; Li, Y., The application of a non-aqueous bis(acetylacetone)ethylenediamine cobalt electrolyte in redox flow battery. *Journal of Power Sources* **2012,** *217*, 199-203.

46. Xing, X.; Zhang, D.; Li, Y., A non-aqueous all-cobalt redox flow battery using 1,10-phenanthrolinecobalt(II) hexafluorophosphate as active species. *Journal of Power Sources* **2015,** *279*, 205-209.

47. Cabrera, P. J.; Yang, X.; Suttil, J. A.; Hawthorne, K. L.; Brooner, R. E. M.; Sanford, M. S.; Thompson, L. T., Complexes Containing Redox Noninnocent Ligands for Symmetric, Multielectron Transfer Nonaqueous Redox Flow Batteries. *The Journal of Physical Chemistry C* **2015,** *119* (28), 15882-15889.

48. Gong, K.; Fang, Q.; Gu, S.; Li, S. F. Y.; Yan, Y., Nonaqueous redox-flow batteries: organic solvents, supporting electrolytes, and redox pairs. *Energy & Environmental Science* **2015,** *8* (12), 3515-3530.

49. Aman Preet Kaur, N. E. H., Selin Ergun, Corringe F. Elliott, Susan Odom, A Highly Soluble Organic Catholyte for Non-Aqueous Redox Flow Batteries. *Energy Technology* **2015,** *3* (5), 476-480.

50. Liu, T.; Wei, X.; Nie, Z.; Sprenkle, V.; Wang, W., A Total Organic Aqueous Redox Flow Battery Employing a Low Cost and Sustainable Methyl Viologen Anolyte and 4-HO-TEMPO Catholyte. *Advanced Energy Materials* **2015**, n/a-n/a.

51. Wang, W.; Xu, W.; Cosimbescu, L.; Choi, D. W.; Li, L. Y.; Yang, Z. G., Anthraquinone with tailored structure for a nonaqueous metal-organic redox flow battery. *Chemical Communications* **2012,** *48* (53), 6669-6671.

52. Brushett, F. R.; Vaughey, J. T.; Jansen, A. N., An All-Organic Non-aqueous Lithium-Ion Redox Flow Battery. *Advanced Energy Materials* **2012,** *2* (11), 1390-1396.

53. Sevov, C. S.; Brooner, R. E. M.; Chénard, E.; Assary, R. S.; Moore, J. S.; Rodríguez-López, J.; Sanford, M. S., Evolutionary Design of Low Molecular Weight Organic Anolyte Materials for Applications in Nonaqueous Redox Flow Batteries. *Journal of the American Chemical Society* **2015,** *137* (45), 14465-14472.

54. Sevov, C. S.; Fisher, S. L.; Thompson, L. T.; Sanford, M. S., Mechanism-Based Development of a Low-Potential, Soluble, and Cyclable Multielectron Anolyte for Nonaqueous Redox Flow Batteries. *Journal of the American Chemical Society* **2016,** *138* (47), 15378-15384.

55. Sevov, C. S.; Hickey, D. P.; Cook, M. E.; Robinson, S. G.; Barnett, S.; Minteer, S. D.; Sigman, M. S.; Sanford, M. S., Physical Organic Approach to Persistent, Cyclable, Low-Potential Electrolytes for Flow Battery Applications. *Journal of the American Chemical Society* **2017,** *139* (8), 2924-2927.

56. Potash, R. A.; McKone, J. R.; Conte, S.; Abruña, H. D., On the Benefits of a Symmetric Redox Flow Battery. *Journal of The Electrochemical Society* **2016,** *163* (3), A338-A344.

57. Duan, W.; Vemuri, R. S.; Milshtein, J. D.; Laramie, S.; Dmello, R. D.; Huang, J.; Zhang, L.; Hu, D.; Vijayakumar, M.; Wang, W.; Liu, J.; Darling, R. M.; Thompson, L.; Smith, K.; Moore, J. S.; Brushett, F. R.; Wei, X., A symmetric organic-based nonaqueous redox flow battery and its state of charge diagnostics by FTIR. *Journal of Materials Chemistry A* **2016,** *4* (15), 5448-5456.

58. Janoschka, T.; Friebe, C.; Hager, M. D.; Martin, N.; Schubert, U. S., An Approach Toward Replacing Vanadium: A Single Organic Molecule for the Anode and Cathode of an Aqueous Redox-Flow Battery. *ChemistryOpen* **2017,** *6* (2), 216-220.

59. Cabral, D.; Howlett, P. C.; Pringle, J. M.; Zhang, X.; MacFarlane, D., Electrochemistry of tris(2,2'-bipyridyl) cobalt(II) in ionic liquids and aprotic molecular solvents on glassy carbon and platinum electrodes. *Electrochimica Acta* **2015,** *180*, 419-426.

60. Laramie, S. M.; Milshtein, J. D.; Breault, T. M.; Brushett, F. R.; Thompson, L. T., Performance and cost characteristics of multi-electron transfer, common ion exchange non-aqueous redox flow batteries. *Journal of Power Sources* **2016,** *327*, 681-692.

61. UniEnergy Technologies Announces Commissioning of Largest Capacity Flow Battery in North America and Europe. http://www.uetechnologies.com.

62. K. Santhanam, A. B., Chemiluminescence of Electrogenerated 9,10-Diphenylanthracene anion radical. *Journal of the American Chemical Society* **1965,** *87* (1), 139-140.

63. K. Santhanam, A. B., The electrochemical reduction of 9,10-Diphenylanthracene. *Journal of the American Chemical Society* **1966,** *88* (12), 2669-2675.

64. L. O. Wheeler, K. S. V. S., A. Bard, Electron Spin Resonance Spectra of 9,10-Diphenylanthracene Anion and Cation Radicals. *Journal of Physical Chemistry* **1966,** *70* (2), 404-406.

65. Sioda, R. E., Electrolytic Oxidation of 9,10-diphenylanthracene and Properties of its Free Radical Cation and Anion. *Journal of Physical Chemistry* **1968,** *72* (7), 2322-2330.

66. Escalante-García, I. L.; Wainright, J. S.; Thompson, L. T.; Savinell, R. F., Performance of a Non-Aqueous Vanadium Acetylacetonate Prototype Redox Flow Battery: Examination of Separators and Capacity Decay. *Journal of The Electrochemical Society* **2015,** *162* (3), A363-A372.

67. Kenneth Michaels, G. H., Cost Projections for Redox Energy Storage Systems. DOE/NASA, Ed. United Technologies Corporation, 1980; p 112.

68. Eckroad, S., Vanadium Redox Flow Batteries. *EPRI Report* **2007,** *1014836*.

69. Darling, R. M.; Gallagher, K. G.; Kowalski, J. A.; Ha, S.; Brushett, F. R., Pathways to low-cost electrochemical energy storage: a comparison of aqueous and nonaqueous flow batteries. *Energy & Environmental Science* **2014,** *7* (11), 3459-3477.

70. Schoenung, S.; Eyer, J., Benefit/Cost Framework for Evaluating Modular Energy Storage. Energy, U. S. D. o., Ed. Sandia National Laboratories: 2008.

71. Jülch, V., Comparison of electricity storage options using levelized cost of storage (LCOS) method. *Appl. Energy* **2016,** *183*, 1594-1606.

72. *Lazard's Levelized Cost of Storage Version 2.0*; Lazard: 2016.

73. Arrow, K.; Cropper, M.; Gollier, C.; Groom, B.; Heal, G.; Newell, R.; Nordhaus, W.; Pindyck, R.; Pizer, W.; Portney, P.; Sterner, T.; Tol, R. S. J.; Weitzman, M., Determining Benefits and Costs for Future Generations. *Science* **2013,** *341* (6144), 349-350.

74. Kempton, W.; Tomić, J., Vehicle-to-grid power fundamentals: Calculating capacity and net revenue. *Journal of Power Sources* **2005,** *144* (1), 268-279.

75. Design Your Powerpack System. https://www.tesla.com/powerpack/design - / (accessed January 12th 2017).

76. Dmello, R.; Milshtein, J. D.; Brushett, F. R.; Smith, K. C., Cost-driven materials selection criteria for redox flow battery electrolytes. *Journal of Power Sources* **2016,** *330*, 261-272.

77. Schoenung, S. *Energy Storage Systems Cost Update*; Sandia National Laboratories: 2011.

78. Viswanathan, V.; Crawford, A.; Stephenson, D.; Kim, S.; Wang, W.; Li, B.; Coffey, G.; Thomsen, E.; Graff, G.; Balducci, P.; Kintner-Meyer, M.; Sprenkle, V., Cost and performance model for redox flow batteries. *Journal of Power Sources* **2014,** *247*, 1040-1051.

79. Arbabzadeh, M.; Johnson, J. X.; De Kleine, R.; Keoleian, G. A., Vanadium redox flow batteries to reach greenhouse gas emissions targets in an off-grid configuration. *Appl. Energy* **2015,** *146*, 397-408.

80. Joerissen, L.; Garche, J.; Fabjan, C.; Tomazic, G., Possible use of vanadium redox-flow batteries for energy storage in small grids and stand-alone photovoltaic systems. *Journal of Power Sources* **2004,** *127* (1–2), 98-104.

81. Kear, G.; Shah, A. A.; Walsh, F. C., Development of the all-vanadium redox flow battery for energy storage: a review of technological, financial and policy aspects. *International Journal of Energy Research* **2012,** *36* (11), 1105-1120.

82. Mark, M.; M, C. R.; JS, W.; AZ, T.; Che-Nan, S., An Analysis of the Contributions of Current Density and Voltage Efficiency. **2016,** - *7* (- 2), -.

83. Vanadium. USGS Mineral Commodity Summaries, 2017.

84. Mineral Commodity Summaries - Vanadium. Survey, U. S. G., Ed. 2015.

85. Henriksen, G. L.; Amine, K.; Liu, J.; Nelson, P. A. *Materials Cost Evaluation Report For High-Power Li-Ion HEV Batteries*; Argonne National Laboratory: 2002.

86. Pollak, P.; Romeder, G.; Hagedorn, F.; Gelbke, H.-P., Nitriles. In *Ullmann's Encyclopedia of Industrial Chemistry*, Wiley-VCH: 2005.

87. Fisher Scientific Best Buy Book. Fisher Scientific, 2015.

88. *Alternative Fuel Price Report*; U.S. Department of Energy: 2017.

89. BatPaC: A Lithium-Ion Battery Performance and Cost Model for Electric-Driven Vehicles. U.S. Department of Energy: 2015.

90. Chromium. USGS Mineral Commodity Summaries, 2017.

91. In *Coal Chemical Weekly*, BAIINFO: 2014; Vol. 14-31.

92. Babich, I. V.; Plyuto, Y. V.; VanderVoort, P.; Vansant, E. F., Thermal transformations of chromium acetylacetonate on silica surface. *Journal of Colloid and Interface Science* **1997,** *189* (1), 144-150.

93. Yurchenko, O.; Belikov, K.; Shevtsov, N., Investigation of chromium(III) acetylacetonate as a calibration reference material for atomic absorption spectroscopy. *Microchimica Acta* **2008,** *160* (1-2), 109-112.

94. Shinkle, A. A.; Sleightholme, A. E. S.; Thompson, L. T.; Monroe, C. W., Electrode kinetics in non-aqueous vanadium acetylacetonate redox flow batteries. *Journal of Applied Electrochemistry* **2011,** *41* (10), 1191-1199.

95. Landsberg, R.; Janietz, P.; Prugel, M., On the electrochemical reduction of some Cr(III) complexes in DMSO investigated by cyclic voltammetry. *Monatshefte für Chemie* **1979,** *110* (4), 831-840.

96. Beaver, B. D.; Hall, L. C.; Lukehart, C. M.; Preston, L. D., Reactions of coordinated molecules. XXVII. Cyclic voltammetry of several transition metal metalla-acetylacetonate complexes. *Inorg. Chim. Acta* **1981,** *47*, 25-30.

97. Urbanczyk, A.; Debek, E.; Kalinowski, M. K., Kinetics of the electroreduction of tris(acetylacetonato) chromium(iii) in nonaqueous solvents. *Journal of Electroanalytical Chemistry* **1995,** *389* (1-2), 141-148.

98. Murray, R. W.; Hiller, L. K., Supporting electrolyte effects in nonaqueous electrochemistry. Coordinative relaxation reactions of reduced metal acetylacetonates in acetonitrile. *Analytical Chemistry* **1967,** *39* (11), 1221-1229.

99. Gritzner, G.; Murauer, H.; Gutmann, V., Polarographic and voltammetric behavior of acetylacetonato and hexafluoroacetylacetonato complexes in acetonitrile. *Journal of Electroanalytical Chemistry* **1979,** *101* (2), 177-183.

100. Landsberg, R.; Janietz, P.; Prugel, M., Ligand exchange reactions of some Cr(III) complexes investigated by cyclic voltammetry. *Monatshefte fur Chemie* **1978,** *109* (6), 1287-1294.

101. Handy, R. F.; Lintvedt, R. L., Polarographic reduction potentials and substituent group electronic effects for a series of tris(1, 3, 5-diketonato)chromium(III) chelates in dimethyl sulfoxide and in dioxane-water. *Inorganic Chemistry* **1974,** *13* (4), 893-896.

102. Tsiamis, C.; Hadjikostas, C. C.; Karageorgiou, S.; Manoussakis, G., Ligand field, electronic and solvent effects in the non-aqueous electrochemistry of tris(β-dionato)chromium(III) chelates. *Inorg. Chim. Acta* **1988,** *143* (1), 17-23.

103. Liu, R.; Conradie, J., Tris(β-diketonato)chromium(III) complexes: Effect of the β-diketonate ligand on the redox properties. *Electrochimica Acta* **2015,** *185*, 288-296.

104. Burnett, J. N.; Hiller, L. K.; Murray, R. W., Supporting Electrolyte Effects in Electrochemistry: Copper and Mercury Acetylacetonates in Acetonitrile Solvent. *Journal of The Electrochemical Society* **1970,** *117* (8), 1028-1032.

105. Misumi, S.; Aihara, M.; Nonaka, Y., Polarography of Iron(III)- and Europium(III)-Acetylacetonate Complexes in *N*,*N*-Dimethylformamide. *Bulletin of the Chemical Society of Japan* **1970,** *43* (3), 774-778.

106. Kalinowski, M. K.; Ćmiel, A., Solvent–solute interaction. Solvent and supporting electrolyte effects in non-aqueous electrochemistry of tris(acetylacetonato)iron(III). *Inorg. Chim. Acta* **1981,** *49*, 179-183.

107. Hartley, R. J.; Faulkner, L. R., Quenching and possible coulombic complexation of the pyrene-n,n-dimethylaniline exciplex by tetraalkylammonium salts. *Journal of the American Chemical Society* **1985,** *107* (12), 3436-3442.

108. Kucernak, A.; Jiang, J. H., Mesoporous platinum as a catalyst for oxygen electroreduction and methanol electrooxidation. *Chemical Engineering Journal* **2003,** *93* (1), 81-90.

109. Compton, R. G.; Banks, C. E., *Understanding Voltammetry*. World Scientific: 2007.

110. Endo, A.; Hoshino, Y.; Hirakata, K.; Takeuchi, Y.; Shimizu, K.; Furushima, Y.; Ikeuchi, H., Electrochemistry of Tris(β-diketonato)ruthenium(III) Complexes at Platinum Electrodes in Nonaqueous Solutions and Substituent Effects on Their Reversible Half-Wave Potentials. *Bulletin of the Chemical Society of Japan* **1989,** *62* (3), 709-716.

111. Bertrand, J. A.; Dollase, W. A.; Cotton, F. A., A spectroscopic study of the behavior of rhenium chlorides in molten salts. *Journal of the American Chemical Society* **1963,** *85* (9), 1349-1351.

112. Lomont, J. P.; Harris, C. B., Primary photochemical dynamics of metal carbonyl dimers and clusters in solution: Insights into the results of metal-metal bond cleavage from ultrafast spectroscopic studies. *Inorg. Chim. Acta* **2015,** *424*, 38-50.

113. Bond, A. M.; Martin, R. L.; Masters, A. F., Influence of oxygen and sulfur donor atoms on the electrochemistry of transition metal tris chelates. *Inorganic Chemistry* **1975,** *14* (6), 1432-1435.

114. Neal, T. E.; Murray, R. W., Autocatalysis of kinetic wave of acetylacetone in acetonitrile solvent. *Analytical Chemistry* **1970,** *42* (13), 1654-1656.

115. Kitamura, M.; Sasaki, K.; Imai, H., Studies of electrode processes of oxovanadium(iv) .4. catalytic reduction of acetylacetone coupled with cathodic reduction of "bis(acetylacetonato)oxovanadium(iv). *Bulletin of the Chemical Society of Japan* **1977,** *50* (12), 3199-3201.

116. Barnum, D. W., Electronic Absorption Spectra of Acetyl-acetonato Complexes .1. Complexes With Trivalent Transition Metal Ions. *Journal of Inorganic & Nuclear Chemistry* **1961,** *21* (3-4), 221-237.

117. Buckley, D. N.; Gao, X.; Lynch, R. P.; Quill, N.; Leahy, M. J., Towards Optical Monitoring of Vanadium Redox Flow Batteries (VRFBs): An Investigation of the Underlying Spectroscopy. *Journal of the Electrochemical Society* **2014,** *161* (4), A524-A534.

118. Forman, A.; Orgel, L. E., The Jahn-Teller effect in manganic acetylacetonate. *Molecular Physics* **1959,** *2* (4), 362-366.

119. Heineman, W. R.; Burnett, J. N.; Murray, R. W., Optically transparent thin-layer electrodes: studies of iron(II)-(III) acetylacetonate ligand exchange reactions in acetonitrile. *Analytical Chemistry* **1968,** *40* (13), 1970-1973.

120. Costa, G.; Puxeddu, A., On chromous acetylacetonate. *Journal of Inorganic and Nuclear Chemistry* **1958,** *8*, 104-112.

121. Cotton, F. A.; Rice, C. E.; Rice, G. W., The crystal and molecular structures of bis(2,4-pentanedionato)chromium. *Inorg. Chim. Acta* **1977,** *24*, 231-234.

122. Visco, R. E.; Chandross, E. A., Electroluminescence in Solutions of Aromatic Hydrocarbons. *Journal of the American Chemical Society* **1964,** *86* (23), 5350-5351.

123. L. O. Wheeler, K. S. V. S., A. Bard, Electron Spin Resonance Spectra of 9-phenylanthracene and 9,10-Diphenylanthracene Anion Radicals. *Journal of Physical Chemistry* **1967,** *71* (7), 2223-2227.

124. Hazelrigg, M. J., A. J. Bard, Chronocoulometric study of adsorption off 9,10-diphenylanthracene anion in dimethylformamide solutions at a platinum electrode. *Electroanalytical Chemistry and Interfacial Electrochemistry* **1973,** *46*, 141-144.

125. Schmidt, R.; Gottling, S.; Leusser, D.; Stalke, D.; Krause, A. M.; Wurthner, F., Highly soluble acenes as semiconductors for thin film transistors. *J. Mater. Chem.* **2006,** *16* (37), 3708-3714.

126. Zimmerman, H. K., The Experimental Determination of Solubilities. *Chemical Reviews* **1952,** *51* (1), 25-65.

127. Herod, A. A.; Ladner, W. R.; Stokes, B. J.; Berry, A. J.; Games, D. E., Coal Tar Analysis by LC/MS. *Preprints / American Chemical Society, Division of Fuel Chemistry* **1986**, 181-190.

128. Cotton, F. A., *Inorganic Syntheses*. McGraw-Hill, Inc.: 1972; Vol. 13, p 121-124.

129. S. Kotha, A. G., K. Deodhar, Synthesis of Symmetrical and Unsymmetrical 9,10-Diarylanthracene Derivatives via Bis-Suzuki-Miyaura Cross-Coupling Reaction. *Synthesis* **2004,** *4*, 0549-0557.

130. Hauptvogel, I. M.; Biedermann, R.; Klein, N.; Senkovska, I.; Cadiau, A.; Wallacher, D.; Feyerherm, R.; Kaskel, S., Flexible and Hydrophobic Zn-Based Metal-Organic Framework. *Inorganic Chemistry* **2011,** *50* (17), 8367-8374.

131. Player, M. R.; Meegalla, S. K.; Illig, C. R.; Chen, J.; Wilson, K. J.; Lee, Y. K.; Parks, D. J.; Huang, H.; Patel, S.; Lu, T., PDE 10a Inhibitors for the Treatment of Type II Diabetes. Google Patents: 2014.

132. CRC Handbook of Chemistry and Physics. 97th ed.; Haynes, W. M., Ed. CRC Press: Boca Raton, 2016-2017.

133. Milshtein, J. D.; Kaur, A. P.; Casselman, M. D.; Kowalski, J. A.; Modekrutti, S.; Zhang, P. L.; Harsha Attanayake, N.; Elliott, C. F.; Parkin, S. R.; Risko, C.; Brushett, F. R.; Odom, S. A., High current density, long duration cycling of soluble organic active species for non-aqueous redox flow batteries. *Energy & Environmental Science* **2016,** *9* (11), 3531-3543.

134. Saraidaridis, J. D.; Bartlett, B. M.; Monroe, C. W., Spectroelectrochemistry of Vanadium Acetylacetonate and Chromium Acetylacetonate for Symmetric Nonaqueous Flow Batteries. *Journal of The Electrochemical Society* **2016,** *163* (7), A1239-A1246.

135. Nawi, M. A.; Riechel, T. L., Electrochemical studies of vanadium(III) and vanadium(IV) acetylacetonate complexes in dimethylsulfoxide. *Inorganic Chemistry* **1981,** *20* (7), 1974-1978.

136. Bruggeman, D. A. G., Berechnung verschiedener physikalischer Konstanten von heterogenen Substanzen. I. Dielektrizitätskonstanten und Leitfähigkeiten der Mischkörper aus isotropen Substanzen. *Annalen der Physik* **1935,** *416* (7), 636-664.

137. Newman, J. S.; Thomas-Alyea, K. E., *Electrochemical Systems*. 3rd ed.; John Wiley & Sons Inc.: Hoboken, New Jersey, 2004.

138. Friedl, J.; Stimming, U., Determining Electron Transfer Kinetics at Porous Electrodes. *Electrochimica Acta* **2017,** *227*, 235-245.

A. Appendix

A.1 Oxford Laboratory

There was another significant research endeavor that falls outside the scope of the symmetric nonaqueous RFB topic: construction of a new laboratory in Oxford to perform research on this and other electrochemical topics. The Monroe Group moved, piece-meal, from University of Michigan to University of Oxford over the period between July 2015 and January 2016. Upon arrival in October 2015 the author began discussing with University of Oxford Estates Services about facility requirements for the Monroe Group laboratory: a 1200 square-foot laboratory space in Begbroke Science Park. These discussions produced a laboratory with a 1000 square-foot open-plan laboratory space, thermography room, chemical storage closet, 9.5 meters of fixed benching, 16 meters of portable benching, corresponding under-bench storage, two 2-meter fume hoods, 3 sinks, an ultrapure water purification system, electrical supplies capable of delivering high amperage power to specialty equipment, 3 air-conditioning units, two bespoke laboratory gas lines for argon and hydrogen gasses fed from cylinders outside the building, two backup argon gas lines, a gas detection system and many additional smaller features. These facilities fully support the group's research activities.

Beyond laboratory design, the author executed the market research, tender, order, and installation of all the most capital-intensive equipment in the laboratory with few exceptions. This included two 4-port Inert PureLab gloveboxes with regenerable solvent traps, air-conditioning units, custom arrays of electrical and gas feedthroughs, and one with a heated mini-antechamber. Other expensive and time-intensive equipment

orders included two Inert PureSolv Micro solvent purification systems, three Autolab PGStat 302N potentiostats, and a Maccor 4000 series battery tester.

From first discussions planning the space in October 2015, renovations began in January 2016 and were mostly completed by June 2016. The gloveboxes arrived by the end of July 2016 and led to the laboratory becoming operational by August. The final delivery of equipment from University of Michigan arrived in January 2017, giving the space its full capabilities.



Figure A.1. Monroe Laboratory at the University of Oxford.



Figure A.2. Monroe Laboratory at the University of Oxford.



Figure A.3. Monroe Laboratory at the University of Oxford.

A.2 Synthesis and Characterization

A.2.1 9,10-di-p-tolylanthracene (DMPA):

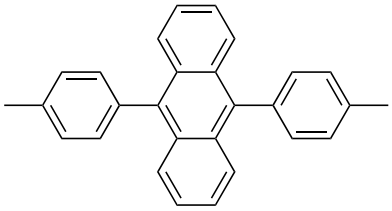

Figure A.4. Chemical structure of DMPA.

Following the general procedure described in Figure 4.2 and guided by reports,[129] 9,10-dibromoanthracene (DBA, 1.00 g, 2.98 mmol), 4-methylphenylboronic acid (1.00 g, 7.35 mmol), and sodium carbonate (0.30 g, 2.89 mmol) were charged into a 100 mL three-necked flask and purged with N_2 for 15 min. Separately, 9.5 mL of water, 28.5 mL of toluene, and 28.5 mL of THF were added together and bubbled with N_2 for 15 min. Palladium *tetrakis* triphenylphosphine ($Pd(PPh_3)_4$, 0.33 g, 0.288 mmol), synthesized as reported and stored in a N_2 glovebox freezer,[128] was added to the reactor and blanketed with N_2. The N_2 bubbled solution was added to the reactor by cannula transfer. The mixture was stirred and refluxed for 72 hours under N_2. Crude product was extracted with ether, washed with brine and dried with $MgSO_4$. The solution was filtered and the solvent was removed by rotary evaporation. The crude solid was purified by column chromatography with hexanes as eluent. The fractions were monitored by thin layer chromatography (TLC) with a UV lamp. Fractions containing the desired di-substituted anthracene product (R_f = 0.2, hexanes) were collected, and the solvent was removed by rotary evaporation. Residual solvent impurities were removed under high vacuum (20 mTorr, 1+ hours) to yield **DMPA** as a pale yellow powder (0.54 g, 52% yield). The ^{1}H NMR spectrum shown in Figure A.5 are consistent with the molecular structure and previous reports.[129]

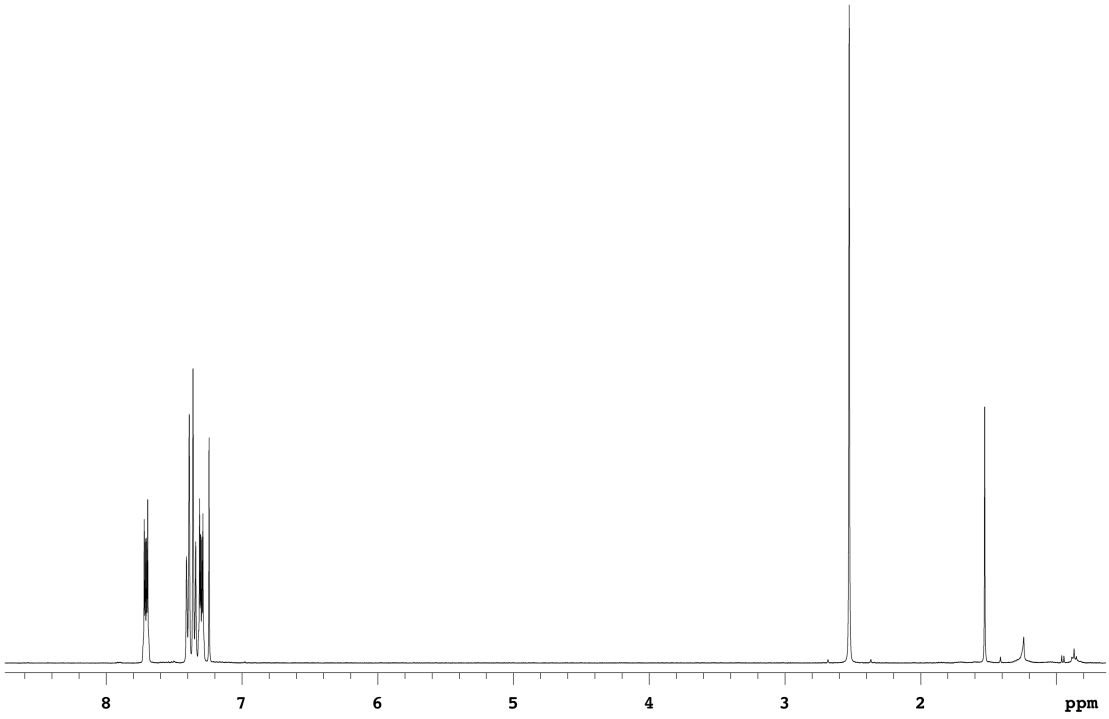

Figure A.5. ^{1}H NMR of DMPA.

A.2.2 9,10-bis(4-methoxyphenyl)anthracene (DMOPA):

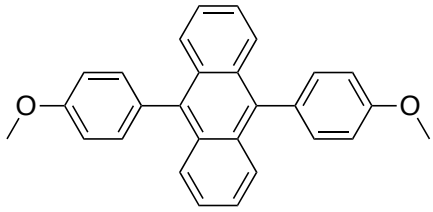

Figure A.6. Chemical structure of DMOPA.

Following the general procedure described in Figure 4.2 and guided by reports,[129] DBA (40 mg, 0.12 mmol), 4-methoxybenzeneboronic acid (58 mg, 0.38 mmol), and sodium carbonate (32 mg, 0.3 mmol) were charged into a 25 ml three-necked flask and purged with N_2 for 15 min. Separately, 1 mL of water, 3 mL of toluene, and 3 mL of THF were added together and bubbled with N_2 for 15 min. $Pd(PPh_3)_4$ (36.1 mg, 0.03 mmol), synthesized as reported and stored in a N_2 glovebox freezer,[128] was added to the reactor and blanketed with N_2. The N_2 bubbled solution was added to the reactor by cannula transfer. The mixture was stirred and refluxed for 72 hours under N_2. Crude product was extracted with ether, washed with brine and dried with $MgSO_4$. The solvent was removed from the filtered solution by rotary evaporation and the crude material was purified by column chromatography with 4% ethyl acetate in hexanes as eluent. The fractions were monitored by TLC with a UV lamp. Fractions containing the desired di-substituted anthracene product (R_f = 0.3, 4% ethyl acetate in hexanes) were collected, and the solvent was removed by rotary evaporation. Residual solvent impurities were removed under high vacuum (20 mTorr, 1+ hours) to yield **DMOPA** as a yellow powder (13.5 mg, 34% yield). The ^1H NMR spectrum shown in Figure A.7 is consistent with the molecular structure and previous reports.[129]

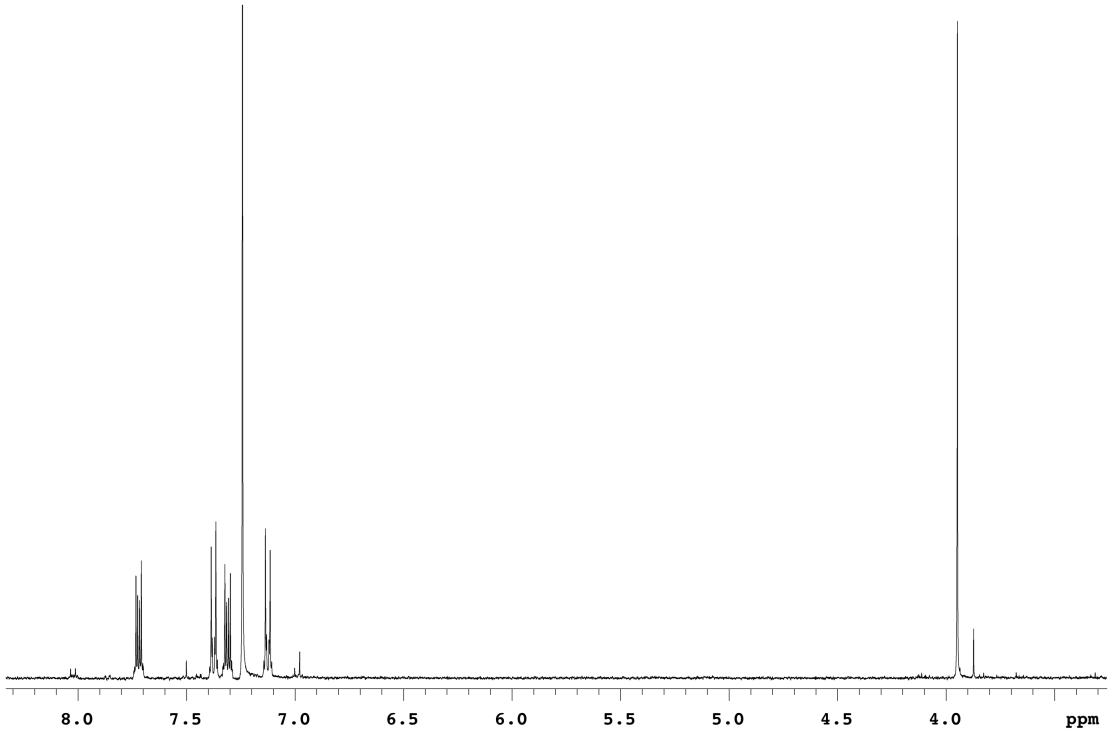

Figure A.7. ^{1}H NMR of DMOPA.

A.2.3 4,4'-(anthracene-9,10-diyl)dibenzoic acid (DMBA):

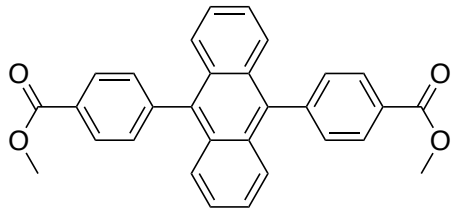

Figure A.8. Chemical structure of DMBA.

Following the general procedure described in Figure 4.2 and guided by reports,[130] DBA (1.80 g, 5.4 mmol) and 4-methoxycarbonylbenzeneboronic acid (2.12 g, 11.8 mmol) were charged into a 250 mL three-necked flask and purged with N_2 for 15 min. Separately, 100 mL of diglyme was bubbled with N_2 for 15 min. Cesium fluoride (3 g, 19.7 mmol) and $Pd(PPh_3)_4$ (36.1 mg, 0.03 mmol), synthesized as reported and stored in a N_2 glovebox freezer,[128] were added to the reactor and blanketed with N_2. The N_2 bubbled solution was added to the reactor by cannula transfer. The mixture reacted at 120°C for 72 hours under N_2. Solvent was removed under heat and vacuum (100°C and 100 mTorr). The remaining solid was suspended in diethyl ether and filtered. The organic solvent was removed by rotary evaporation. The crude material was purified by column chromatography with dichloromethane as eluent. The fractions were monitored by TLC with a UV lamp. Fractions containing the desired di-substituted anthracene product (R_f = 0.2, dichloromethane) were collected, and the solvent was removed by rotary evaporation. Residual solvent impurities were removed under high vacuum (20 mTorr, 1+ hours) to yield DMBA as a pale yellow powder (1.42 g, 62% yield). The ^{1}H NMR spectrum shown in Figure A.9 is consistent with the molecular structure and previous reports.[130]

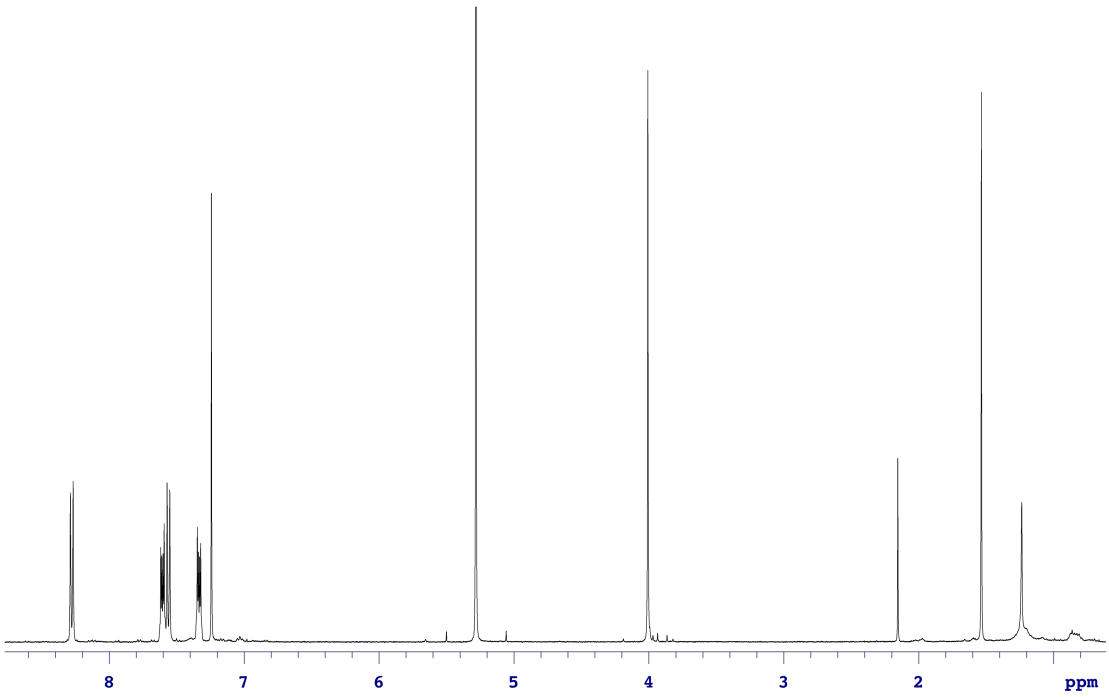

Figure A.9. ^{1}H NMR of DMBA.

A.2.4 Bis(2-methoxyethyl) 4,4'-(anthracene-9,10-diyl)dibenzoate (DePA)

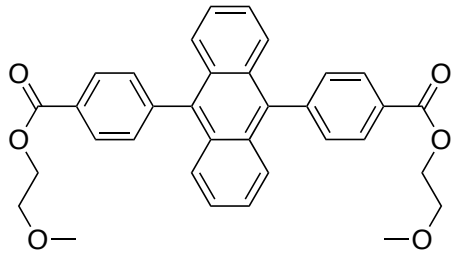

Figure A.10. Chemical structure of DePA.

Following the general procedure described in Figure 4.6, DMBA (356 mg, 0.80 mmol) was allowed to react with 2-methoxyethanol (7 mL, 88.7 mmol) in a Lewis acidic environment caused by $MgBr_2$-Et_2O(473 mg, 1.83 mmol) under N_2 for 48 hours at 130 °C. Upon cooling, crystal formation was observed. The crystals were filtered and washed with ethanol. Residual solvent impurities were removed under high vacuum (20 mTorr, 1+ hours) to yield **DePA** (R_f = 0.6, 50% ethyl acetate in hexanes) as yellow crystals (320 mg, 75% yield). The ^{1}H NMR spectrum shown in Figure A.11 is consistent with the expected spectrum of the structure and the molecular weight, 534 g/mol as determined by GC-MS, corroborates the molecular mass of this structure.

^{1}H NMR (401 MHz, Chloroform-*d*): δ 8.30 (d, *J* = 8.2 Hz, 4H), 7.60 (dd, *J* = 6.8, 3.3 Hz, 4H), 7.56 (d, *J* = 8.2 Hz, 4H), 7.33 (dd, *J* = 6.8, 3.2 Hz, 4H), 4.60–4.52 (m, 4H), 3.83–3.75 (m, 4H), 3.47 (s, 6H).

HR-MS (ESI$^+$): exact mass calculated for $C_{34}H_{30}NaO_6^+$: *m*/*z* 557.1940 ([Na-M]$^+$); Found, 557.1937 ([Na-M]$^+$).

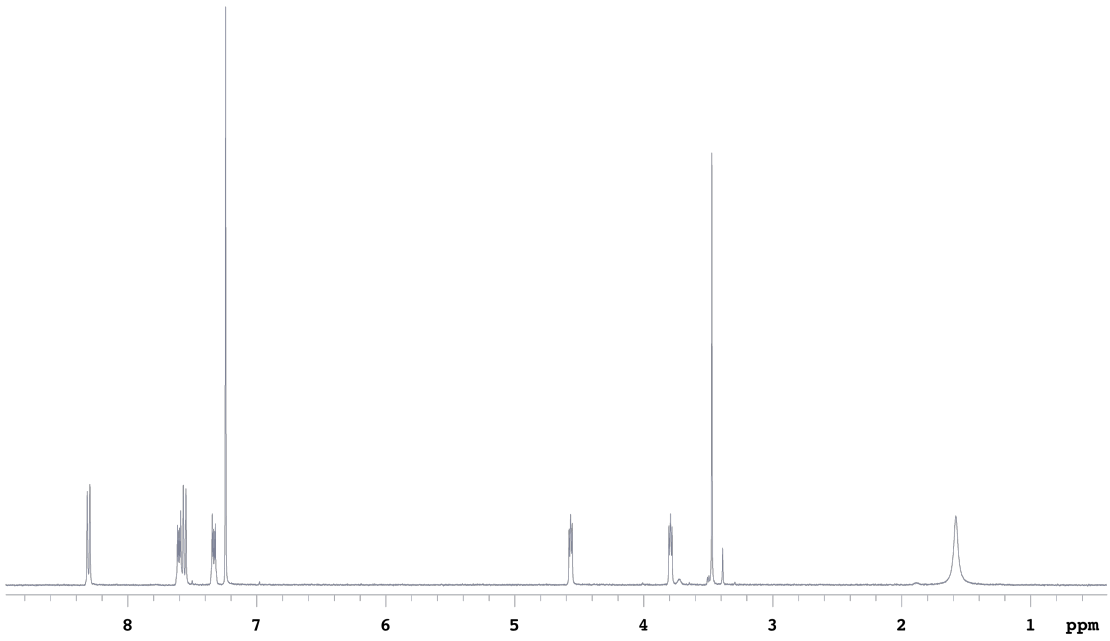

Figure A.11. ^{1}H NMR of DePA.

A.2.5 Bis(2-(2-methoxyethoxy)ethyl) 4,4'-(anthracene-9,10-diyl)dibenzoate (DdPA)

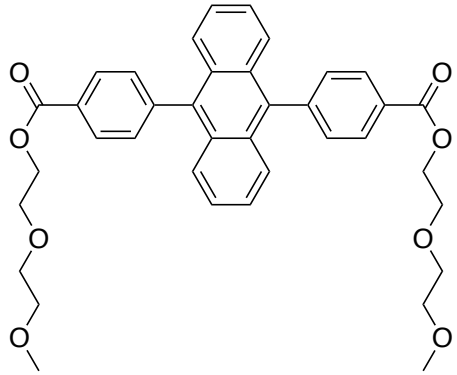

Figure A.12. Chemical Structure of DdPA.

Following the general procedure described in Figure 4.6, DMBA(0.2 g, 0.45 mmol) was allowed to react with 2-(2-methoxyethoxy)ethanol (4 mL, 34 mmol) in a Lewis acidic environment caused by $MgBr_2$-Et_2O(0.11 , 0.45 mmol) under N_2 for 48 hours at 150 °C. Remaining 2-(2-methoxyethoxy)ethanol was evaporated under vacuum (100°C and 100 mTorr). This left behind a residue of tarry brown material, which was suspended in dichloromethane, run through a plug of silica and washed with ethyl acetate. Washing continued until the eluent from the plug stopped giving off an iridescent purple color under visible light (indicative of dissolved DdPA). The solvent was removed *via* rotary evaporator and the crude product was purified using column chromatography with 40% ethyl acetate in hexanes. The fractions were monitored by TLC with a UV lamp. Fractions containing the desired trans-esterified anthracene product (R_f = 0.2, 50% ethyl acetate in hexanes) were collected, and the solvent was removed by rotary evaporation. Residual solvent impurities were removed under high vacuum (20 mTorr, 1+ hours) to yield **DdPA** as an oily yellow powder (129 mg, 46% yield). The ^{1}H NMR spectrum shown in Figure A.13 is consistent with the expected

spectrum of the structure and the molecular weight from GC-MS, 622 g/mol, corroborates the molecular mass of this structure.

^{1}H NMR (401 MHz, Chloroform-*d*): δ 8.30 (d, *J* = 8.0 Hz, 4H), 7.61 (dd, *J* = 6.8, 3.2 Hz, 4H), 7.56 (d, *J* = 8.0 Hz, 4H), 7.33 (dd, *J* = 6.8, 3.1 Hz, 4H), 4.63–4.53 (m, 4H), 3.95–3.86 (m, 4H), 3.79–3.72 (m, 4H), 3.64–3.56 (m, 4H), 3.40 (s, 6H).

HR-MS (ESI$^+$): exact mass calculated for $C_{38}H_{38}NaO_8^+$: *m*/*z* 645.2465 ([Na-M]$^+$); Found, 645.2472 ([Na-M]$^+$).

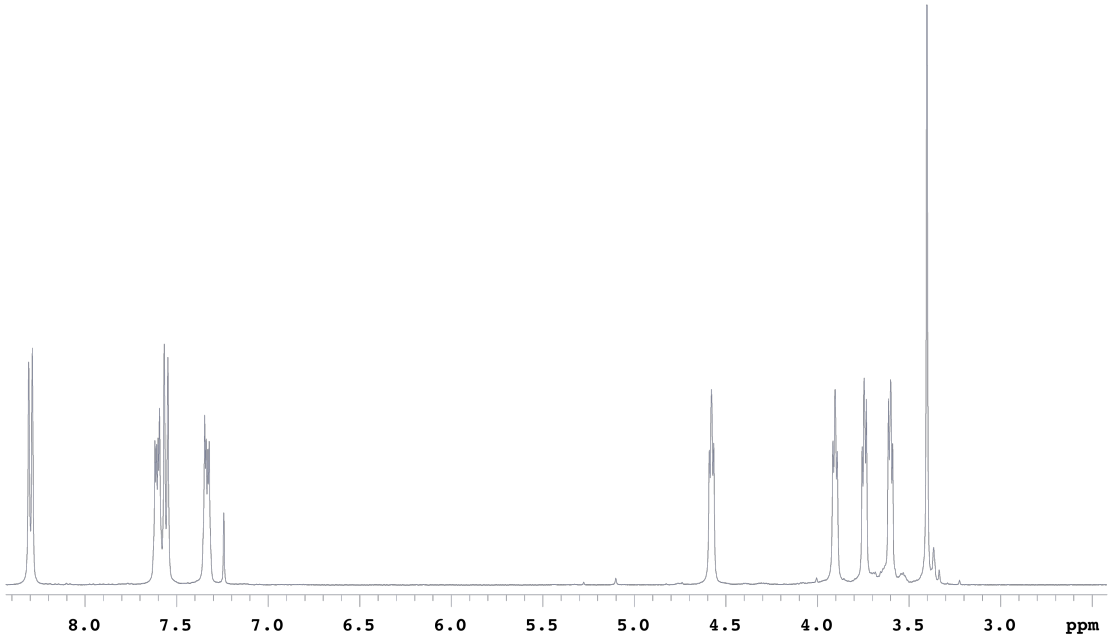

Figure A.13. ^{1}H NMR of DdPA.

A.2.6 dimethyl 3,3'-(anthracene-9,10-diyl)dibenzoate (*m*-DMBA)

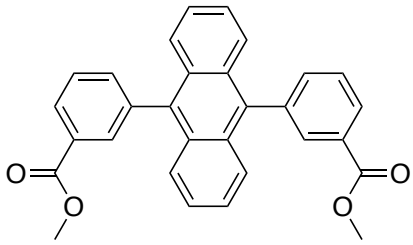

Figure A.14. Chemical structure of *m*-DMBA.

Following the general procedure described in Figure 4.2 and guided by reports,[130], DBA (0.86 g, 2.6 mmol) and 3-methoxycarbonylbenzeneboronic acid (1.02 g, 5.67 mmol) were charged into a 100 mL three-necked flask and purged with N_2 for 15 min. Separately, 48 mL of diglyme was bubbled with N_2 for 15 min. Cesium fluoride (1.42 g, 9.3 mmol) and $Pd(PPh_3)_4$ (0.188 g, 0.16 mmol), synthesized as reported and stored in a N_2 glovebox freezer,[128] were added to the reactor and blanketed with N_2. The N_2 bubbled solution was added to the reactor by cannula transfer. The mixture reacted at 120 °C for 48 hours under N_2. Solvent was removed under heat and vacuum (100°C and 100 mTorr). The remaining solid was suspended in diethyl ether and filtered. The organic solvent was removed by rotary evaporation. The crude material was purified by column chromatography with dichloromethane as eluent. The fractions were monitored by TLC with a UV lamp. Fractions containing the desired di-substituted anthracene product (R_f = 0.2, dichloromethane) were collected, and the solvent was removed by rotary evaporation. Residual solvent impurities were removed under high vacuum (20 mTorr, 1 h) to yield ***m*-DMBA** as a pale yellow powder (0.67 g, 58% yield). Unfortunately, successful synthesis of this material coincided with a move from University of Michigan to University of Oxford and NMR characterization was not performed on the material.

A.2.7 9,10-bis(4-(2-(2-methoxyethoxy)ethoxy)phenyl)anthracene (eDdPA)

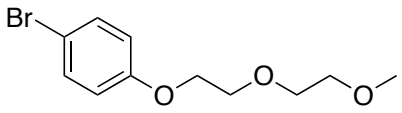

Figure A.15. Chemical structure of Br-Ph-dEG precursor to boronic acid reagent in eDdPA coupling reaction.

In order to produce a 4-(2-(2-methoxyethoxy)ethoxy)phenyl boronic acid ($B(OH)_2$-Ph-dEG) for the general reaction scheme described in Figure 4.2, 1-Bromo-4-(2-(2-methoxyethoxy)ethoxy)benzene (Br-Ph-dEG) was synthesized according to reports.[139] A 100 mL reaction flask was charged with NaH (0.512 g, 21.4 mmol) under an inert N_2 environment. Then, a solution of 20 mL of DMF and 4-bromophenol (3.11 g, 17.8 mmol) was added slowly to the reaction flask and stirred. While stirring, 1-bromo-2-(2-methoxyethoxy)ethane was slowly added and heated to 65 °C for 12 hours. The solution was concentrated under vacuum (100 mTorr, 65 °C), diluted with brine and extracted with ethyl acetate. Solvent was evaporated off in the presence of silica using a rotary evaporator. The charged silica was dry loaded onto a chromatography column and run with hexanes, building to 30% ethyl acetate in hexanes as the eluent. The fractions were monitored by TLC with a UV lamp. Fractions containing the desired 2(2-methoxyethoxy)ethoxy functionalized product (R_f = 0.25, 30% ethyl acetate in hexanes) were collected, and the solvent was removed by rotary evaporation. Residual solvent impurities were removed under high vacuum (20 mTorr, 1+ hours) to yield Br-Ph-dEG as a white powder (3.35 g, 67% yield). The ^{1}H NMR spectrum shown in Figure A.16 is consistent with the expected spectrum of the structure and the molecular weight, 274 g/mol as determined by GC-MS, corresponds to the molecular mass of the expected molecule.

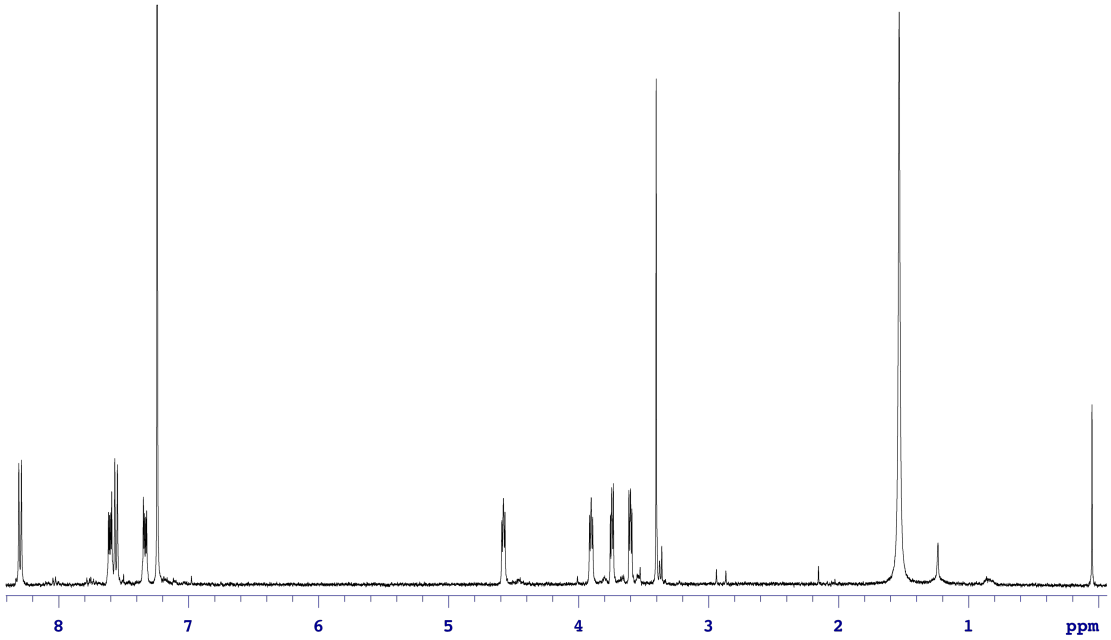

Figure A.16. ^{1}H NMR of bromide precursor with diethyleneglycoxy signature.

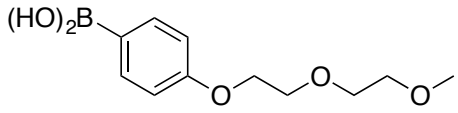

Figure A.17. Chemical structure of B(OH)$_2$-Ph-dEG reagent for eDdPA cross-coupling reaction.

Br-Ph-dEG still needed conversion to a boronic acid to participate in the cross-coupling reaction shown in Figure 4.2. A 1 M solution of 1-bromo-4-(2-(2-methoxyethoxy)ethoxy)benzene (3.35 g, 12 mmol) in diethyl ether (12 mL) was reacted with butyl lithium (5.1 mL) for 30 minutes at 0 °C. Afterwards, a diluted solution of triisopropyl borate (5.6 mL) in ether (6.4 mL) was added to the stirred solution, allowed to return to room temperature, and left to react for 12 hours. The resulting solution was acidified with 1 M HCl in water (100 mL), extracted with ethyl acetate, washed with brine, and dried with $MgSO_4$. The mixture was filtered and washed with hexanes. Solvent was removed with a rotary evaporator, yielding B(OH)$_2$-Ph-dEG as a white powder (1.7 g, 58% yield). Characterization by NMR shown in Figure A.18-19 reveal that the ^{1}H NMR spectrum is consistent with the chemical structure, but that ^{13}B NMR

spectrum is inconsistent with the expected boronic acid. The reaction was carried forward to see if cross-coupling would occur despite the unexpected ^{13}B NMR.

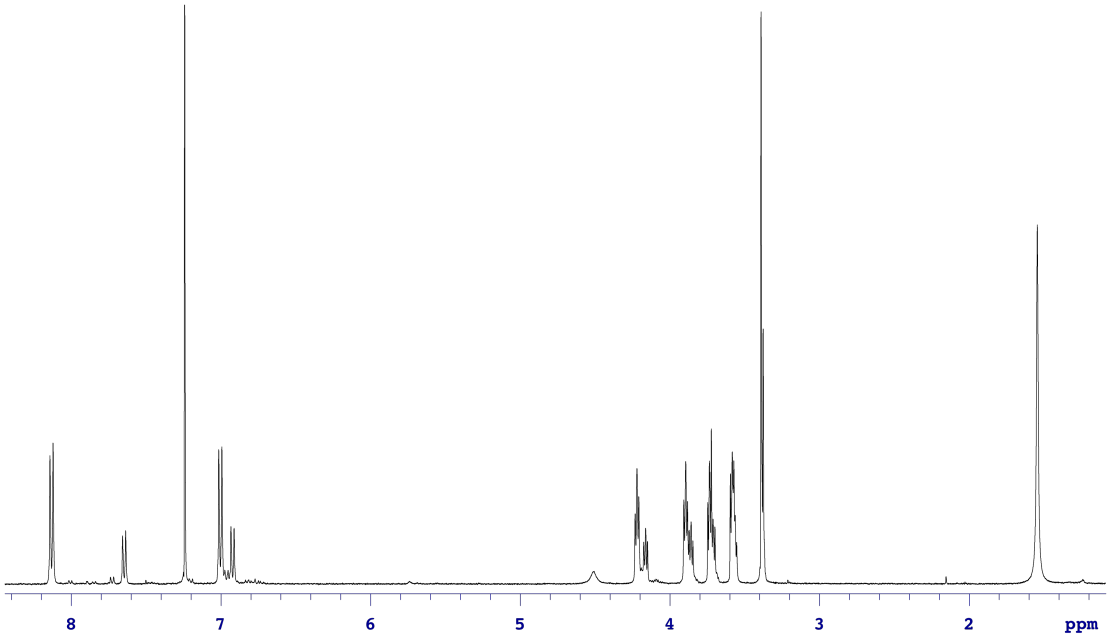

Figure A.18. ^{1}H NMR of the boronic acid reagent for eDdPA coupling reaction.

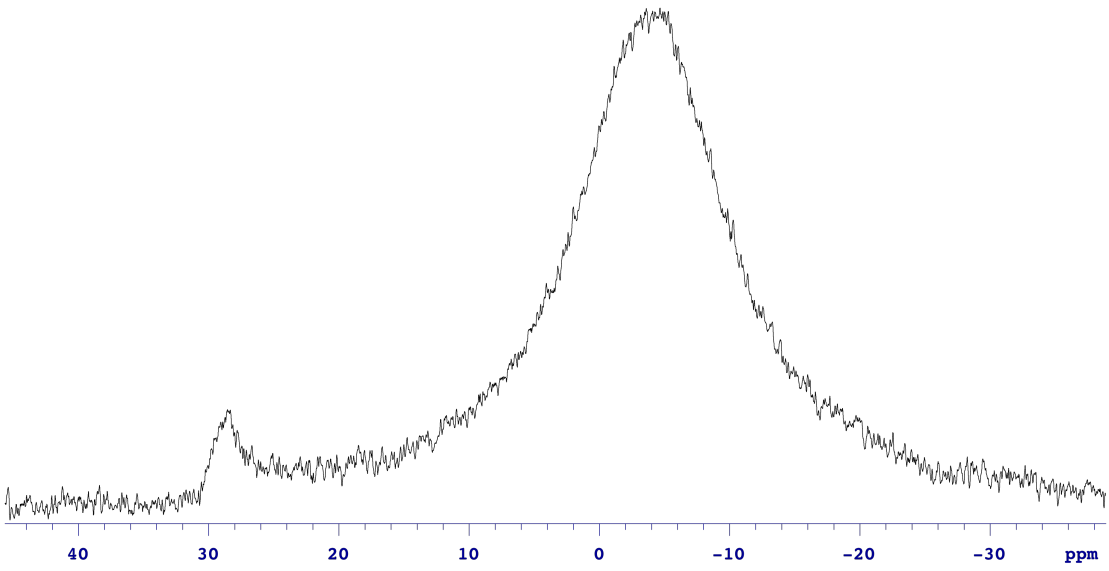

Figure A.19. ^{11}B NMR of the boronic acid reagent for eDdPA coupling reaction.

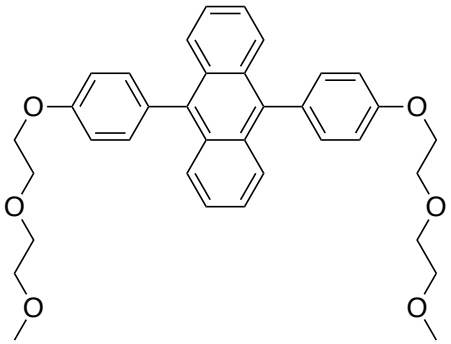

Figure A.20. Chemical Structue of eDdPA.

Following the general procedure described in Figure 4.2, DBA (0.09 g, 0.27 mmol), $B(OH)_2$-Ph-dEG (0.17 g, 0.71 mmol), sodium carbonate (0.0785 g, 0.74 mmol), $Pd(PPh_3)_4$ (0.0397 g, 0.034 mmol), synthesized as reported and stored in a N_2 glovebox freezer,[128] and 7 mL of THF were charged into a 50 mL three-necked flask from within a N_2 glovebox. Separately, 2.3 mL of water and 7 mL of toluene were added together and bubbled with N_2 for 15 min. The charged reactor was removed from the glovebox and the mixed solvent was added to the reactor *via* cannula transfer. The mixture was stirred and heated to 85 °C for 18 hours under N_2. Crude product was extracted with ethyl acetate, washed with brine and dried with $MgSO_4$. After filtration, the solvent was removed by rotary evaporation in the presence of silica. The crude solid, charged on silica, was loaded onto a chromotography column with hexanes and the product was isolated with 30 % ethyl acetate in hexanes as eluent. The fractions were monitored by TLC with a UV lamp. Fractions containing the desired di-substituted anthracene product (R_f = 0.1, 30 % ethyl acetate in hexanes) were collected, and the solvent was removed by rotary evaporation. Residual solvent impurities were removed under high vacuum (20 mTorr, 1+ hours) to yield **eDdPA** as a light brown powder (0.08 g, 52% yield). The ^{1}H NMR spectrum shown in A.21 is consistent with the chemical structure and the molecular weight, 566 g/mol as determined by GC-MS, corroborates this structure.

^{1}H NMR (401 MHz, Chloroform-*d*): δ 7.71 (dd, *J* = 6.8, 3.3 Hz, 4H), 7.35 (d, *J* = 8.5 Hz, 4H), 7.31 (dd, *J* = 6.8, 3.2 Hz, 4H), 7.13 (d, *J* = 8.6 Hz, 4H), 4.33–4.25 (m, 4H), 4.00–3.92 (m, 4H), 3.79 (dd, *J* = 5.6, 3.7 Hz, 4H), 3.63 (dd, *J* = 5.6, 3.7 Hz, 4H), 3.42 (s, 6H).

HR-MS (ESI$^+$): exact mass calculated for $C_{36}H_{38}NaO_6^+$: *m*/*z* 589.2566 ([Na-M]$^+$); Found, 589.2563 ([Na-M]$^+$).

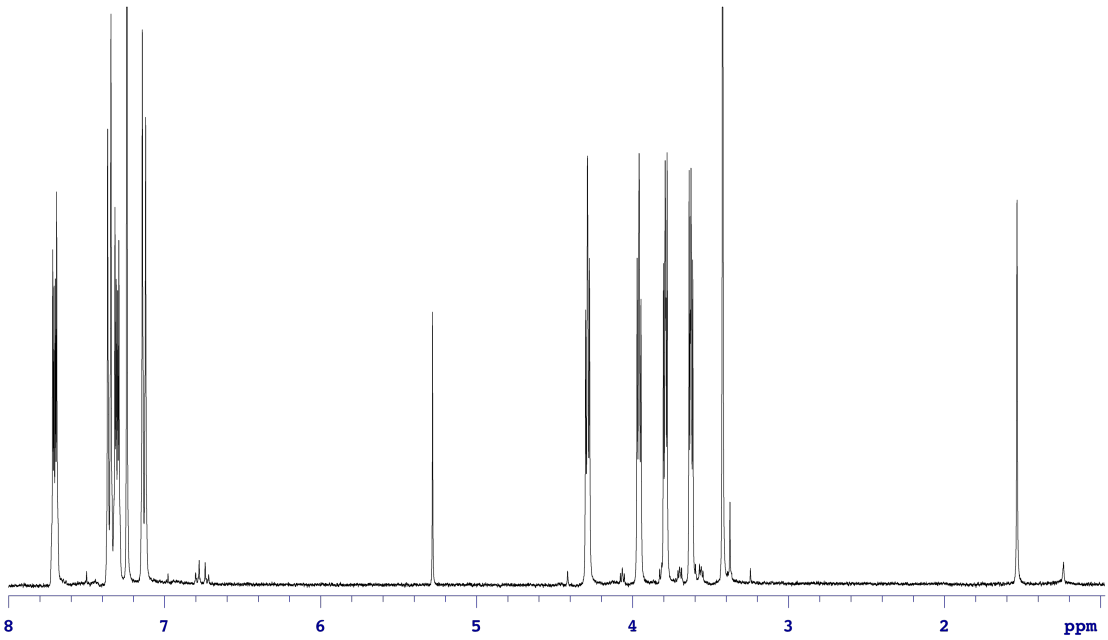

Figure A.21. ^{1}H NMR of eDdPA.

A.2.8 Dimethyl 4,4'-(naphthalene-1,4-diyl)dibenzoate (DMBN)

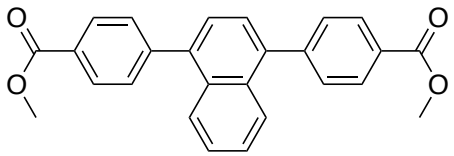

Figure A.22. Chemical Structure of DMBN.

Adapting the general procedure described in Figure 4.2 for a naphthalene center and guided by reports,[130] DBN (0.40 g, 1.4 mmol) and 4-methoxycarbonylbenzeneboronic acid (0.54 g, 3.0 mmol) were charged into a 100 mL three-necked flask and purged with N_2 for 15 min. Separately, 25 mL of diglyme was bubbled with N_2 for 15 min. Cesium fluoride (0.75 g, 4.95 mmol) and $Pd(PPh_3)_4$ (46.5 mg, 0.04 mmol), synthesized as reported and stored in a N_2 glovebox freezer,[128] were added to the reactor. The N_2 bubbled diglyme was added to the reactor *via* cannula transfer. The mixture reacted at 120 °C for 48 hours under N_2. Solvent was removed under heat and vacuum (100 °C and 100 mTorr). The remaining solid was extracted with dichloromethane, rinsed with water, then brine, and dried with $MgSO_4$. The mixture was filtered and the organic solvent was removed by rotary evaporation. The crude material was purified by column chromatography with dichloromethane as eluent. The fractions were monitored by TLC with a UV lamp. Fractions containing the desired di-substituted naphthalene product (R_f = 0.2, dichloromethane) were collected, and the solvent was removed by rotary evaporation. Residual solvent impurities were removed under high vacuum (20 mTorr, 1+ hours) to yield **DMBN** as a pale yellow powder (0.354 g, 69 % yield). The ^{1}H NMR spectrum shown in Figure A.23 is consistent with the expected structure.

^{1}H NMR (401 MHz, Chloroform-*d*): δ 8.18 (d, 4H), 7.90 (dd, 2H), 7.60 (d, 4H), 7.47 (s, 2H), 7.45 (dd, 2H), 3.97 (s, 6H).

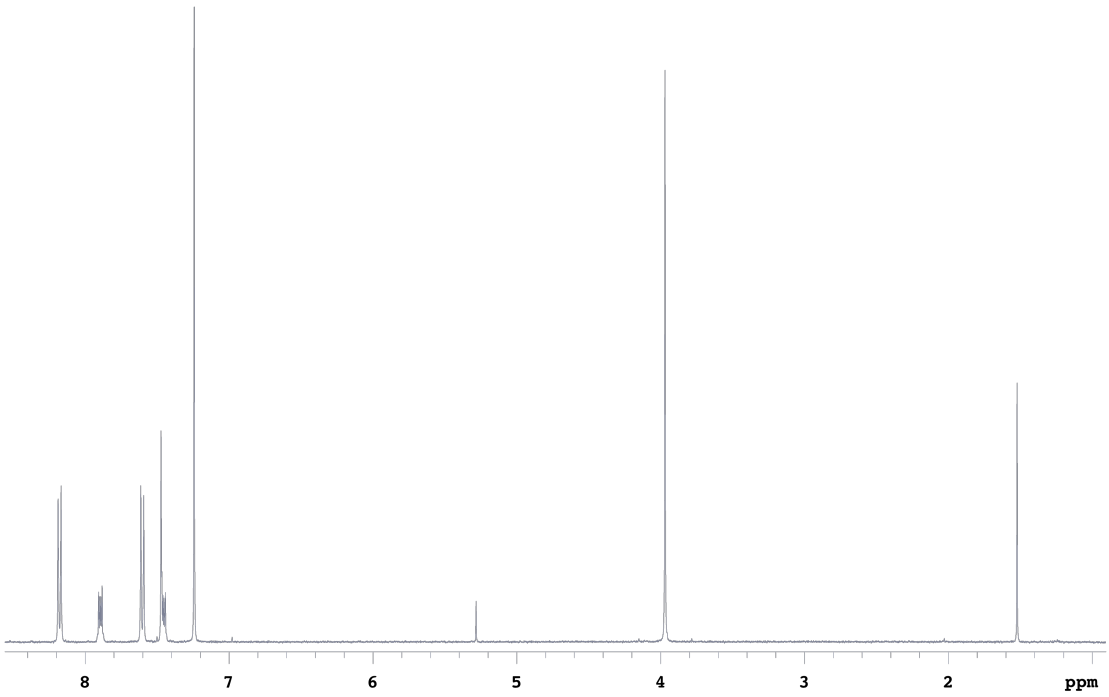

Figure A.23. ^{1}H NMR of DMBN.

A.2.9 Bis(2-(2-methoxyethoxy)ethyl) 4,4'-(naphthalene-1,4-diyl)dibenzoate (DdPN)

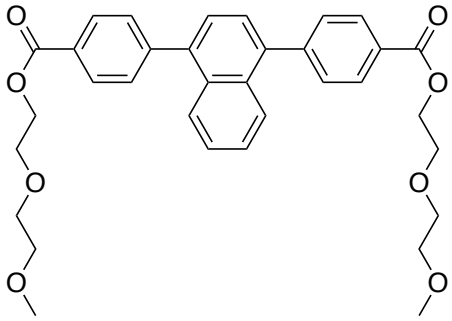

Figure A.24. Chemical structure of DdPN.

Following the general procedure described in Figure 4.6, adapted for a naphthalene center, DMBN (128 mg, 0.35 mmol) was allowed to react with 2-(2-methoxyethoxy)ethanol (3 mL, 25.5 mmol) in a Lewis acidic environment caused by $MgBr_2$-Et_2O(197 mg, 0.76 mmol) under N_2 for 24 hours at 150 °C. Remaining 2-(2-methoxyethoxy)ethanol was evaporated under vacuum (100°C and 100 mTorr). This left behind a residue of tarry brown material. This material was suspended in dichloromethane, run through a plug of silica, and washed with ethyl acetate. Washing continued until the eluent from the plug no longer had an iridescent purple color under visible light. Solvent was removed *via* rotary evaporator and the crude product was purified using column chromatography with 33% ethyl acetate in hexanes. The fractions were monitored by thin layer chromatography with a UV lamp. Fractions containing the desired trans-esterified naphthalene product (R_f = 0.2, 33% ethyl acetate in hexanes) were collected, and the solvent was removed by rotary evaporation. Residual solvent impurities were removed under high vacuum (20 mTorr, 1+ hours) to yield **DdPN** as a yellow oil (123 mg, 67% yield). The ^{1}H NMR spectrum shown in Figure A.25 is consistent with the expected structure.

^{1}H NMR (401 MHz, Chloroform-*d*): 8.20 (d, 4H), 7.90 (dd, 2H), 7.60 (d, 4H), 7.46 (s, 2H), 7.44 (dd, 2H), 4.52 (m, 4H), 3.88 (dd, J = 5.6, 3.7 Hz, 4H), 3.72 (dd, J = 5.6, 3.7 Hz, 4H), 3.62 (dd, J = 5.6, 3.7 Hz, 4H), 3.39 (s, 6H).

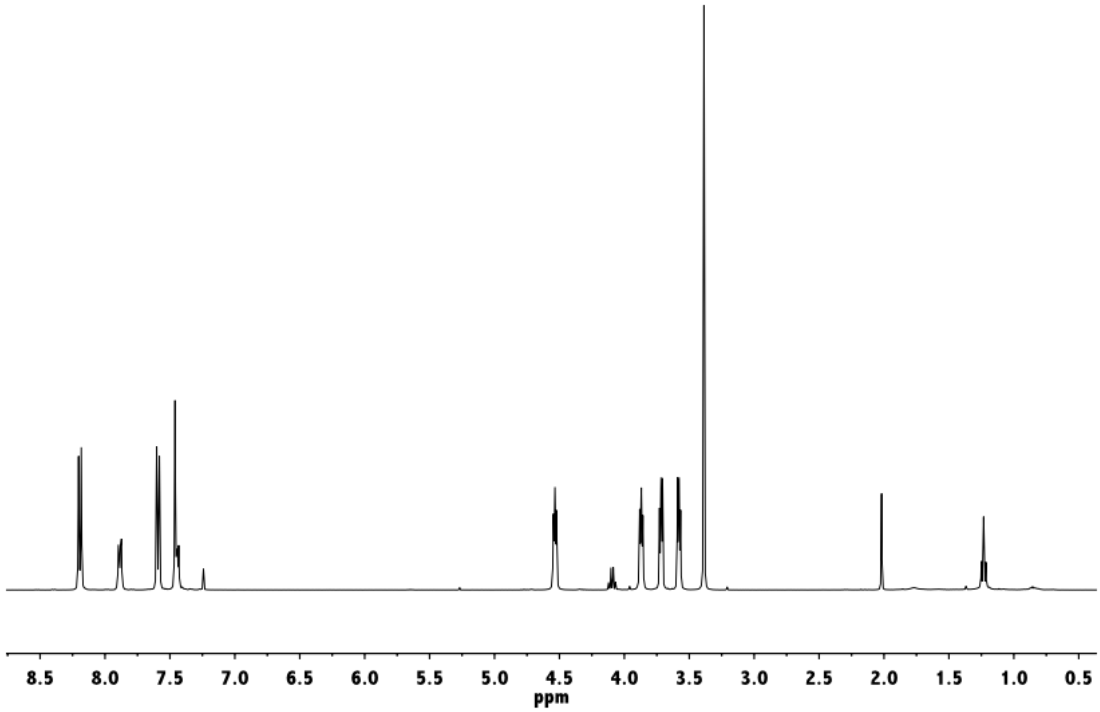

Figure A.25. ^{1}H NMR of DdPN.

A.3 Scale-Up Synthesis and Characterization

A.3.1 Scale-Up Procedure: Suzuki Coupling Using $Pd(OAc)_2$

According to the procedure of Buchwald *et al.*,[140] aryl bromide (1.0 equivalents), boronic acid (2.5 equivalents), palladium acetate (5 mol%), (2-biphenyl)dicyclohexylphosphine-2'-(*N,N*-dimethylamino)biphenyl ('DavePhos', 10 mol%) and potassium fluoride (5 equivalents) were suspended in THF (3 mL/mmol). The reaction mixture was heated to 50 °C and stirred for 16 hours under argon. The reaction mixture was partitioned between water (10 mL/mmol) and chloroform (10 mL/mmol), and the aqueous layer separated and extracted with chloroform (2 x 10 mL/mmol). The combined organic extracts were dried over $MgSO_4$ and concentrated *in vacuo*.

A.3.2 DMBA

Prepared according to the scale-up procedure in A.3.1 using DBA (10.0 g, 29.8 mmol) and 4-methoxycarbonylphenylboronic acid (13.39 g, 74.4 mmol). The crude material was purified by column chromatography with 50% dichloromethane in petroleum ether to give **DMBA** as an off-white microcrystalline solid (7.50 g, 16.8 mmol, 56%).

IR (thin film, ν_{max}/cm^{-1}) 3071, 2951, 1724, 1605, 1460, 1436, 1281, 1211, 1107;

^{1}H NMR (400 MHz, Chloroform-*d*) δ_H 8.68 (4H, d, *J* = 9.0 Hz, Ar*H*), 8.28 (4H, d, *J* = 8.5 Hz, Ar*H*), 7.61 (4H, ddd, *J* = 9.0, 6.5 and 1.0 Hz, Ar*H*), 7.58 (4H, d, *J* = 9.0 Hz, Ar*H*), 7.51 (4H, d, *J* = 8.5 Hz, Ar*H*), 7.40 (4H, ddd, *J* = 9.0, 6.5 and 1.0 Hz, Ar*H*), 4.03 (6H, s, CO_2CH_3).

^{13}C NMR (400 MHz, Chloroform-*d*) δ_C 167.1, 143.6, 136.5, 131.5, 130.7, 130.3, 129.9, 129.8, 128.1, 127.2, 127.0, 126.0, 123.5, 52.5.

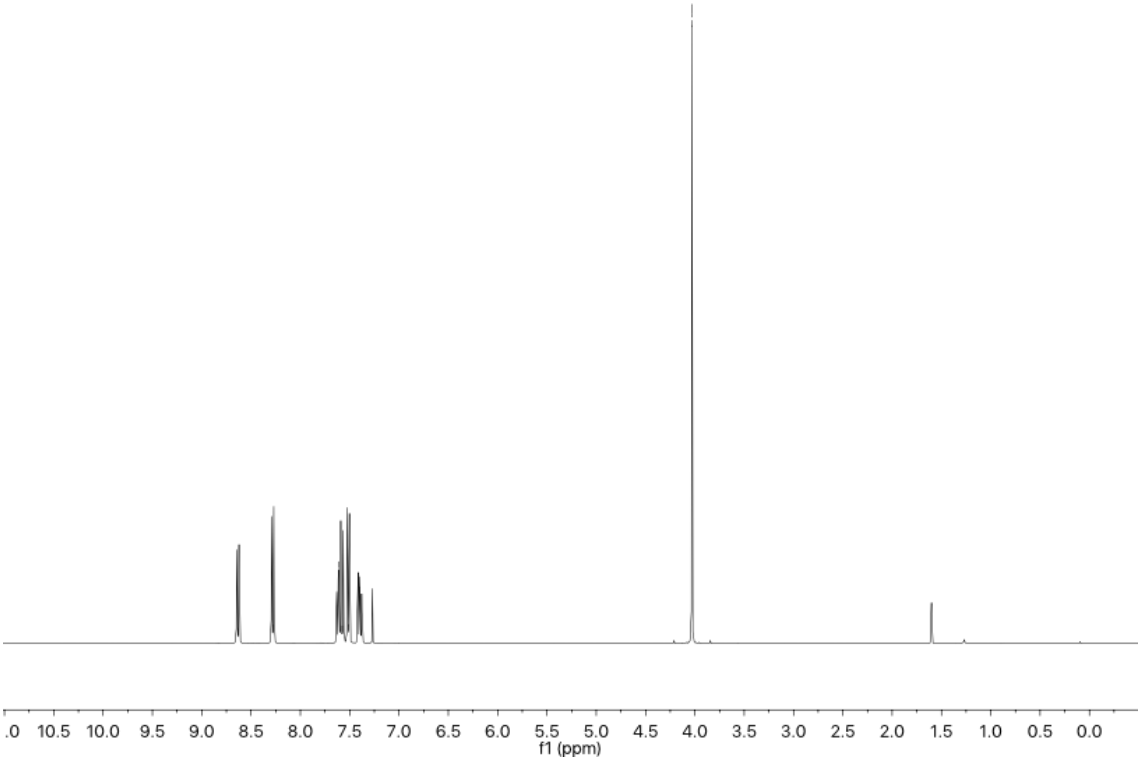

Figure A.26. ^{1}H NMR of DMBA.

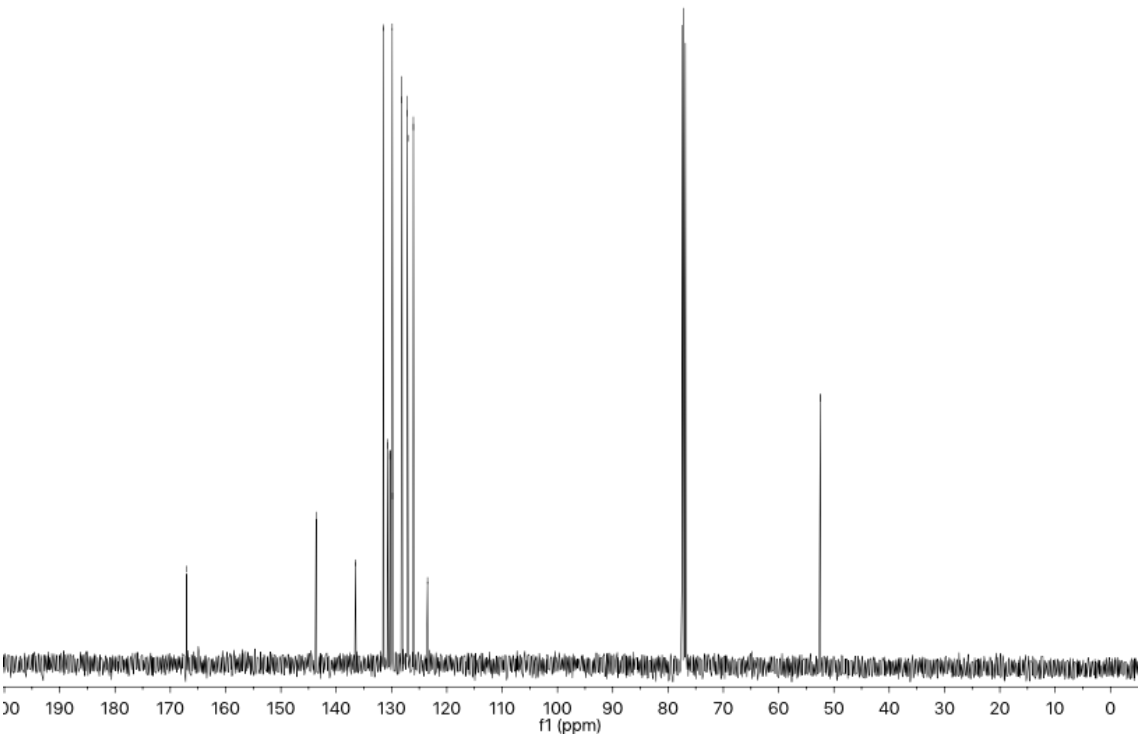

Figure A.27. ^{13}C NMR of DMBA.

A.3.3 DdPA

To a suspension of **DMBA** (7.50 g, 16.8 mmol) in 2-(2-methoxyethoxy)ethanol (39.6 mL, 336.0 mmol) and *ortho*-dichlorobenzene (168 mL), was added titanium isopropoxide (5.0 mL, 16.8 mmol) dropwise. The mixture was heated to 100 °C and stirred for 16 hours under argon. The reaction mixture was diluted with chloroform (200 mL) and water (200 mL), and the aqueous layer extracted with chloroform (2 x 200 mL). The combined organic extracts were dried over $MgSO_4$ and concentrated *in vacuo*. The crude material was washed with petroleum ether to give **DdPA** as an off-white microcrystalline solid (4.90 g, 7.9 mmol, 47%).

IR (thin film, ν_{max}/cm^{-1}) 3066, 2879, 1714, 1607, 1457, 1272, 1099, 1021;

^{1}H NMR (400 MHz, Chloroform-*d*) δ_H 8.32 (4H, d, *J* = 8.5 Hz, H7), 7.64-7.61 (4H, m, H2), 7.57 (4H, d, *J* = 8.5 Hz, H6), 7.36-7.34 (4H, m, H1), 4.61-4.59 (4H, m, H11), 3.93-3.91 (4H, m, H12), 3.77-3.75 (4H, m, H14), 2.63-3.61 (4H, m, H15), 3.42 (6H, s, C*H*$_3$).

^{13}C NMR (400 MHz, Chloroform-*d*) δ_C 166.6, 144.2, 136.4, 131.5, 130.0, 129.6, 126.7, 125.6, 72.1, 70.8, 69.5, 64.4, 59.3.

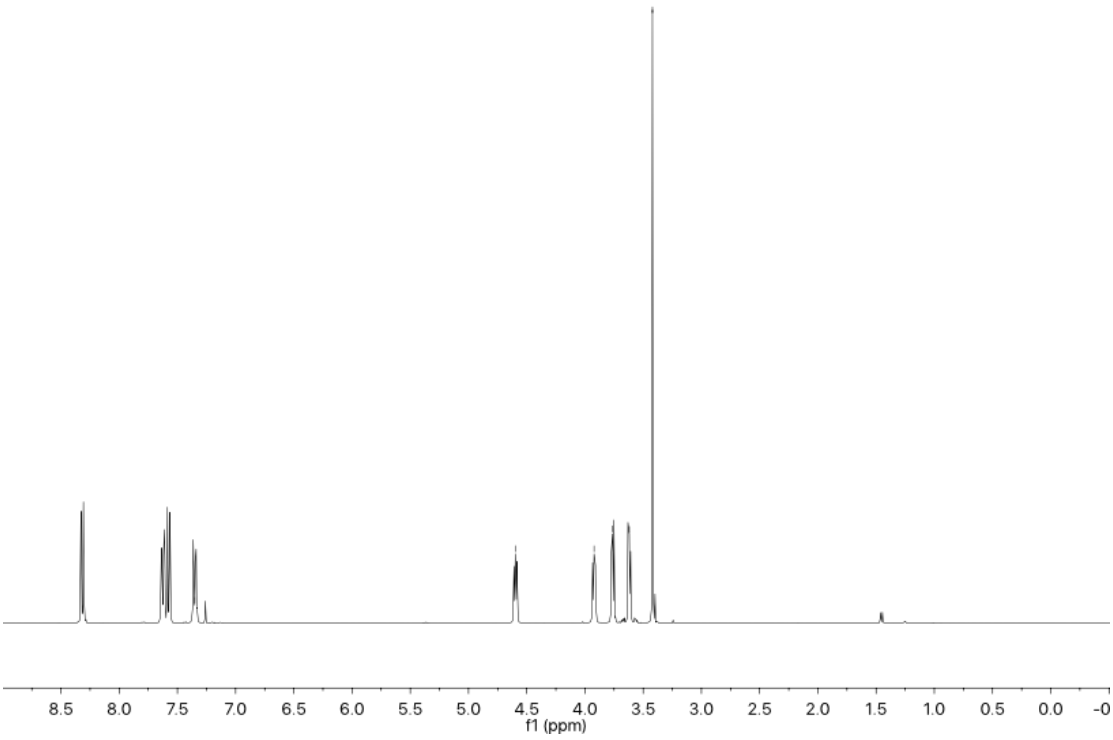

Figure A.28. ^{1}H NMR of DdPA.

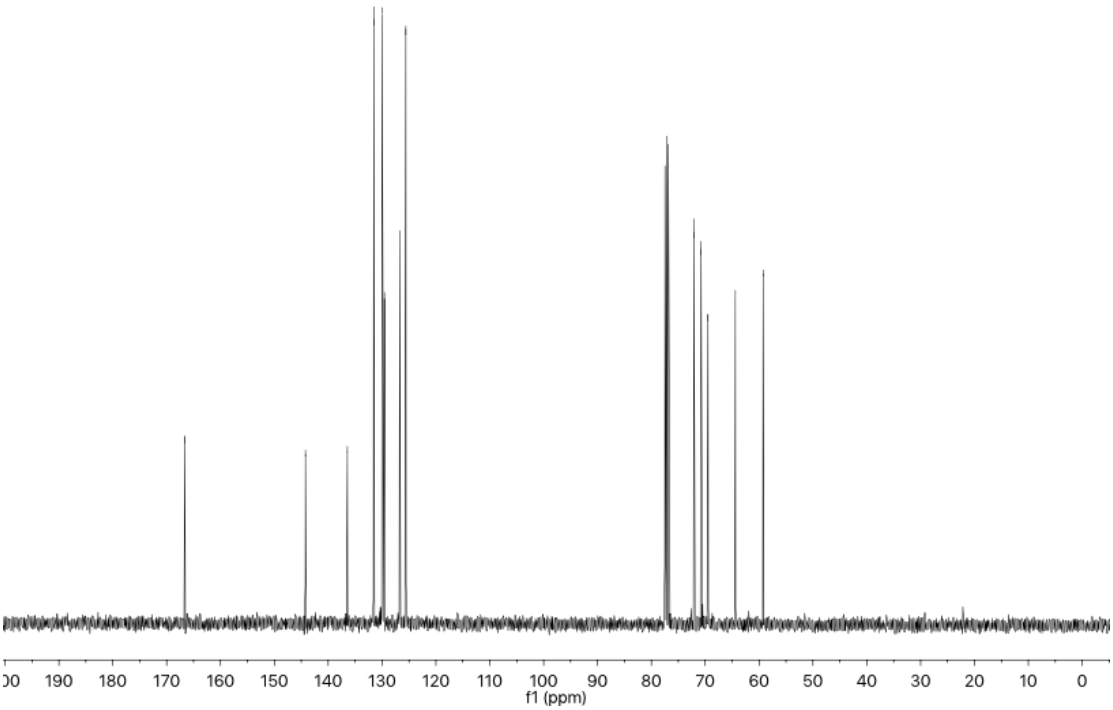

Figure A.29. ^{13}C NMR of DdPA.

A.3.4 DMBN

Prepared according to the scale-up procedure in A.3.1 using DBN (10.0 g, 35.0 mmol) and 4-methoxycarbonylphenylboronic acid (13.2 g, 73.4 mmol). The crude material was purified by column chromatography with 50% dichloromethane in petroleum ether to give **DMBN** as an off-white microcrystalline solid (10.8 g, 27.1 mmol, 78%).

IR (thin film, ν_{max}/cm^{-1}) 2951, 1721, 1608, 1435, 1276, 1179, 1119, 1102;

^{1}H NMR (400 MHz, Chloroform-*d*) δ_H 8.20 (4H, d, *J* = 8.5 Hz, Ar*H*), 7.93-7.90 (2H, m, Ar*H*), 7.62 (4H, d, *J* = 8.5 Hz, Ar*H*), 7.48 (2H, s, Ar*H*), 7.48-7.46 (2H, m, Ar*H*), 3.99 (6H, s, CO_2CH_3).

^{13}C NMR (400 MHz, Chloroform-*d*) δ_C 167.1, 145.5, 139.5, 131.7, 130.3, 129.8, 129.3, 126.5 (2C), 126.3, 52.4.

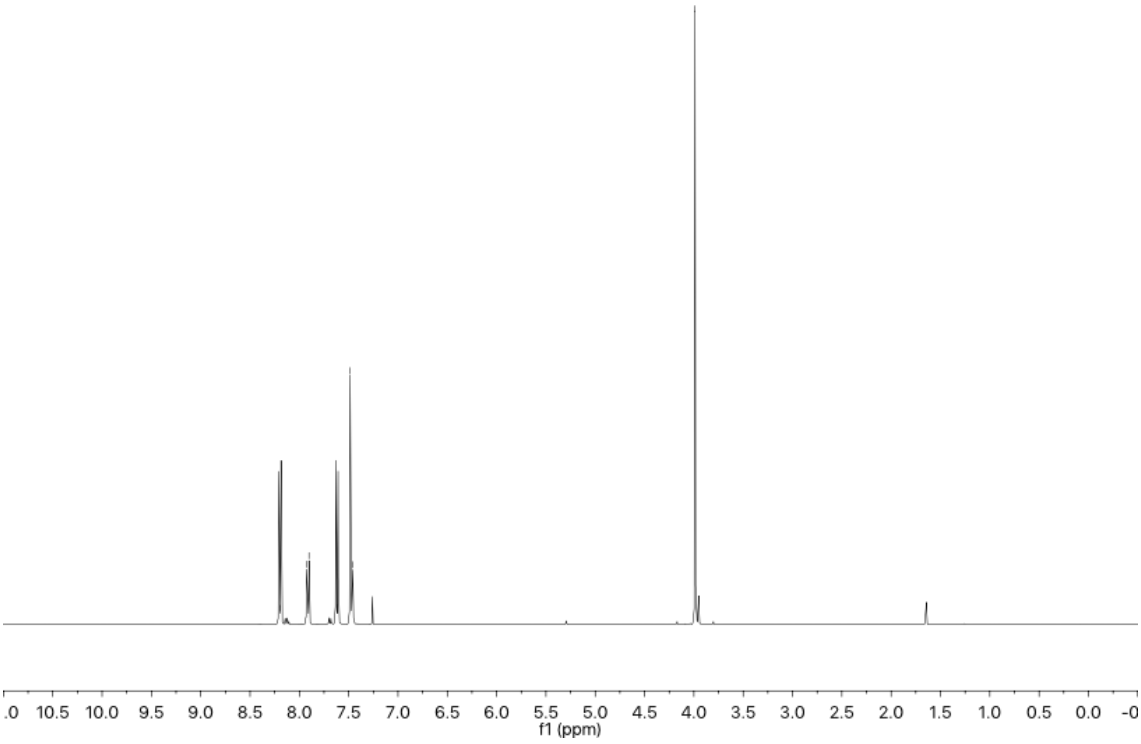

Figure A.30. ^{1}H NMR of DMBN.

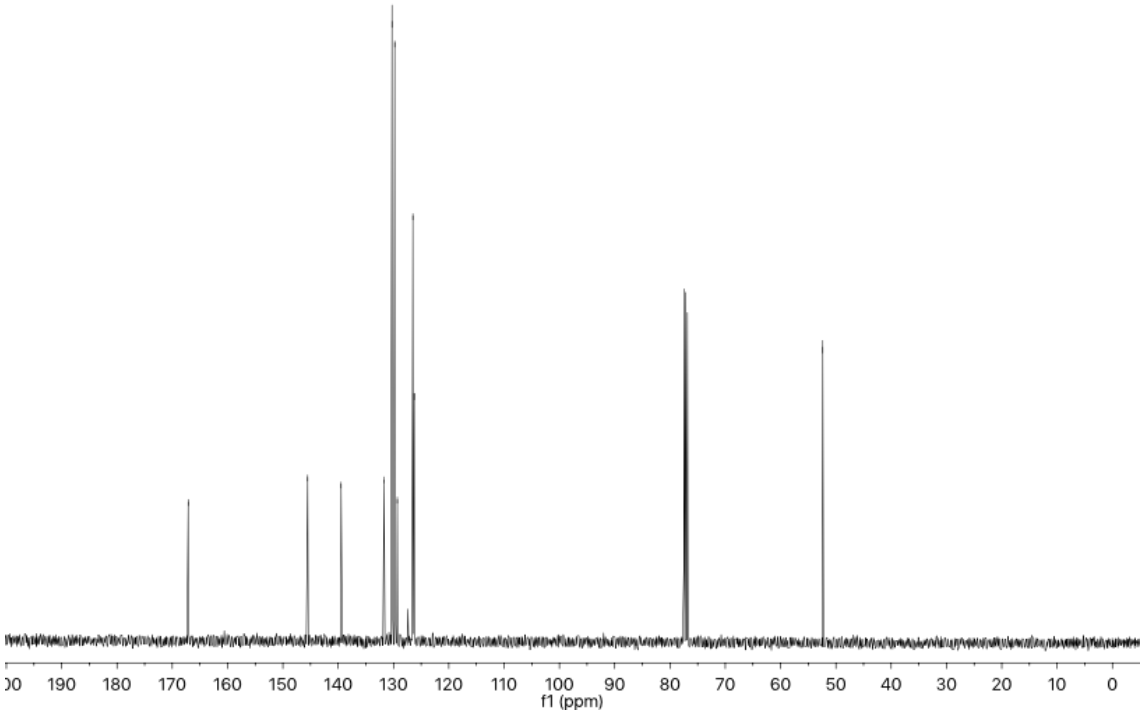

Figure A.31. ^{13}C NMR of DMBN.

A.3.5 DdPN

To a suspension of **DMBN** (9.0 g, 22.7 mmol) in 2-(2-methoxyethoxy)ethanol (227 mL) was added titanium isopropoxide (6.76 mL, 22.7 mmol) dropwise. The mixture was heated to 100 °C and stirred for 16 hours under argon. The reaction mixture was diluted with chloroform (20 mL) and water (200 mL), and the aqueous layer extracted with chloroform (2 x 200 mL). The combined organic extracts were dried over $MgSO_4$ and concentrated *in vacuo*. The crude material was purified by column chromatography with 50% ethyl acetate in petroleum ether to give **DdPN** as a brown oil (8.2 g, 14.3 mmol, 63%).

IR (thin film, ν_{max}/cm^{-1}) 3043, 2877, 1716, 1607, 1452, 1269, 1179, 1098

^{1}H NMR (400 MHz, Chloroform-*d*) δ_H 8.21 (4H, d, *J* = 8.5 Hz, Ar*H*), 7.92-7.89 (2H, m, Ar*H*), 7.61 (4H, d, *J* = 8.5 Hz, Ar*H*), 7.48 (2H, s, Ar*H*), 7.48-7.45 (2H, m, Ar*H*), 4.56-4.54 (4H, m, $CO_2CH_2CH_2$), 3.90-3.88 (4H, m, $CO_2CH_2CH_2$), 3.75-3.72 (4H, m, $CH_2CH_2OCH_3$), 3.61-3.59 (4H, m, $CH_2CH_2OCH_3$), 3.41 (6H, s, OCH_3).

^{13}C NMR (400 MHz, Chloroform-*d*) δ_C 166.5, 145.5, 139.4, 131.6, 130.2, 129.9, 129.2, 126.5 (2C), 126.2, 72.0, 70.7, 69.4, 64.3, 59.2.

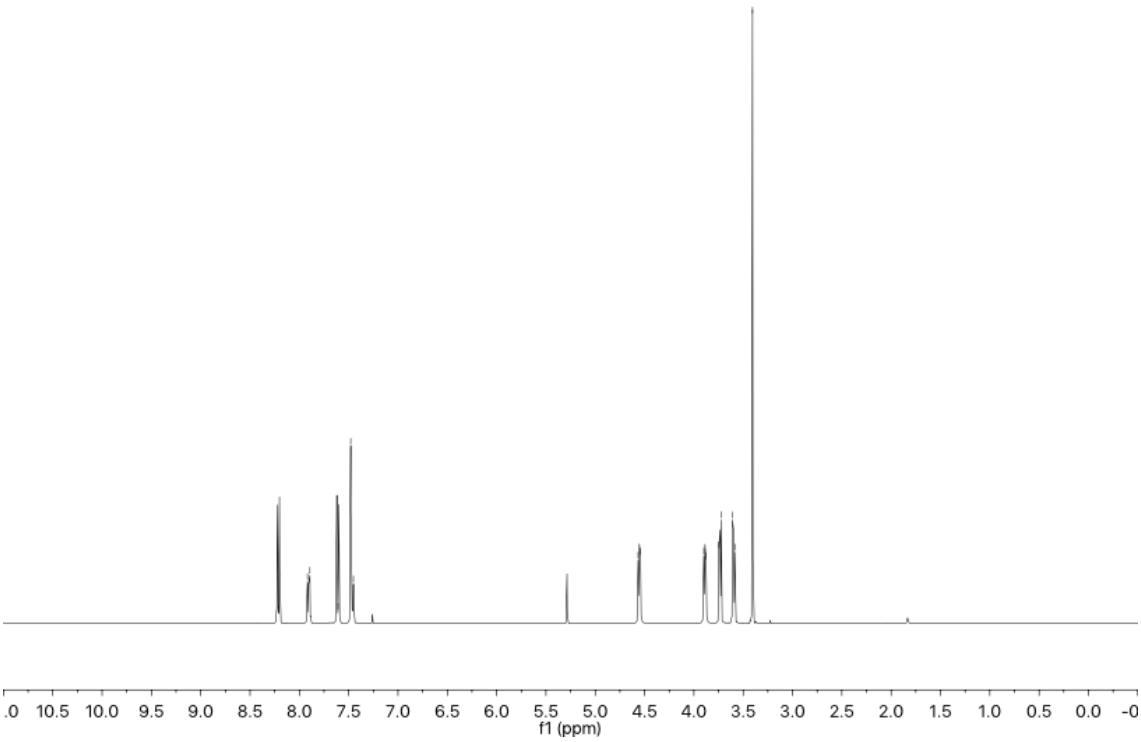

Figure A.32. ^{1}H NMR of DdPN.

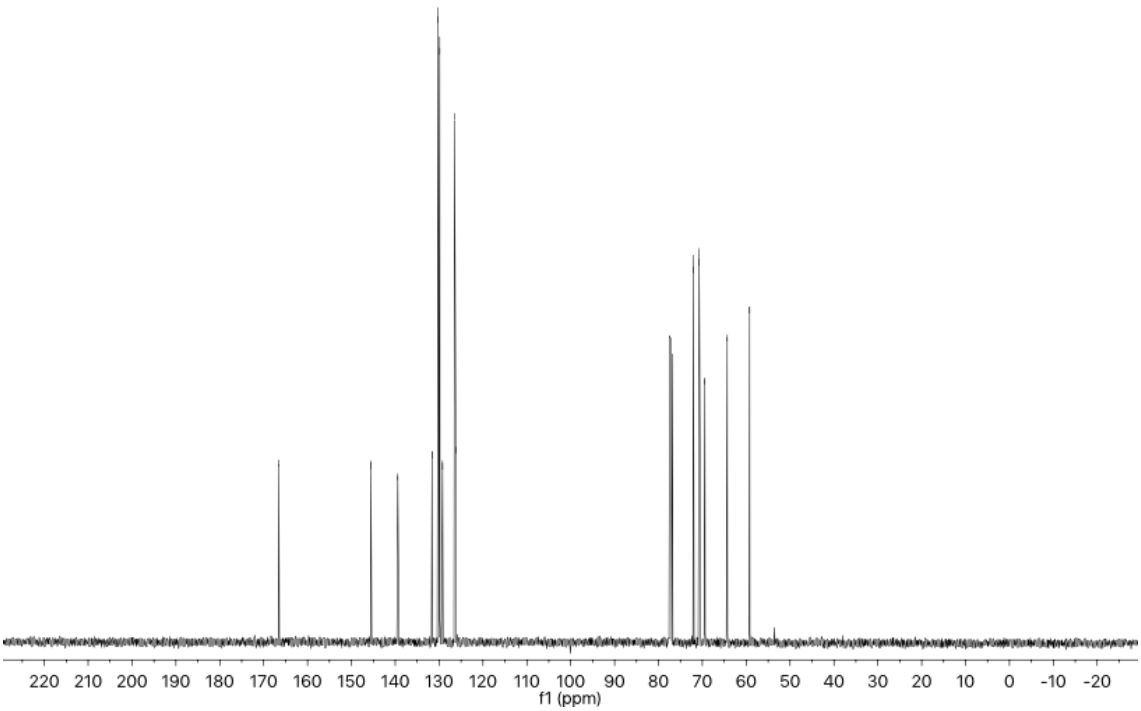

Figure A.33. ^{13}C NMR of DdPN.

Appendix References

128. Cotton, F. A., *Inorganic Syntheses*. McGraw-Hill, Inc.: 1972; Vol. 13, p 121-124.

129. S. Kotha, A. G., K. Deodhar, Synthesis of Symmetrical and Unsymmetrical 9,10-Diarylanthracene Derivatives via Bis-Suzuki-Miyaura Cross-Coupling Reaction. *Synthesis* **2004,** *4*, 0549-0557.

130. Hauptvogel, I. M.; Biedermann, R.; Klein, N.; Senkovska, I.; Cadiau, A.; Wallacher, D.; Feyerherm, R.; Kaskel, S., Flexible and Hydrophobic Zn-Based Metal-Organic Framework. *Inorganic Chemistry* **2011,** *50* (17), 8367-8374.

139. Player, M.; Meegalla, S.; Illig, C.; Chen, J.; Wilson, K.; Lee, Y.-K.; Parks, D.; Huang, H.; Patel, S.; Lu, T. PDE 10 A Inhibitors for the Treatment of Type II Diabetes. 2014.

140. Wolfe, J. P.; Singer, R. A.; Yang, B. H.; Buchwald, S. L., Highly Active Palladium Catalysts for Suzuki Coupling Reactions. *Journal of the American Chemical Society* **1999,** *121* (41), 9550-9561.